Measuring The Star Formation Rate Density from CNOC2

Richard James Whitaker

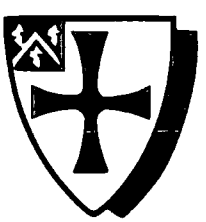

University of Durham

February, 2006

A thesis submitted to the University of Durham
in accordance with the regulations for admission to the
Degree of Doctor of Philosophy.

Abstract

This thesis charts the evolution of the Universal Star Formation Rate Density (SFRD) across the redshift range $0.2 \lesssim z \lesssim 0.6$, using the 2nd Canadian Network for Observational Cosmology Survey (CNOC2). The redshift range covered by the Survey marks an important transitional period in the history of the Universe, over which the SFRD is thought to undergo rapid evolution.

The various Star Formation Rate (SFR) indicators from the literature are reviewed and it is shown that the [O II] forbidden emission line can provide a very similar SFR to that reported by the Hα recombination line, if reddening is accounted for.

We explain the CNOC2 Survey in detail, including the observation strategy and the instrumentation used. The Survey weighting scheme is also discussed.

The purpose written code, used to measure the strengths of the [O II] emission line in each of the Survey spectra, is explained and tested, against both another automated code and by-eye measurements from IRAF. The procedure of re-normalising the [O II] equivalent width errors that are reported by the code is also detailed. This leaves the line measurement errors very well quantified.

We investigate the accuracy of the photometric redshift codes ImpZ and Hyperz in returning dust estimates, A_V from photometry alone. The benchmark for this comparison is set by Balmer Decrement measurements of a sub-set of the CNOC2 dataset.

Combining the [O II] line strength measurements with the dust correction from the photometric redshift code ImpZ, we compute SFRs for individual galaxies in the CNOC2 Survey. These are combined with a weighting scheme to chart the evolution of SFRD with redshift and luminosity.

It is found that giant galaxies undergo a strong evolution in terms of the fraction of those galaxies that are rapidly star forming, but that the absolute SFRD from giants does not change as quickly as that from lower luminosity galaxies.

At all redshifts and luminosities covered by the Survey, galaxies with [O II] emission < 30Å contribute roughly half the total SFRD. This means narrow band imaging surveys may miss a large fraction of star formation activity at those epochs.

At $z \sim 0.25$ it is found that dwarf galaxies dominate the overall SFRD, in-keeping with results from the local Universe.

We produce a best estimate Lilly-Madau plot based on our findings and compare it to several studies from the literature. It is shown that although the overall rise found by previous studies is confirmed, the shape of the rise is not consistent with other works, showing a sharper increase at low ($0.2 \lesssim z \lesssim 0.4$) redshift followed by a slowing at $z \sim 0.6$. The significance of this result remains unquantified however.

Declaration

The work described in this thesis was undertaken between October 2002 and February 2006 whilst the author was a research student under the supervision of Dr. S. Morris in the Department of Physics at the University of Durham.

With the exception of some sections of Chapter 3 (detailed below), none of the work presented here has been submitted for any other degree at this, or any other, university.

Chapter 3 was written in collaboration with Dr. S. Morris of the University of Durham and Dr. T. S. R. Babbedge of Imperial College London and has been published in the following paper.

- Babbedge, T. S. R.; Whitaker, R.; Morris, S. Monthly Notices of the Royal Astronomical Society, Volume 361, Issue 2, pp. 437-450

I am solely responsible for the work presented in Sections 3.2.2, 3.2.3, 3.2.4 and 3.2.5 of Chapter 3; the remaining sections of that chapter were either written by Dr. Morris, Dr. Babbedge or a combination of all three authors.

Acknowledgments

I owe very many people a great deal of thanks for helping me along the way with this thesis, both in terms of academic input, but also, and at least equally as importantly, in terms of encouragement and friendship. I am very grateful to my supervisor, Simon Morris, without whose expert tutelage and guidance this thesis would not be. I am also deeply indebted to my fellow students with whom I have shared my life in Durham. Claudio Dalla Vecchia, Noam Libeskind and Rob Crain all receive a special mention: office mates of the highest calibre. I hope that they enjoyed my company as much as I enjoyed theirs.

There are so many other people who I want to mention in these acknowledgments. In Durham: Mark Swinbank, Craig Booth, Bill Frith, John Helly, Carlton Baugh, and Jurgen Schmoll; around the world: Duncan Forbes, Keith Knoll, Alan Dressler, Nelson Padilla, and Alejandra Romano. Thank you all.

Thank you to my house mates, Dave Haigh, Mark Morley-Fletcher and Greig Coull. It was excellent to share with you (The Peth in particular). Thank you also to all at Ustinov College Pool League, especially Vicky Jupp, Christophe Grosjean, Romain Fournier, Ian Vernon, and Frankie - four fingers - Chau (barman extraordinaire).

From St Nic's I want to thank David and Rosemary Day (thank you so much for all your kindnesses), and Tim and Hannah Murray.

I am exceedingly grateful to my family for all their support. To my Mum, Dad, and to my brothers Andrew and James, thank you.

Finally, and above all, I am thankful to God, for making a Universe that we can enjoy, study and even understand; and also to Emma, my wonderful wife. Thank you for all your love and encouragement.

Richard Whitaker

God made two great lights – the greater light to govern the day and the lesser light to govern the night. He also made the stars. God set them in the expanse of the sky to give light on the earth, to govern the day and the night, and to separate light from darkness. And God saw that it was good.

Genesis, Chapter One

Contents

List of Tables

List of Figures

1

The Estimation Of Star Formation Rates

This thesis measures Star Formation Rates (SFRs) in distant galaxies. Understanding how to measure these rates is therefore essential. In this chapter I present a review of different methods for measuring the SFRs of galaxies – so-called SFR indicators. I explain the physical reasons which underpin each indicator's relation to the true SFR and explain the problems and shortcomings associated with each one.

I begin with a discussion of the motivation for studying the evolution of SFRs and then present a very short overview of the historical advancement of the field. I then introduce the Initial Mass Function, and discuss its importance to SFR measurement. I also explain the use of Population Synthesis Models in calibrating the indicators. The indicators themselves are then described in detail, and a comprehensive inter-comparison is made. Particular conclusions are drawn on the use of the [O II] line luminosity as a SFR indicator and the various [O II]-SFR calibrations available in the literature are assessed.

1.1 Motivation for studying the evolution of SFRs

The goal of astrophysics is to understand the universe, to study what it was like in the past and hence predict what it might be like in the future.

A question which is central to this goal is how do galaxies form? There are essentially two main competing ideas: the classical picture of monolithic collapse (e.g. Larson 1974) and the hierarchical picture in which clumps of matter join together over time to form galaxies (e.g. White and Frenk 1991).

Star formation is a process that is key to the formation of galaxies. Indeed the concept of galaxy formation is linked to when the stars within a galaxy "turn on" or ignite. Being able to understand how the star forming properties of galaxies vary with redshift therefore helps us to distinguish between the various theories.

Thankfully, star formation is a process that is detectable by a number of means. Young, hot stars have a large impact on a galaxy's spectral energy distribution; these effects are observable in a number of ways depending on the amount of dust within the galaxy. The methods for detecting star formation are discussed in the remainder of the chapter.

1.2 Historical Overview

The first quantitative SFRs were derived by Tinsley (1968) and Searle et al. (1973). They were based on stellar population models of galaxy colours in which one fits the observed SED of a galaxy with a linear combination of stellar spectra, taken from a large library. A problem arises that the number of free parameters in the fit becomes too large to be constrained by typical quality spectra.

Nowadays, SFR indicators rely on evolutionary population synthesis models in which there are only a small number of parameters, typically the Initial Mass Function, the SFR and the metallicity. How these models are used will be explained in Section 1.4.

1.3 The Initial Mass Function

Stars form during the collapse of giant clouds of dust and gas. The distribution of stellar masses that arises from the collapse of a cloud is known as the Initial Mass Function (IMF).

The universality of the IMF is something upon which each and every SFR indicator's calibration relies. The reason for this crucial dependence is that SFR indicators generally detect only the highest mass stars produced during an episode of star formation (this is because those stars are the most luminous and hence dominate the radiation field). With the information from the highest mass stars, the indicators then have to use the IMF to extrapolate across the distribution of stellar masses and determine how many stars have been produced in total. Changes in the IMF therefore result in different SFRs for a given amount of flux from high mass stars.

Certain indicators have an especially strong dependence on the IMF because they only capture information from the *very* highest mass stars at the top of the IMF. Other indicators have a lesser dependence on the IMF because they are sensitive not only to the very highest mass stars, but also to those slightly further down the IMF.

If the IMF is shown to be changing with cosmic epoch, or environment, then the SFR indicator calibrations would also require modification to compensate for this.

The IMF is described by a series of power-laws across different mass intervals. The number of stars, dN, in a mass interval m to $m+dm$ is a function of the mass of the stars m, such that

$$dN \propto m^{-\gamma} dm, \tag{1.1}$$

where γ is referred to as the slope of the IMF.

The first measurement of the IMF was made by Salpeter (1955), using stars in the solar neighbourhood, over a somewhat limited mass range ($0.4\mathrm{M}_{\odot} \lesssim \mathrm{M} \lesssim 10\mathrm{M}_{\odot}$). Today the IMF has been measured for a much larger range of stellar masses, from sub-solar-mass Brown Dwarfs, to very high mass stars.

The original Salpeter determination placed $\gamma = 2.35$, although for higher mass stars Scalo (1986) measured a value of $\gamma \sim 2.7$, which is often employed today. Massey (1998) measured a Salpeter IMF over an extended range of stellar masses (up to $M \sim 120\mathrm{M}_{\odot}$) and across a large range in metallicity and environment density. There are recent determinations of the IMF in the literature, although the most widely used in SFR studies remain those of Salpeter (1955), Miller and Scalo (1979) and Scalo (1986).

The measurement of the IMF can be either relatively simple or complicated, depending

on the population under examination. For a coeval population of stars, one measures the slope of the so-called Present Day Mass Function (PDMF)[1]. This will have the same slope as the original IMF, since at any time after the star formation event it is only the higher mass stars which will have evolved and hence been removed from the mass distribution function. The lower mass stars will be remain very similar to as they were at birth. Typically, masses are measured either using a mass-to-light ratio or, more accurately, spectrometry. For mixed age populations the determination of the IMF is a more complex procedure. Massey (1998) provides a review of the necessary methodology.

Thankfully, the potential source of complication from a changing IMF is avoided. There is evidence that the IMF has a very similar form over a wide range of cosmic conditions. These include the Galactic Bulge (Holtzman et al., 1998), the LMC (Holtzman et al., 1997), the Ursa Minor dwarf galaxy (Wyse et al., 2002) and several Globular Clusters (Paresce and De Marchi, 2000). In addition, Gilmore and Howell (1998) show there is little evidence for IMF variation across star-forming galaxies. Nevertheless, we note that *every* indicator reports a total SFR that possesses an underlying uncertainty due to the shape of the assumed IMF.

1.4 Synthesis Models

The integrated light from galaxies contains within it information about their previous Star Formation History (SFH) and current SFR. Since stars are among the building blocks of galaxies, the ability to extract information relating to the SFR from a galaxy's spectral energy distribution (SED) requires an understanding of stellar evolution. Furthermore, the ability to correlate a certain feature in a galaxy's spectrum with the SFR requires models of stellar evolution which can accurately predict observable quantities of stars as a function of age and chemical composition. To this end, as well as depending on the IMF, each and every SFR indicator is reliant ultimately upon a set of synthesis models for their calibration. A description of how these models are constructed and used is therefore warranted. For a more comprehensive discussion the reader is referred to Kennicutt (1998) and Bruzual and Charlot (2003).

As indicated in Section 1.2, the first studies to interpret integrated galaxy light fit

[1]The Present Day Mass Function is analogous to the IMF, the difference being that it describes the current distribution of stellar masses, not the initial one.

the observed colours with linear combinations of individual stellar spectra, drawn from an extensive library. Notable exponents of this approach include Spinrad and Taylor (1971) and Faber (1972). The problem with this approach is that too many free parameters exist and the typical quality of spectra is not sufficient to constrain these accurately.

Today, the method of choice is to employ evolutionary population synthesis models which are able to predict the positions of stars on the HR diagram as a function of age and chemical composition. We begin with a grid of stellar evolution tracks for various masses and metallicities of star. These output effective temperatures and bolometric luminosities. Using atmosphere models, the temperatures are converted into spectra.

The spectra of individual stars of the same age are summed together, weighted by the IMF, producing so-called isochrones. These isochrones are summed together in linear combinations to model the observed SEDs.

Knowing the relative contributions of each stellar type, one is then able to estimate the SFH and current SFR. We note that both "nebular" emission (from gas around young stars) *and* extinction from dust must also be modelled when trying to understand the SED of a galaxy.

It is important to note that there are particular phases of stellar evolution that, even today, are not well understood. An example is the thermally-pulsating asymptotic giant branch (AGB); this is not well modelled by any current stellar evolution code. Because stars in such phases tend to be very bright they have a considerable impact on a galaxy's SED. For these reasons many authors prefer an empirical approach to ill-understood phases. The lack of understanding of complex stellar evolutionary phases is considered to be the single largest cause of error and disagreement between different models. Obviously it also leads to potential problems with their subsequent use in SFR calibrations.

Figure 1.1 shows the movements of a $5M_{\odot}$ star around the HR diagram (taken from Carroll and Ostlie, 1996). The star leaves the Main Sequence when its core of hydrogen has been exhausted; as hydrogen burning continues in the shell surrounding the core the star expands in size and heads up the Red Giant Branch (RGB). At the top of the RGB He burning begins and the star moves blueward. As He in the core is exhausted the star moves redward again and up the AGB. He shell burning at this stage produces explosions in the star, known as Helium Flashes; it is these explosions that cause the star to pulsate and give rise to the name of this stage of evolution: the thermally-pulsating asymptotic

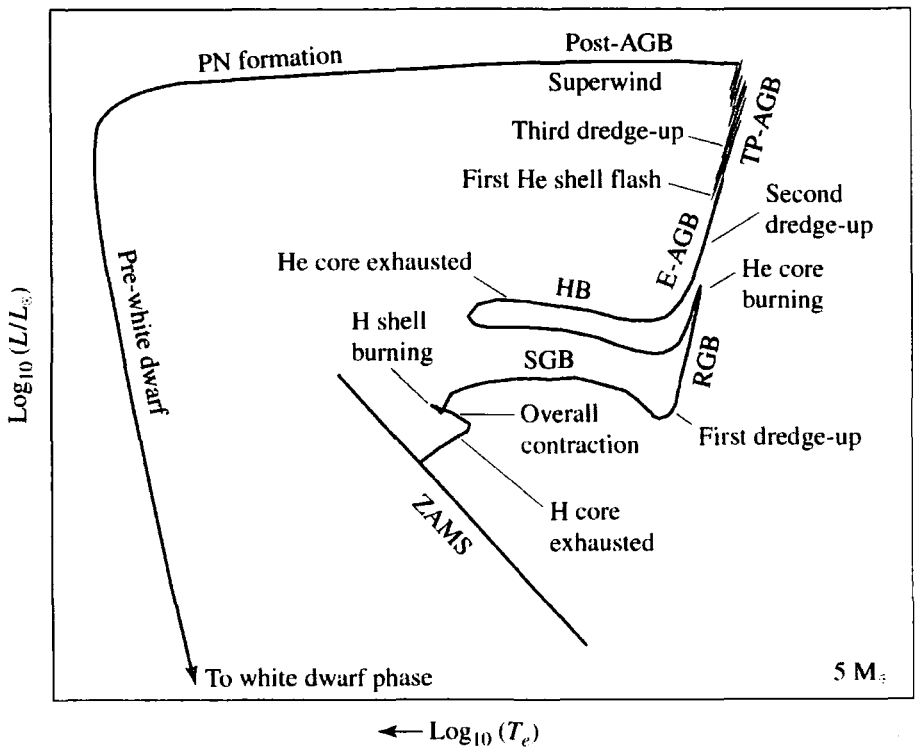

FIGURE 1.1: The movements of a $5M_{\odot}$ star around the HR diagram. The figure has been taken from Carroll and Ostlie (1996).

giant branch. The explosions are very difficult to model and so the properties of stars in this phase are difficult to predict. After this stage the star either goes supernova (not shown), or expels its outer envelope and creates a planetary nebula on its way to becoming a white dwarf. The planetary nebula phase drives the star swiftly through a very blue position on the HR diagram

As we will see with certain indicators, the further down the IMF they probe, the more some of them are affected by stars in the latter stages of evolution (i.e. those stars not on the Main Sequence). The largest stars simply go supernova after leaving the Main Sequence and so produce no additional flux after that stage; lower mass stars ($3M_{\odot} < M_{star} < 5M_{\odot}$) on the other hand move around the HR diagram (as described above) and hence move in and out of phases that produce ionising radiation. Most of the indicators are sensitive to this radiation, which mimics that produced by young stars, hence producing confusing results.

The reader is referred to Iben (1967) for a further discussion of stellar evolution.

1.5 Star Formation Indicators

I now review the most commonly used SFR indicators in the literature. The discussion of each indicator is split into three sections, the first explaining the physics behind the use of the particular indicator and the underlying reasons why it *should* be an accurate tracer of the SFR. Secondly, the problems and caveats associated with that indicator are discussed and thirdly a micro-bibliography of its usage in galaxy surveys is presented. An inter-comparison of the indicators is presented in Section 1.6.

The following SFR indicators are presented: U-band, U.V., FIR, Radio, Hα, [O II], X-ray and a unique method of Heavens et al. (2004).

Before I examine each one in turn, there are several points which should be noted; these are applicable to each and every indicator, with the exception of the Heavens et al. technique.

Firstly, one might assume that a so-called "SFR" measured by any of the following methods is the *instantaneous SFR at the present day.* In reality, the indicators communicate to us an echo of the actual star formation event, and the rates we measure are therefore based on that echo. An example of this might be the Far Infrared Continuum luminosity which, since it relies on the heating and subsequent re-emission from dust grains around young stars, has a certain lag time in responding to star formation. In a similar manner, radio emission at 1.4 Ghz is only sensitive to the *death* of large stars, not their formation; this means it necessarily lags the stellar birth by approximately the lifetime of the largest stars (they are the first to go supernova, causing the radio emission). Every indicator suffers a certain lag time in responding to star formation. As stated above, radio emission suffers from a lag equal to the lifetime of the highest mass stars, some $\sim 10^7$yr. Alternatively, Hα emission is initiated relatively shortly after a star formation event, almost as soon as the highest mass stars join the Zero Age Main Sequence. Most lag times are short compared to the Hubble Time (see Appendix A), but nevertheless it still means that the rates measured are not truly instantaneous.

Secondly, as we have already mentioned, the indicators are in general only sensitive to the number of high mass stars formed in a given event, and *not* the full range of stellar masses. The SFR returned by any indicator hence relies crucially on extrapolation across the IMF, from high mass stars to low mass ones. An additional note is that different

indicators are dominated by the contribution of slightly different stellar mass ranges, and so this naturally means that some require greater extrapolation than others. It must be noted that the fitting of synthesis models to an SED is not sensitive to only high mass stars, since by their very nature synthesis models take contributions from all masses of star contributing to the SED into account. The underlying concept behind all the other methods remains the same however: To obtain some measure of the number of large stars present today and then by extrapolating over the IMF, compute the total SFR.

With the above subtleties in mind, we now examine each of the indicators in turn.

1.5.1 U-Band Luminosity

Physics

Certain stellar types dominate the integrated flux from a galaxy at particular wavelengths and hence the intrinsic colours of a galaxy are (to first order) related to the ratio of young to old stars contained within it. It is known for example that main sequence A – F stars and G – K giants provide the majority of the light over the optical wavelengths of any galaxies' spectrum (e.g. Kennicutt, 1998) whereas older stars dominate the K-band light in the Near Infrared. K-band measurements are often used as a tracer of the older, underlying stellar mass in galaxies (see e.g. Barger et al., 1996, who exploit this by measuring the K-band galaxy luminosity function to trace the evolution of mass in galaxy clusters). In principle then, the observed colours should be able to provide us with an estimate of the young (or indeed old) stellar content of galaxies.

Synthesis models can be used to produce predictions of colours as a function of age, or – more usefully for this discussion – SFR per unit mass or luminosity, allowing us, very crudely, to measure SFRs from simple photometric observations. Indeed, this is how the first investigations into SFRs of galaxies were conducted. If the colours can provide an (albeit crude) estimate of the SFR, what about the broadband luminosity by itself?

The U-band ($\lambda \sim 3600$Å) is the optical band which is most sensitive to newly formed stars (in a very similar fashion to the UV, which is discussed below; a few additional caveats apply to the U-band however). In starburst galaxies, this region of the spectrum is dominated by contributions from young stellar populations. One might assume therefore that it could be an accurate tracer of star formation activity.

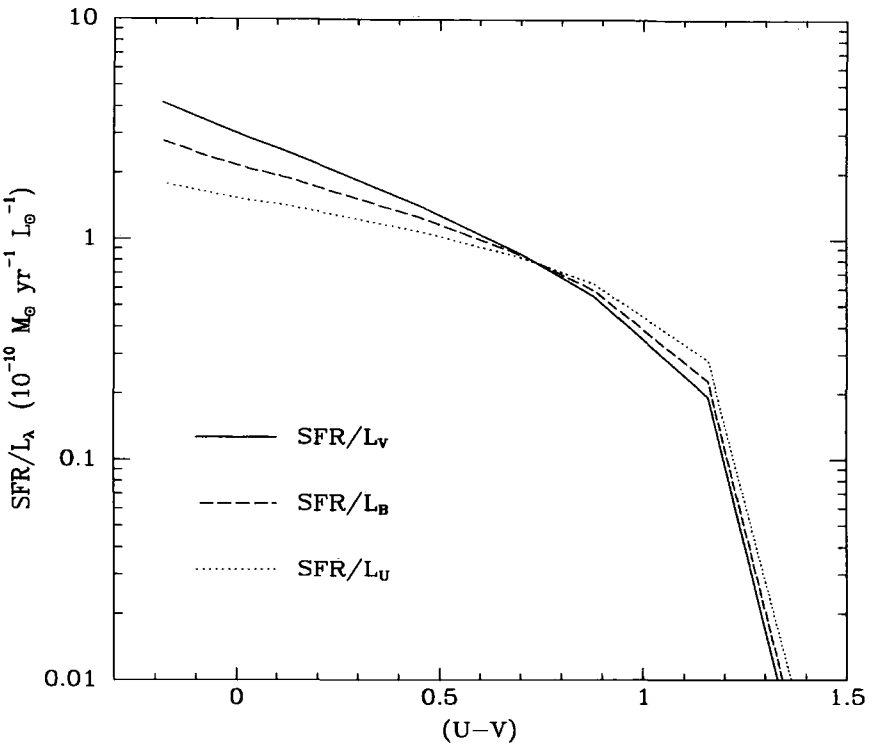

FIGURE 1.2: The SFR per unit solar luminosity as a function of galaxy colour, taken from Kennicutt (1998). The SFR per unit U- B- and V-luminosity is shown. Note that the SFR per unit U-band luminosity varies by over an order of magnitude across this range of colours (the same can also be said of the B- and V-bands). This shows that the broadband U-luminosity is not an accurate tracer of SFR in galaxies.

There is considerable motivation for calibrating the U-band since it would provide a simple way of determining SFRs, photometry being inherently simpler task than spectroscopy, which many other indicators rely on.

Problems and Caveats

Unfortunately the U-band luminosity is not an excellent tracer of star formation, principally because the band pass is not blue enough to exclude contributions from older stars.

Figure 1.2 (taken from Kennicutt, 1998) shows that the SFR per unit solar U-band luminosity varies by more than an order of magnitude over a range of U − V colour. Were we to use the U-band as a SFR indicator, we would need to alter the calibration depending on the galaxy colour. Failure to do this could lead to a misestimation of the SFR by over a factor of 10! Despite this problem, the U-band has been employed in SFR studies in the past.

As we have said, although the U-band is most sensitive to newly formed stars, it also is affected by older underlying stellar populations. These contribute to the U-band flux, albeit in a lesser fashion than their newly formed counterparts. For this reason, any calibration of the U-band-SFR relation is non-linear. The non-linearity is more of a problem in low SFR systems, since here the ratio of young-to-old stellar contributions to the U-band flux is smaller, meaning the old stars hold greater weight. In this instance, a linear relationship would produce an over-estimate of the true SFR (Bell, 2003).

One way of avoiding the problem of old star contamination is to calibrate the U-band via the UV, making use of synthetic spectra to extrapolate from $\sim$ 2500Å. The UV has problems of it's own (see the following subsection for a discussion). This technique of extrapolation was done by Cram et al. (1998) in their inter-comparison of several SFR indicators.

The other main problem with the U-Band is that of dust extinction. This causes trouble for many SFR indicators in the optical; it will be discussed in full when we examine the UV indicator.

Micro-Bibliography

The U-band has recently been tested against other SFR indicators by Hopkins et al. (2003) and Cram et al. (1998).

1.5.2 Rest Frame Ultra Violet Continuum

Physics

High mass stars on the Zero Age Main Sequence (i.e. late O/early B spectral types) have temperatures $T \gtrsim 10,000\,\mathrm{K}$ meaning their blackbody emission peaks in the Ultra Violet (UV)[2], at wavelengths $\sim 10^{-8}\,\mathrm{m}$. Assuming that all of these photons can escape the host galaxy, we therefore expect the UV flux to be a good measure of the SFR. At first sight, this method might appear to be *the best* SFR indicator; it is arguably the most intuitive, being linked directly to the number of high-mass stars. The physics of radiation reprocessing need not concern us (c.f. Far Infrared luminosity), neither do the details of any ill-understood and complex emission mechanisms, such as those of the 1.4 Ghz radio

[2]According to Wein's Law: $\lambda_{\mathrm{max}} = 2.898 \times 10^{-3}/T$

method. I note that the UV continuum in high redshift galaxies is not affected by the Lyα forest, since, as defined below, it lies redward of the rest wavelength of Lyα.

For galaxies with redshifts $z \gtrsim 0.4$, UV emission is redshifted into the optical, making it available to ground based observatories. If studying lower redshift galaxies from the ground however, one must extrapolate to the UV from optical data. This is an uncertain process, since small changes in the dust content or SFH of a galaxy can substantially alter the estimated UV flux.

Problems and Caveats

Despite its appeal of a seemingly direct physical link to the true SFR, there are several subtleties which must be considered when using the UV. These have severe effects on its utility. The largest and most obvious problem is that of dust extinction, the importance of which cannot be overstated. The presence of dust has an *enormous* effect on the UV flux which escapes from a galaxy. Using the dust curves for the Milky Way and SMC (measured by Pei, 1992), it is estimated that between $2-7$ times more magnitudes of extinction are suffered by UV photons than Hα photons. The corresponding attenuation factors for UV radiation are hence *very* large. When one considers that starbursting galaxies are often very dusty in nature, then this alone may well deter one from using the UV. There are more complex issues related to dust extinction and we will examine these later. For now we begin by looking at a similar issue to one which the U-band is susceptible to: the effect on the UV flux of longer lived stellar populations formed at the same time as the O and B stars.

The UV covers a bluer bandpass than the U-band (its central wavelength being defined typically to be 1500Å or 2500Å compared to $\sim$ 3600Å), however this does not mean that it suffers negligible contamination from longer lived stars. Glazebrook et al. (1999) have demonstrated, using the models of Bruzual and Charlot (1993), that the UV flux at both 1500Å and 2800Å actually increases as the stellar population evolves. This is evident in the bottom plot of Figure 1.3 which shows a galaxy SED at 0.01, 0.1 and 1.0 Gyr after a star formation event. The band passes at 1500Å and 2800Å are shown as the hashed regions. It is evident that the flux in both bands increases with age, up to 1 Gyr, after which it stabilises. If we wish to measure the SFR of a galaxy from the flux in these bands we would have to use a non-linear calibration that changes with the age of the

population. This same conclusion has been reached by Sullivan et al. (2000). Indeed this is why both Sullivan et al. and Pettini et al. (1998) choose to use different conversion factors in the UV–SFR relation, depending on the age of the population. Without the non-linear calibration one could misestimate the SFR by roughly a factor of 2 (compare fluxes at 0.1 and 1 Gyr in Figure 1.3).

Seemingly in contradiction with this, some authors (e.g Madau et al., 1998; Kennicutt, 1998) have argued that the UV flux is produced exclusively by young, high mass stars and the effects of longer lived stars formed in the same star formation event are minimal. This is only true if the star formation taking place within a galaxy is occurring on timescales that are much greater than the main sequence lifetime of the massive, UV producing stars. We note that the main sequence lifetime of such stars is indeed short ($\sim 2 \times 10^7$ yr), however studies have shown that the corresponding timescale for on going star formation needs to be $\gtrsim 1$ Gyr in order to validate the claims of Madau et al..

To illustrate this point further, consider the SFR–UV power curves of Madau et al. (1998) shown in Figure 1.4. These use the models of Bruzual and Charlot (1993). The true SFR is plotted as a function of power radiated at 1500Å and 2800Å, for times 0.01 to 15 Gyr after the star formation event. Different star formation laws are shown, parameterised such that SFR $\propto e^{\tau/t}$, where τ is the burst duration, quantised to 1, 5, 10 and 20 Gyr. The effects of different IMFs are shown by the two sets of curves (Scalo on the left, Salpeter on the right).

It can be seen that initially the UV luminosity increases drastically even though the SFR changes only slightly; eventually however, the luminosity does become proportional to the SFR. We note that the curves shown here are for SF bursts with a minimum duration of 1 Gyr. The Glazebrook et al. results mentioned above refer to SF on timescales less than 1 Gyr and as such they are not in disagreement.

There is another issue highlighted in Figure 1.4: that of the IMF. Comparing the IMF of Scalo to that of Salpeter, we see a relatively small offset in SFR of ~ 0.3 in the log, for a given luminosity. This relative insensitivity to the form of the IMF is an advantage to the UV. It arises because it is not only stars at the *very* top of the IMF which contribute to the UV flux, but also some of those lower down (the mass limit is $M \gtrsim 5M_\odot$). Ironically this is the same reason why a non-linear calibration is needed if the SF timescale is short. In addition, note from the same Figure that for a Scalo IMF the relation between 2800Å

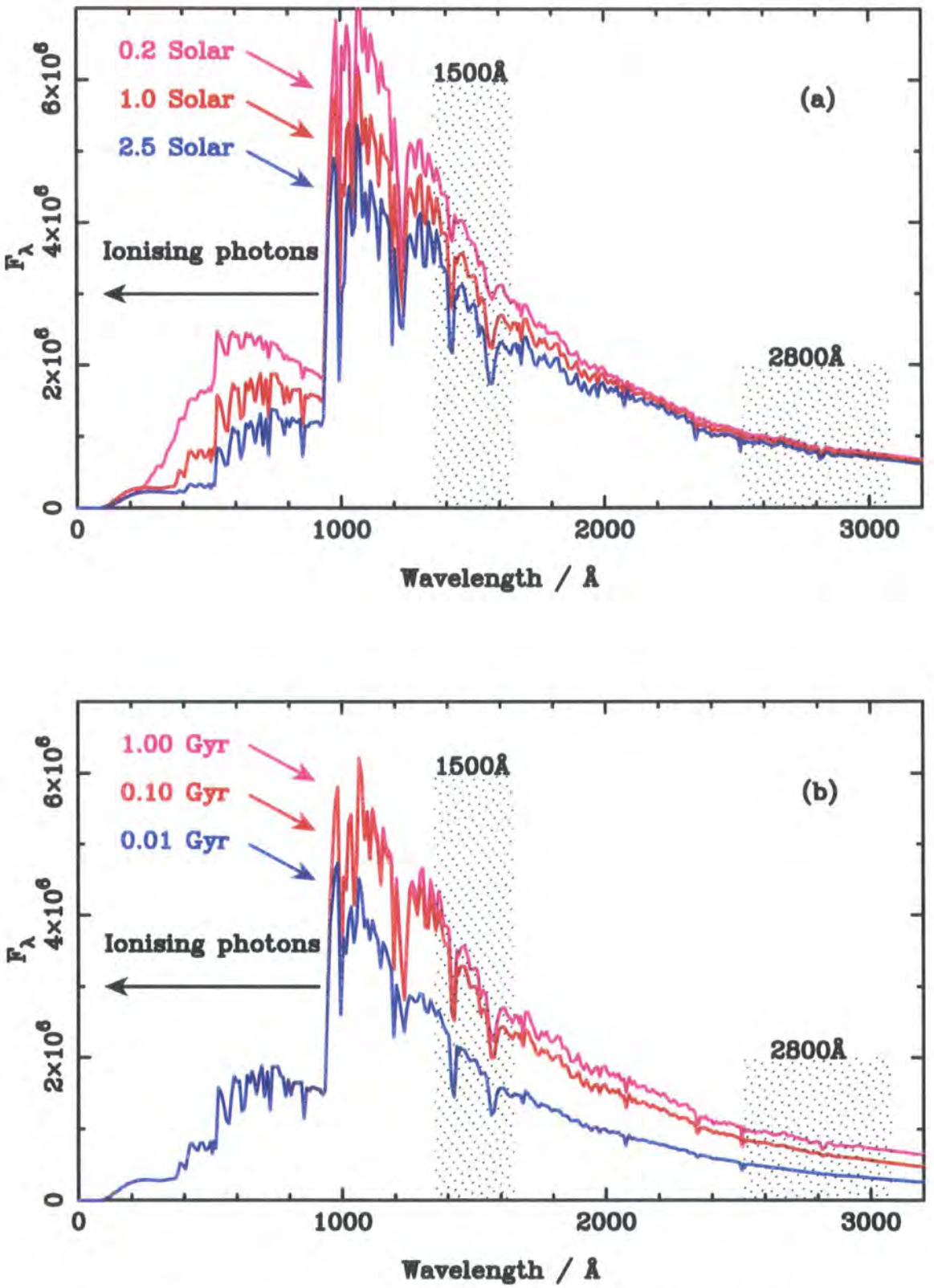

FIGURE 1.3: **Top:** The UV region of an SED of a galaxy 1 Gyr after a star formation event. Various metallicities are shown. It is clear that the flux at 2800Å is relatively unaffected by metallicity while the 1500Å flux shows some dependence. **Bottom:** The UV region of an SED of a galaxy at various times after a star formation event. It is evident that the UV flux in both bands *increases* with time and does not curtail to zero after star formation. See text for additional comments. The figure has been taken from Glazebrook et al. (1999)

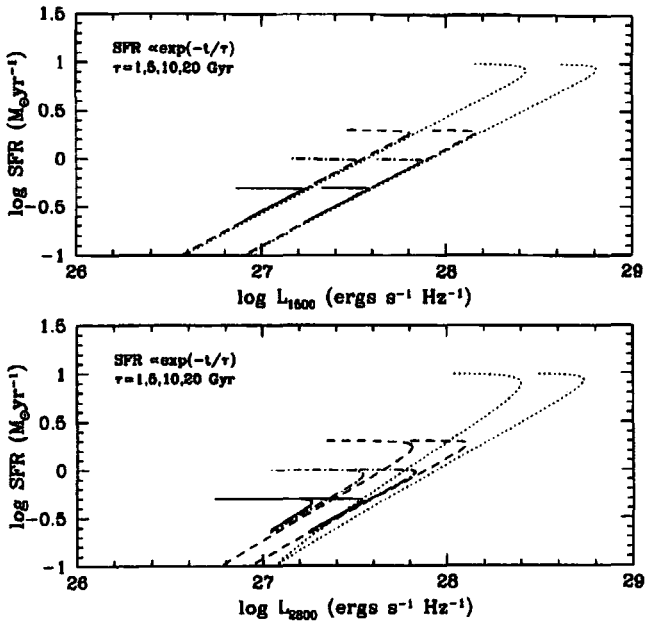

FIGURE 1.4: The relationship between SFR and the power emitted in the 1500 and 2800 Å UV bands. The curves are plotted for star formation parameterised as an exponential of various lengths (see text). Two different IMFs are shown, the left hand set of curves are for a Scalo IMF and the right hand set for a Salpeter IMF. The figure has been taken from Madau et al. (1998)

luminosity and SFR is non-linear unless the SF is occurring on timescales of 5 Gyr or greater, not the 1 Gyr previously mentioned. This is because the Scalo IMF is less rich in high mass stars than the Salpeter one.

As we have discussed, the increase in luminosity with age is a distinct disadvantage of the UV method when attempting to measure SFRs. The top plot of Figure 1.3 however highlights an advantage. The UV is relatively insensitive to metallicity. In the Figure, three galaxy SEDs of age 1 Gyr but of varying metallicities are shown. There is negligible variation between the fluxes in the 2800Å band as the metallicity changes although the 1500Å band suffers by a factor of ~ 1.3 as the metallicity is increased from 0.2 to 2.5 solar.

Comparing the many calibrations which have been published for the UV (e.g. Buat et al., 1989; Deharveng et al., 1994; Cowie et al., 1997), we see they differ by factors of 2 even after normalising to the same IMF and UV waveband (Kennicutt, 1998). This is attributable to a combination of assumptions about star formation timescales (as above), and use of different stellar libraries in the calibrations.

Our conclusions thus far are that, *in the absence of dust at least*, the UV may be used to determine the SFRs of galaxies which have on-going star formation on timescales of greater than 1 Gyr. Star formation occurring in bursts lasting less than 1 Gyr require a

non-linear calibration if they are to be measured with an accuracy better than a factor of 2. A change in IMF produces a small (~ 0.3 in the log) difference in measured SFR while a change in metallicity produces a factor of anywhere between zero and 1.3 difference, depending on which UV band is used.

As we mentioned earlier, there is also the issue of dust extinction. Dust extinction more seriously affects the bluer indicators such as the UV. The corrections are difficult, since it is not possible to know precisely the geometric distribution of dust in the host galaxy. A typical method for dealing with the dust problem is to employ a relationship between the spectral slope, β ($\beta \propto \lambda^{-\beta}$), and the extinction, A_{FUV}. A correlation has been found between the two by several authors (e.g. Calzetti et al., 1994; Meurer et al., 1999). However Bell (2002) finds that the relation does not hold for normal galaxies, but only for starbursts. This has implications for the many works that chart the Star Formation Rate Density (SFRD) through use of the UV continuum luminosity.

Micro-Bibliography

The UV has been used extensively in studies of the evolution of the SFRD. Famously, Lilly et al. (1996) used the UV measurements from the Canada-France Redshift Survey (Lilly et al., 1995) to chart the evolution of the luminosity density with epoch. This was the first version of the now famous "Lilly-Madau" plot. Cowie et al. (1999) have also used the UV to chart the evolution of the luminosity density, as measured from data in the Hubble Deep Field (Williams et al., 1996). They find a much shallower increase than do Lilly et al.. Wilson et al. (2002) use the UV and study a similar sample to Cowie et al.. More recently the results of the Galex UV satellite have been published by Arnouts et al. (2005); Schiminovich et al. (2005).

1.5.3 Far Infrared Continuum

Physics

Sites of star formation are by their nature very dusty places. The Orion Nebula in our own galaxy allows us the opportunity of close inspection of a typical stellar birthplace. Images from the both the Hubble Space Telescope (e.g. O'dell and Wen, 1994) and ground based observatories (e.g. Robberto et al., 2005) reveal that the nebula contains young

stars, set amidst vast amounts of dust and gas. These parental clouds prevent the escape of hard radiation emitted by the hot, young stars which are forming there (as detailed in the previous section). This problem is not limited to solely UV radiation; both Hα and [O II] SFR indicators suffer from dust extinction problems. Thankfully, the very presence of dust which so strongly affects the other indicators may itself be exploited to provide another SFR indicator, namely the Far Infrared continuum (FIR).

The absorption cross section of dust peaks very strongly in the UV (Kennicutt, 1998; Li and Draine, 2001), so dust which surrounds young stars will tend to soak up the intense, hard radiation fields produced. This energy is then re-radiated in the FIR wavelength range, from $30 \lesssim \lambda \lesssim 300\,\mu$m. The FIR should therefore accurately track the production of hot, UV producing stars and consequently the SFR (assuming of course that only those stars heat the dust, but see below for continued discussion). Of course there is also a certain lagtime associated with this process of absorption and re-emission.

There is observational data which might sway one towards using the FIR as a SFR indicator. For instance, from IRAS[3] we know that in the local universe $\sim 30\%$ of starlight is reprocessed into the FIR – meaning optical indicators miss relatively little star formation activity in nearby galaxies (Soifer and Neugebauer, 1991). However this fraction increases as one moves to higher SFRs (Sanders and Mirabel, 1996). The trend suggests that rates determined using optical tracers alone will underestimate the SFR in very highly star forming galaxies, and – for those objects at least – the FIR provides the best possible measurement of the SFR.

To highlight the point of possible underestimation further, consider Figure 1.5. The normalised SFR as measured by the UV and FIR indicators is shown as a function of reddening for a Starburst99 galaxy spectrum. At higher reddenings the UV is seen to sample only a few percent of the total star formation while the FIR samples almost all of it (although we note that some UV flux does still escape the galaxy). The reverse situation is true at low reddenings, with the UV being the most suitable indicator.

It seems that the best possible way of measuring the SFR is to employ both indicators. Taking this argument further, it would lead us to believe that a perfect measure of the SFR could be obtained by summing the contributions from all wavelengths; in reality this is not necessary. If the figure was perfectly reddening-corrected then we would find

[3] *The Infrared Astronomical Satellite*

agreement between the two indicators: in the extremely dusty case, the correction applied to the UV would bring it into line with the measurement given by the FIR. The idea that dust corrections can give agreement between indicators is important since it allows us to use only one indicator. The idea must be caveatted by stating that it is often difficult to determine the dust correction that should be applied.

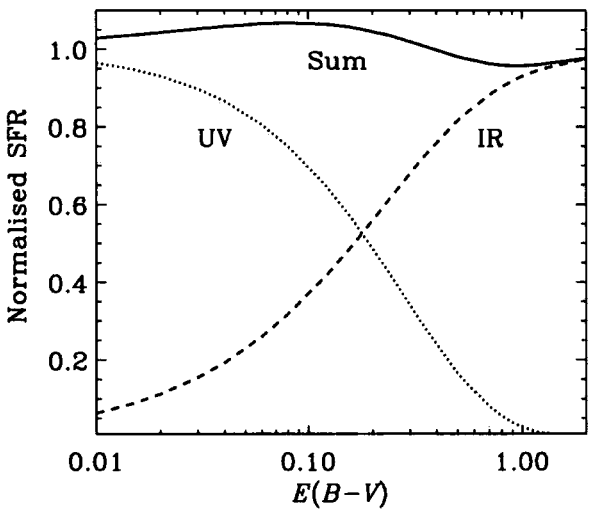

FIGURE 1.5: The fractional SFR measured by the FIR and UV indicators as a function of reddening. It is evident that with increasing reddening (dust extinction) the UV flux becomes a poorer and poorer measure of the SFR since less hard radiation escapes from the galaxy. Conversely the FIR becomes a better SFR with increased dust content since more of the hard radiation is reprocessed. It is obvious that one should employ both indicators in order to get a true measure of the SFR. The figure has been taken from Hirashita et al. (2003)

Problems and Caveats

As we have stated, Figure 1.5 highlights the potential importance of the FIR, particularly if an especially dusty galaxy is being studied. The simplest physical situation (re-created in such a dusty galaxy) is where the young stars are completely covered by dust and all of the UV radiation they produce is absorbed and reprocessed by the dust grains. In this limiting case the FIR is the "perfect" SFR indicator. Of course the real situation in any galaxy will be somewhere between this extreme and the opposite "no dust" case. With this is mind, it is clear that the escape fraction of ionising photons from a galaxy is an important quantity to establish. A high escape fraction implies that the dust grains are not able to soak up all the hard radiation and hence do not accurately track the SFR. Conversely a low escape fraction implies that the hard radiation fields are being

reprocessed and the FIR is an accurate SFR indicator.

There is work to suggest that the factor of UV light reprocessed by dust is close to unity, even for small amounts of reddening (e.g. Mas-Hesse and Kunth, 1991). Also supporting this idea, Heckman et al. (2001) have shown that for five UV-bright local galaxies the escape fraction of ionising photons ($\lambda < 912$Å) is very low, $\sim 6\%$. Leitherer et al. (1995) find a value of $\sim 3\%$, again for local galaxies. Note however that a subsequent re-analysis of the Leitherer et al. data by Hurwitz et al. (1997) showed the escape fraction could range from anywhere between 3 – 57%. At higher redshift, Steidel et al. (2001) find the escape fraction to be somewhat larger than Heckman et al.. The Steidel et al. study uses Lyman Break Galaxies ($z \sim 3$) and so those results may not be in disagreement. Using models, Tenorio-Tagle et al. (1999) have shown that the escape fraction from starburst galaxies may evolve with time, being larger soon after a starburst and then settling down to very low fraction after 3 – 5 Myr. There remains an uncertainty over the escape fraction of ionising photons; recall that if this fraction is high it means the FIR actually misses some of the star formation activity.

Another issue of debate is whether the young high-mass stars are the exclusive heating source for dust grains or if there exist other alternate sources. If so, then these sources could contaminate the SFR measurement. At first glance this may not appear to be a problem since we know from the IMF that although low mass stars are much more numerous than their high mass cousins, it is the high mass stars which dominate the overall luminosity. We therefore expect a relatively small contribution from low mass stars.

Despite this assertion, there is observational evidence to suggest that high-mass stars are not the sole heating source for dust grains. Helou (1986); Cox et al. (1986); Walterbos and Schwering (1987) and Rowan-Robinson and Crawford (1989) among others have put forward the idea of a two component model for FIR emission. In these models both star forming regions and cirrus-like regions contribute to the total FIR flux. The cirrus-like emission comes from regions of diffuse dust that are heated by the disk of older stars which contribute to the interstellar radiation field. One of the main successes of this idea is that it accurately reproduces the observed colour-colour distribution of IRAS disk galaxies.

Further support for the two component model comes from Sauvage and Thuan (1992) who find a strong non-linearity in the Hα–FIR relation. This is only explainable if the FIR

emission is modelled in a two component fashion, as suggested above. The Sauvage and Thuan results show a decreasing cirrus contribution towards late type galaxies, ranging from 86% (Sa) to 3%(Sdm). They suggest a correction based on morphological type should be made to all FIR-SFR calibrations.

Clearly it is crucial to determine the fraction of FIR emission from cirrus, especially if it is potentially as high as 86%. If left unaccounted for this contribution means one could massively overestimate the SFR.

Lonsdale Persson and Helou (1987) used the two component model to show that as much as 50 – 70% of FIR flux can be attributable to cirrus in most spiral galaxies. Bothun et al. (1989) also find that the contributions of old stars to dust heating are comparable with the effects of UV photons from newly formed stars. Xu et al. (1994) find that the contribution from old stars is on average 27% of the total FIR emission, but that this fraction may be considerably larger for galaxies with very little star formation activity in the last 10^8 yrs.

In contrast, Devereux and Young (1991) claim that the FIR emission can be described by a one parameter model, consisting solely of the SFR and that there is no need to include the cirrus contribution. Their claim is based on the idea of energy balance, where the FIR emission balances the ionising energy emitted by O and B stars. They assess the amount of ionising radiation using the Hα line.

Among others, Buat and Xu (1996) and Popescu et al. (2000) also argue in favour of a small contribution from cirrus to the overall FIR emission, finding that young stellar populations provide the predominant heating source ($\sim$ 70%).

More recently Kewley et al. (2002) and Bell (2003) have examined SFRs derived using the FIR. Kewley et al. find that the FIR emission is well correlated with Hα after the latter has been corrected for extinction; they do not observe the non-linearity reported by Sauvage and Thuan (1992), but find an agreement of Hα and the FIR to within 10%.

On the other hand, Bell argues that the FIR traces the true SFR in the most luminous galaxies (around $L_\star$), but that it drastically underestimates the SFR in lower luminosity ($0.01L_\star$) galaxies. The latter of conclusion has also been arrived at by other authors e.g. Klein et al. (1984); Dale et al. (2001). However Dopita et al. (2002) find only the former result to be true.

Clearly the fractional contribution to the FIR flux from cirrus and star forming regions

is still under debate. As such, it potentially causes considerable uncertainty for FIR SFR measurements.

There are other disadvantages to using the FIR. Aside from the ubiquitous issue of AGN contamination (thought to make up $\sim$ 10 – 20% of the IR background, Granato et al. 1997), the wavelengths of interest are not accessible from the ground because of atmospheric absorption. FIR emission must therefore be extrapolated from the Sub-millimetre or Near Infrared. Note that due to the large beam sizes of sub-mm instruments ($\sim 15''$ on SCUBA), and the extincted nature of some of the strongest sources, optical identifications and redshifts are often difficult to obtain.

Micro Bibliography

High redshifts FIR surveys, such as those on ISO[4] (e.g. Oliver et al., 1997; Kawara et al., 1998; Puget et al., 1999; Takeuchi et al., 2001) and those on the JCMT[5] using SCUBA[6] (e.g. Smail et al., 1997; Blain et al., 1999; Chapman et al., 2001, 2003) have found populations of very highly star forming galaxies, with individual star formation rates of order $500\,M_{\odot}\,yr^{-1}$. More recently, the advent of the Spizter Infra-red Telescope has also confirmed such high SFR objects (e.g. Choi et al., 2006). Given the very large SFRs it is possible for a small number of galaxies such as these to dominate the SFRD at a given epoch.

1.5.4 1.4 Ghz Radio Continuum

Physics

Use of the 1.4 GHz continuum luminosity as a measure of the SFR relies on the assumption that the dominant process contributing to the luminosity at that frequency is synchrotron emission from accelerated relativistic electrons, in the strong magnetic fields surrounding supernova remnants. The idea has been put forward by Biermann (1976) and Kirk (1994).

Only stars with masses $M > 8M_{\odot}$ end their lives in Type II or Type Ib supernovae, the kinds thought to be responsible for causing most of the synchrotron emission, and so the 1.4 GHz luminosity should be proportional to the supernovae rate and hence the star

[4] *The Infrared Space Observatory*
[5] *James Clerk Maxwell Telescope*
[6] *Submillimetre Common-User Bolometer Array*

formation rate. The time lag for the response of this indicator is roughly the lifetime of a $8M_{\odot}$ star.

Radio has the advantage of total insensitivity to dust extinction, meaning it does not suffer from one problem which so strongly affects the other indicators. Another advantage is that due to the high spatial resolution with which radio maps can be made, the star formation activity can be mapped out to sub-arcsec precision.

One support for the use of the radio as a SFR indicator is that there exists a very tight relation between radio flux and FIR flux. This spans over five orders of magnitude in luminosity (e.g. de Jong et al., 1985; Condon et al., 1991)

Problems and Caveats

Although the radio luminosity may at first glance seem appealing – especially in light of its dust independent measure of SFR – there are serious issues which might drastically limit its utility.

The radio is a rather indirect method of measuring the SFR. The major problem lies in the understanding of the detailed physics of cosmic ray generation and confinement resulting from the supernovae event itself. These remain relatively poorly understood despite attempts to explain them (Condon, 1992; Price and Duric, 1992; Chi and Wolfendale, 1990).

Supernovae rates predicted by dividing a galaxy's radio luminosity by the model luminosity of an individual supernova remnant, are thought to be too high (Biermann, 1976; Gehrz et al., 1983; Condon and Yin, 1990). One solution is that the lifetimes of the relativistic electrons causing the emission and/or the acceleration process itself, are longer than the lifetime of the observed supernovae remnants in our own galaxy ($\gtrsim 20,000$ yrs, Condon and Yin, 1990).

Additional uncertainties arise when one attempts to quantify the relative contributions of thermal and non-thermal processes to the radio continuum emission. Non-thermal emission has a frequency dependent spectral shape $\propto \nu^{\alpha}$. It is thought that α may also vary with frequency itself (Condon, 1992). Thermal emission has a similar spectral shape, although it is somewhat shallower than the non-thermal emission. Clearly then, the relative contributions of each type of emission vary with frequency. At 1.4 GHz the standard model for luminous spiral galaxies predicts a contribution of $\sim$ 90% from

non-thermal processes. This fraction however, is not well constrained observationally and there is evidence that it even varies with galaxy mass. This could mean that dwarf galaxies have lower contributions from non-thermal emission than do normal spirals (Klein et al., 1984, 1991; Klein, 1991; Price and Duric, 1992). Even for very well studied galaxies, the contributions are uncertain to greater than a factor of 5. This therefore represents a very serious cause of error in the returned absolute SFR.

The best argument for using 1.4 Ghz radio emission is that it is so well related to FIR emission. Despite this, Bell (2003) has argued that both the FIR and the radio underestimate the SFRs at low luminosities. He argues that the radio-FIR correlation is a conspiracy.

Finally, we must mention AGN contamination; most high luminosity radio sources are AGN and not star forming regions.

Micro Bibliography

The radio has been tested against other SFR indicators by Hopkins et al. (2003); Cram et al. (1998); Cardiel et al. (2003); Sullivan et al. (2001); Bell (2003). Also, Haarsma et al. (2000) have used the radio luminosity to measure the star formation of the Universe.

1.5.5 The Hα Emission Line

Physics

As we discussed in Section 1.5.2, young, high-mass stars shine very brightly at UV wavelengths for some time after they reach the Zero Age Main Sequence. The bluest photons, emitted shortward of 912Å (the so-called Lyman-limit), are of sufficient energy to totally ionise hydrogen atoms in the parental clouds of gas surrounding stellar birthplaces. The photon energy at 912Å matches exactly that of the transition of an electron from the ground state to infinity (an energy gap of $E = 13.6\,\mathrm{eV}$). Any shorter wavelength photons are clearly also capable of ionisation. The large cross section for this process is evident in the lower panel of Figure 1.3 which shows the SED of a galaxy at certain fractions of a Gyr after a star formation event. The flux at wavelengths $\lambda < 912$Å is low due to photons at these energies being used in ionisation. Note as an aside that this has allowed the detection of star forming galaxies at high redshift due to the break across the Lyman-limit

(Steidel et al., 1996).

After ionisation has occurred, the electrons are able to recombine with the free-floating ions to form Hydrogen atoms. This process occurs by an electron entering at a high energy level and then cascading down through the various intermediate levels until it comes to rest in the ground state. Several series of lines are emitted in the process, each taking its name from the terminating level (the Balmer series terminates at n=2, the Paschen series terminates at n=3 etc.).

One line in particular that is emitted is that of Hα at 6536 Å. This is the lowest order Balmer transition arising from decay to the n=2 level from the n=3 level.

It is clear to see how this line is related to the SFR of a galaxy, since only very high mass stars ($M > 10\,M_{\odot}$, Kennicutt 1998) contribute to the flux at $\lambda < 912$ Å. The lifetimes of these stars are very short (~ 20 Myr) and so the $\lambda < 912$ Å flux drops to zero when they die, making the Hα flux a good measure of the "instantaneous" SFR of a galaxy. This is a particular advantage over using the slightly softer UV radiation as a SFR indicator, since as we have shown the flux in some UV bands can actually increase with age.

Another advantage of Hα is that because it lies in a relatively red region of the spectrum it is considerably less affected by dust than some indicators.

The higher order Balmer lines, such as Hβ (4861 Å) should also track SFR since they rely on the same mechanism for production as Hα. Aside from lying in a bluer region of the spectrum (and therefore being more susceptible to dust problems), Hβ is also strongly affected by absorption from stellar atmospheres. This needs to be corrected for if the line is to be used in SFR measurements. It is often difficult to obtain spectra with the necessary resolution to disentangle the effects of emission and absorption (a high quality spectrum suffering from Balmer absorption is shown in Figure 1.6). For this reason Hβ and the higher order lines are not as useful as Hα in quantifying the SFR.

Problems and Caveats

The physics of Hα formation has been outlined above and shows the good reason why many authors prefer Hα over other indicators. There are however still some problems with associated with its use.

Firstly there is the issue of AGN contamination. It is possible for the Hα emission to be created by physical processes relating to the AGN, and not to star formation. Measure-

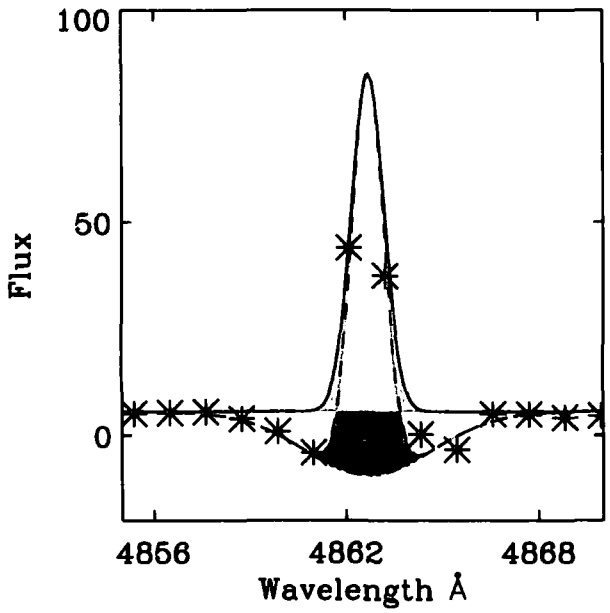

FIGURE 1.6: The figure shows the Hβ line in emission, sitting in an absorption trough. The absorption comes from stellar atmospheres. With low resolution spectra it can be difficult to disentangle the effects of emission and absorption. This can lead to mismeasurement of the true line flux. The figure has been taken from Hopkins et al. (2003)

ments of other spectral lines are necessary to distinguish between these two possibilities. Of course AGN contamination affects almost all SFR indicators so it is unfair to level this criticism solely at Hα.

Another problem is that for redshifts $\gtrsim 0.3$ the Hα line moves out of the optical and into the near-infrared. Observing in the near-infrared is not as simple as working in the optical, in part because the instrumentation is not as plentiful.

As we stated, only very high-mass stars contribute to the ionising flux required to form Hα. Although this is an advantage in terms of obtaining an "instantaneous" measure of SFR it also means that Hα relies crucially on the form of the IMF, more so than other indicators. Glazebrook et al. (1999) and Kennicutt (1998) show that the absolute SFR returned varies by factors of ~ 3 when using a Scalo vs Salpeter IMF (c.f. a factor of ~ 2 when using the UV, Glazebrook et al. 1999).

A considerable problem arises from the effects of metallicity on the Hα flux. This is highlighted in the top panel of Figure 1.3 which shows a galaxy SED at age 1 Gyr but for varying metallicities. It is clear that a decrease in metallicity drastically increases the flux blueward of 912 Å. Glazebrook et al. (1999) find a increase of a factor of 1.7 in ionising

flux when moving from a 0.2 solar to 1.0 solar metallicity model. The increase in flux is even larger for the 2.0 solar model. Clearly these effects should be accounted for when using this indicator, however they are often ignored.

There also remains the problem of the escape fraction of ionising photons, discussed in Section 1.5.3.

Micro Bibliography

The Hα line has been used extensively in studies of the cosmic SFRD. Among the first was that of Madau et al. (1998). Also of note are the studies of Gallego et al. (1995); Tresse and Maddox (1998) and Hippelein et al. (2003).

1.5.6 The [O II] Emission Line Doublet

Physics

The [O II] emission line doublet is formed by forbidden transitions in singly ionised Oxygen. A full discussion of the physics behind the emission process is presented in Appendix B; here we restrict ourselves to the statement that [O II] emission arises from forbidden transitions, the upper states of which are collisionally excited. The two transitions of the doublet, at wavelengths of 3726 and 3729 Å normally appear as one transition at 3727Å in modest resolution spectrographs.

Typical temperatures around young stars of order $10-20,000$K. At these temperatures the difference between the energy levels responsible for [O II] emission is of order the electron thermal temperature, kT. Because of this, free floating electrons are able to promote the captive electrons in the ionised Oxygen species.

[O II] emission is well correlated with Hα emission in the local universe (Kennicutt, 1992b; Gallagher et al., 1989; Aragón-Salamanca et al., 2003; Hopkins et al., 2003).

The main advantage of using the [O II] emission line is that it is accessible to optical spectrographs across a large redshift range. [O II] allows a single diagnostic to be used across the range $0 < z < 1$, over which the SFRD of the Universe evolves very strongly.

Problems and Caveats

Since [O II] emission is collisionally excited, it is clear that its strength should have some dependence on the temperature and density of the exciting species. Furthermore, because

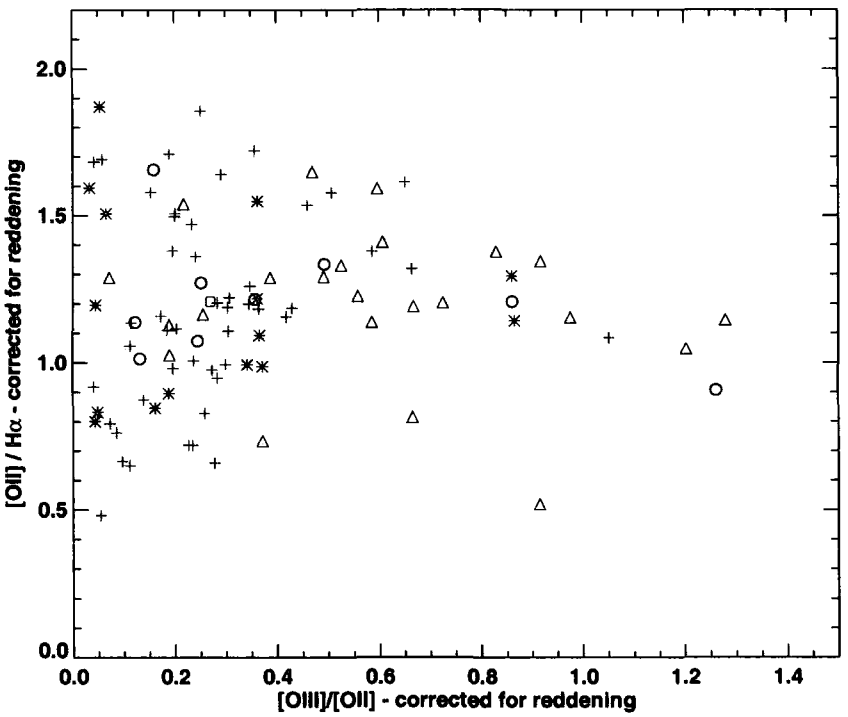

FIGURE 1.7: The dependence of [O II]/Hα ratio on the ionisation-sensitive [O III]/[O II] ratio. There is no statistical dependence of reddening corrected [O II]/Hα on the ionisation-sensitive [O III]/[O II]ratio. The figure has been taken from Kewley et al. (2004).

the exciting species are free floating electrons, one would expect to find some dependence of [O II] emission strength on the ionisation state of the circumstellar nebula gas. Also, we expect a dependence on the metallicity of the circumstellar gas. A low metallicity nebula should have weaker [O II] emission than an Oxygen-rich one.

With regards the ionisation state concerns, Kewley et al. (2004) have shown there to be no dependence of the [O II]/Hα ratio on the ionisation-sensitive ratio [O III]/[O II], as shown in Figure 1.7.

There is however, a dependence of [O II] strength on metallicity (indeed [O II] enters several abundance indicators e.g. Pagel et al., 1980). Both Kewley et al. (2004) and Jansen et al. (2001) find the reddening corrected [O II]/Hα ratio to be correlated with metallicity.

Finally, since [O II] lies in the blue region of the spectrum it is affected by reddening, and this must be accounted for when using it. Further discussion of how [O II] compares to the other indicators is presented in Section 1.6.

Micro Bibliography

Hogg et al. (1998); Hippelein et al. (2003); Teplitz et al. (2003) and Hammer et al. (1997) have all used the [O II] line to trace the evolution of SFRD with cosmic epoch.

1.5.7 Alternative Methods

In addition to the more typical methods detailed above, there are other, less well known and less used SFRs indicators. They are summarised briefly below.

X-ray Emission

X-ray emission in the energy range $2 - 10$ KeV may be correlated with SFR, the emission being thought to originate from High Mass X-ray Binaries and Type II Supernovae (Fabbiano, 1989).

If we assume X-ray emission is only from supernovae, then the X-ray-SFR relation is easy to understand because the relation between SFR and supernovae rate is conceptually simple: If one can determine the *death rate* of stars through the supernovae rate, then it is simple to convert this back to a birthrate.

X-ray emission from High Mass X-ray Binaries is more difficult to understand. This type of emission is caused by accretion of material from the larger star onto the companion black hole/neutron star. Emission from such binary systems should be correlated with SFR for several reasons. Firstly, in order to form a black hole or neutron star the progenitor must have been a high mass star itself, and therefore have been short-lived. Secondly the presence of a high mass companion means that the evolutionary timescales are drastically reduced when compared to Low Mass Binary star systems. Since they are short-lived, High Mass X-ray Binaries should therefore give a measure of SFR.

X-ray emission has the advantage of being insensitive to dust, although it does require use of space satellites to be observed.

There is evidence that X-ray emission is correlated with FIR emission (David et al., 1992), radio emission (Ranalli et al., 2003), and UV emission (Laird et al., 2005). The FIR correlation found by David et al. (1992) is however in disagreement with the large scatter reported in the same relation by Griffiths and Padovani (1990).

Method of Heavens et al. (2004)

Heavens et al. (2004) and Panter et al. (2003) use the compression algorithm MOPED (Heavens et al., 2000) to obtain the history of star formation in the Universe, from data from the Sloan Digital Sky Survey (SDSS). The technique is not to measure emission line strengths, but rather to model each individual spectrum with a SFH of its own. Given the large number of spectra available in the SDSS, and the number of data points per spectrum, the task would normally be intractable, requiring an almost infinite amount of computing time. Through the compression of MOPED however, the number of parameters required to describe an individual spectrum is drastically reduced and so is the computational power required to model it.

One advantage of this technique is that the entire spectral range of the data is used, instead of just one or two spectral features. One must recall however, that individual SFRs are not actually being *measured* directly.

1.6 Intercomparison

U-Band

The U-band has been compared to the radio SFR indicator by Cram et al. (1998) and Hopkins et al. (2003). The bottom plot of Figure 1.8 shows the Cram et al. comparison. The sample is 700 local galaxies, taken from various literature sources. Considerable scatter between the two indicators is observed. The U-band appears to predict high SFRs in systems with relatively low radio derived SFRs. The opposite occurs at higher radio derived SFRs, with the U-band estimate being somewhat below the radio. The first of these observations can be understood in terms of the U-band's contamination from longer lived populations, while the difference at high SFRs may be attributable to an excess of dust in rapidly star forming systems.

The Hopkins et al. comparison from the First Data Release of the Sloan Digital Sky Survey (SDSS, Abazajian et al., 2003) is shown in Figure 1.9. The Figure shows the comparison both before (panel a) and after (panel b) dust corrections have been made. Panel c shows a comparison to the alternative U-band calibration of Afonso et al. (2003).

There appears good agreement between the two indicators in panel b, however one must consider the corrections that have been made to the data in order to obtain such a

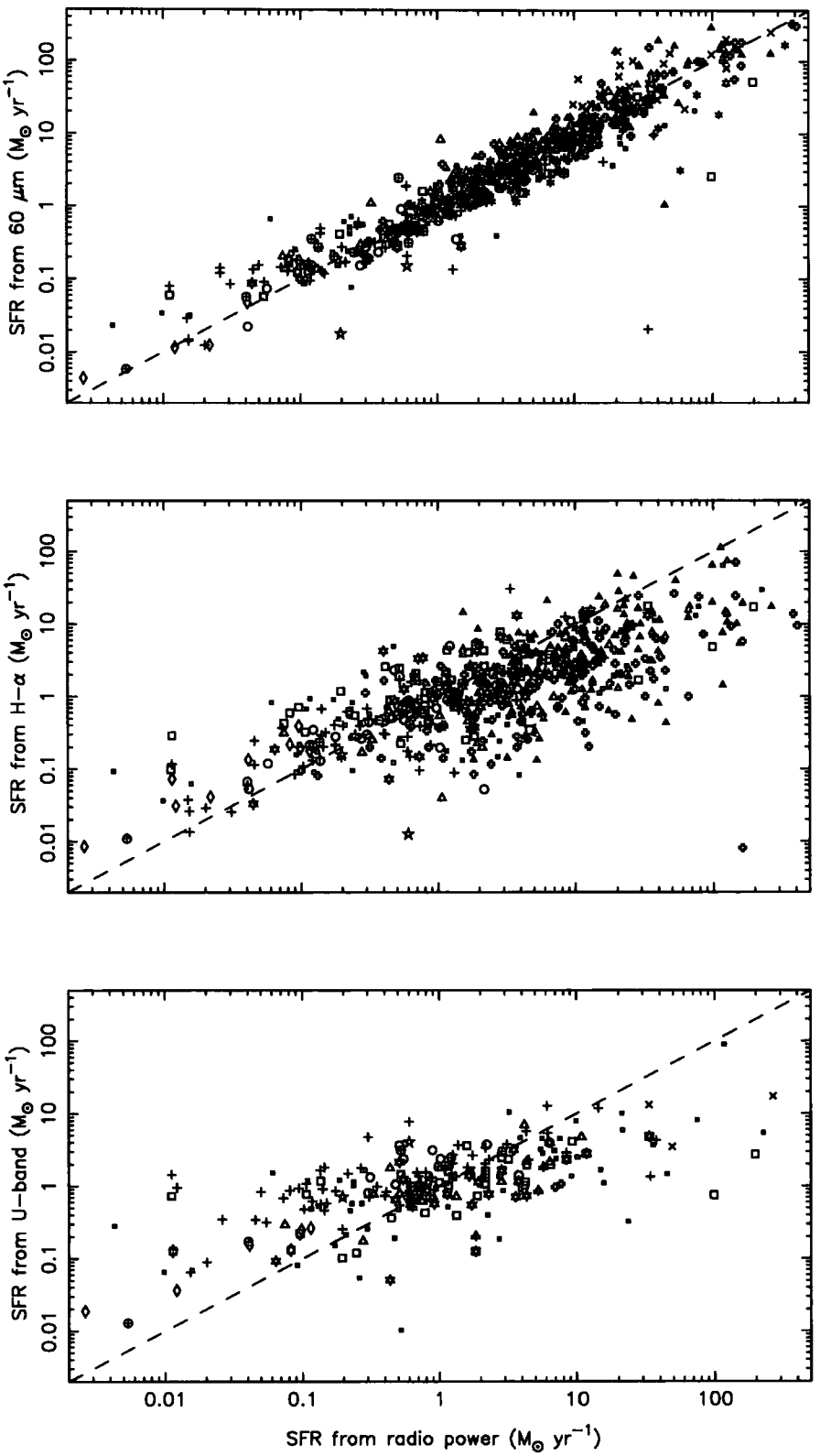

FIGURE 1.8: An intercomparison of SFR indicators taken from Cram et al. (1998). **Top:** A comparison between FIR and radio 1.4 Ghz SFRs. There is agreement over four orders of magnitude, although some outliers are seen. See text for additional comments. **Middle:** A comparison between Hα and radio 1.4 Ghz SFRs. Considerable scatter is observed. This may be attributable to increased extinction in high SFR galaxies, which would more heavily affect the Hα emission than the radio. **Bottom:** A comparison between U-band and radio 1.4 Ghz SFRs. The U-band is seen to overestimate the SFR at low radio SFRs, while it underestimates the SFR at high radio SFRs.

match. Firstly, we note that k-corrections have been made to the U-band magnitudes in both panels (Blanton et al., 2003); this is only possible because the redshifts are known. Also, in panel b the U-band fluxes have been corrected for dust extinction, measured from the stellar absorption corrected Balmer Decrement. Hopkins et al. (2003) find correction factors in the range 3 – 10 for the dust extinction. By comparing to panel a, it is evident that without such a dust correction there remains a substantial offset between the two indicators. In summary, despite the apparent concordance shown in panel b, one must consider that *many* additional pieces of information have been used to create such agreement. It appears that the U-band can be correlated with the radio, but only if the redshifts and reddenings of the galaxies are known. As such, the agreement is of little use if one is undertaking a study using solely the U-band, since both the redshifts and reddenings will not be known. Furthermore, if one is to know the reddenings precisely, the Balmer Decrement should be used. In such a case, use of Hα directly as the SFR indicator would probably be the best choice.

Rest Frame Ultra Violet Continuum

Figure 1.10 shows a comparison between the radio, UV and Hα SFR indicators, taken from Sullivan et al. (2001). The sample is from a radio survey of nearby galaxies. In the lower panel the UV and radio indicators are compared. The UV flux has been corrected for extinction using the Balmer Decrement. The solid lines in each of the panels denote the one-to-one relation for two different parameterisations of the SFR. It is clear that the UV seems to underestimate the SFR relative to the radio.

Far Infrared Continuum and 1.4 Ghz Radio

Figures 1.8 (top panel) and 1.11 (left panel) show comparisons between the radio and FIR SFR indicators, taken from Cram et al. (1998) and Hopkins et al. (2003) respectively. Both Figures show excellent agreement between the FIR and radio. This is a reflection of the well known FIR-radio relation (e.g. de Jong et al., 1985). In the top panel of Figure 1.8, the relation is seen to hold over 4 orders of magnitude, although there are some outliers. The small number of galaxies with very low radio SFRs, but with increased FIR SFRs, may be indicative of alternate heating sources for the dust grains responsible for FIR emission. Also, the small number of low FIR SFR galaxies with high radio SFRs may be

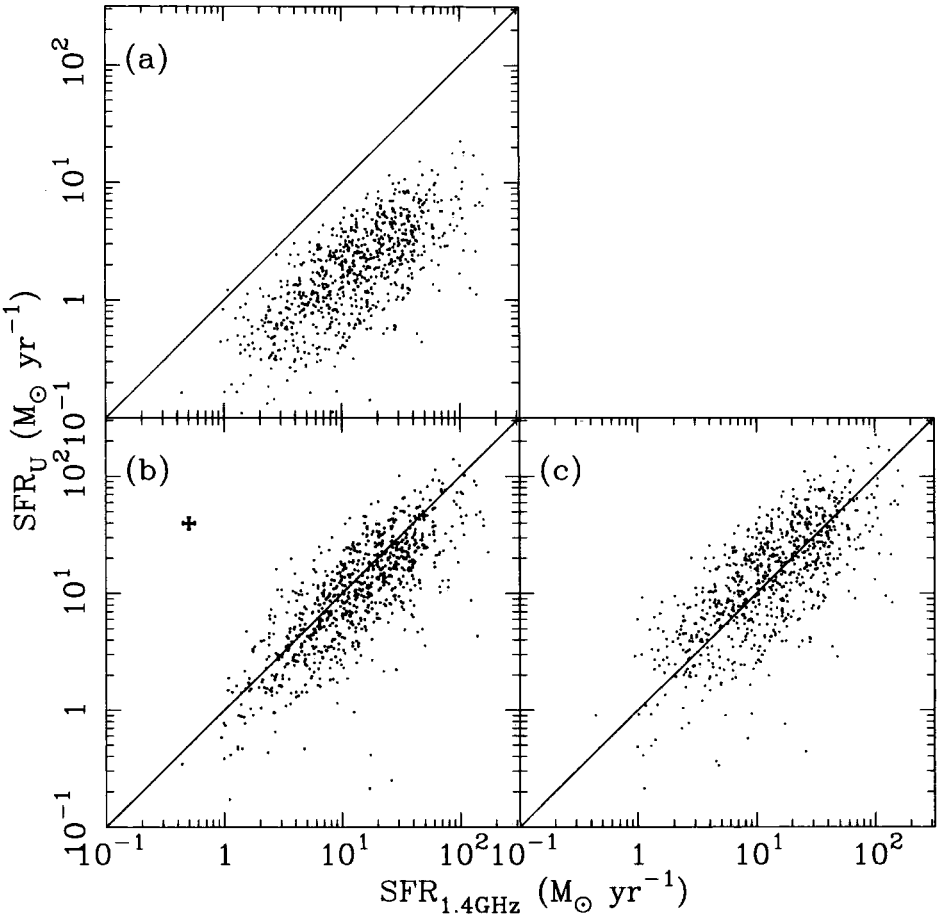

FIGURE 1.9: A comparison of radio and U-band SFR indicators from the SDSS. The solid line shows the one-to-one relation. The U-band data in all panels has been k-corrected, while that in panel b has also been extinction corrected using reddenings derived from stellar absorption corrected Balmer Decrement measurements. Panel c shows an alternative U-band calibration of Afonso et al. (2003). The figure has been taken from Hopkins et al. (2003)

examples of the radio indicator being contaminated by AGN.

The Hα Emission Line

The middle panel of Figure 1.8 shows the Cram et al. comparison between Hα and radio 1.4 Ghz derived SFRs. The considerable scatter observed may be attributable to an increased amount of extinction in high SFR galaxies. This would more heavily affect the Hα emission than the radio.

The right panel of Figure 1.11 shows the Hα comparison to the FIR from Hopkins et al. (2003). The Hα fluxes have been corrected for reddening using absorption corrected Balmer Decrement measurements. There is a scatter of factor ~ 1.7 about the one-to-one relation.

Figure 1.12 shows the results of an investigation by Kewley et al. (2002). The FIR SFR

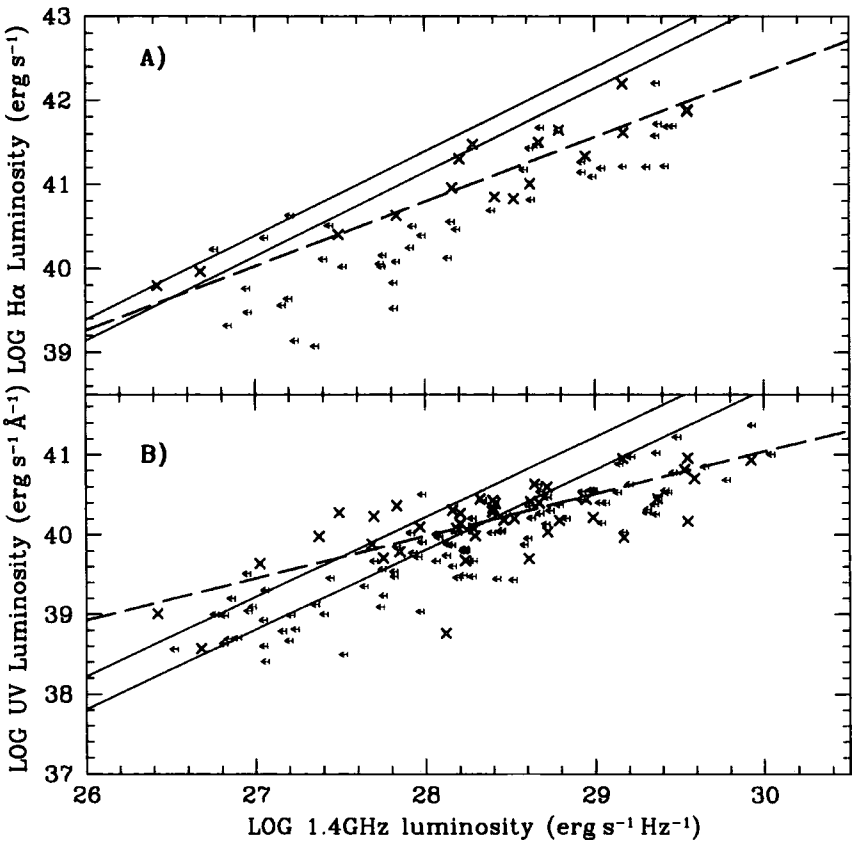

FIGURE 1.10: A comparison of radio, UV and Hα SFR indicators from Sullivan et al. (2001). Both the UV and Hα fluxes have been corrected for dust extinction using the measurements of the Balmer Decrement. In both panels the dashed line shows the least squares best fit relation. "X"s mark the detections in both bands, while the arrows indicate upper limits in radio flux. The solid lines in both panels indicate the one-to-one relation for two different parameterisations of the SFR. Both the UV and Hα are seen to underestimate the SFR relative to the radio.

is plotted against the reddening corrected Hα SFR for galaxies in the Nearby Field Galaxy Survey (Jansen et al., 2000). The two indicators agree to within 10%. This relation shows considerably less scatter than the Hopkins et al. (2003) study, above.

The top panel of Figure 1.10 shows the Sullivan et al. (2001) comparison of Hα flux to the radio. As noted earlier, the solid lines show two different parameterisations of the SFR. The Hα fluxes have been corrected for dust extinction using the Balmer Decrement. There is remarkable agreement between the two, although there is a slight trend that Hα gives a lower SFR than the radio.

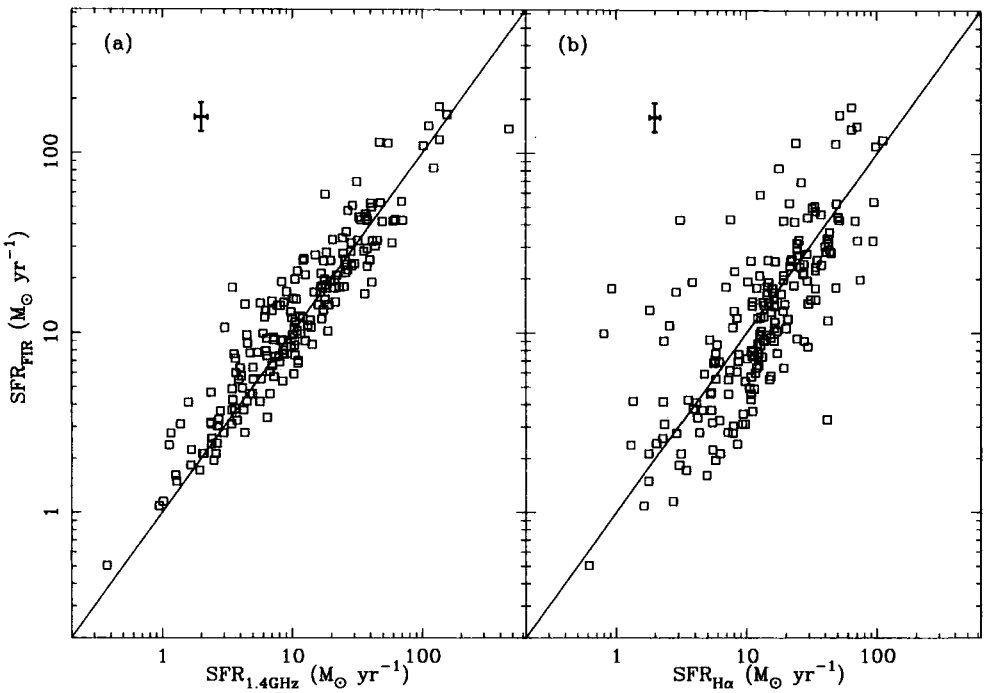

FIGURE 1.11: A comparison of FIR, radio and Hα SFR indicators from the SDSS (Hopkins et al., 2003). In both panels the solid line shows the one-to-one relation. The well known FIR-radio relation is observed is panel a. Panel b shows a scatter of a factor of 1.7 between the FIR and Hα. Typical errors bars are shown n the top left corner of each panel.

The [O II] Emission Line Doublet

The Kewley et al. (2004) comparison between [O II] and Hα derived SFRs is shown in Figure 1.13. In this study a new [O II]-SFR calibration is derived and it is this new calibration that has been used in the production of the Figure. Note that both [O II] and Hα fluxes have been corrected for reddening. The solid line shows the one-to-one relation. There is excellent agreement between the two indicators.

The SDSS comparison of [O II] to both the radio and Hα is shown in the right panel of Figure 1.14 (Hopkins et al., 2003). A factor of 1.4 scatter is seen around the one-to-one relation. This is somewhat different to the Kewley et al. result above. The disparity can be traced to the use of different calibrations in the two papers. Kewley et al. (2004) use a reddening corrected [O II]/Hα ratio to obtain their [O II]-SFR relation whereas Hopkins et al. use the observed values, uncorrected for reddening.

In the left panel of Figure 1.14 we see the SDSS comparison of [O II] and the radio (Hopkins et al., 2003). A scatter of a factor of 1.7 around the one-to-one relation is observed.

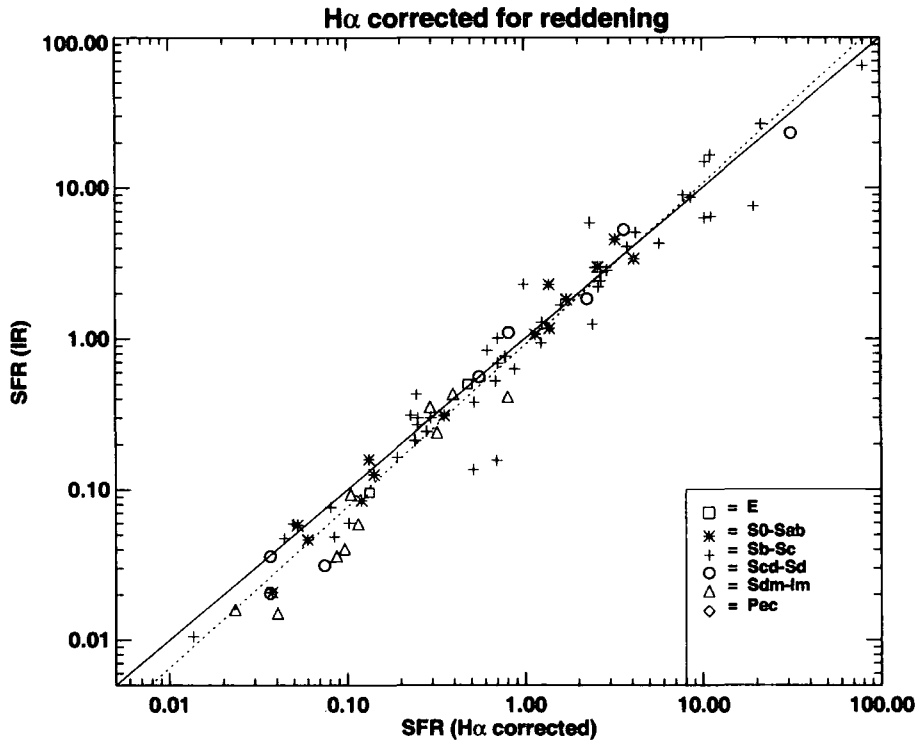

FIGURE 1.12: A comparison of FIR and Hα SFR indicators from Kewley et al. (2002). The solid line shows the one-to-one relation while the dotted line shows the best fit. Hubble type is indicated in the legend. The Hα fluxes have been corrected for reddening using measurements of the Balmer Decrement. The two indicators agree to within 10%.

1.6.1 Relative Merits and Defects

We have compared the various SFR indicators with one another and seen how they offer complementary views of the star formation activity in a galaxy.

We have seen that the U-band and UV indicators offer a glimpse of the direct effect of star formation on the broad spectrum. At the other extreme, the FIR and radio indicators show the indirect effects of star formation; one indicator is well understood (FIR) and the other not so (radio). The relatively poor understanding of the physics behind radio emission is off-set somewhat by its excellent relationship to the FIR. Hα and [O II] fall midway between the direct and indirect extremes of the UV and the radio. These emission line indicators rely on excitation of atoms in gas, which is caused by star formation activity. Although they are not direct methods in the sense that the young stars do not emit these lines themselves, it is nonetheless very simple to see how they are related to the SFR.

Table 1.1 lists the qualitative properties of the six main indicators reviewed in this chapter. They are ranked from "best" through to "worst", according to the opinion of the author and having taken into account all the information and research that has been laid

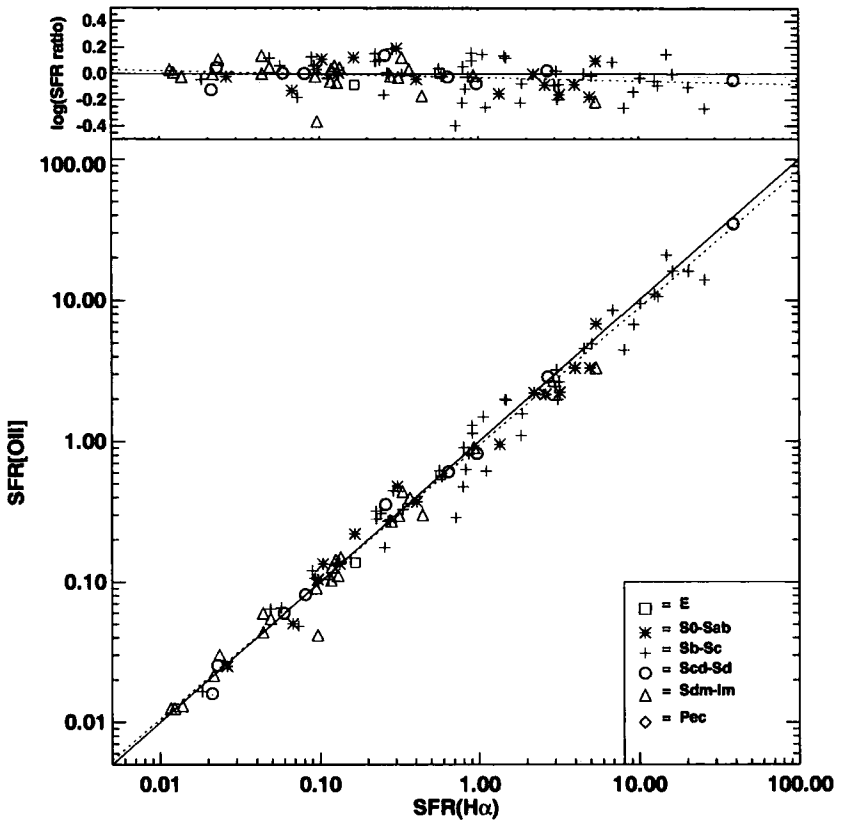

FIGURE 1.13: A comparison of [O II] and Hα SFR indicators from Kewley et al. (2004). The [O II]-SFR calibration derived in that paper is used here. The [O II] and Hα fluxes have been corrected for reddening. There is excellent agreement between the two indicators.

out in this chapter thus far.

1.6.2 The Use Of [O II]

We have seen that [O II] compares well with other SFR indicators. The comparison with Hα is particularly important, since that indicator's relation to the SFR is both simple and direct, also, being in a relatively red region of the spectrum, it does not suffer the same strength of dust extinction that affects the bluer indicators. From Figures 1.14 and 1.13 we can see an excellent agreement between [O II] and Hα, especially using the reddening corrected Kewley et al. (2004) calibration. Aragón-Salamanca et al. (2003) report a tightening in the [O II]/Hα ratio after applying a dust correction, using galaxies from the Universidad Compultense de Madrid Survey (Gallego et al., 1996). A similar result is

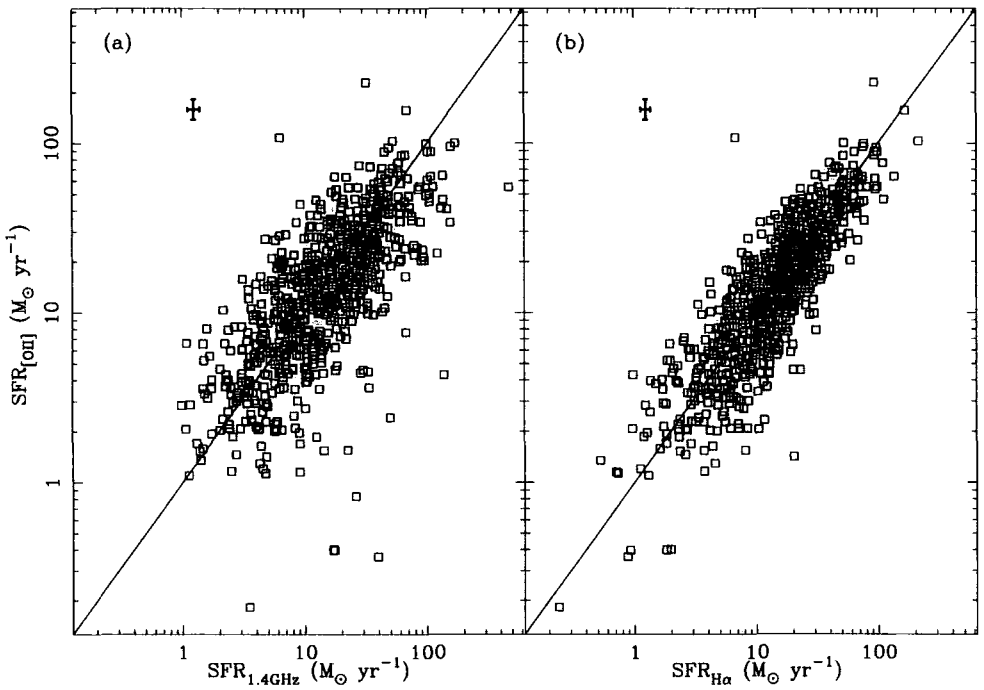

FIGURE 1.14: A comparison of [O II], radio and Hα SFR indicators from the SDSS (Hopkins et al., 2003). The solid line indicates the one-to-one relation in both panels. There is a scatter of factor 1.7 between [O II] and the radio and 1.4 between [O II] and Hα.

reported by Kewley et al. (2004). It is evident therefore that if one has an understanding of the individual reddenings, [O II] gives very similar results to Hα.

[O II] is, of course, known to have a dependence on metallicity (e.g. Jansen et al., 2001). Ideally this should be considered and accounted for in the analysis. Kewley et al. (2004) also confirm the metallicity dependence, and define a [O II]-SFR relation in which a correction for metallicity exists. However, the overall match to Hα does *not* improve by a substantial amount (without metallicity correction a scatter of 0.08 dex in the [O II]-Hα SFRs is observed, c.f. a factor of 0.03 dex scatter with metallicity correction.)

1.7 Choice Of [O II] Calibration

The [O II] emission line will be used in this thesis to measure the SFRs of distant galaxies. There remains the question of which calibration one should employ when using the [O II] line. This is a very important issue if one is interested in determining absolute SFRs, since a major cause of systematic error is the calibration one chooses.

Many authors have published [O II]-SFR calibrations in the literature. One of the most widely used is that of Kennicutt (1998), although many more exist. Here I review briefly a

selection of some of the most recent and commonly used ones. Their properties are shown in Table 1.2. All the calibrations discussed here are of the form

$$SFR(M_{\odot}/yr) = L_{[O\,II]} \times R, \tag{1.2}$$

in which $L_{[O\,II]}$ is the [O II] luminosity and R is the conversion co-efficient.

1.7.1 Calibration of Gallagher et al. (1989)

The calibration of Gallagher et al. (1989) is one of the earliest [O II]-SFR calibrations in the literature. It is based on spectroscopy of [O II] and Hβ emission lines in local, optically blue galaxies, at redshifts $z < 0.1$.

The [O II] flux was found to be correlated with Hβ flux, after the latter had been corrected for stellar absorption. A scatter of a factor of ~ 3 is observed in the relation however.

This calibration of the [O II]-SFR relation relies on two additional steps. Firstly the assumption of no dust extinction in the host galaxies: the dust-free Balmer Decrement ratio of emission line strengths is used to convert the observed Hβ flux into an Hα flux. Secondly the Hα-SFR calibration of Hunter and Gallagher (1986) is used to convert the [O II]-Hα relation into [O II]-SFR.

The calibration has two readily apparent problems, most obviously the assumption of no dust in the calculation of the Hα flux. Secondly the possible problem of poorly dealt with stellar absorption for Hβ. This was done using linear combinations of stellar spectral as a template for the overall galaxy emission, although because of the relatively low resolution spectra used, the absorption could easily have been estimated inaccurately.

1.7.2 Calibration of Kennicutt (1992b)

The Kennicutt (1992b) calibration is based on integrated spectra of 90 galaxies at redshifts $z < 0.03$. The methodology differs from Gallagher et al. (1989) in that here Hα fluxes are measured directly, rather than by proxy from Hβ. An average Hα/[O II] ratio is again determined from the data, and used to convert an Hα-SFR relation (in this case that of Kennicutt, 1983) into an [O II]-SFR relation.

One problem with this work is that the Hα line is blended with the [NII] line in many

of the spectra. This necessarily means a blanket correction for the [NII] flux must be applied to the whole dataset, in order that the Hα flux be obtained. The author adopts a [NII]/Hα ratio of 0.5 for this purpose, which is based on the unblended data in the sample. There is some debate as to whether this is a reasonable value to use. Jansen et al. (2001) for example report an [NII]/Hα ratio of 0.27 from the Nearby Field Galaxy Survey, somewhat different to the Kennicutt value.

Another problem is that the value of [O II]/Hα used by Kennicutt is not corrected for reddening. This means that if one were to employ the calibration its accuracy would depend upon the galaxies under study possessing similar reddenings to those in the original sample. Any deviation from these – unknown – reddenings would result in mismeasurement of the SFR.

1.7.3 Calibration of Kennicutt (1998)

The Kennicutt (1998) calibration is based on an average of the Kennicutt (1992b) and Gallagher et al. (1989) calibrations, after normalising to the same IMF and Hα-SFR relationship.

Since this calibration is based on the two previously discussed, all the problems associated with them are equally applicable here.

1.7.4 Calibration of Hopkins et al. (2003)

The Hopkins et al. calibration is based on data from the Sloan Digital Sky Survey (SDSS) Data Release One. The methodology is again similar to that of Kennicutt (1992b). An [O II]/Hα ratio is found from the data – some 791 galaxies in this case – and then the Hα-SFR relation of Kennicutt (1998) is used to find the [O II]-SFR relation.

A correction for stellar absorption is applied to the Hα fluxes before the average [O II]/Hα ratio is determined, although there is the problem of no dust correction being applied to the observed [O II]/Hα ratio.

1.7.5 Calibration of Rosa-González et al. (2002)

The Rosa-González et al. calibration is derived from an analysis of the effects of dust extinction on the [O II] indicator as calibrated by Kennicutt (1998). By comparing with the FIR as the fiducial indicator, a new [O II]-SFR calibration is found. The new calibration

includes a dust correction based on the Balmer Decrement, made after the effects of stellar absorption have been accounted for.

Since the calibration already has a dust correction built in, it is potentially very useful since it could be used on samples of galaxies for which no extinction information is available. Of course care must be taken to ensure that the sample under study is similar to that of Rosa-González et al.

1.7.6 Calibration of Kewley et al. (2004)

The calibration of Kewley et al. (2004) is one of the most recent studies of the relation between [O II] flux and SFR. Kewley et al. deal with the complications that arise in many of the other calibrations (e.g. those above), which rely on using the Kennicutt (1998) Hα-SFR calibration and a [O II]/Hα ratio, measured for each sample under examination. To recap, the problems associated with that methodology are as follows.

- Due to the low resolution spectra used to derive it, the Kennicutt (1992b) calibration (on which the Kennicutt, 1998 calibration is based), assumes an [NII]/Hα ratio of 0.5. There is no guarantee that this ratio is (even broadly) the same for all galaxies. Indeed Kewley et al. (2001) have shown that the number may be as low as 0.01 in low metallicity galaxies.

- The Kennicutt (1992b) calibration uses an [O II]/Hα ratio to convert from a Hα-SFR relation to an [O II]-SFR relation. The ratio used is not corrected for reddening. There is no guarantee that any other sample will have the same reddening properties as the Kennicutt (1992b) sample.

- There is no correction for stellar absorption in the Kennicutt (1992b) [O II]/Hα ratio estimate.

- There is no correction for metallicity effects in the Kennicutt (1992b) calibration.

The benefit of the Kewley et al. (2004) calibration is that it deals with all of these issues. Firstly, the spectra used (from the Nearby Field Galaxy Survey, Jansen et al., 2000), are of sufficient resolution to separate the Hα and [NII] lines. This means an [NII]/Hα ratio does not need to be assumed. Furthermore, the spectra have high quality Hα and Hβ lines, meaning reddenings can be determined from the Balmer Decrement.

Finally, it is possible to measure the amount of absorption suffered by the Balmer lines, and this too can be corrected for.

There are two [O II]-SFR relations derived by Kewley et al., one for use when the metallicity of the sample is known and one for use if the metallicity is unknown. For the CNOC2 sample in this thesis, we have no way of determining the metallicities of individual galaxies. The calibration for galaxies with unknown metallicities is therefore the most suitable of the two.

1.7.7 Conclusions

In this chapter we have reviewed some of the most commonly used SFR indicators from the literature. We have shown that use of the [O II] emission line as a SFR indicator is perfectly viable, so long as the reddenings are properly considered. If they are, then [O II] compares favourably to other measures, especially Hα.

We must now decide between using the Kewley et al. (2004) calibration, or creating our own [O II]-SFR calibration, specific to CNOC2. This would be done using the common methodology of measuring an [O II]/Hα ratio for the sample, and then using the Kennicutt (1992b) Hα-SFR relation to convert to [O II]-SFR.

Unfortunately, the wavelength range of spectra in the CNOC2 dataset does not extend to Hα and so there are actually no CNOC2 spectra from the main Survey that could be used to estimate the [O II]/Hα ratio. There is however, a small extension to the main Survey that includes some longer wavelength range spectra of a subsample of CNOC2 galaxies (see Chapter 3). In principle this subsample could be used to measure the [O II]/Hα ratio, although in that case the line Hα and [O II] line fluxes would be measured from separate spectra. This would introduce some error into the determination of the [O II]/Hα ratio. As a result we chose the Kewley et al. (2004) route and do not measure the [O II]/Hα ratio for CNOC2.

The cosmology used in this thesis is a flat, Ω_Λ=0.70 model with H_0=72 km s^{-1}Mpc^{-1}.

1./ Hα

Advantages

Simple, well understood physical relation to the SFR
Does not require non-linear calibration; provides a good "instantaneous" measure of SFR

Disadvantages

Slight sensitivity to dust
Above $z = 0.3$ Hα moves to the Infrared, making it more difficult to observe
Affected by metallicity
AGN contamination is possible

2./ FIR

Advantages

Dust enhances its ability to determine the SFR
Picks up star formation missed by optical indicators

Disadvantages

The possibility of alternate heating sources for the dust makes the calibration uncertain
It is impossible to observe FIR directly from the ground
AGN contamination is possible

3./ [O II]

Advantages

Well correlated with Hα emission
Accessible over the $0.2 < z < 1.0$ range

Disadvantages

Affected by metallicity
Susceptible to dust obscuration
AGN contamination is possible

4./ UV

Advantages

Simple and direct physical relation to the SFR for young stellar populations
Relatively insensitive to the assumed IMF

Disadvantages

Non-linear calibration is required to compensate for the age of the stellar population
Exceedingly susceptible to dust obscuration
AGN contamination is possible

5./ Radio

Advantages

Not affected by dust
Excellent relation to FIR emission

Disadvantages

Complex, indirect and ill-understood relationship to the SFR
The fraction of non-thermal emission varies from galaxy to galaxy making calibration difficult
AGN contamination is possible

6./ U-band

Advantages

Relatively simple to observe

Disadvantages

Non-linear calibration is required to compensate for the age of the stellar population
Susceptible to dust extinction

TABLE 1.1: The author's subjective ranking of the six main SFR indicators reviewed in this chapter. Qualitative advantages and disadvantages are also listed.

Author	Coefficient[a]	λ Extinction correction (Å)	IMF
Gallagher et al. (1989)	6.5×10^{-42}	6563	Salpeter
Kennicutt (1992b)	2.0×10^{-41}	6563	Miller-Scalo
Kennicutt (1998)[b]	1.4×10^{-41}	6563	Salpeter
Hopkins et al. (2003)	3.4×10^{-41}	6563	Salpeter
Rosa-González et al. (2002)	8.4×10^{-41}	n/a[c]	Salpeter
Kewley et al. (2004)	6.58×10^{-42}	3727	Salpeter

[a]The conversion coefficient for [O II] flux, calibrated to erg/s.
[b]Based on the mean of Kennicutt (1992b); Gallagher et al. (1989), after conversion to the same IMF.
[c]This calibration uses observed [O II] fluxes and hence no extinction correction can be applied.

TABLE 1.2: Properties of some widely used [O II]-SFR calibrations from the literature.

2

CNOC2: Introduction and Spectral Line Measurement

In this chapter I present a detailed introduction to the 2nd Canadian Network for Observational Cosmology Field Galaxy Redshift Survey (CNOC2). We begin with a brief description of the data set and then delve into how it was produced and details of the spectrograph used etc.

2.1 CNOC2: Dataset Overview

The CNOC2 Survey (Yee et al., 2000) is a multi-band photometric and spectroscopic survey of faint galaxies covering a total of 1.5 square degrees of the sky. The redshift ranged probed by the survey is $0.2 \lesssim z \lesssim 0.65$ with the nominal spectroscopic limiting magnitude being R = 21.5 mag. We will discuss the detailed limits in both redshift and magnitude below.

The CNOC2 Survey of field galaxies complements the original Canadian Network for

Observational Cosmology Cluster Survey (CNOC1, Yee et al., 1996), which targeted rich clusters of galaxies. The two surveys share several collaborators. CNOC2 was carried out on the on the 3.6 m Canada France Hawaii Telescope (hereafter CFHT) over a period of 53 nights, in seven separate observing runs beginning in February 1995 and ending in May 1998. Table 2.1 shows the duration and date of each run as well as which CCD in use at the time (note that the CCD changed three times over the duration of the Survey, as discussed in Section 2.1.2).

The full dataset for the Survey includes photometry in 5 optical bands (U, B, V, R_c, I_c) for $\sim 40,000$ galaxies (discussed in Section 2.1.3) and spectroscopy for $\sim 6,000$ individual galaxies, representing a sampling rate of $\sim 45\%$ at R = 21.5 mag (discussed in Section 2.1.4).

Run	Start Date	Number of Nights	CCD
1.	1995/02/27	8	ORBIT1
2.	1995/10/20	8	LORAL3
3.	1996/02/13	9	LORAL3
4.	1996/10/11	8	STIS2
5.	1997/02/04	8	STIS2
6.	1997/08/30	6	STIS2
7.	1998/05/23	6	STIS2

TABLE 2.1: The dates and durations of the observing runs that made up the CNOC2 Survey. Also shown is the name of the CCD in use on the telescope at the time of the run (the properties of the detectors are shown in Table 2.3). The data above has been taken from Table 3 of Yee et al. (2000).

2.1.1 Patch Selection, Size and Shape

The main goal of the Survey was to measure the clustering of galaxies over the redshift range $0.1 < z < 0.6$, and it is this aim which shaped the overall design of the project. In particular, the desire to minimise sensitivity to large scale structures on the sky lead to the Survey being divided into four widely separated areas, referred to as "Patches". These are spaced every $5^h - 7^h$ in RA and together cover the total survey area of 1.5 square degrees. Table 2.2 shows some general properties of each Patch observed, including their positions on the sky, their galactic coordinates and their total area.

Aside from avoiding the large structure issue, the spacing of the Patches has other advantages over a "one-area" survey: Firstly a better sampling of the clustering is obtainable from four separate areas as compared to using only one; secondly the four Patches

Name	RA[a]	Dec [a]	b	$E(B-V)$ [b]	No. of Fields	Total Area [c]	No. of Mask
CNOC $0223+00$	02 23 30.0	+00 06 06	−54.3	.036	19	1408.7	39
CNOC $0920+37$	09 20 40.7	+37 18 17	+45.6	.012	19	1366.9	40
CNOC $1447+09$	14 47 11.6	+09 21 21	+57.2	.029	17	1240.0	34
CNOC $2148-05$	21 48 43.0	−05 47 32	−41.6	.035	19	1417.9	39

[a]Right Ascension and Declination are given in the B1950 system.
[b]The galactic extinction is obtained from the dust maps of Schlegel et al. (1998).
[c]Area in square arcmins.

TABLE 2.2: General properties of the Patches observed by the CNOC2 Survey including position, galactic coordinates and total area. The data has been taken from Table 1 in Yee et al. (2000).

can be used to give an estimate of the effects of cosmic variance and thirdly, being spaced in RA ensures good observing efficiency since at least two Patches are visible at any given time of year from the CFHT.

The shape and dimensions of each Patch are illustrated in Figure 2.1. A single Patch is made up of a square central region of $\sim 30' \times 25'$ from which two "legs" protrude extending the coverage to $\sim 60' \times 80'$ at the extremities. The numbering scheme in the Figure refers to separate fields – individual telescope pointings – that make up a Patch; the labelling schemes of numbers (e.g. 02) or letter-number (e.g. a2) are fully equivalent. It can be seen that approximately 20 MOS fields make up each full Patch. The peculiar shape is a derivative of the original inverted-Y design which was altered after the first observing run. The original Y design was chosen since it provides equal power on all scales when performing the Fourier Transforms necessary to measure the clustering. The alteration that give rise to the central square area was motivated by the decision to give more power to smaller scales; some vestiges of the legs still needed to be retained however as otherwise all signal on the larger scales would have been lost.

As we have noted, a field may be thought of as the area covered by an individual telescope pointing. Photometry and spectroscopy are conducted on a per-field basis. A field is first imaged and then candidate galaxies are selected for spectroscopy from the imaging data (this procedure is discussed in Section 2.1.4). The size of each field is roughly $10'$ across, corresponding to the instrumental field of view (see Table 2.3).

Adjacent fields overlap by some small amount (typically $10'' - 20''$) in order to allow consistency checks on astrometry and redshift measurement.

The Patches were chosen to avoid known low-redshift structures (e.g. the Abell clusters) which would have heavily affected the clustering results. In addition, any bright, low-

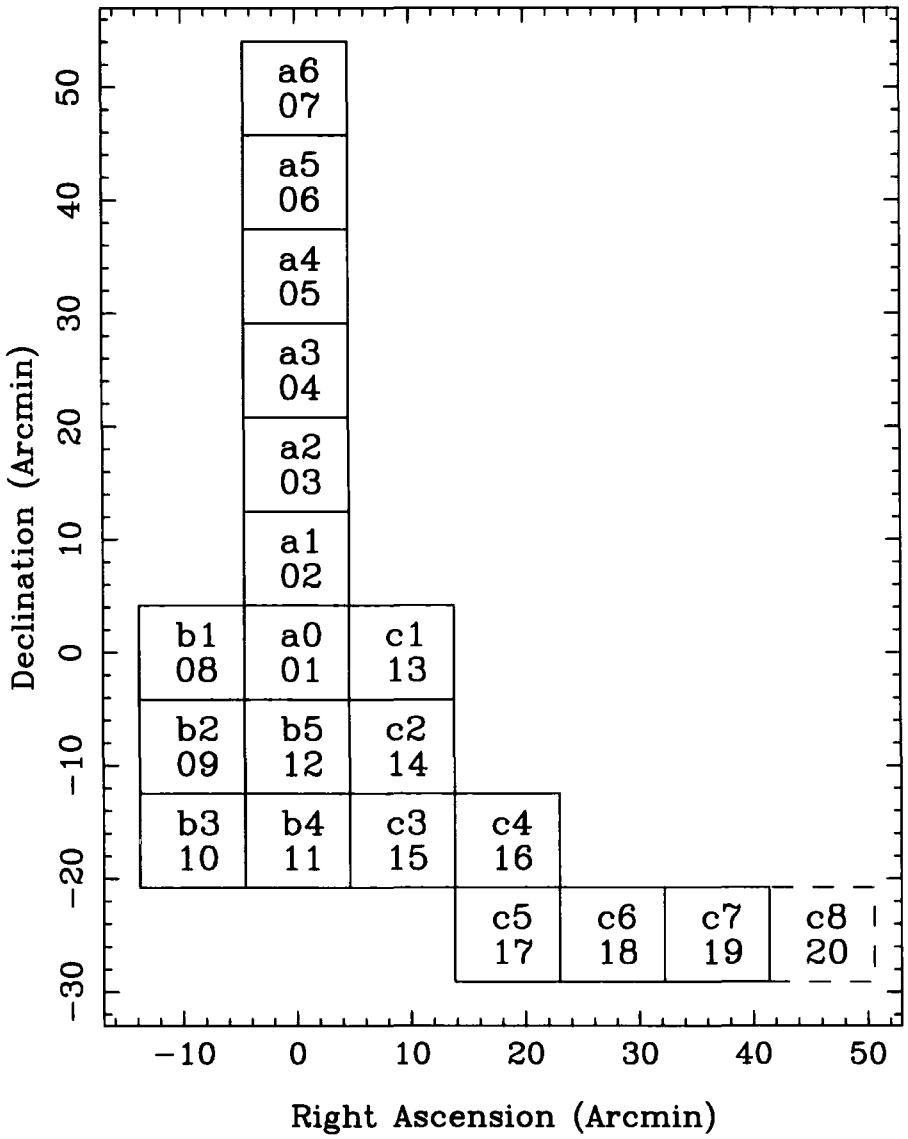

FIGURE 2.1: The shape and dimension of each Patch from the CNOC2 Survey. The numbering schemes of letter-number (e.g. a2) or number (e.g. 02) refer to the fields – individual telescope pointings – within the Patch and the conventions are fully equivalent. Approximately 20 MOS fields make up each Patch.

redshift galaxies were specifically avoided, as were known quasars and AGNs.

The galactic latitudes of the Patches range from $45° < |b| < 60°$, ensuring an avoidance of high extinction zones within the Milky Way, while also including a reasonable number of stars in each field. It is necessary to observe some stars as part of the Survey as they are needed to provide a reliable star-galaxy classification. Since the stellar point spread function (PSF) varies quite significantly over even a single field (Section 2.1.3) it is important that there are several stars available for use in the star-galaxy analysis.

2.1.2 Instrumentation

Before we discuss the methodology used for the photometry and spectroscopy in the Survey, the instrumentation must be described. Therefore we examine now the CCDs and spectrograph used to do the Survey.

CCD Detectors

Three CCD detectors were used during the course of the Survey, these were the ORBIT1, LORAL3 and the STIS2. The ORBIT1 CCD was only used for the very first of the observing runs after which it failed. It was replaced by the LORAL3 CCD which was employed for runs 2 and 3. From run 4 onwards the STIS2 CCD was used. 78% of the data in the Survey was collected using the STIS2 unit.

Table 2.3 shows the characteristics of the three detectors. Evident in the table are the differing spectral resolutions of the CCDs and their differing imaging area. This necessarily means that the spectra obtained are not all of the same resolution and neither do all of the images have a common pixel scale. Note that the STIS2 chip has a slightly larger pixel scale than the other chips and so only a 1416×1368 subraster of the full chip (2048×2048) was used.

Not shown in the table is the fact that the different CCDs have different quantum efficiencies. This meant that the exposure time for observations had to be adjusted accordingly with some chips requiring longer integration times than others to achieve comparable signal to noise ratios. Table 2.4 shows how the exposure times used for imaging and spectroscopy vary according to the CCD in use.

Parameter	ORBIT1	LORAL3	STIS2
Pixel Size (μm)	15	15	21
Pixel Scale (arcsec)	0.313	0.313	0.438
Imaging Area (pixels)	2048×2048	2048×2048	1416×1368
Defined field area (arcmin)	7.3×9.2	7.3×9.2	8.3×9.2
Å/pixel	3.55	3.55	4.96

TABLE 2.3: General properties of the three CCD detectors used during the CNOC2 survey. The pixel scales on the chips are not consistent across all three units, neither is the imaging area used. The data has been taken from Table 2 in Yee et al. (2000).

The CHFT Multi Object Spectrograph

All the data collected by the Survey were taken on the Multi Object Spectrograph arm of the MOS-SIS instrument on the CFHT (Multi Object Spectrograph – Subarcsecond Imaging Spectrograph). The instrument is described comprehensively in Le Fevre et al. (1994) although certain details of the design can also be found in Morbey (1992) and Crampton et al. (1992). Here I present an overview.

The CHFT MOS is part of the two component MOS-SIS instrument. As the name suggests, MOS-SIS can be used in one of two modes: A MOS mode for spectroscopy and imaging work over a field of $\sim 10'$ (as used in CNOC2), or SIS mode for high resolution imaging over a smaller field of view ($\sim 3'$). The details of the latter instrument do not concern us in this thesis.

Two diagrams that illustrate the structure of the MOS-SIS instrument are shown together in Figure 2.2. The MOS instrument allows both spectroscopy and imaging to be undertaken. The mask slide assembly can either hold a mask (for spectroscopy mode) or allow an unobstructed light path to the CCD (for imaging mode). In imaging mode the grism must, of course, also be removed from the light path. The field of view is $10'$. In spectroscopy mode the simultaneous capturing of tens to hundreds of individual galaxy spectra is possible, depending on the target density on the sky and spectral resolution selected (a higher spectral resolution means the spectra take up more space on the CCD and so less spectra may be taken in one exposure). Of note is the fact that the filter wheel can contain band limiting filters to restrict the wavelengths of light hitting the CCD during spectroscopy. This means that the number of spectra on the chip can be increased considerably since each spectrum occupies a well defined area that is smaller than it would be without the filter. CNOC2 did use such a filter in order to increase the multiplexing of spectra on the chip. The filter is discussed in Section 2.1.4, although here I note that the half-power limits are ~ 4300 and ~ 6300Å.

As indicated in Figure 2.2 the MOS uses masks to select galaxies for spectroscopy (c.f. the 2dF instrument on the Anglo-Australian Telescope that uses optical fibres for this task). The masks need to be prepared and cut before any spectroscopy is possible; this was done with a laser drilling machine at the CHFT. The procedure of selecting targets for spectroscopy is described in Section 2.1.4.

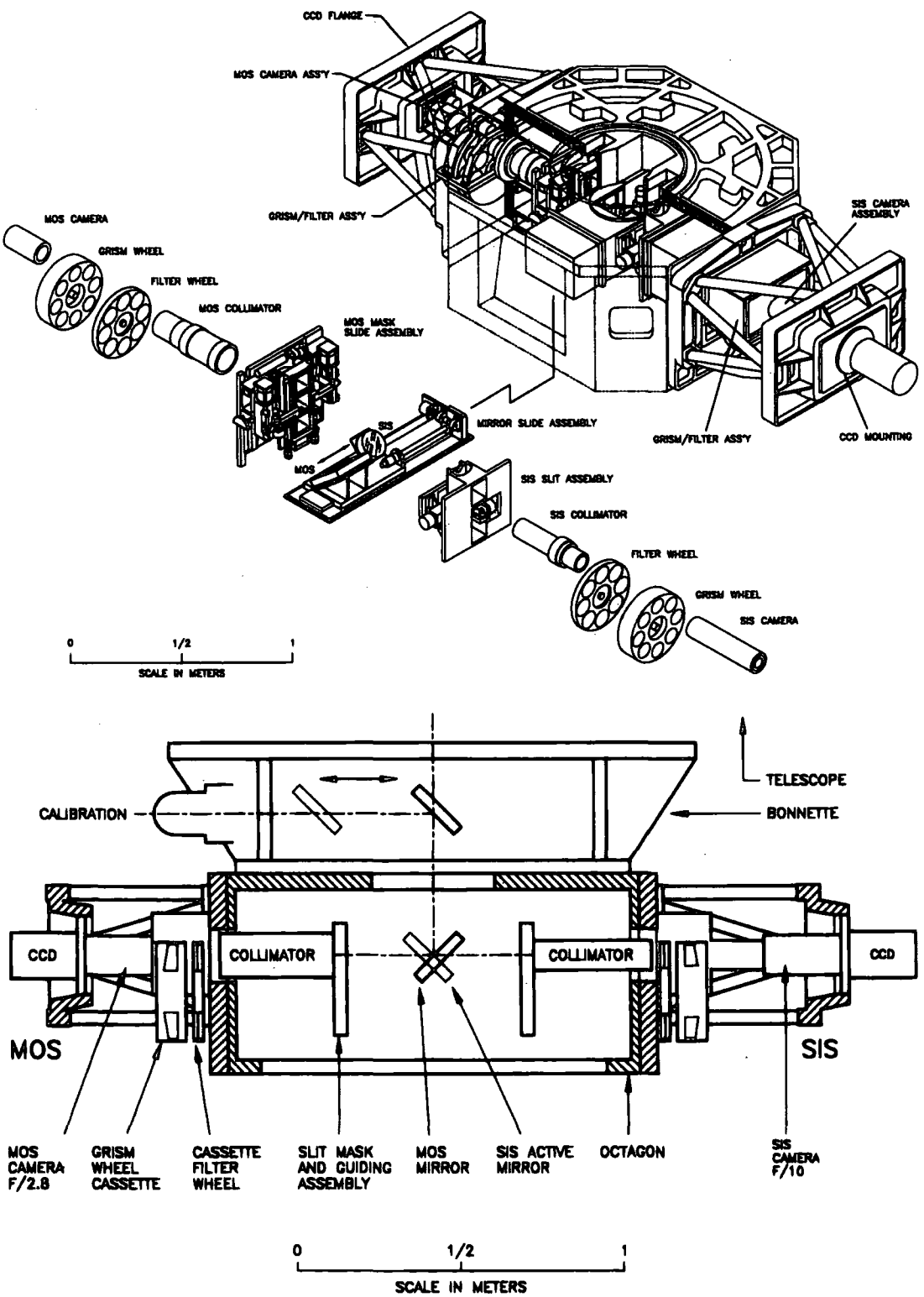

FIGURE 2.2: 3D and 2D schematic drawings of the CFHT MOS at the time of the CNOC2 Survey. The MOS uses plates as masks to select galaxies for spectroscopy; these are cut with a laser drilling machine at the CHFT. These figures have been extracted from Le Fevre et al. (1994).

	ORBIT1	*LORAL3*	*STIS2*
Spectroscopy Exposure Times (s)			
Mask A	~ 3000	~ 3600	~ 2400
Mask B	~ 7000	~ 7200	~ 4800
Imaging Exposure Times (s)			
Filter I_c	420	600	360
Filter R_c	420	600	420
Filter V	420	600	420
Filter B	420	900	480
Filter U	–	–	900

TABLE 2.4: Exposure times for imaging and spectroscopy for the different CCDs used over the course of the CNOC2 Survey. The concept of Mask A and Mask B and the types of galaxies selected by each mask is discussed in Section 2.1.4. The data above has been taken from Table 2 in Yee et al. (2000).

2.1.3 Photometry and Imaging

As noted, the CNOC2 Survey contains photometry for $\sim 40,000$ galaxies in the five optical bands U, B, V, R_c, I_c. We discuss now how the photometry was calibrated and how accurate it is. This is of considerable importance to us since in Chapter 3 we will need the photometry to obtain dust estimates from Photometric Redshift codes.

Object Identification

Imaging was conducted in the 5 bands according to the exposure times shown in Table 2.4. The Picture Processing Package (hereafter PPP – Yee, 1991; Yee et al., 1996) was used to obtain positions and fluxes (in ADU) for all the objects in a given field. A master catalogue is first created from the R band image with the magnitudes in other filters being computed as discussed in the following subsection.

However before the images are examined using PPP, the cosmic ray hits in each CCD frame are rejected so to avoid their misidentification as galaxies or stars. This is particularly important in the U band since the exposure time required to reach reasonable signal to noise levels is somewhat longer than the other filters. Cosmic rays are rejected via a selection of pixels that are more than 9σ away from the local sky rms, these are then examined to see if they belong to a nearby galaxy or star using a sharpness test. If they are not associated with a nearby galaxy then the affected pixels are corrected using a simple linear interpolation. The cleaned images are then processed by PPP.

Since several different CCDs were used during the Survey, the images have different pixel scales. This means that the master list of positions and sizes of galaxies found by PPP from the R band image in one field will not necessarily match the positions and sizes of the same objects in that same field as observed through the other filters. A transform must be done to ensure that the geometries in the master catalogue map onto the other filter images. This was achieved by comparing the position of several bright objects in the images. After this has been done a common database of positions and object sizes can be used for all the filters.

PPP identifies galaxies using a method similar to that of Kron (1980). A local maximum in pixel intensity is found and the flux from the adjacent 9 pixels summed to give an object flux. If this is higher than some fraction of the local sky background then the coordinates of the object are stored in the master database. An object identification number is also assigned to the object based on its position on the CCD. There are some modifications to this identification scheme to correct for the algorithm's bias against low surface brightness galaxies and the reader is referred to Yee (1991) for the full details.

The accurate positions of objects on the frame are determined iteratively using an intensity centroid algorithm which yields an accuracy of ~ 0.01 pixels for bright objects and ~ 1 pixel for objects near the 5σ detection limit. The main source of uncertainty however is the pincushion distortion effect of the MOS optics, which is of order $5-6$ pixels at the edges of the images. The effect was corrected for by imaging a back-illuminated mask of pinholes of known separation.

The measurement of the total flux from an object is done via use of growth curves. A growth curve describes how the total flux from an object varies as a function of distance from its centre. PPP uses concentric circular discs to compute the growth curves, summing the flux from within each radius. Note that elliptical apertures are not used. The concentric discs are centred on the position determined using the intensity weighted centroid procedure above and extend out to a maximum of some predefined radius (typically $12''$). Contamination from nearby objects should not heavily affect the determination of another object's growth curve since they are masked out: every object falling within twice the predefined maximum allowed radius is masked.

Once the growth curve has been measured, the optimum extraction aperture is determined for the object. This is defined to be the radius at which the curve deviates from

having a monotonically increasing flux and a monotonically decreasing first derivative.

For some galaxies the maximum aperture of 12″ is too small to produce an accurate flux determination. After the first pass PPP recomputes the growth curves for very bright and large objects using a larger maximum allowed aperture (set at 24″ for CNOC2).

The optimal extraction aperture size is determined for all objects in all filters, although only the fluxes through the R band filter are measured. Fluxes from the other filters are computed using a colour term between themselves and the R band, as described in the next subsection.

Standard Star Calibration and Magnitude System

The bands shown in Table 2.4 are not exactly what they appear at first glance. The photometry is taken through Johnson filters for the U and B bands, Cousins filters for the I and R bands (hence the naming R_c and I_c) and through a Gunn g filter for the V band. Calibration was performed via observation of Landolt standard fields (Landolt, 1992) and the M67 star cluster (when possible), once per run for each of the five filters.

Worthy of note is that fact that the g filter on the CHFT at the time of CNOC2 was a somewhat redder filter than the original definition by Thuan and Gunn (1976). This lead to the problem of an uncertain colour term being required for its calibration, because there are a relatively small number of standard stars available for that particular filter. As a result the images were calibrated to the Johnson system using the Landolt standards. The colour term in this calibration is smaller than that needed for the "natural" calibration and so the resulting magnitudes are more accurate.

The R band magnitude is derived according to the growth curve methodology and the standard star calibration procedure detailed above (see also Yee, 1991). To compute the magnitude in any of the remaining bands, a colour term is used. This colour term between the reference and target bands is computed using a specially determined aperture that is the minimum of three quantities: the default colour aperture (set at 4″, a large value to take account of the variable PSF across the MOS field), and the two optimum apertures found by the growth curves for each filter. The total magnitude in the target band is then found by adding the colour term to the reference band. The R band is the reference band for every filter with the exception of the U band, for which B is used – it being closer in wavelength to U than R is.

The above method has the advantage of the colour term always being defined from a common aperture over the two filters and in principle this means that the uncertainty in the fainter band's magnitude should be smaller than were it computed differently. It does of course require that the colour gradient across an object be uniform and this is not obviously the case for all galaxies.

The error in the colour term is computed as the quadrature sum of the uncertainties from the photometry using the colour aperture in each filter.

Yee et al. (2000) report that the typical uncertainties in the zero-point of the calibrations are 0.04, 0.04, 0.05, 0.05, 0.07 magnitudes for U, B, V, R_c, I_c respectively. All magnitudes in the Final Survey Catalogue are reported in the Vega system.

Star-Galaxy Classification

Star-galaxy classification is done by PPP as part of the main reduction. The R band is selected as the sole band to used for this purpose, which is a sensible choice given that it is the deepest in the Survey.

PPP determines if any object is a star or a galaxy by comparison of its growth curve to those of nearby reference stars. Note that the classification is hampered by the variability of the PSF across the MOS field of view. To compensate for the optics' effect the target object's curve is compared to the four nearest reference star curves. Typically $20 - 40$ reference stars are used over one field and these are found automatically by the code (Yee, 1991).

The procedure is susceptible to errors, in particular from stars with projected close companions (be they stellar or galactic). However the classification is thought be be robust down to a limit of $R = 22$ mag.

2.1.4 Spectroscopy

We discuss now the procedures associated with the acquisition and calibration of galaxy spectra in CNOC2. This is of utmost importance since these spectra will be used to analyse the Star Formation History in Chapter 4.

Mask Design and The Selection of Targets For Spectroscopy

The production of the CNOC2 photometric catalogues was described above. From these catalogues of (amongst other quantities) position, magnitude and star-galaxy class, a list of targets to be observed spectroscopically was selected. An automated mask design programme was used to make this selection and design the masks needed to perform the observations. The clear advantage of using of a computerised algorithm is that it allows us to know precisely the selection function of galaxies being targeted. This is of huge importance as it permits the calculation of a statistical weight associated with each galaxy. These weights can be used to make corrections for galaxies that were not observed during the Survey. This is needed when one is measuring e.g. the luminosity function, or indeed studying the star formation history.

The algorithm that assigns optimal slit placements on a mask is the same as that used in the CNOC1 Survey (Yee et al., 1996). The method of selecting galaxies for spectroscopy is different however, with CNOC2 using both the R and B band catalogues to produce the sample. Only objects classified as galaxies by PPP are considered in the mask design process and any stars that are observed spectroscopically are done so unintentionally, by either chance alignment down a slit or through misclassification as galaxies.

The observational strategy was to use two masks per field, referred to as masks A and B. If, for reasons of poor weather, the data from either one of them was considered to be substandard, then a third mask (C) was designed and observed. Of the 74 fields observed in total, 4 required third masks be to designed.

Using two masks allows the fainter objects to be grouped into one exposure and the brighter ones into another, meaning the integration times can be geared to the average brightness of targets in each mask. To this end, mask A is used for brighter galaxies, while mask B targets the fainter ones.

The procedure for the design of mask A is simply to order targets by ascending brightness to a limit of $R = 20.25$ mag. Highest priority is given to galaxies nearest the $R = 20.25$ limit. Based on the order of the magnitude ranking, slits are assigned to the mask if they produce nonoverlapping spectra on the CCD. An extra constraint is also enforced, to account for the fact that this scheme would normally allow galaxies at the edges of the field to get priority. This is because some fraction of the area occupied by their spectra falls

outside the defined spectroscopic field area on the chip. It is therefore almost guaranteed to not overlap with other spectra. To counteract this effect, a galaxy is only ever placed at the edge of the field if the fraction of its spectrum falling outside the defined field area is larger than a random number picked between 0 and 1. This ensures that the placement of targets in the central regions of the mask is not driven by an overabundance of slits at the edges.

After the scheme above has been followed, the slits are shifted in the spatial direction (such that a target may no longer be at the centre of its slit) and any additional space is used assigned to new slits.

The mask B design procedure is more complicated. The primary sample for mask B consists of all galaxies whose magnitude lies between R = 20.25 and R = 21.5 or B = 22. The galaxies are again ordered in ascending R magnitude, just like the mask A design. A second ranking scheme is also employed however. This concerns the selection of targets in close-pairs which is important for the clustering analysis. It is also important for our study of the SFH, since galaxies in close-pairs may be interacting with one another, meaning some star formation could be taking place. If so, we certainly want to observe it.

The close-pair ranking is done as follows. Firstly the ratios of numbers of pairs as a function of separation for galaxies in the mask A sample and those in the mask B sample are computed. For a galaxy not already placed in mask A, the separation to the nearest target that is assigned to mask A is found. The ratio of the pair distributions at this separation is used to form the close-pair ranking, the lower the ratio the higher the priority.

The final ranking is computed as the quadrature sum of the magnitude ranking and the close-pair ranking. Targets are then assigned to the mask according to their positions in this list. The procedure of shifting the positions of galaxies in their slits is again followed, and more targets are added if space becomes available.

After all targets from the primary sample for mask B have been assigned, a secondary sample is drawn up. This consists of any R $<$ 20.25 galaxies that were not placed in mask A. Ranking is again done on magnitude and close-pair separation. After all of those targets have been placed, repeat observations of galaxies already in mask A are chosen, ranked on magnitude (see comment below). Lastly any available space is assigned to faint galaxies with R $>$ 21.5, ranked on magnitude alone.

By virtue of each individual field being observed spectroscopically at least twice (mask A, mask B), some galaxies are purposefully observed more than once, in some cases up to three times. These repeat observations allow the redshift accuracy to be assessed. For our purposes they are especially useful in determining the nature of the true errors on our measurements of the [O II] line strength (see Section 2.2.2).

Observational Details and Instrumental Setup

The exposure times for spectroscopic observations are shown in Table 2.4. They vary according to the quantum efficiency of the CCD in use and are on average ~ 3000 s for A masks and ~ 6300 s for B masks, consistent with mask A targeting brighter galaxies. Each mask is typically observed twice and the exposures are co-added as part of the reduction process.

The B300 CFHT grism was used as the dispersion element. It has 300 lines/mm giving a dispersion of 233.6 Å/mm. The corresponding on-CCD resolutions are shown in Table 2.3. The silt width used in the masks was $1.3''$ which gives a spectral resolution of ~ 14.8 Å. This is derived by considering the pixel scale on the detector.

A band-limiting filter was used in order to increase the number of spectra that would fit onto the CCD. The filter is effectively a top-hat function whose half-power wavelength range is $4387 < \lambda < 6285$ Å. It works to reduce the area occupied by individual spectra and hence more targets can be observed in any one exposure. The wavelength limits of the filter were chosen so as to coincide with the onset of inefficiencies in the CCD/grism transmission function at the blue end of the spectrum and regions of heavy sky line contamination at the red end.

It is clear that use of the band limiting filter effectively defines the redshift range of the Survey. Factoring together the half-power cut-off limits with the wavelengths of strong spectral features for different galaxy types gives the effective redshift limits of the Survey. Taking strong spectral features such as the H and K lines of Calcium or the [O II] line, give low redshift limits of $z \sim 0.12 - 0.16$. The corresponding high redshift limit for the Calcium lines is $z \sim 0.55$.

We note for some emission line galaxies the [O III] lines will also be present in the spectrum. The [O III] lines enter the red end of the spectrum at $z \sim 0.25$ and hence bring the low redshift limit of the Survey to $z = 0$. The high redshift limit for emission line

galaxies is set by the [O II] line and is $z = 0.68$.

The redshift range for emission line galaxies is then $0 < z < 0.68$ while it is $0.2 < z < 0.55$ for the CNOC2 full sample (as computed from the H and K lines).

Spectral Extraction

The spectra were processed from the raw CCD frames using semi-automated IRAF routines. The end result of the extraction and calibration procedure is a multi-fits format file, one for each mask, the levels of which contain various data relating to the individual spectra from the mask. One level, for instance, contains the sky background, another the extracted spectrum etc. (Section 2.2.1 discusses the format explicitly).

As noted, IRAF routines are used to perform the extraction and calibration of spectra, the final reduced spectra being both wavelength and flux calibrated. I outline how this is done below. Before the individual CCD frames are processed by IRAF however, cosmic rays are removed from the raw data using the procedure described in Yee et al. (1996). The method is similar to that used by the PPP package in processing the imaging data. Pixels $7 - 9\sigma$ above the local median are tagged as possible cosmic rays and are then interpolated over after the full extent of their contamination has been ascertained (by a connected area routine). The procedure of cleaning cosmic rays by creating a median image from separate exposures is not followed, not least because the shorter exposure times necessary to produce the multiple frames would have resulted in a lower signal to noise ratio in the data. After the raw frames have been cleaned of cosmic rays they are co-added to produce one frame and then passed to IRAF for reduction.

Since the positions and areas occupied by spectra on the chip are known ahead of time (by virtue of the mask design algorithm) it is possible to process each spectrum individually. To this end each area occupied by an individual spectrum is copied to a separate subimage. Every "on-sky" CCD frame has associated with it a flat-field and arc lamp exposure and subimages from these are also created, again using the regions defined by the mask design algorithm. The extraction and calibration then proceeds on a subimage-by-subimage basis.

Firstly the flat field subimage is used to remove the pixel-to-pixel variations across the CCD. A spline fit to the mean profile in the wavelength direction is used to normalise the flat and it is then divided into the object spectrum. The spectra are then extracted using a

variance weighting scheme. Because the exact location of spectra is known, in principle no additional input is needed. The extraction windows are however verified by eye. The arc lamp spectrum is also extracted from its subimage, corresponding to an identical location on the CCD and again using the same weighting scheme.

To wavelength calibrate the spectra, arc lines at known wavelengths are identified interactively and a wavelength solution for each spectrum is found. Yee et al. (2000) report typical rms residuals from the wavelength fit of ~ 0.1Å although the wavelength solution changes depending on the initial location of the spectrum on the raw CCD frame. For this reason, as a final part of the calibration, the spectra are all linearised to run from exactly $4390 - 6292.21$Å with a uniform dispersion of 4.89Å/pixel.

After the wavelength calibration, the spectra are corrected for atmospheric extinction using the typical $sec(z)$ prescription and the CHFT atmospheric curve (z being the zenith distance in this case). They are then flux calibrated by comparison with standard star observations. The standard stars are usually taken through a near-central aperture in the mask. Yee et al. (2000) report that the relative flux calibration is accurate to $\sim 20\%$ but that the absolute calibration could be off by considerably more.

The final process in the reduction is the removal of strong sky emission lines and interference from zero orders. The skylines at 5577 and 5892Å are automatically interpolated over using a 45Å wide band. Zero orders are found from by-eye inspection and interpolated over using a 125Å wide band.

Redshift Measurement

To find redshifts, object spectra are cross-correlated against three galaxy templates from Kennicutt (1992a). These are the elliptical, Sbc and Scd templates. In order to verify the redshifts determined by the cross-correlation programme, each object's spectrum and its cross-correlation function to the templates are examined by eye. Also inspected are the raw 2D spectra on the CCD both before and after cosmic ray rejection; this allows another level of checking for cosmic rays that might otherwise be thought to be emission lines. At this stage a flag is assigned to each spectrum according to the best matching template.

The cross-correlation of template spectra with object spectra that have a large amount of emission or absorption features is conceptually simple. However, if an object spectrum contains no features other than the continuum and a single emission line then it is still

possible to accurately determine the redshift. This is because it is known that there are regions of galaxy's spectrum that contain single features but that are otherwise empty, being composed mostly of continuum radiation. If a single emission line is observed in an object then it is likely that it can be attributed to such a "lonely line" in the template spectrum.

The redshifts determined for each spectrum above are then further checked through two more procedures. Firstly another visual inspection of the whole catalogue by one individual who assigns a quality flag to each redshift (good, probable, bad). The "good" redshifts are kept, while the "bad" redshifts suffer a third inspection (see below). The "probable" redshifts are verified through a photometric redshift test. If they do not pass then they are also re-examined in the third inspection.

The third inspection consists of two individuals checking any uncertain redshifts, the selection of which is described above. If both inspectors agree on a redshift then it is kept. Likewise it may be rejected if they both agree it is a poor match. A tie is decided by the vote of an outside individual. Mistakes arising from the misidentification of emission lines are also corrected at this point in the pipeline.

The repeat observations are then used to assess the redshift accuracy. Yee et al. (2000) report that the typical random error on any one redshift is $\sim$ 103km/s and that the systematic error in the zero point is $\sim$ 30km/s.

2.1.5 Statistical Weights and Survey Completeness

Since CNOC2 uses a computerised routine for targeting galaxies for spectroscopy, the selection function can be very well understood. In this section I outline how the statistical weights associated with each galaxy spectrum observed in the Survey are calculated. These are important since we will use the weights to correct for missing galaxies when we analyse the star formation history in Chapter 4.

The sampling rate in CNOC2 is $\sim$ 45% at R = 21.5 mag, although it is not uniform over the total area. This is due to a combination of factors, e.g. because galaxies in low density environments are more likely to be selected simply because their spectra are easier to fit onto the CCD than galaxies from high density environments. There is also an effect from the selection algorithm, in that targets near the edge of fields are more likely to be selected, again due to the geometric considerations of placing spectra on the CCD.

Even if a spectrum is obtained for a galaxy, there is an additional question of whether it will yield a redshift. This is affected by issues such as whether the galaxy has an emission or absorption line spectrum and whether there are any strong spectral features in the relatively short wavelength window probed by CNOC2.

The aim in calculating the statistical weights is to account for both the objects missed by the sparse sampling of galaxies and the non-uniform sampling of those that were targeted. The method used to compute them in CNOC2 is similar to that of CNOC1 (Yee et al., 1996) with some modifications.

The main idea is to construct a selection function S such that $S = S(m, xy, c, z)$. That is to say, the selection function S depends on galaxy magnitude m, position on the chip xy, galaxy colour c and redshift z. It is presumed that the function is separable such that

$$S = S_m(m)\, S_{xy}(m, x, y)\, S_c(m, c)\, S_z(m, z). \tag{2.1}$$

Once each of the selection functions is know, the statistical weight for each galaxy, W, is computed as $W = 1/S$.

For CNOC2 S_m is chosen as the primary selection function, i.e. its values run between 0 and 1. The other selection functions are modifiers to S_m and they are normalised to have a mean over the whole survey of 1 (except S_z).

S_m, S_{xy} and S_c are all computed directly from the Survey catalogue; they are obtained as follows.

- S_m is computed on a per filter basis by taking the ratio of the number of galaxies with redshifts to the number in the photometric catalogue lying within ± 0.25 mag. The values of S_m are calculated on a per field basis, *not* per Patch as in CNOC1.

- S_{xy} is the geometric selection function; it is based on the position, x, y, of the object and accounts for smaller scale sampling variations due to crowding on the chip and the high density of targets on the sky. S_{xy} is computed for each galaxy as the ratio of the number of galaxies with redshifts within ± 0.5 mag and inside an area $2'$ of that galaxy, to the number in the photometric catalogue, within the same magnitude and area ranges.

- S_c is derived from the number of galaxies within ± 0.25 mag in colour of each filter.

For the bands U, B, V, R_c, I_c the following colours are used to compute S_c: U − B, B − R_c, V − R_c, B − R_c and R_c − I_c respectively.

The computation of the redshift selection function, S_z, is somewhat more complex than the derivation of the other three selection functions. This is because it requires knowledge of how the luminosity function of galaxies changes with redshift – in order that we can assess what fraction of galaxies we have or have not observed. This is of course a goal of the CNOC2 Survey and hence the calculation of S_z is particularly difficult. For CNOC2, S_z was computed iteratively using the luminosity functions measured by Lin et al. (1999), from two of the four CNOC2 Patches. Note that Lin et al. use a different set of redshift weights (based on galaxy colours) to derive their luminosity functions. The method is to compute S_z such that

$$S_z = N_z(z_1,\ z_2)/N_{LF}(z_1,\ z_2), \tag{2.2}$$

where $N_z(z_1,\ z_2)$ is the fraction of galaxies in the redshift sample of CNOC2 between z_1 an z_2 and $N_{LF}(z_1,\ z_2)$ is the fraction predicted by the luminosity function over the same range. S_z is calculated over certain ranges z_1, z_2 and then the values for individual galaxies are found by interpolation.

An important note is that the S_z weights are only computed between $0.12 < z < 0.55$ whereas the sample under examination in this thesis covers the full redshift range out to $z = 0.68$. The issue is addressed in Section 4.3.1.

2.2 Dataset Analysis

2.2.1 Spectral Measurement Code

We have reviewed the properties of the CNOC2 dataset and how the Survey was undertaken. I now present my work in analysing the dataset, beginning with the development of a programme to measure line fluxes from the Survey spectra.

Overview

I have written a programme to measure the fluxes, equivalent widths and associated errors of spectral lines in the CNOC2 dataset. The code is fully automated and conducts the

measurements in a non-interactive fashion. The following section outlines how the code works in detail including full details of the error estimation procedure.

As noted above the code is fully automated and does not rely on user input to measure the line strengths. There are of course alternative methods which could have been used in analysing this data. Given the number of individual spectra available ($\sim$ 8400) it could have been possible to measure each line by hand using, for example, the SPLOT routine in IRAF. This would have taken considerable time, and aside from being a very tedious procedure, the main disadvantage from a scientific point of view is that the results are not easily reproducible. By-eye estimates of the continuum level differ from person to person and so the reported line strength will also depend on the individual who does the measuring.

The code in this thesis uses "spectral windows" to define regions of interest over which to measure the line strength. Each window comprises three regions: a blue continuum region, a line region and a red continuum region. These are from published definitions in the literature and the exact format is discussed in more detail below. In this manner the approach is similar to that used in measuring the now famous Lick Indices (defined in Faber et al., 1985; Burstein et al., 1986; Worthey et al., 1994).

I note that the code presented here is broadly similar to that of Balogh (1999), the chief differences being that it is written in Fortran 90 as opposed to Fortran 77 and that it uses the `cfitsio` package[2] (Pence, 1999) to read in the spectra and associated header information (as opposed to the IRAF[3] IMFORT routines used by Balogh). Using these new libraries ensures that the code runs on almost all Unix systems, the only condition being the presence of a Fortran 90 complier (since the `cfitsio` libraries can be easily built for the system and root access is not required to do this); it is not necessary to have an IRAF installation. In addition the Balogh code required the spectral resolution be input in a separate text file at runtime. This not is necessary with my code since the resolution is extracted from the fits header as a matter of course.

Another difference between the codes is in the methods used to determine the continuum fit when measuring line strengths and their errors; this is also explained in detail

[2]Available from `http://heasarc.gsfc.nasa.gov/docs/software/fitsio/fitsio.html`

[3]IRAF is distributed by the National Optical Astronomy Observatories, which are operated by the Association of Universities for Research in Astronomy, Inc., under cooperative agreement with the National Science Foundation.

below.

Spectra Data Format

The CNOC2 Survey spectra are fully wavelength and flux calibrated (see Yee et al., 2000). The spectra are stored in a "multi-fits" 3-dimensional data-cube format with one file per mask pointing. The levels within a cube contain sets of data relating to a particular galaxy, one level for instance contains the optimally extracted spectrum, another the error vector; the full data structure is shown in Table 2.5. The fits file is specified as a command line argument to the code and read in using `cfitsio` routines. To process every fits file (mask) in the survey we use a shell script to call the measurement code the necessary number of times.

Fits Keyword	Header comment
BANDID1	spectrum - background fit, weights variance, clean no
BANDID2	raw - background fit, weights none, clean no
BANDID3	background - background fit
BANDID4	sigma - background fit, weights variance, clean no

TABLE 2.5: The multi-fits format data structure for the spectra in the CNOC2 Survey. The information has been extracted from the header of one of the Survey fits file. The header comments correspond to various procedures undertaken during the reduction process. Band 1 holds the optimally extracted spectra, that is to say that the extraction procedure takes into account the variances in each pixel's value in determining the best spectrum when extracting it from the CCD. Band 2 contains the non-optimally extracted spectra – the variances are not taken into account in this extraction. The keyword "clean no" refers to whether or not IRAF replaced bad pixels during the reduction ("no" in this case). Band 3 contains the sky (background) spectra, derived using a spline fit to the sky over several pixels in the spatial direction on the CCD. Band 4 holds the error vector (the variances).

CNOC2 Catalogue Information

In addition to the actual spectra themselves, a subset of the full CNOC2 catalogue is read in by the code during the line measurement process. The original catalogue (prepared by Yee et al., 2000, see Section 2.1 above) required substantial reformatting prior to being able to be read in by a computer. It was sub-divided such that every fits file has a companion catalogue associated with it, containing only the entries relevant to the spectra in that fits file.

The entries from the catalogue are linked with their companion spectra by cycling through each spectra-catalogue pair until the correct match is found.

Once all the measurements have been performed, the catalogue information is output with the line strengths and errors.

Spectral Windows

The third and final file read in at runtime is the spectral definitions file which includes the definitions for the continuum and line regions of any features that we wish to measure from the data. The regions are not hard-wired into the code since re-reading at runtime allows changes to be made to the definitions and/or number of lines being measured without the need to recompile.

Each spectral window consists of a central line region, braced by two continua regions. Although other lines are measured by the code, for this thesis we concern ourselves chiefly with measurements of the [O II] line at 3727Å (see Appendix B for a full discussion concerning the physics of its formation). In Chapter 3 we will discuss the measurement of Hα and Hβ line strengths. The [O II] band definition is taken from Dressler and Shectman (1987) and is presented in Table 2.6 for completeness. Figure 2.3 shows a CNOC2 sample spectrum with the two continua regions marked as the blue and red points. These regions are used to create a fit to the continuum level which is needed to measure the equivalent width and flux of the line. The fitting procedure is discussed below.

Also shown in Table 2.6 is a modified version of the [O II] definition. This was derived by myself in the course of testing and improving the code. During development of an earlier version of the code it was found that the continuum fit was (for some spectra) being thrown off by outlying data points towards the extreme edges of the continuum regions. This in turn adversely affected the equivalent width measurement. To remedy this, a shorter continuum region was tested. The current code does *not* use this modified definition since a more advanced solution was found: a sigma-clipping routine is now used to reject spurious data points from the fit – as is discussed in the Continuum Fit subsection below.

Line	Blue Continuum (Å)	Line Region (Å)	Red Continuum (Å)
[O II]	3653 – 3713	3713 – 3741	3741 – 3801
[O II] Modified	3668 – 3713	3713 – 3741	3741 – 3786

TABLE 2.6: The [O II] definition of Dressler and Shectman (1987) which we use in this thesis. Also shown is a modified definition that was tested as an alternative. The modified definition is *not* used in this thesis.

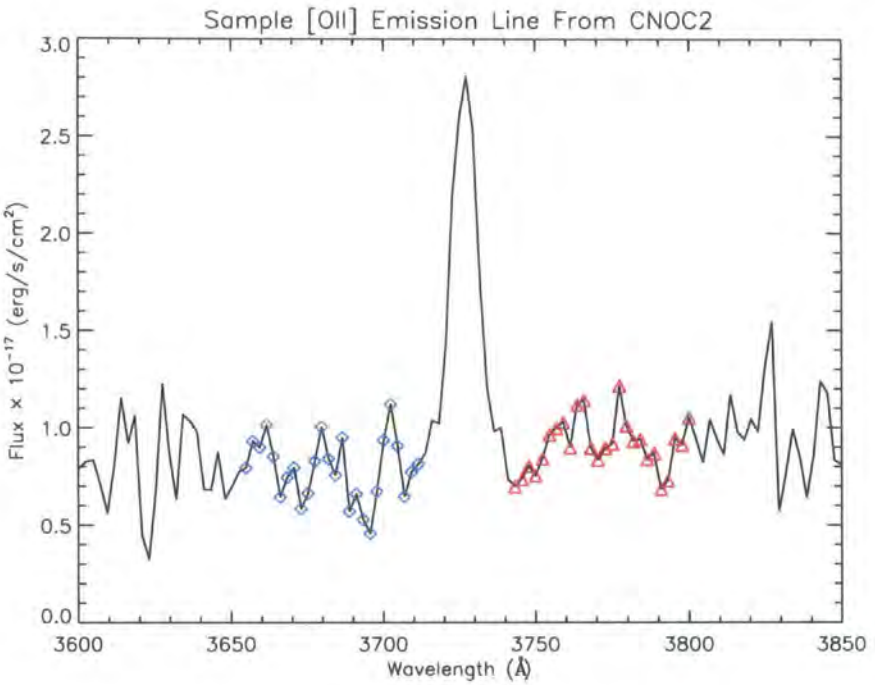

FIGURE 2.3: An example [O II] emission line spectrum from CNOC2. The blue squares and red triangles mark the full range of the blueward and redward continuum regions which bracket the [O II] line itself.

The measurement of both equivalent width and line flux are discussed below. It is noted that for certain studies, the equivalent width has advantages over the line flux: It is certainly easier to measure since the data do not require flux calibrating. Additionally, due to the way it is defined, the equivalent width gives a measure of the star formation rate per unit luminosity (mass) whereas the line flux alone cannot do this. The line flux does however allow the measurement of absolute star formation rates, which can not be obtained from the equivalent width alone.

Equivalent Width and Line Flux Measurement

Once the spectra, catalogue information and line definitions file have been read in, the next step is to loop over each spectrum and measure the both the equivalent widths and fluxes for the lines defined in the spectral definitions file.

As we have said, each line definition includes the start and end points of three separate regions, two continuum regions and one line region; these are set in wavelength units and so the first step is to convert them to pixel number on the CCD. For CNOC2 it is not possible to use a line definition based on pixel number since several different CCDs were used over the lifetime of the survey, each with slightly different spectral resolution (Section 2.1.2).

The conversion of wavelength to pixel number is done as follows:

$$n_{pixel} = (\lambda(z+1) - \lambda_0)/\Delta\lambda + 1 \tag{2.3}$$

where n_{pixel} is the (decimal) pixel number corresponding to the wavelength λ of the feature in question; λ_0 is the wavelength of the first pixel on the CCD and $\Delta\lambda$ is the wavelength increment per pixel on the CCD. These two numbers are extracted from the header information of the multi-fits cube when it is loaded.

It is clear from Table 2.6 that the end point of the blue continuum region and the start point of the line region are identical in our chosen [O II] definition, meaning they fall in the same pixel on the CCD. This potentially leads to the problem of using one pixel for a dual purpose: to both evaluate the line strength and also estimate the continuum level. Clearly this is not ideal and so we adopt the following scheme to correct for the problem: If the pixel value (n_{pixel}) is identical for both the start of line region and the end of the blue continuum region or the end of the line region and the start of the red continuum region then the pixel is assigned to the line region and lost from the continuum fit. For the purposes of evaluating the equivalent widths and fluxes however we only use the fraction of that pixel occupied by the line (explained below). The approach is sensible since in this application there are many data points used in the continuum fit and so loosing only two of them is expected to have minimal effect.

Another problem may arise if the computed pixel number of the start or end of the spectral window lies beyond the dimensions of the CCD. In such cases, rather than abandoning the whole measurement, we continue if the offset is 5 pixels or less. This necessarily means that the number of data points used in the continuum fit in these cases is reduced, but it has the advantage of making maximum use of the dataset (it would be wasteful to not measure the lines in spectra that fell such a small margin short of being fully covered by the CCD).

Aside from the above subtleties, the decimal pixel values for the start and end of each continuum region are rounded to the nearest whole pixel.

Once the regions have been successfully identified in terms of pixel number, the code measures the equivalent widths (W) as follows:

$$W = \Delta\lambda \sum_i \left(1 - \frac{I_i}{C_i}\right) \tag{2.4}$$

where I_i is the data value at pixel i and C_i is the continuum level at that same pixel, evaluated as described below. $\Delta\lambda$ is the wavelength interval per pixel on the CCD. The sum runs over all pixels covering the line and includes the fractional pixels at the edges.

The flux (F) is measured in a similar fashion:

$$F = \Delta\lambda \sum_i (I_i - C_i)\,. \tag{2.5}$$

The fractional pixels at the extremes of the line are included by replacing the $\Delta\lambda$ in Equation 2.4 by the fractional pixel covered di. $di = 1$ in the central regions of the line while $di < 1$ at the edges, allowing the end points to be taken as fractions. The sum is then finally multiplied by $\Delta\lambda$ to compute the true equivalent width and/or flux.

Thus far we have not taken into account the fact that the measurements are conducted in the observed frame. To account for the effect of redshift both the flux and equivalent width are divided by a factor $1 + z$ such that

$$W = W/(1+z)$$

$$F = F/(1+z).$$

The Continuum Fit

The continuum fit is evaluated from the data contained in both continuum regions using a least squares linear method, after a one-pass sigma-clip at 1.5σ. This ensures that the fit is not unduly weighted by outlying data points which could otherwise adversely affect it and hence the measurement of equivalent width and flux.

The continuum fitting routine also checks for the existence of regions which have been interpolated over during the reduction process to remove skyline artifacts and such like. Depending on whether these spectra have had the line region itself interpolated over or just one side of the continua regions then they are either flagged as errors and no result is produced (if the interpolation runs over the line region) or the measurement proceeds as normal (the interpolation does not run over the whole "window" but only covers one of

the continuum regions).

Error Measurement

Once the equivalent widths and line fluxes have been measured the associated errors are computed. In this section I detail how the error on the equivalent width is estimated and note that for the flux error we first compute the equivalent width error and then adopt the formula

$$\sigma_F = \sigma_W \frac{F}{W}, \tag{2.6}$$

where σ_F and σ_W are the errors on the flux and equivalent width respectively (the above equation is derived from the relationship between flux and equivalent width).

Proceeding now with the equivalent width errors, these are calculated according to the prescription derived in Bohlin et al. (1983). The method is to consider the contribution to the error from both the uncertainty in the continuum fit and also the uncertainty in the actual pixel values that make up the line.

The contribution to the overall uncertainty in the equivalent width from an individual line pixel, i, with flux I_i may be computed from Equation 2.4. It is the partial derivative

$$\frac{\partial W}{\partial I_i} = -\frac{\Delta\lambda}{C_i} \tag{2.7}$$

multiplied by the uncertainty in the value of I_i which we signify by the symbol σ_i. In our application the value of σ_i is read from the error vector stored in the Survey fits files.

The contributions from each pixel making up the line add in quadrature to give the total error, $\sigma_{w,I}$, such that

$$\sigma_{w,I}^2 = \sum_i \left(\sigma_i \frac{\partial W}{\partial I_i}\right)^2. \tag{2.8}$$

The contribution to the overall uncertainty in the equivalent width from the continuum fit (signified by $\sigma_{w,C}$) may be computed in a similar fashion. We require the partial derivative

$$\frac{\partial W}{\partial C_i} = -\Delta\lambda \frac{I_i}{C_i^2}, \tag{2.9}$$

and the uncertainty on the continuum fit, σ_c. These add over the line to give

$$\sigma_{w,C} = \sum_i \sigma_c \frac{\partial W}{\partial C_i}. \tag{2.10}$$

Combining the contributions from both factors we derive the total error on the equivalent width ($\sigma_{w,tot}$), given by

$$\sigma^2_{w,tot} = \sigma^2_{w,C} + \sigma^2_{w,I}. \tag{2.11}$$

The expression may be simplified somewhat if the values of σ_i/C_i and σ_c/C_i are approximately constant over every pixel i making up the line. In this case we reduce the above formula to

$$\sigma_{w,tot} = \Delta\lambda \left[\langle \sigma_I/C \rangle^2 N + \langle \sigma_c/C \rangle^2 \left(N - \frac{W}{\Delta\lambda} \right)^2 \right]^{1/2}, \tag{2.12}$$

where N is the number of pixels covering the line.

The quantity $\langle \sigma_I/C \rangle$ is computed from the sum of pixel uncertainties divided by the sum of continuum values, that is

$$\langle \sigma_I/C \rangle = \frac{\sum \sigma_i}{\sum C_i}.$$

$\langle \sigma_c/C \rangle$ is computed by dividing the sum of the uncertainty in the continuum at each pixel by the sum of continuum values over the line, that is

$$\langle \sigma_c/C \rangle = \frac{N\sigma_c}{\sum C_i}.$$

The uncertainty in the continuum level, σ_c, is calculated as the rms dispersion of data points about the fit. Data points in the continuum region that were rejected in the sigma-clip earlier are not included in this calculation.

2.2.2 Error Renormalisation

In Section 2.1.4 we discussed how the CNOC2 survey contains several sets of multiple observations of the same galaxy. The total number of galaxies with repeat observations is 1897; some galaxies have one repeat (1788 galaxies), some two repeats (91 galaxies) and

some three repeats (18 galaxies). This gives us a substantial dataset with which to assess the quality of the errors that we estimated using the Bohlin et al. methodology above.

For every repeat observations we compute a quantity ϵ such that

$$\epsilon = \frac{W_1 - W_2}{(\sigma_1^2 + \sigma_2^2)^{1/2}} \tag{2.13}$$

where the symbols retain their meaning from the previous section and the subscripts refer to the two galaxies in a pair of repeat measurements. The galaxies for which there is more than one repeat measurement available (a total of 109 galaxies) were included by computing ϵ for every possible combination of measurements, i.e. $\epsilon(gal_1, gal_2)$, $\epsilon(gal_1, gal_3)$, $\epsilon(gal_1, gal_4)$ etc.

Figure 2.4 shows the sum of the square of the errors $(\sigma_1^2 + \sigma_2^2)$ plotted against the quantity ϵ. If we have accurately measured the true errors without any systematic under- or over-estimates then the distribution of ϵ should be a unit Gaussian about a mean of zero.

The distribution of ϵ produced by the raw errors is shown in the top panel Figure 2.5, with the blue curve showing the best-fit Gaussian to the data ($\sigma \sim 1.13$). This is close to unit Gaussian we desire, indicating that the measured errors are almost ideal but have actually been slightly underestimated.

To transform the error distribution we apply a scale factor, C, to the errors such that

$$\sigma_{new}^2 = C\sigma_{raw}^2 \tag{2.14}$$

where σ_{raw} are the errors we measure from the data and σ_{new} are their transformed values. A scaling using a value of $C = 1.25$ produces the distribution shown in the lower panel of Figure 2.5 in which $\sigma = 1.009$ (as shown by the red line). This is very close indeed to the perfect case. We use this scale factor to multiply up the raw errors.

We conclude that the errors are very well estimated for the CNOC2 survey and represent a close to perfect Gaussian distribution.

2.2.3 Comparison of The Code with Other Measures

A useful test is to compare the results of my code with that of other measurement methods.

The SPLOT task in IRAF was used to measure by-hand the equivalent widths of 20

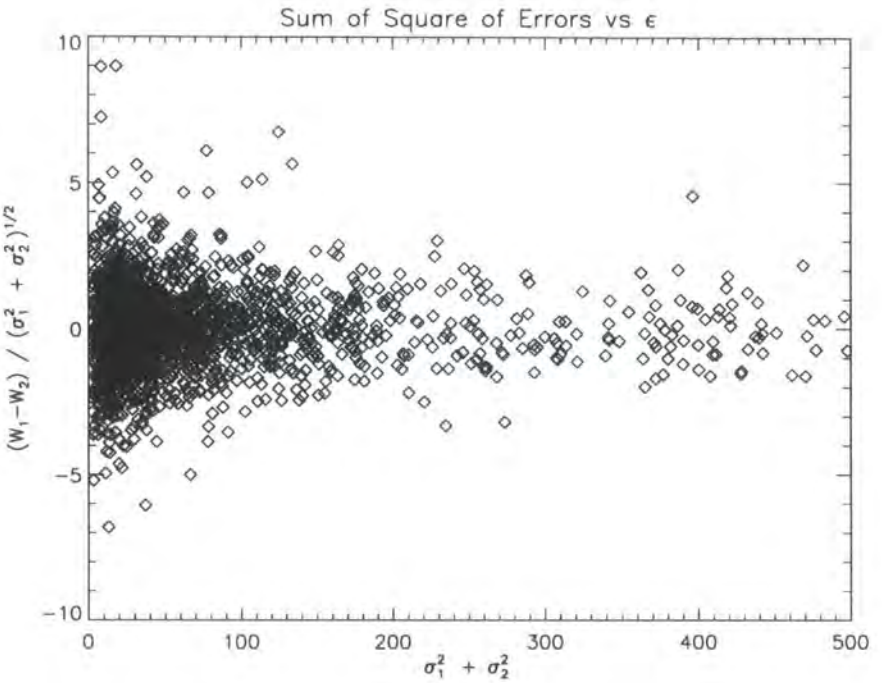

FIGURE 2.4: The distribution of ϵ as a function of the quadrature sum of the [O II] equivalent width errors. See text for the definition of ϵ.

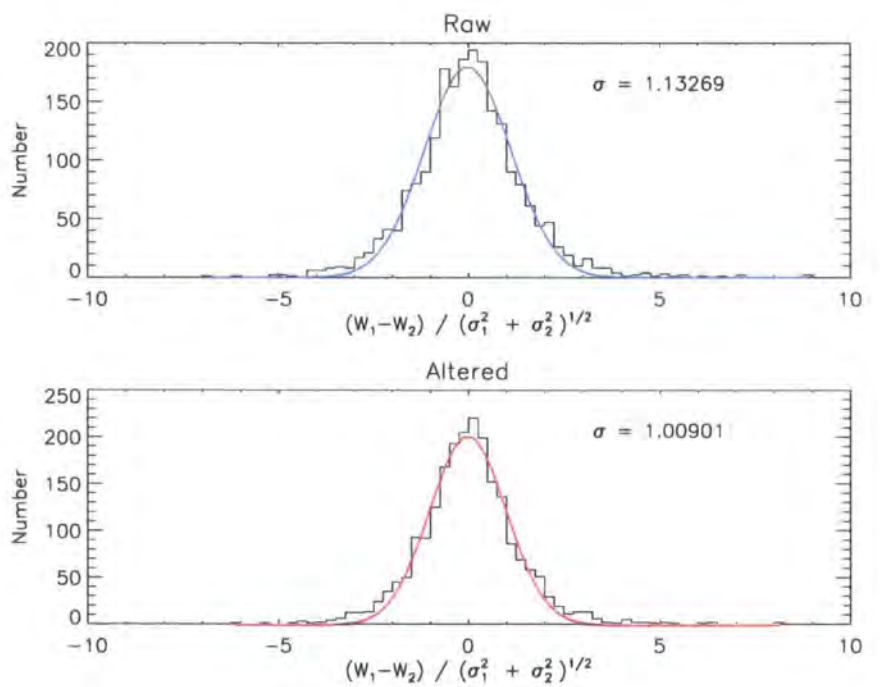

FIGURE 2.5: The distribution of ϵ before (top) and after (bottom) the renormalisation procedure. The Gaussian fits to the data are shown in blue and red. The labels on the plots refer to the fitted Gaussian's standard deviation.

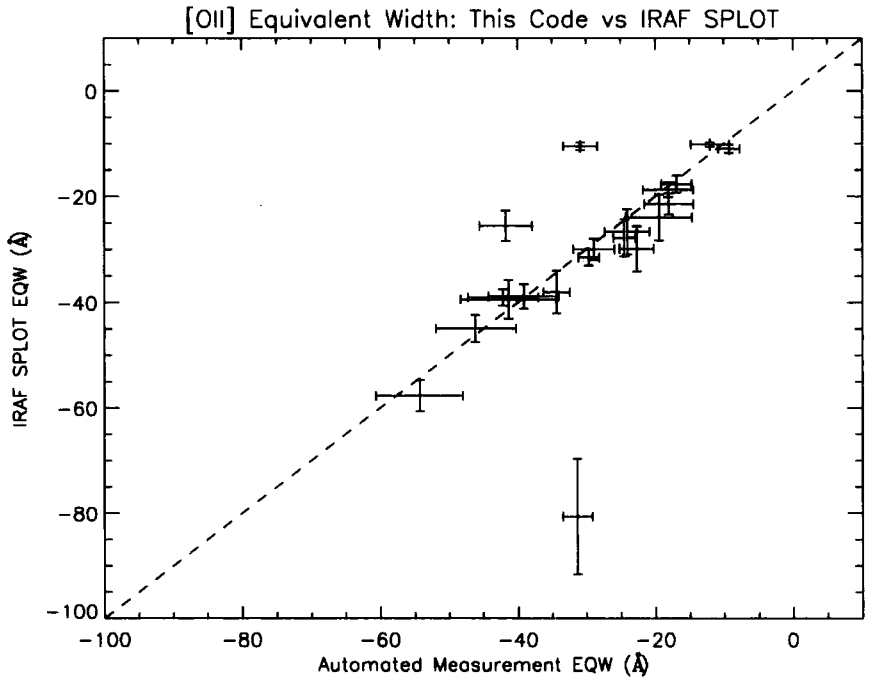

FIGURE 2.6: The [O II] equivalent widths reported by the automated measurement code vs those measured by SPLOT in IRAF. The selection criteria for the galaxies shown in this plot was that they had measurements at above 4σ certainty. The errors on the IRAF points are the rms of five separate measurements of the same line; those on my code are the errors after they have been rescaled according to Equation 2.14. The dashed line shows the one-to-one relation. There is excellent agreement between the two methods.

galaxies from the CNOC2 Survey, 5 from each patch. A comparison between the results determined using IRAF and those of my code is shown in Figure 2.6. The selection criteria for the galaxies used in this comparison was that the ratio of equivalent width to error be no lower than a value of 4. The errors on the IRAF measurements are the rms of five separate measurements of the same line; those on my code are the errors after they have been rescaled according to Equation 2.14 above. Even with the strict selection criteria there are still some outliers although the general agreement about the one-to-one relation (shown by the dashed line) is excellent. On inspection of their spectra, the outliers are all very strong, well defined lines with no clear reason why there should be a mismatch. This suggests that even for high signal-to-noise spectra there is the possibility that the by-eye judgement of the continuum level will differ from the automated version. The automated version should be trusted over the by-eye approach since it is readily reproducible and more accurate. The smaller "error bars" on the IRAF equivalent widths show that repeat by-eye measurements may underestimate the measurement uncertainties.

Another useful comparison is to the code of Balogh (1999) as used by Wilman et al.

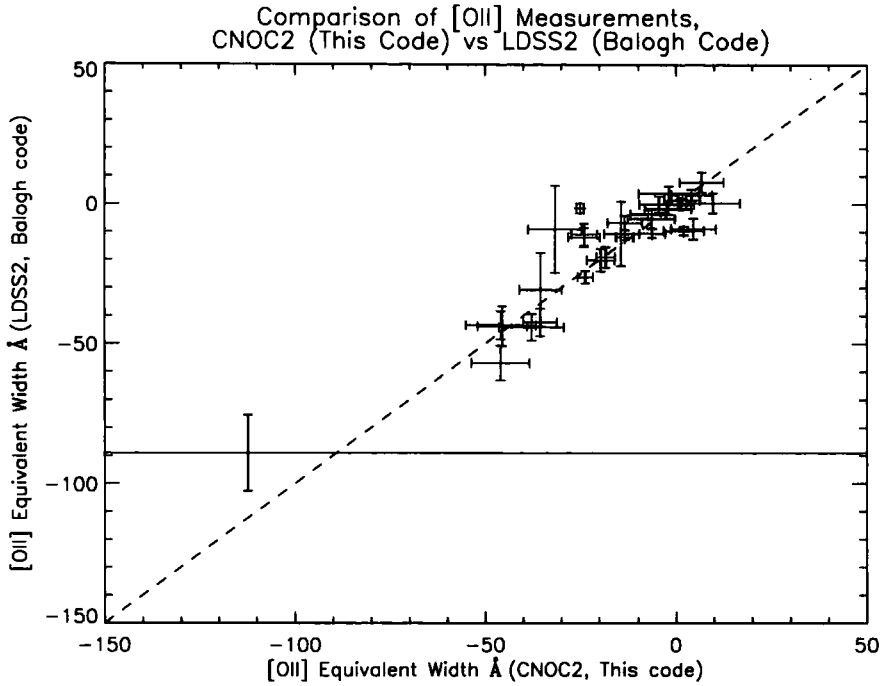

FIGURE 2.7: The [O II] equivalent widths reported by the automated measurement code using CNOC2 spectra vs those measured by Wilman et al. (2005) using spectra obtained on LDSS2 and measured using the Balogh (1999) code. The data has been replotted from Wilman et al. Figure 1b.

(2005) who obtain LDSS2 spectra of CNOC2 group galaxies. Comparing the two datasets it was found that several objects had been observed in both samples. A comparison of the measurements is shown in Figure 2.7. There is excellent agreement, especially when one considers that not only are the codes different but so are the datasets themselves, the CNOC2 data being taken on the 4m CFHT and the LDSS2 data being collected on the larger 6.5m Magellan Telescope at Las Campanas.

2.2.4 [O II] Equivalent Width Distribution

The distribution of [O II] equivalent widths from the CNOC2 Survey is shown in the top panel of Figure 2.8. The distribution of [O II] equivalent width errors (after the rescaling described in Section 2.2.2) is shown in the bottom panel of the Figure.

The Figure shows the results for every galaxy that did not cause the measurement programme to fail. Note that a cut will be applied later in order to remove erroneous measurements from the sample (Section 4.2.3).

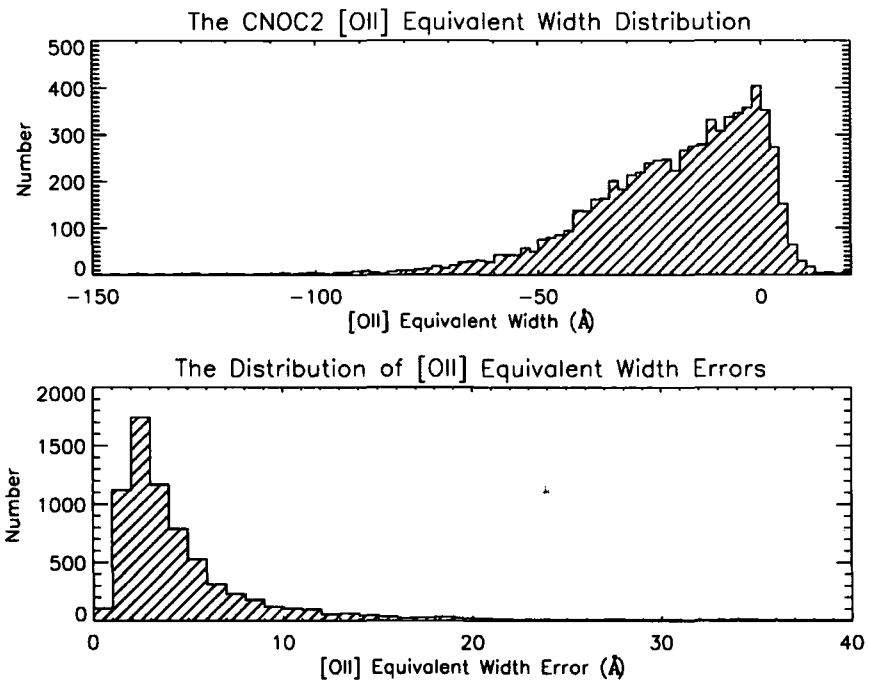

FIGURE 2.8: The distribution of [O II] equivalent width and associated error. Negative values for thequivalent width correspond to line emission.

3

Reddening Estimates From Photometric Redshift Codes

As stated in the Declarations at the beginning of this thesis, the work in this chapter was completed in collaboration with Dr. S. Morris of the University of Durham and Dr. T. Babbedge of Imperial College London. This chapter has been published in Babbedge, T. S. R.; Whitaker, R.; Morris, S. Monthly Notices of the Royal Astronomical Society, Volume 361, Issue 2, pp. 437-450

I am solely responsible for Sections 3.2.2, 3.2.3, 3.2.4 and 3.2.5. The remaining sections of this chapter were written by Dr. Morris, Dr. Babbedge or a combination of all three authors.

The text is largely unchanged from the original paper and so there is some repetition from the remainder of this thesis.

3.1 Introduction

Star formation rates (SFRs) and their global history (SFH) form the backbone of a slew of methods (observational, numerical, and analytical) investigating the processes of galaxy formation and evolution over cosmic time. The SFH is important in indicating likely eras of dominant activity and in providing a self–consistent picture of chemical enrichment. This can then be compared to the predictions of semi–analytical models of galaxy formation and with inter–galactic medium (IGM) absorption line diagnostics. However, SFRs can be imprecise due to complications arising from dust extinction.

COBE measurements of the cosmic far–IR/sub–mm background energy density (Puget et al. 1996) showed it to be equal to, or greater than, the UV/optical background (e.g. Hauser et al. 1998), implying that a large fraction of the energy from stars over the history of the Universe is hidden in the optical due to dust. The role of dust in high redshift galaxies has been discussed by many authors (e.g. Rowan-Robinson et al. 1997; Pettini et al. 1998; Calzetti and Heckman 1999; Adelberger and Steidel 2000). For example, star forming galaxies detected via the Lyman break technique at z$\sim$2 - 4 are estimated to be highly extincted in the rest–frame UV, meaning star formation rates are $\sim 3 - 10$ times higher than if dust is ignored (e.g. Meurer, Heckman, and Calzetti 1999). Correction factors found for other high redshift star forming galaxies are of a similar order. The exact form of this extinction correction remains uncertain and in particular so does its evolution with epoch.

Hence an important improvement for optical–based SFH studies is the determination of the extinction of galaxies, in addition to their redshifts. In order to fully allow for variation from galaxy to galaxy, extinction needs to be measured as an additional free parameter to redshift. However the study of Bolzonella, Miralles, and Pelló (2000) found that the inclusion of A_V as a free parameter in photometric redshift codes caused significant increases in aliasing. In a similar technique developed in Rowan-Robinson (2003), hereafter RR03, and extended in Babbedge et al. (2004), hereafter B04, these aliasing problems were reduced by setting several A_V priors.

In this paper a sample of galaxies from the Canadian Network for Observational Cosmology (CNOC2) Field Galaxy Redshift Survey (Yee et al. 2000) is used to investigate the

reliability of A_V values as determined by two SED template fitting photometric redshift codes – HYPERZ (Bolzonella et al. 2000) and IMPZ (see B04) – by comparing the returned [z_{phot}, A_V] to the spectroscopically derived redshifts and Balmer decrement derived A_V's as calculated from CFHT MOS spectroscopic data.

In §3.2 the CNOC2 galaxy sample is set out, along with the follow-up CFHT spectroscopic data and Balmer decrement calculations. In §3.3 we discuss the link between Balmer extinction and photometry. The photometric redshift method is briefly outlined in §3.4 and the results of applying the two redshift codes to the CNOC2 sample are presented in §3.5. Overall discussions and conclusions are presented in §3.6.

Note that for these investigations the flat, Ω_Λ=0.70 cosmological model with H_0=72 km $s^{-1}Mpc^{-1}$ is used.

3.2 CNOC2 overview

The 2nd Canadian Network for Observational Cosmology Field Galaxy Redshift Survey (CNOC2) was conducted over a series of 53 nights on the Canada-France-Hawaii Telescope from 1995 – 1998 (Yee et al. 2000). The survey covers a total area of 1.5 sq. deg. spread over 4 patches equally spaced in RA. The dataset includes $\sim$ 6000 galaxy spectra with spectroscopic redshifts to a nominal limit of $R_c \sim 21.5$ in addition to 5-colour (I_c, R_c, V, B, U)[1] photometry of 40,000 galaxies, complete to R_c=23.0 mag. The mean limiting magnitudes (Vega, 5σ) in each filter for the four areas are given in Table 3.1 and the filter response curves are shown in Figure 3.1.

Use of a band-limiting filter restricted the spectral window in the survey to 4400 – 6300Å. This includes the [O II] emission line for redshifts between 0.18 and 0.69. The survey's results on galaxy clustering over this range have been published (Shepherd et al. 2001; Carlberg et al. 2000) whilst an analysis of cosmic star formation history is in preparation (this thesis).

3.2.1 Extension of the CNOC2 Survey

In this paper we present follow-up observations of a subset of the CNOC2 sample of galaxies. The goal of the additional observations was to observe wavelength ranges including

[1] V photometry is actually g–band data calibrated to the V system based on Landolt standards

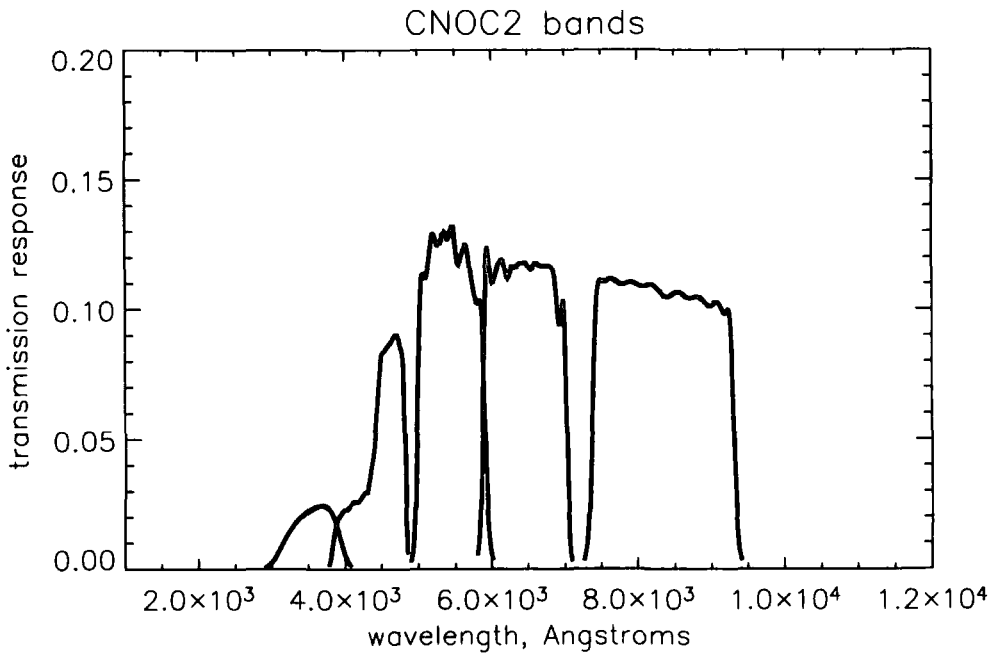

FIGURE 3.1: CNOC2 passbands combined with CCD response. From short to long wavelength they are U, B, V, R_c, I_c.

Area	I_c	R_c	V	B	U	$E(B-V)$
0223	22.97	24.02	23.95	24.55	22.98	0.036
1447	23.52	23.72	24.35	24.76	23.27	0.029
0920	22.85	24.03	23.94	24.55	23.18	0.012
2148	22.69	23.88	23.70	24.48	23.08	0.035

TABLE 3.1: 5-sigma limits (Vega) for the four CNOC2 areas, and the Galactic extinction $E(B-V)$ in each area. This can be converted to a correction in each band via Cardelli et al. (1989) with R_V=3.1.

the Hα and Hβ lines in order to set limits on the reddening of the objects and hence to allow estimation of the unreddened star formation rates for this subsample. As will be shown below, this subsample then allows us to test other means of reddening estimation and hence obtain reddening measurements for the entire CNOC2 sample.

In order to maximise the run efficiency, masks were designed with slits assigned as a first priority to objects with $0.2 < z_{spec} < 0.37$ (allowing observation of both Balmer lines) and detected [O II] λ3727 emission. Second priority was assigned to objects within the same redshift range, but no detected [O II], and third priority to galaxies within the CNOC2 magnitude range which did not yet have redshifts. This last sample will not be used in this paper.

Data was taken with the CFHT MOS spectrograph (Crampton et al., 1992) during

a 4 night observing run in August 1999. 17 masks containing a total of 719 slits were observed, spread across 3 of the CNOC2 'patches'. The R300 grism was used giving a potential wavelength coverage from 4000-10,000Å (depending on slit location), with a dispersion of 5Å per CCD pixel. A slit width of 1.5″ was used giving a nominal spectral line FWHM of 3.4 pixels or 17Å.

The data were reduced in IRAF (Tody, 1993)[2]. The reduction was based on a slightly modified version of the CNOC2 standard reductions of Yee et al. (2000). The steps included object finding, tracing and extraction, wavelength calibration, flux calibration, and interpolation over bad sky subtraction and zero order residuals. Error vectors were carried through the same procedure.

3.2.2 Measurement of the Balmer Decrement from CNOC2

Our own purpose written code (this thesis, based on the code by Balogh 1999) was used to measure the fluxes and equivalent widths of the Balmer lines in each spectrum. In brief, the code measures the flux and equivalent width over pre-defined spectral windows, set for each line. Each window includes two continuum regions and a line region. We perform a 1.5σ clip on the continuum regions to reject outliers and improve the quality of the continuum fit. Table 3.2 shows the windows we use for Hα and Hβ in this study. We note that our Hα definition is similar to that of Balogh et al. (2002) with two minor modifications: Firstly we use a wider line region in order to fully encompass the Hα+[NII] flux in our measurement; this necessarily reduces the size of the blue continuum region by 1Å. This should have minimal affect on the quality of the continuum fits. The Hβ window we use is identical to that of Dressler and Shectman (1987).

While it is true that the continuum fit is obtained from only 7 (4) independent points for Hα (Hβ), the actual number of data points used in the fit is considerably more: 23 (13) for Hα (Hβ), i.e. $\sim$ 3 data points per resolution element. As a result, any spurious points, from cosmic rays or the like will be safely rejected without substantially reducing the quality of the fit.

Figure 3.2 shows 3 typical spectra from our sample – the window regions are overplot-

[2]IRAF, the Image Reduction and Analysis Facility, is a general purpose software system for the reduction and analysis of astronomical data. It is written and supported by programmers in the Data Products Program of the National Optical Astronomy Observatory, which is operated by the Association of Universities for Research in Astronomy, Inc., under cooperative agreement with the National Science Foundation.

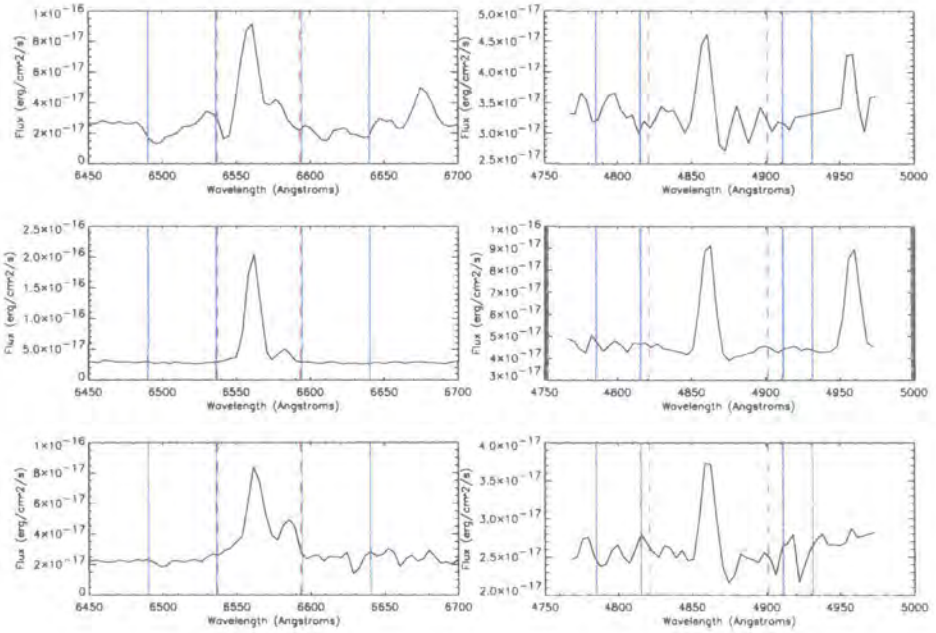

FIGURE 3.2: Three typical spectra from which we measure the Balmer decrement. **Left column** shows the Hα region, the **right column** shows the Hβ. The window regions are overplotted: the solid (blue) lines show the continua regions, the dashed (red) lines the line region. The spectra are shown in rest-frame wavelength, the mean redshift of the whole sample is ~ 0.286

Feature	Window (Å)	
	continua	line
Hα	6490–6536; 6594–6640	6537–6593
Hβ	4785–4815; 4911–4931	4821–4901

TABLE 3.2: Windows used for Hα and Hβ in this study

ted.

Error estimates on the equivalent widths are computed using the formulae set out by Bohlin et al. (1983). For the error on the flux measurement we employ the following rule:

$$\sigma_F = F\frac{\sigma_W}{W} \tag{3.1}$$

where F and W signify the measured flux and equivalent width and σ_F and σ_W their respective errors.

The original CNOC2 dataset contains multiple observations of certain galaxies and using these we are able to assess whether we systematically under- or over-estimate the equivalent width errors. Our procedure is to compute for each pair of repeats a quantity ϵ such that:

$$\epsilon = \frac{W_1 - W_2}{(\sigma_1^2 + \sigma_2^2)^{\frac{1}{2}}} \tag{3.2}$$

Where W and σ are as in Equation 3.1; the subscripts 1 and 2 refer to the separate observations. The perfect case is where the distribution of ϵ is a unit Gaussian of mean zero. This would imply that we have accurately measured the errors and there are no systematic under- or over-estimates.

Such a unit Gaussian is not found using the raw errors and so they are scaled according to the following equation.

$$\sigma_{true}^2 = A\sigma_{raw}^2(1 + B(\sigma_{raw}^2 - ave^2)) \tag{3.3}$$

Where A and B are multiplying factors to be determined and *ave* is the average raw [O II] equivalent width error larger than 2Å. We recompute the distribution of ϵ for a range of A and B and check whether it is a unit Gaussian. The process is repeated until a unit Gaussian is found.

The same scaling we apply to the [O II] errors is then applied to the Hα errors in this work (Section 2.2.2 or Balogh 1999 for the full details of this procedure).

3.2.3 Correction For [NII] Emission and Stellar Absorption

The window we employ in our spectral measurement code encompasses both the Hα and [NII] lines. We cannot separate the two lines in our data, nor are we able to accurately de-blend them using Gaussian fitting tools (e.g. splot in IRAF) since the data is not of high enough resolution. Instead, to correct for [NII] we assume an [NII]/Hα ratio of 0.5 (as per Kennicutt 1992b). This is a simple approximation, however a by-eye examination of spectra in our sample reveals that it is not obviously incorrect (see e.g. Figure 3.2). Using an extreme value for the NII/Hα ratio such as 0.33 which Kennicutt (1983) find for HII regions, results in a difference of $\sim$ 0.4 in A_V compared to the [NII]/Hα=0.5 case. This value for HII regions does not incorporate the effects of interstellar gas with its higher mean [NII]/Hα ratio, and since our spectra are from the galaxy as a whole rather than individual HII regions we assume the 0.5 factor to be the most reasonable.

The Balmer emission lines sit on top of stellar absorption due to the presence of young and intermediate age stars in the line-emitting galaxy, so any measurement of their fluxes

must take this into account. This is particularly true for Hβ, where one often finds an emission line sitting in an absorption trough (see the middle right-hand panel of Figure 3.2 for an example of this).

A reliable way to correct for stellar absorption is to fit separately the emission and absorption components of a given line. Due to the restrictions imposed by the quality of the data used in this study it is not possible to construct these fits with a large degree of confidence. Instead we choose to apply common-value (blanket) corrections that have been derived by other authors. For Hα we choose to apply the correction measured in the Sloan Digital Sky Survey (SDSS: Hopkins et al. 2003): Using galaxies in the local universe they measure a median stellar absorption at Hα of 2.6Å (note that their correction of 1.3Å is only relevant to measurements made using the Gaussian fitting routines of the SDSS pipeline; we are using a "window" measurement code to obtain our fluxes and so that value is not of concern to us; see Hopkins et al. 2003 for further discussion). For Hβ we choose the correction value of 2Å, as derived by Miller and Owen (2002) for Sb Galaxies. This value is in good agreement with that measured by other authors (e.g. Georgakakis et al. 1999; Tresse et al. 1996).

In addition to the two flux corrections described above, we also do the following: For sources with a secure Hα detection but either a low significance detection of Hβ in emission or an any significance detection of Hβ in absorption, we reset the Hβ flux to be its positive 3σ error value (i.e. to be in emission). For the low significance emission detections this is an obvious action to perform; for the absorption cases however, it should be explained that the maximum *emission* flux possible from the galaxy is still the 3σ error value, hence it is legitimate to replace it in the manner described. Of course, the absorption component may be stronger than this, but physics tells us that since the galaxies are emitting at Hα, they must also be emitting at Hβ.

Figures 3.3 and 3.4 show the flux distribution of Hα and Hβ both before and after the above corrections for [NII] and stellar absorption. In figure 3.4 the reset Hβ values are plotted as arrows, indicating an upper limit on the flux.

3.2.4 Balmer Line Detections and Limits

We divide the 719 objects observed in the extension to the CNOC2 dataset as follows:

- 367 objects do not have redshifts in the original CNOC2 survey and so are removed

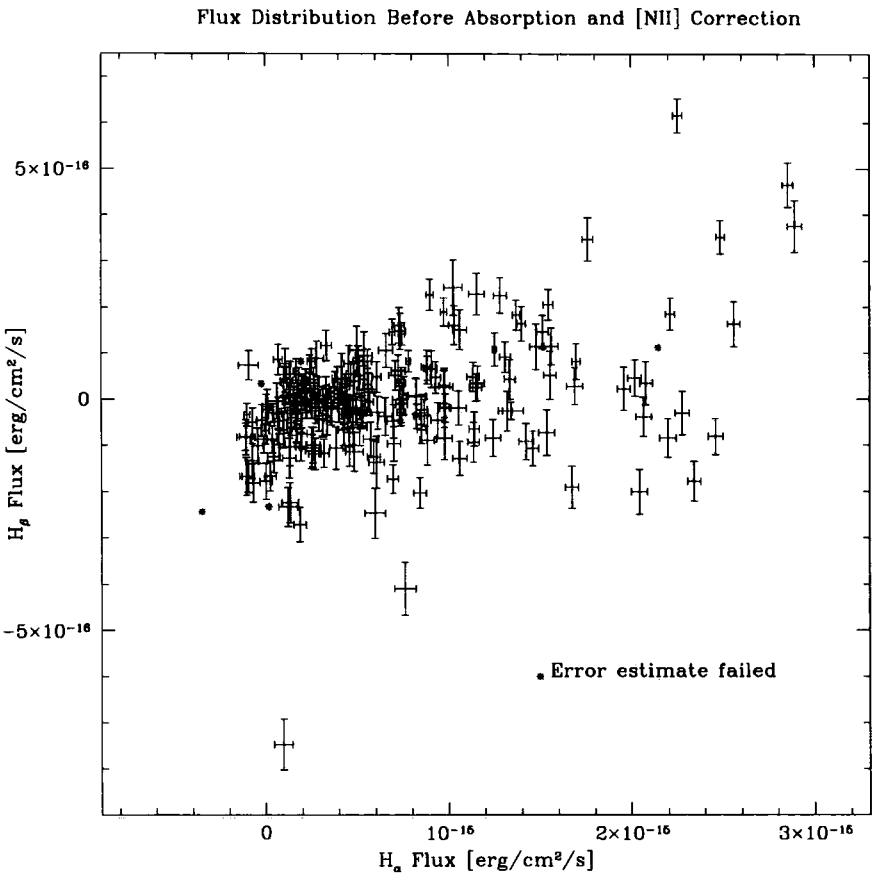

FIGURE 3.3: The flux distribution of Hα and Hβ prior to corrections for [NII] and stellar absorption.

from our sample.

- Of the remaining 352 objects, 46 are removed, either due to skylines obscuring the Hβ line (33 objects), or problems with the noise measurements arising from the data reduction procedures (13 objects).

This leaves 306 objects, and of this subset:

- 46 objects possess both emission lines measurable at above 3σ accuracy (we refer to these as 'measure' cases).
- 153 objects have only Hα measurable to an accuracy above 3σ – Hβ is not measurable to such accuracy in these spectra (we refer to these as 'limit' cases, i.e. we obtain a lower limit to the reddening for these objects).
- 107 objects have neither Hα or Hβ emission detectable at above 3σ accuracy, thus we are unable to estimate a lower limit on the reddening from these galaxies.

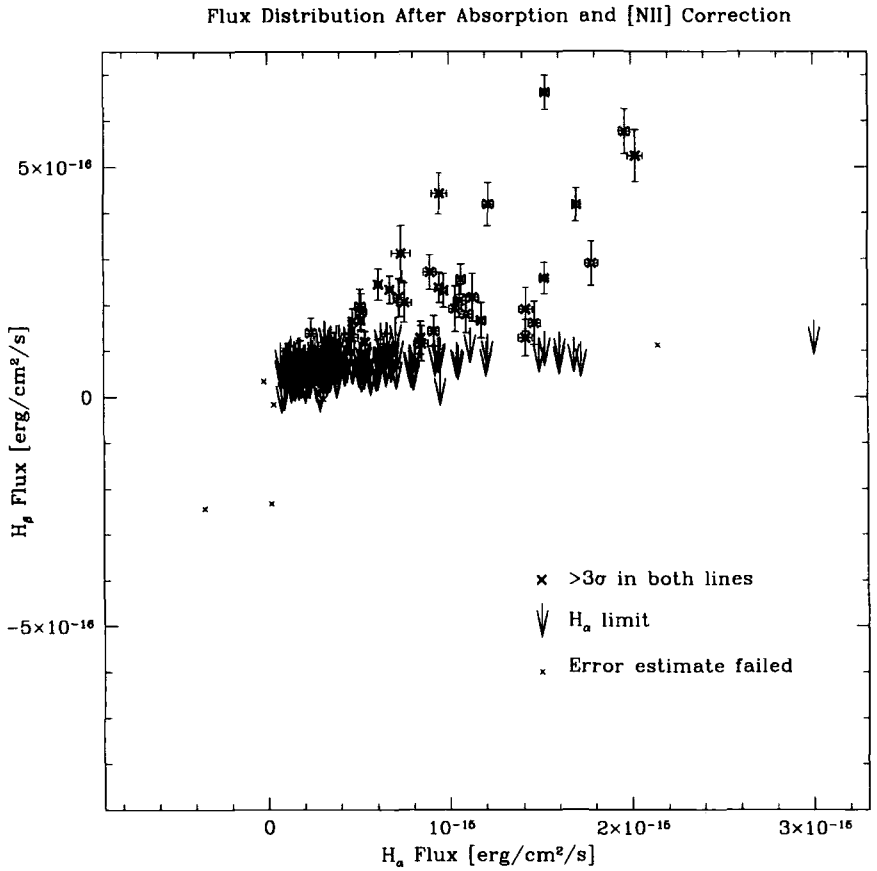

FIGURE 3.4: The flux distribution of Hα and Hβ after corrections for [NII] and stellar absorption. Crosses are sources with a detection of at least 3σ in both Hα and Hβ, arrows denote sources with an Hα detection of at least 3σ but where the Hβ flux has been reset to a 3σ limiting value. Sources in which neither line could be measured at above 3σ are not plotted.

Of the set of 46 measurements, five of them fall $> 3\sigma$ below zero and of these five, four are removed (see below). This leaves 42 measured sources for the analyses carried out later in this paper. We note that in a large enough sample, some objects are expected to lie 3σ below zero reddening, due to the nature of the statistics. Another reason for the apparently negative reddenings could be inaccuracies in the assumptions regarding the intrinsic ratio of Hα to Hβ (which is central to the calculation of reddenings); these assumptions are discussed in Section 3.2.6. We now describe the five objects with measured negative reddenings:

- Three objects appear to be blends where two (or more) galaxies are co-extracted from the slit; it is impossible to derive a reddening measurement from these spectra.

- One object has an error in the noise vector.

- One object has a high quality spectrum but a relatively small [NII] flux. Our methodology of using a coarse correction for the [NII] flux serves to push extra objects into the 3σ-below-zero reddening range (in addition to those we naturally expect from Gaussian statistics). This object is retained in the sample.

Of the set of 153 lower limit cases we note that 70 produce limits below zero reddening. Again, given our error approach, this is not surprising.

The mean redshift of the sample of 'limits' and 'measures' (Figure 3.4) is ~ 0.262 while that of every object (Figure 3.3) is ~ 0.286.

3.2.5 Selection Effects

The 'measures' sample we define and use in this work is subject to certain selection effects.

The observations are clearly most sensitive to galaxies which have strong emission lines and low to moderate A_V. Any galaxies with weak emission lines and moderate A_V will be lost from our sample since the lines will have been diminished to the extent where they are undetectable. This is also true for galaxies with large extinction – at least Hβ, if not both Balmer lines, will have been diminished by too great an amount to be detectable. The best that can be accomplished in that case is to estimate a limit on the extinction, as we have done here.

The problem of skyline contamination of the Hβ line is one which all projects attempting reddening measurements in external galaxies will suffer from. However this will not affect our results unless there exists a strong correlation of extinction with redshift such that certain extinctions occur at certain redshifts where the Hβ line is obscured. Given the narrow redshift range of the survey and the strength of correlation that would be required this is not anticipated to be an issue.

3.2.6 Calculation of extinction from the Balmer ratio

Light from galaxies and stars that passes through dust on its journey to Earth is selectively extincted. The dust has the effect of scattering the blue light more strongly than the red and for this reason dusty objects appear not only dimmer, but also redder than they would otherwise be. The reddening effect of dust causes a difference between the observed and intrinsic colour indices of the object; this is called the colour excess, CE, and is defined as

$$CE = CI_{obs} - CI_{int}, \tag{3.4}$$

where CI_{obs} and CI_{int} are the observed and intrinsic colour indices respectively. The B and V bands are commonly used to measure colour indices so the colour excess is frequently denoted by the term $E(B-V)$.

As we have stated, the effects of dust are different for each wavelength of light. In general, the magnitudes of extinction caused by dust at a given wavelength of light is denoted by the symbol $A(\lambda)$. $A(\lambda)$ is related to the colour excess, $E(B-V)$, by an extinction law, $k(\lambda)$, such that

$$A(\lambda) = k(\lambda)E(B-V). \tag{3.5}$$

Extinction laws therefore describe the amount of extinction at each wavelength, given a measured colour excess. In the past, the shape of these curves has been determined by observations of stars of similar spectral types at varying degrees of reddening.

More recently, Calzetti et al. (1996) have derived an extinction law for starburst galaxies. Their methodology is to use UV and optical spectra to compare the differences between the UV and optically derived extinctions. They test various dust configuration models and find that the models are unable to account for the correlation between the UV spectral slope and the optical depth as measured from the Balmer lines. Using this observed correlation they derive an extinction law for the galaxies in their sample. This is done by producing template galaxy spectra at various different optical depths (from the observed galaxy spectra) and then quantifying the ratio of the fluxes in each of these templates to those in a reference spectrum, which is picked arbitrarily. By factoring in the difference in optical depth between the template and the reference spectrum, an extinction law for each template is produced. These laws are combined together by weighting each according to the difference between the optical depth of its template and that of the reference spectrum, thus deriving the effective extinction law.

Figure 3.5 shows the reddening curves of Calzetti et al. (1996) and Cardelli et al. (1989) for comparison. The feature at 2175Å is the main difference between the two curves. The uncertainties introduced in this work by choosing one curve over the other are discussed below.

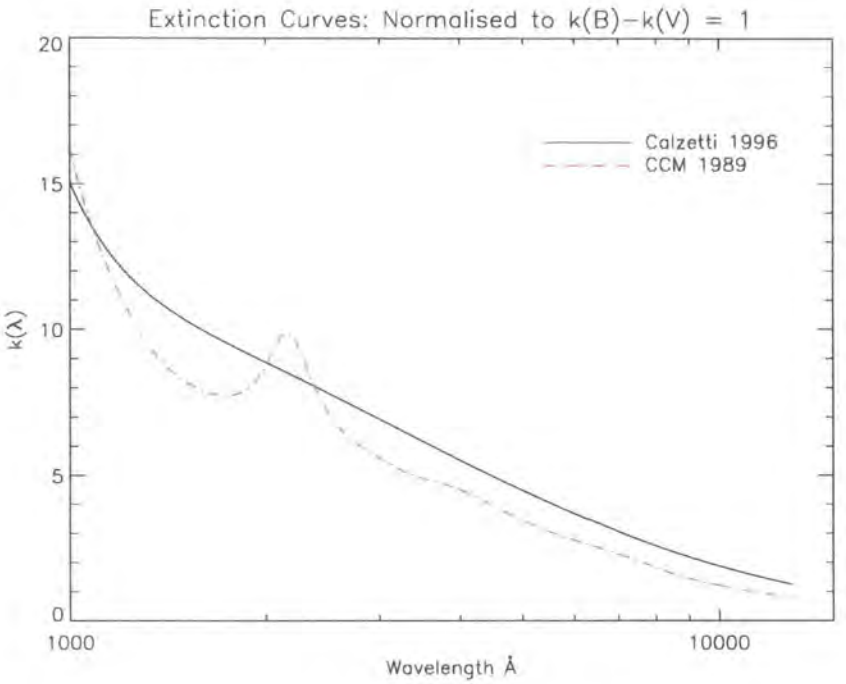

FIGURE 3.5: The reddening curves of Calzetti et al. (1996) and Cardelli et al. (1989). The feature at 2175Å is the main difference between the curves, since they otherwise share reasonably similar shape, if not normalisation. Reddening curves for the SMC are also devoid of the 2175Å feature. The non-detection of the feature by Cardelli et al. (1989) is widely attributed to the Starburst galaxies in that sample having similar dust properties to the SMC.

Even if the shape of the extinction law is known precisely, there remains the problem of how to determine the colour excess of individual objects under investigation, since their intrinsic colour index is not known in general. Fortunately, the Hα and Hβ Balmer lines provide such a means. Their relative intrinsic strengths are well established by atomic physics; this allows a determination of the colour excess, $E(B-V)$, from their observed intensities. Specifically, the unextincted intensity ratio of Hα to Hβ, R_{int}, is known to be 2.86 in typical nebula conditions (T=10,000K, $n_e = 10^2 - 10^4$ cm^{-3}; Osterbrock, 1989). The observed ratio, R_{obs}, is related to the difference in optical depth, τ, between Hα and Hβ and therefore provides a measure of the dust content due to the internal reddening along the line of sight (e.g. Calzetti et al. 1994).

R_{obs}, can be shown to be related to the colour excess of the gas, $E(B-V)_g$, according to the following equation (e.g. Calzetti et al. 1996; Afonso et al. 2003):

$$E(B-V)_g = \frac{2.5[log(R_{int}) - log(R_{obs})]}{k(H\alpha) - k(H\beta)}, \tag{3.6}$$

where R_{int} is as above and $k(H\alpha)$ and $k(H\beta)$ are the values of the extinction curve at

the wavelengths of Hα and Hβ respectively.

In this work, the Calzetti curve (Calzetti et al. 1993) was used to compute A_V's from measurements of the Balmer decrement. The lowest measured A_V being -2.25 (this is the source previously mentioned that has low [NII] flux) and the highest 5.15. These values are typically accurate to 30%; the mean of the ratio ($A_V/\sigma A_V$) is 0.27. Figure 3.6 shows histograms of the 42 Balmer-measured A_V values as well as the 153 limit cases.

The choice of extinction curve is one of the sources of uncertainty when measuring reddenings. The extinction curves of local galaxies do differ (e.g. see the review by Calzetti 2001a); the largest differences are due to the strength of the feature at $\sim$ 2175Å, thought to result from graphite grains, amorphous carbon or PAH. However, for the Balmer lines, this feature is not a factor: The Balmer lines are sampling the longer wavelength region where the extinction curves have a more constant slope, meaning the difference between any two curves is reduced. The main difference in the Balmer region of the spectrum can be parameterised by the chosen value of the ratio R_V, which is the total-to-selective extinction ratio at the V band (Calzetti et al. 1993). In these investigations R_V=4.05 is used.

An additional source of uncertainty when computing reddenings from the Balmer decrement is the assumed intrinsic ratio of Balmer line intensities, R_{int}. As discussed above, a value of $R_{int} = 2.86$ is commonly adopted. This corresponds to a physical situation often referred to as "Case B" recombination.

Different assumptions underlie the Case A and Case B recombination scenarios. Case A assumes that every line photon created within the nebula escapes without interaction with other atoms; the escaping photons are not able to cause excitations that would give rise to further emission. Case B assumes that this is not the case, but rather that the nebula gas is optical thick and *can* absorb/scatter the escaping photons. This assumption results in every Lyman-α photon (and, indeed, every ionising photon) being absorbed; this is known as the "on-the-spot" approximation.

The question remains of which Case is the more accurate representation of what actually occurs. In reality there exists *very* little difference between the Balmer decrements predicted by Case A and Case B scenarios so the debate is somewhat moot.

It is noted that due to the high column densities in broad-line AGN, the Balmer decrement can not be predicted by either Case A or Case B assumptions. It is possible

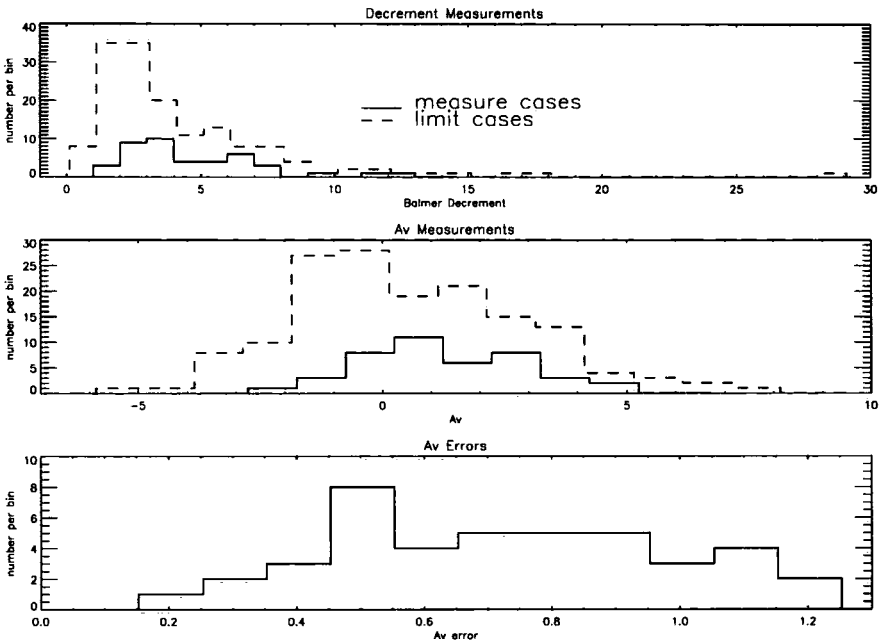

FIGURE 3.6: The distribution of Balmer decrements (top panel), Balmer-derived A_V values (middle panel) and associated error (bottom panel). The solid line shows results for the sources measured at above 3σ accuracy, the dashed line the limit cases (in this case the decrements and Balmer-derived A_V values are lower-limits).

that the presence of AGN could be the reason for our negative A_V measurements. However, in reality it is exceedingly unlikely that any such AGN have been included in our sample since the CNOC2 survey deliberately avoided targeting such objects. We therefore hold to the assertion that the negative A_V's are purely a result of statistics.

3.3 Balmer extinction vs. photometry

Are we able to compare photometry–derived extinction values, hereafter Phot-A_V, to Balmer-A_V values in order to better understand the accuracy and/or reliability of photometry–derived extinction measurements?

The crucial point here is that the Balmer decrement probes the extinction A_V of the ionised gas in the source – the extinction of molecular clouds/HII regions (star-forming regions), $E(B-V)_g$. In the SED template-fitting method where photometry in a number of bands is compared to a library of templates with variable internal A_V, the resulting best-fit returns a template type, redshift and A_V. In this case the extinction is due to the ISM acting on the stellar continua within the galaxy as a whole. Thus Phot-A_V probes the dust obscuration of the stellar continuum, $E(B-V)_s$. This is more complicated than just

the total amount of dust between the observer and the source, as would be the case for a single star, as folded into this is information on scattering and the geometrical distribution of dust within the galaxy.

Since the Balmer and photometry methods are probing different regimes of the galaxy extinction, they might well be expected to give differing results. In a galaxy such as starburst where there is a significant amount of heavily–obscured star formation the two regimes will be linked - the galaxy's overall emission is dominated by the young star formation. At the opposite end of the scale an elliptical galaxy will have little dust or ongoing SFR. In this case the two measures are un–correlated (though both measures are likely to be low). For intermediate–type galaxies the relationship falls somewhere between these two regimes.

The following relationship between the colour excess of the stellar continuum and of the nebular emission lines is given in Calzetti (2001b) and Calzetti (1997) and is as follows:

$$E(B-V)_s = (0.44 \pm 0.03)E(B-V)_g \tag{3.7}$$

This follows on from Calzetti et al. (1994) where 39 starburst and blue compact galaxies were used to derive an *effective* extinction law. From this, it was found that the difference between the optical depth to the Balmer lines, and to the underlying stellar continuum at the lines was approximately a factor two. Calzetti's relationship is a purely empirical one but it has often, in the past, been assumed to yield the most appropriate reddening corrections for the integrated light of extended star-forming regions or galaxies (e.g Calzetti et al. 2000; Westera et al. 2004). Here we start with this ratio of 0.44 but then consider other possible values in order to see how the results are affected.

3.4 Photo-z Methodology

The main outcome of applying a redshift code is the best–fitting redshift, extinction and template SED of each source. In the template–fitting procedure, the observed galaxy magnitudes are converted for each i^{th} photometric band into an apparent flux, f_i^{obs}. The observed fluxes can then be compared to a library of template (T) fluxes, f_i^{templ}(z,T,A_V), as calculated by convolving the template SEDs with the filter response functions. The reduced χ^2, χ^2_{red}, is computed for each point in the hyper-cube of redshift/template/A_V

flux values and the best–fitting solution is selected.

3.4.1 The templates

Here, we use six galaxy templates, presented in B04; E, Sab, Sbc, Scd, Sdm and starburst galaxies. These were generated via spectrophotometric synthesis (see Berta et al. 2004 for more on this procedure) of several Simple Stellar Populations (SSPs), each weighted by a different SFR and extinguished by a different amount of dust, and were designed to reproduce in more detail the empirical low-resolution templates of RR03. These SSPs have been computed with a Salpeter Initial Mass Function (IMF) between 0.15 and 120 solar masses, adopting the Pickles (1998) spectral atlas and extending its atmospheres outside its original range of wavelengths with Kurucz (1993) models from 1000Å to 50,000Å, as described in Bressan, Granato, and Silva (1998). Nebular emission is added by means of case B HII region models computed through the ionisation code CLOUDY of Ferland et al. (1998). The adopted metallicity is solar. In addition to the galaxy templates, two AGN templates can be considered. However, for the CNOC2 sample used here it was found that the AGN templates did not provide the best fit to any of the sources, (as expected based on their spectra) so in this paper only the six galaxy templates are considered - they are plotted in Figure 3.7.

One important consideration for the investigations here, and template-fitting codes in general, is that the extinction output by the photometric redshift codes refer to the Phot-A_V values of the best-fitting solutions. However, these values are those of the variable A_V which has been *added* to the template in question. In addition to this there is also the issue of the *inherent* A_V of the templates. This is problematic in that the templates originate from empirical templates drawn from observations, along with alterations found to optimise redshift solutions in previous studies. Their re–generation via spectrophotometric synthesis where the overall template is re-produced using a small number of simple stellar populations (SSPs) is designed to give some insight into the underlying physics of each template. Hence an overall A_V can be defined, based on the A_V's of the contributing SSPs.

In B04 these inherent A_V values were given (ranging from 0 for the elliptical to 0.74 for the starburst). However it is possible to reproduce the same[3] overall template using

[3]here, 'same' means from the point of view of flux through a set of broad-band filters

different proportions of SSPs with differing A_V contributions. For example, the starburst template can be generated from young SSPs to give the 'same' overall template, but with a total A_V of either 0.05 or 0.74. Similarly, the Scd can be generated with an A_V of 1.6 or 0.27. Clearly, then, we should not take the inherent A_V's of the SSP solutions at face value (we note that in the case of fitting SSPs to spectroscopic data most of these degeneracies can be expected to be broken). Empirically, we would expect the inherent A_V of the late-type galaxies (Sab, Sbc, Scd, Sdm) to have an extinction to the gas of perhaps $A_V \sim 0.5 - 1.0$, and starbursts to be more dusty ($A_V > 1.0$, say).

These SSP degeneracies would imply, then, that photometric data is not able to constrain the extinction to an accuracy of less than perhaps ± 1 in A_V. If this is the case, then one would not expect a correlation to be found between the Phot-A_V solutions and the Balmer-derived A_V even if the two methods were probing the extinction to the same regions of the galaxy. The results in §3.5 will show that this is overly pessimistic, thus implying that SSP fitting considers more possible combinations than actually occur - there are additional constraints imposed in reality due to the nature of star formation, fuelling and feedback that such fits do not incorporate. Since the details of inherent A_V are undetermined, inclusion in the analysis would introduce an additional free parameter. For this relatively small sample there is insufficient data to properly constrain this so here it is merely noted that inherent A_V is an additional complication and that it is expected to act to increase the Phot-A_V estimates. If the issue of inherent A_V is a large one then we will expect it to swamp any Phot-A_V/Balmer-A_V correlation - §3.5 will show that, in practice, this is not the case.

3.4.2 The ImpZ code

This code was presented in B04. At high redshift, Massarotti, Iovino, and Buzzoni (2001) have shown that correct treatment of internal (to the galaxy) dust reddening (the Interstellar Medium) and IGM attenuation (between the galaxy and observer) are the main factors in photometric redshift success. The effect of internal dust reddening for each galaxy is alterable via fitting for A_V, using the reddening curve of Savage and Mathis (1979), and the effects of the IGM are incorporated as in Madau et al. (1996). Observed fluxes are compared to template fluxes for $0.01 \leqslant \log_{10}(1+z) \leqslant 0.90$, equivalent to $0.02 < z \leqslant 6.94$.

Galactic extinction in the CNOC2 regions is low; using the extinction–wavelength

relation in Cardelli et al. (1989) we can calculate Galactic extinction in each of the CNOC2 bandpasses and correct for it (see Table 3.1), though the resulting corrections are negligible.

For the CNOC2 sample survey the following parameters were used, adapted from investigations presented in B04:

Templates: The six galaxy templates (E, Sab, Sbc, Scd, Sdm and Starburst), with IGM treatment and Galactic extinction corrections.

Internal extinction: A_V limits of -0.3 to 3.0 in the A_V freedom. Negative A_V was allowed since the inherent A_V of the templates is non–zero. For the elliptical template A_V can take the value zero only, since ellipticals are not expected to have significant internal extinction.

Magnitude limits: B04 found it necessary to apply redshift–dependent absolute magnitude limits to exclude unphysical solutions (such as super-luminous sources at high redshift). Here, the same limits are used: Absolute magnitude limits of $[-22.5-2\log_{10}(1+z)]<M_B<-13.5$ for galaxies.

Prior: ImpZ usually applies a prior expectation that the probability of a given value of A_V declines as $|A_V|$ moves away from 0. This is introduced by minimising $\chi^2_{red} + \alpha A_V^2$ rather than χ^2 (α=2 here). This use of a prior can be viewed as a weak implementation of Bayesian methods and was reached at based on degeneracy studies in B04 and RR03. For this investigation it was of interest to turn off this prior. This is because the Balmer-A_V values of the sample range from -2.25 to 5.15, or for the starlight (multiplying by 0.44) -1 to 2.3. Hence applying an A_V prior would naturally tend to limit the A_V solutions to values in a similar range, regardless of the input A_V limits, and so some correlation could be achieved simply because the sample all have Balmer-A_V values that equate to the lower end of the A_V parameter space.

Table 3.3 shows the parameters used in the final setup for ImpZ and HYPERZ.

3.4.3 HYPERZ

HYPERZ is described in full in Bolzonella et al. (2000). Here we present an overview of the code and the parameters we used for each run. The HYPERZ code also uses SED fitting in its determination of photometric redshifts and for this work we chose to use the same templates as ImpZ. However, for the investigations presented here, we choose to apply HYPERZ for a 'best-case' scenario where both the redshift and template type is constrained

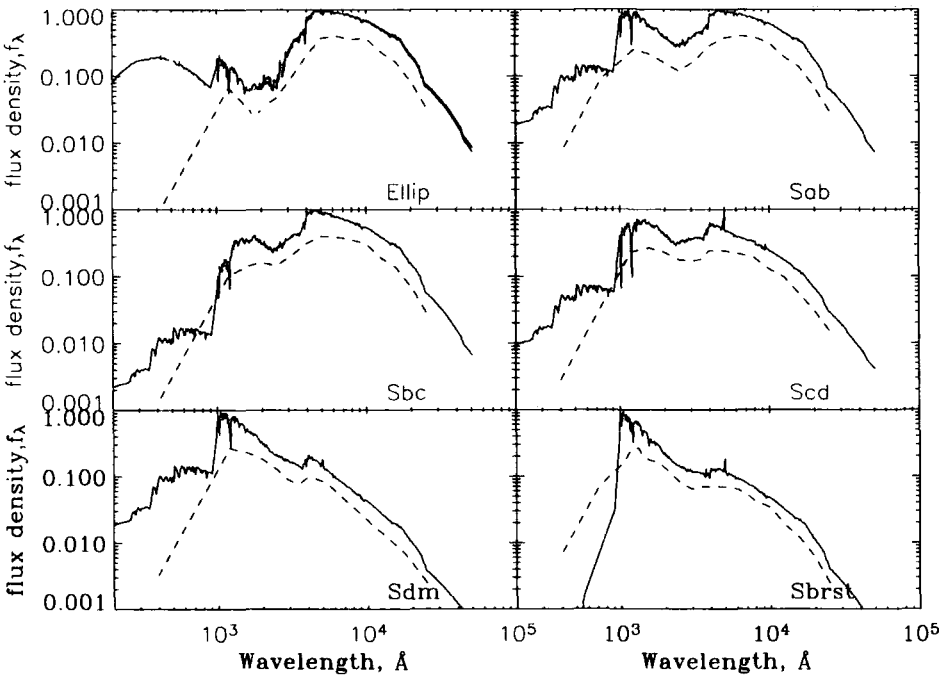

FIGURE 3.7: The 6 galaxy templates used. Dashed lines show the original RR03 templates (offset for clarity), solid lines shows the SSP generated versions, along with extension into the Far-UV (sub–1000Å) as discussed in B04.

in order to optimise the resulting accuracy of the extinction values. In order to create such a 'best-case' scenario, we choose to remove one degree of freedom by constraining the photometric redshift solution to within $(z_{spec}/100)$ of the known spectroscopic redshift. Additionally, we choose not to use the elliptical template in the analysis presented since none of the galaxies with detected Balmer lines are ellipticals based on visual inspection of the spectra.

We do not correct for Galactic extinction when running HYPERZ. This correction is negligible in comparison to the photometric errors (see Table 3.1 for extinction across the CNOC2 patches) and would not affect the results. Any non-detections in a given band were replaced with a flux of zero, the error being the limiting flux in the band (see Table 3.1 for 5σ limits). Ideally, one would want to provide the measured flux in an aperture placed at the location of the object even when that measurement is fainter than the nominal flux-limit of the survey and the resulting value has very poor S:N. However, the CNOC2 catalogue used here has had such measurements replaced by a 'non-detection' flag. Thus the best treatment in the template-fitting procedure is to restrict solutions to those that predict the flux in the non-detected band to be at or below the flux limit in that band.

The HYPERZ code was run in its standard form, with the flat, Ω_Λ=0.70 cosmological

model with H_0=72 km $s^{-1}Mpc^{-1}$ used elsewhere in this paper and variable A_V in the range $0 < A_V < 3$. Table 3.3 shows the parameters used in the final setup for ImpZ and HYPERZ.

	IMPZ	HYPERZ
Templates	E, Sab, Sbc, Scd, Sdm, Sb	Sab, Sbc, Scd, Sdm, Sb
M_B limits	$[-22.5-2log_{10}(1+z)] < M_B < -13.5$	not constrained (but set by z_{spec})
A_v limits, A_v step	$-0.3 \leq A_v \leq 3.0$, step 0.1	$0.0 \leq A_v \leq 3.0$, step 0.27
Reddening law	Cardelli 1989	Calzetti 2000
Galactic extinction correction?	Yes	No
Constrained to z_{spec}?	One run unconstrained, one run constrained	Yes
Cosmology	$\Omega_0=1$, $\Omega_\Lambda=0.70$, $H_0=72$ km s^{-1}Mpc^{-1}	$\Omega_0=1$, $\Omega_\Lambda=0.70$, $H_0=72$ km s^{-1}Mpc^{-1}

TABLE 3.3: Final parameters for the two photometric redshift codes.

3.5 Results

3.5.1 ImpZ redshifts

First, it is of interest to see how successful the photometric redshifts are when there is no A_V freedom - that is, A_V=0 in the solutions. The results of this are plotted in the left panel of Figure 3.8, for 'measure' cases (black squares) and 'limit' cases (red crosses). It is immediately clear that not allowing A_V freedom has caused many of the ImpZ solutions to be incorrect - the code has been forced to substitute (incorrectly) additional redshift in place of the reddening action of dust. Indeed, there are a total of 11 of the 42 'measure' and 70 of the 153 'limit' sources (48% of the sample) whose photometric redshifts lie outside the $\log(1+z_{spec})\pm$ 0.1 boundaries.

If we now run ImpZ in the optimal manner, as discussed in §3.4.2, so that now A_V freedom is allowed, the solutions dramatically improve. ImpZ was highly successful at deriving photometric redshifts in close agreement with the spectroscopic values for 40 of the 42 'measure' and 147 of the 153 'limit' sources (95% of the sample). Note we consider redshift solutions in the range [0:7]). There were 8 (2 'measure' and 6 'limit') sources that obtained solutions at incorrect redshifts due to degeneracies in [z, template, A_V] space. We measure the accuracy of the photometric redshifts via the *rms* scatter σ_z, calculated as follows:

$$\sigma_z^2 = \sum \left(\frac{z_{phot} - z_{spec}}{1 + z_{spec}} \right)^2 /N \tag{3.8}$$

with N being the number of sources with both spectroscopic redshifts and photometric redshifts. For this data, the *rms*, σ_z=0.32 when including the 8 outliers, or 0.07 when they are excluded. The comparison of spectroscopic and ImpZ redshifts is plotted in the middle panel of Figure 3.8.

ImpZ is therefore successful at returning accurate redshifts. However, can it also provide a measure of the extinction compatible with that implied by the Balmer decrement? Since 2 of the 42 'measure' sources obtain an incorrect photometric redshift this also means their extinction values are likely to be incorrect. In order to remove this (small) source of error in the following comparisons to the Balmer-derived extinction, we now constrain the redshift range explored by ImpZ to lie within 0.05 in $\log(1+z_{phot})$ of z_{spec} (plotted in the

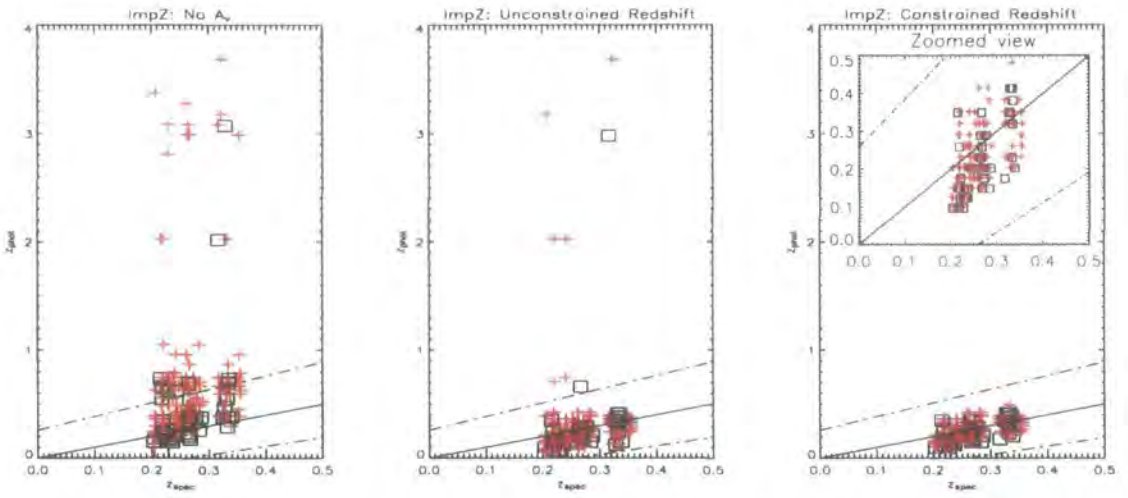

FIGURE 3.8: **Photometric redshifts from IMPZ.** Comparison of spectroscopic and IMPZ-derived redshifts for 'measure' cases (black squares) and 'limit' cases (red crosses): **Left panel** shows results when A_V freedom is not considered; **middle panel** shows results for unconstrained redshift and A_V space; **right panel** shows results for redshift space constrained to be within 0.05 in $\log(1+z_{phot})$ of z_{spec}, but A_V unconstrained. Dot-dashed lines denote an accuracy of 0.1 in log(1+z), a typical photometric redshift accuracy.

right panel of Figure 3.8). Now, good solutions are found for all 42 'measure' cases and 153 'limit' cases, with σ_z=0.06. It is the resulting IMPZ A_V values from this setup that are considered from now on in the investigation.

3.5.2 Range of IMPZ A_V allowed values

Although we wish to explore the accuracy of the extinction output from redshift codes by comparing to a sample with Balmer-derived measurements, we can also obtain an internal estimate of how well constrained the [z,template,A_V] solution is from the reduced χ^2 distribution. For the solution with the minimum χ^2, χ^2_{min}, the question can be asked: 'What range of A_V produces a fit at or near the correct redshift (within 0.05 of $\log[1+z_{spec}]$), with a reduced χ^2 within χ^2_{min}+1?'

The results of asking this question of each source is illustrated in Figure 3.9. It can be seen that for the majority of 'measure' cases (black), the A_V is quite well constrained, in most cases to within 0.3 or so in A_V. Note that the lines in this plot can be discontinuous - for example, object 150 in the plot has a best-fitting A_V of 1.9 but has reasonable solutions in the A_V range -0.3 to 0.4 and 0.8 to 1.1 which arise from fitting two other templates to the source. It is of interest to note that whereas 57% of 'measure' cases do not have discontinuous solutions, this is only true for 43% of the 'limit' (cyan) cases.

Thus, determining the A_V via photometry for these sources is more problematic, just as it is via the Balmer ratio method. Considering the 'measure' cases in more detail, there are two objects where the A_V is poorly constrained (objects 83 and 159 in the Figure, evidenced by their long black lines). Their best-fitting A_V values are, respectively, 2.3 and 1.7, making them the most heavily extincted of the ImpZ 'measure' cases. Comparison to their Balmer-derived A_V (3 ± 1 and -1.6 ± 0.5 respectively) would support the result for the first source but the Balmer decrement for the second source would imply negative, or zero extinction, disfavouring the ImpZ best-fitting result or resulting in the interpretation that this source is problematic.

Figure 3.10 illustrates the width of A_V parameter space that lies within +1 of χ^2_{min} by plotting the distribution of this 'width' value (here the 'width' is simply defined as the maximum allowed A_V minus the minimum allowed A_V). For 'measure' cases (black) the distribution drops quite steeply with width such that more than half the sources have a width of 0.4 or less. There is then a slight tail made up primarily of sources which had discontinuous solutions (such as one template with low A_V and another template with higher A_V) whilst the two sources with poorly constrained A_V can be seen as a spike towards the maximum width of 3.3 (i.e the full -0.3 to 3 A_V range). The distribution for the 'limit' cases is more clearly bimodal, with a similar set of reasonably well-constrained sources with an A_V-width of 0.4 or less, but a much larger set of sources with poorly constrained A_V. Again, this is likely to be due to the nature of these 'limit' sources for whom the dust extinction is hard to determine (either via the Balmer lines or photometry).

This analysis suggests that the photometric redshift solution has an inherently low extinction precision (at least with five band photometry), such that A_V is only precise to perhaps 0.3 for most sources, and is poorly constrained for a small subset. Rather than defining this internally estimated width value as the error in the Phot-A_V value we choose instead to take the opposite approach for the comparison with the Balmer-derived A_V. We will take the Phot-A_V at face value and use the supposed relation to the Balmer-derived A_V to provide an external estimate of the precision of the Phot-A_V measurements.

3.5.3 ImpZ - comparison to Balmer

We can test how well the Calzetti ratio holds by comparing the Phot-A_V to 0.44*Balmer-A_V. The distribution of A_V residuals for ImpZ is plotted in Figure 3.11. It can be seen

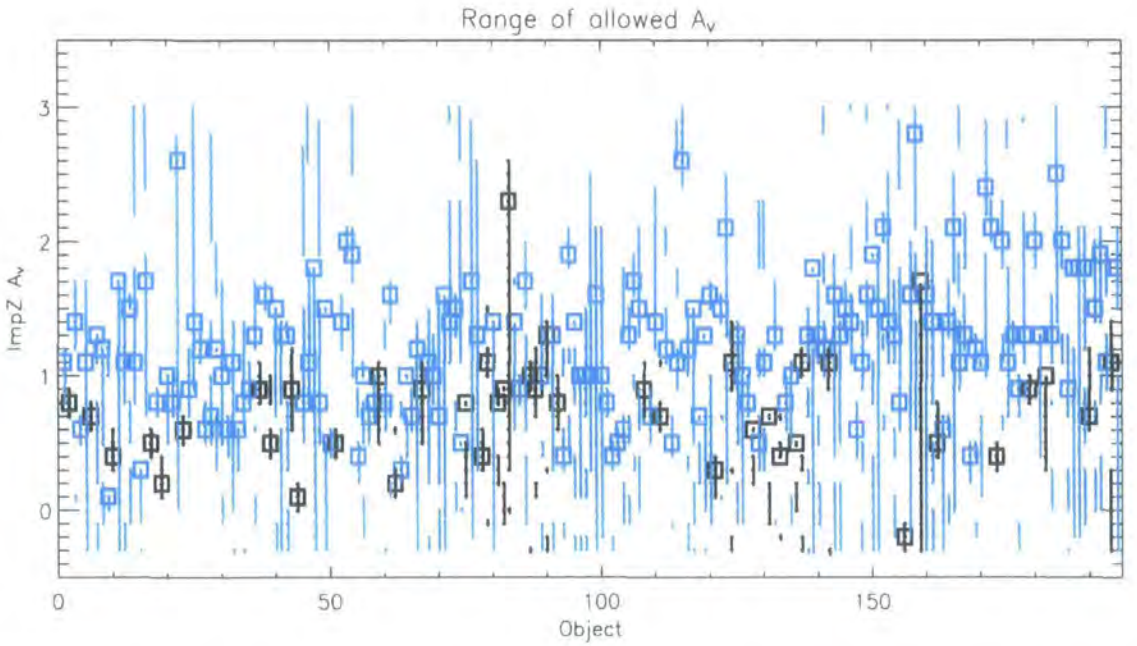

FIGURE 3.9: **IMPZ A_V allowed values**. The range of A_V parameter space for each source that provides a solution with a reduced χ^2 within $\chi^2_{min}+1$ and that is at or near the correct redshift (within 0.05 of $\log[1+z_{spec}]$). 'Measure' sources are shown as black lines, 'limit' sources as cyan lines. The best A_V solution value is indicated as a black ('measure' case) or cyan ('limit' case) square.

that there is quite a spread to the distribution, though it is broadly centred on zero. Based on the findings in §3.5.2 on the precision of the Phot-A_V solutions some of this spread can be expected to arise from this low precision. Some of it can also be attributed to the accuracy of the Balmer-derived A_V, which is typically accurate to around 30%.

Figure 3.12 plots (purple squares) the ImpZ A_V values and residuals as a function of Balmer-A_V (multiplied by the Calzetti 2001b factor of 0.44). Note that the ImpZ A_V values have been taken at face-value and have not had an error assigned to them, since we wish to derive an error based on the comparison to the Balmer-A_V's.

It can be seen that the residuals are smallest for Phot-A_V values of around 0.5 to 1 and that the residuals increase as we move away from this region (to either higher A_V or lower/negative A_V). Hence, the correlation to Balmer-derived A_V appears to be best for sources of intermediate extinction. It is also clear that none of the sources that were calculated as having negative A_V based on their Balmer lines obtain similar Phot-A_V values, lending weight to the supposition that the Balmer method has fallen down for these sources due to limitations in the technique. The source with the largest Balmer-A_V, of 5.15±0.5, is also the source with the largest residual (of sources with non-negative A_V).

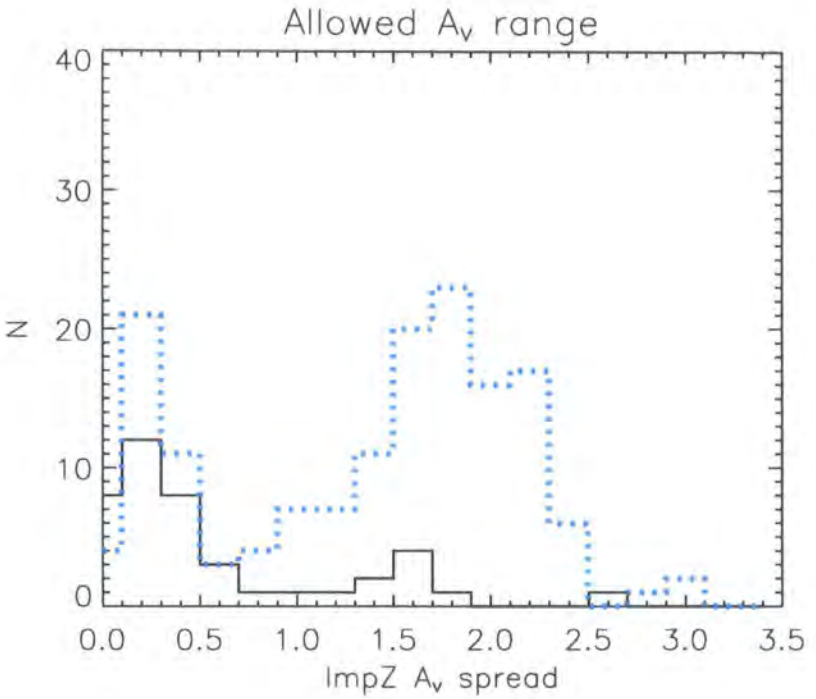

FIGURE 3.10: **Histogram of the width of IMPZ A_V allowed values.** Distribution of the width of A_V parameter space (defined by the minimum and maximum allowed A_V) that lies within +1 of χ^2_{min}. 'Measure' sources are shown as a black line, 'limit' sources as a cyan dotted line.

Being so extincted, it is likely that this object is quite extreme, so disagreement between the star- and gas-derived extinction measures is to be expected.

Calculating the following statistics:

$$\overline{\Delta A_V} = \sum \left(Balmer[A_V] - Phot[A_V] \right) / N \tag{3.9}$$

and

$$\sigma^2_{A_V} = \sum \left(Balmer[A_V] - Phot[A_V] \right)^2 / N \tag{3.10}$$

and outliers are defined by

$$|\Delta A_V| > 0.5 \tag{3.11}$$

gives $\overline{\Delta A_V} = -0.2$, σ_{A_V}=0.83 and an outlier fraction, η, of 50 per cent. These results are better than one would infer from the large extinction degeneracies seen in the SSP fitting which were discussed in §3.4.1. Thus, a relationship between Balmer-derived and photometry-derived extinction measures is obtainable, though not a strong one.

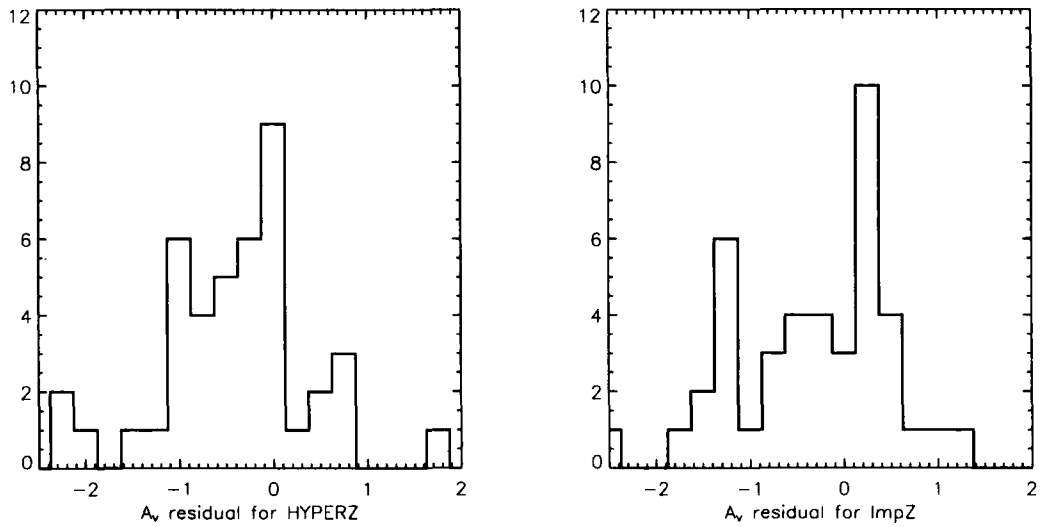

FIGURE 3.11: **A_V residuals for HYPERZ (left panel) and IMPZ (right panel).** The residual is (0.44*Balmer[A_V]-Phot[A_V]).

3.5.4 HYPERZ - comparison to Balmer

Applying HYPERZ in a 'best-case' configuration (constraining the HYPERZ redshift solutions to the spectroscopic values and excluding the elliptical template) gives similar statistics of $\overline{\Delta A_V} = -0.3$, σ_{A_V}=0.84 and an outlier fraction, η, of 50 per cent. The distribution of A_V residuals for HYPERZ is plotted in Figure 3.11. As with IMPZ, the distribution is broad but reasonably centred on zero.

Figure 3.12 plots (cyan triangles) the HYPERZ A_V values and residuals as a function of Balmer-A_V (multiplied by the Calzetti 2001b factor of 0.44). The residuals are again correlated with the Balmer-A_V, being smallest for Phot-A_V values of around 0.5 to 1, and the negative Balmer-A_V sources are again in poor agreement.

Thus, HYPERZ and IMPZ portray a similar correlation to the Balmer-A_V, though the agreement is noisy.

3.5.5 Comparison of IMPZ and HYPERZ

As well as comparing the two photometric redshift code's extinction outputs to the Balmer-derived values, it is instructive to compare them to one another to see if they tend to agree on a similar extinction value for a given source. A plot of IMPZ-A_V versus HYPERZ-A_V is given on Figure 3.13.

This shows that the two codes are in reasonable agreement about the extinction of a

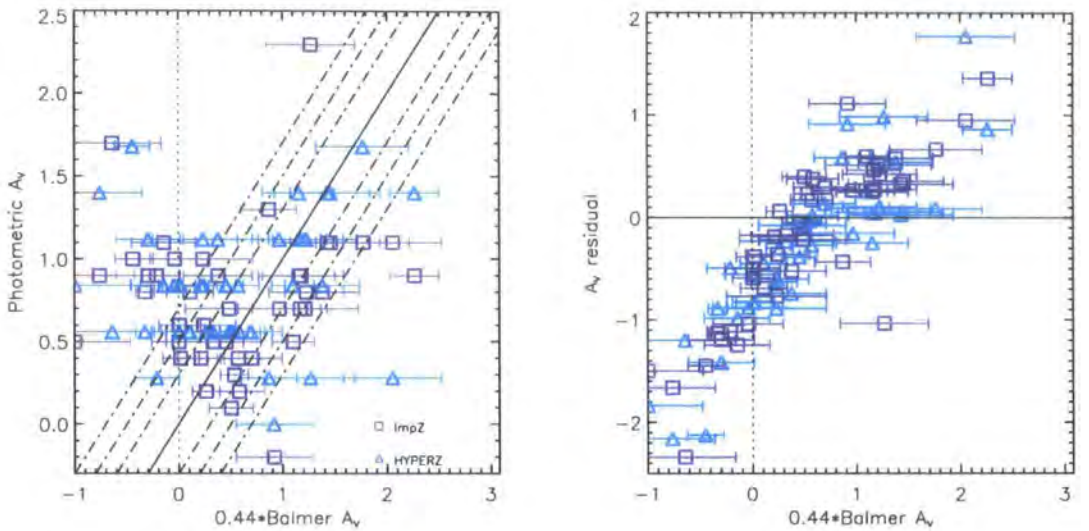

FIGURE 3.12: **Left:** A_V results for HYPERZ (cyan triangles) and IMPZ (purple squares). Plot is the Balmer[A_V] (multiplied by the Calzetti (2001) factor of 0.44) versus the photometrically–derived A_V . Dot–dashed lines denote residuals of 0.3, 0.5 and 0.7 in A_V. Errors are not defined for the Phot-A_V values. **Right:** A_V residuals for HYPERZ (cyan triangles) and IMPZ (purple squares). Plot is Balmer-A_V (multiplied by the Calzetti 2001 factor of 0.44) versus the residual (0.44*Balmer[A_V]-Phot[A_V]).

given source. Twenty-five of the forty-two sources (60%) agree within < 0.4 in A_V, thirty-five sources (83%) agree within < 0.5. The main difference appears to be for five sources where IMPZ gives a high value of $A_V > 0.8$ whilst HYPERZ tends to return a smaller A_V estimate. Two of these sources (this includes object 159 mentioned in §3.5.2) have Balmer decrements that imply negative, or zero extinction, favouring the HYPERZ result or the interpretation that the sources are problematic. Two others have intermediate Balmer-A_V consistent with either code's results and one has a larger Balmer-A_V (this is object 83 mentioned in §3.5.2) thus favouring the IMPZ result.

Calculating similar statistics as when comparing to the Balmer-A_V, comparison between the two codes' A_V values gives $\overline{\Delta A_V} = -0.09$, σ_{A_V}=0.53 and an outlier fraction, η, of 17 per cent. This internal consistency check between the two codes gives increased confidence in the photometric redshift template-fitting method as a technique to obtain extinction.

3.5.6 The Calzetti ratio

We now consider the empirical ratio of 0.44 introduced by Calzetti (1997) and set out in Eqn. 3.7. We consider a range of other ratios, γ, so that

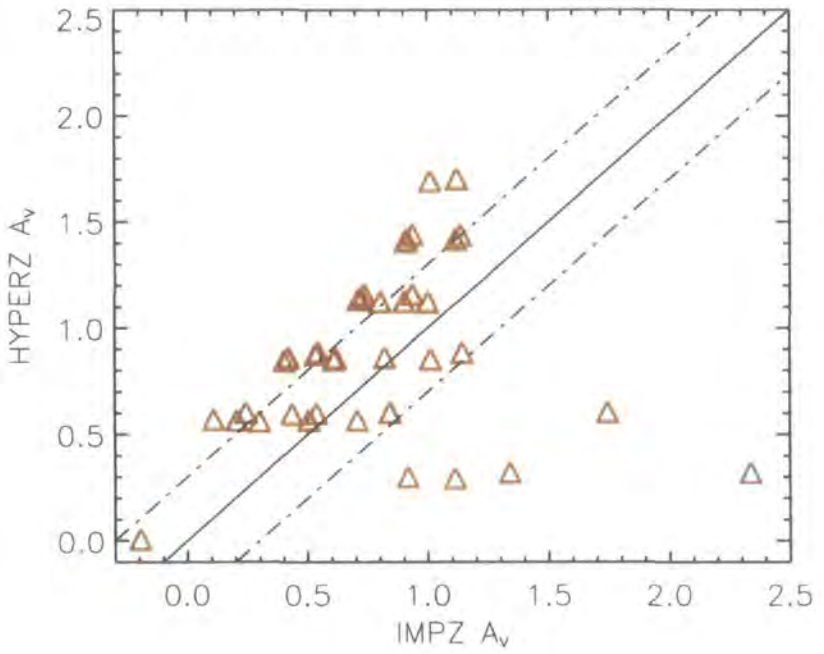

FIGURE 3.13: **Comparison between IMPZ and HYPERZ:** A_V results for IMPZ versus those from HYPERZ. Solid line is exact agreement, dot-dashed lines are residuals of 0.3 in A_V. Note that for plotting purposes the values have been randomly altered by up to 0.02 in the x and y directions in order to separate points with the same/very similar values.

$$E(B-V)_s = \gamma E(B-V)_g \tag{3.12}$$

Varying this ratio from $0.05 < \gamma < 1$, a χ^2 minimisation analysis is carried out in order to find the ratio that gives the best correlation between the Phot-A_V and the Balmer-A_V, weighted by the errors in the Balmer-A_V measurements. The results of this analysis are shown in Figure 3.14. For both IMPZ and HYPERZ, the lowest reduced χ^2 is reached for $\gamma \sim 0.25$. Based on the change in γ that increases the reduced χ^2 by one, the 1σ error on this value is $\gamma = 0.25 \pm 0.25$ for IMPZ and $\gamma = 0.25 \pm 0.1$ for HYPERZ.

The resulting statistical measures, σ_{A_V} and the outlier fraction, η, are also plotted as a function of γ for the IMPZ and HYPERZ results (Figure 3.15). The left panel shows how the *rms* in the residual, σ_{A_V}, varies with γ. A clear minimum is seen at $\gamma \sim 0.15$ to 0.35 for IMPZ results, and at around 0.2 to 0.4 for HYPERZ. A similar minimum is seen in the range $\gamma \sim 0.2$ to 0.35 for IMPZ results when the outlier fraction, η, is plotted against γ in the right-hand panel. For HYPERZ, the minimum is at around $\gamma \sim 0.3$ to 0.45.

	$\overline{\Delta A_V}$	σ_{A_V}	outlier fraction, η
IMPZ, γ=0.44	-0.2	0.83	50%
HYPERZ, γ=0.44	-0.3	0.84	50%
IMPZ, γ=0.25	-0.4	0.72	38%
HYPERZ, γ=0.25	-0.5	0.76	57%
IMPZ/HYPERZ comparison	-0.09	0.53	17%

TABLE 3.4: Statistical results for the different comparisons between Balmer-A_V and Phot-A_V.

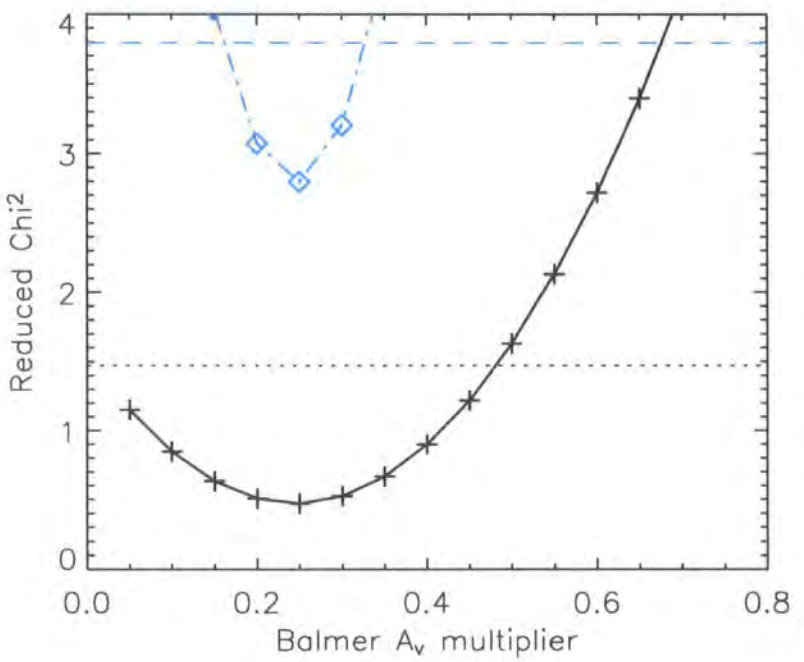

FIGURE 3.14: χ^2 **analysis**. The reduced χ^2 for IMPZ (solid line with crosses) and HYPERZ (dot-dashed line, diamonds) as a function of γ, the chosen ratio between photometrically-derived and Balmer ratio-derived extinction measures. The χ^2 values that are 1 above the minimum in the two distributions are indicated by horizontal lines (IMPZ, dotted; HYPERZ, dashed).

This analysis suggests that for this sample, the Calzetti ratio of 0.44 is a reasonable choice for γ within the accuracy of the method, though a value of ~ 0.25 is preferred. A choice of γ=0.25 gives the following statistics:

For IMPZ; $\overline{\Delta A_V} = -0.4$, σ_{A_V}=0.72 and an outlier fraction, η, of 38 per cent.

For HYPERZ; $\overline{\Delta A_V} = -0.5$, σ_{A_V}=0.76, η, of 57 per cent.

As before, the distribution of A_V residuals is plotted (Figure 3.16). It can be seen that the distribution is more peaked, though offset from zero.

Figure 3.17 plots the Phot-A_V values and residuals as a function of Balmer-A_V (multiplied by γ=0.25). It can be seen that for lower Balmer-A_V, the Balmer-A_V tends to

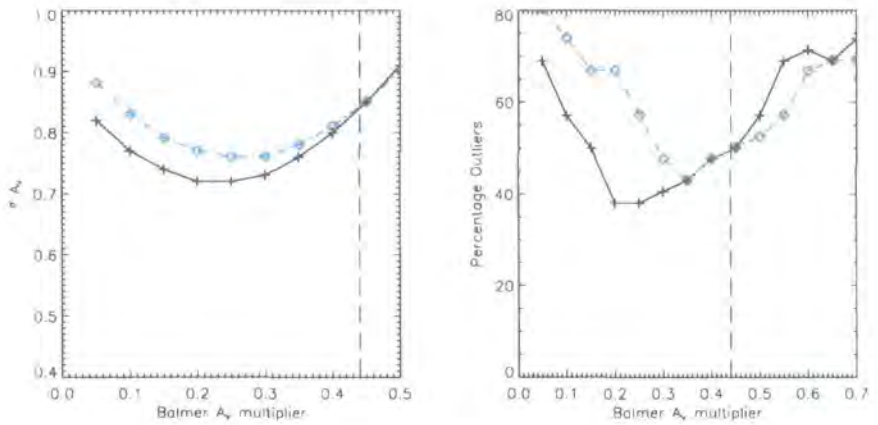

FIGURE 3.15: **Left panel:** σ_{A_V} for IMPZ (solid line with crosses) and HYPERZ (dot-dashed blue line, diamonds) as a function of γ, the chosen ratio between photometrically-derived and Balmer ratio-derived extinction measures. The Calzetti value of $\gamma = 0.44$ is indicated as a long-dashed line. **Right panel:** Percentage outliers for IMPZ (solid line with crosses) and HYPERZ (dot-dashed blue line, diamonds) as a function of γ, the chosen ratio between photometrically-derived and Balmer ratio-derived extinction measures. The Calzetti value of $\gamma = 0.44$ is indicated as a long-dashed line.

underestimate the extinction in comparison to the Phot-A_V value. If the negative Balmer-A_V are excluded, then the remaining sources with positive Balmer-A_V do tend to follow the line denoting agreement, albeit with large scatter.

In Figure 3.18 the sources with only a lower limit on their Balmer-derived extinction (that is, a minimum 3σ Hα detection but only a limit on the Hβ line detection) are plotted in comparison to the extinction as derived from the photometric redshift codes. Here, no ratio γ is applied to the Balmer A_V. Instead straight lines indicating different ratios are overplotted. Since these are lower limits, sources need to lie on, or to the left of a line to imply consistency with that chosen ratio. It can be seen that these lower limit sources are more consistent with lower values of γ. Of the 153 such sources, 146 (95%) are consistent with the γ=0.25 line when considering IMPZ solutions (purple squares), but only 130 (85%) are consistent when considering the HYPERZ solutions (cyan triangles).

3.6 Discussions and conclusions

A number of redshift codes routinely output an A_V value in addition to the best-fitting redshift, but little has been done to investigate the reliability and/or accuracy of such extinction measures. The main reason for this lies in the aim of such codes - they have been developed and optimised in order to derive *redshifts*. However, as the field of photometric

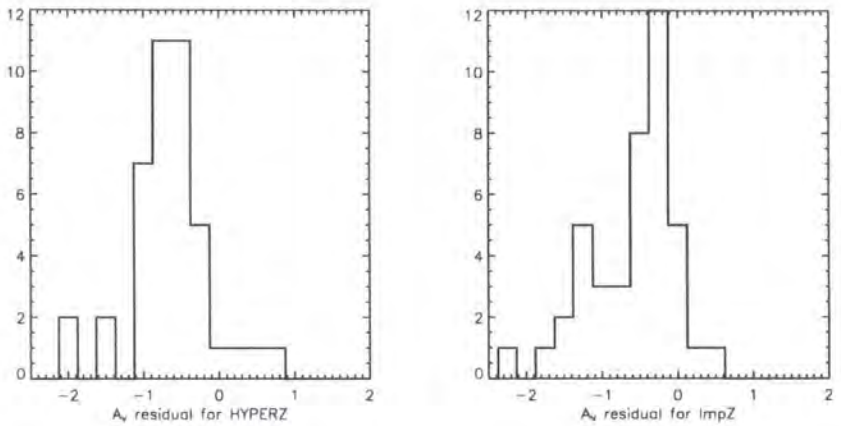

FIGURE 3.16: **A_V residuals for HYPERZ (left panel) and IMPZ (right panel) with γ=0.25.** The residual is now (0.25*Balmer[A_V]-Phot[A_V]).

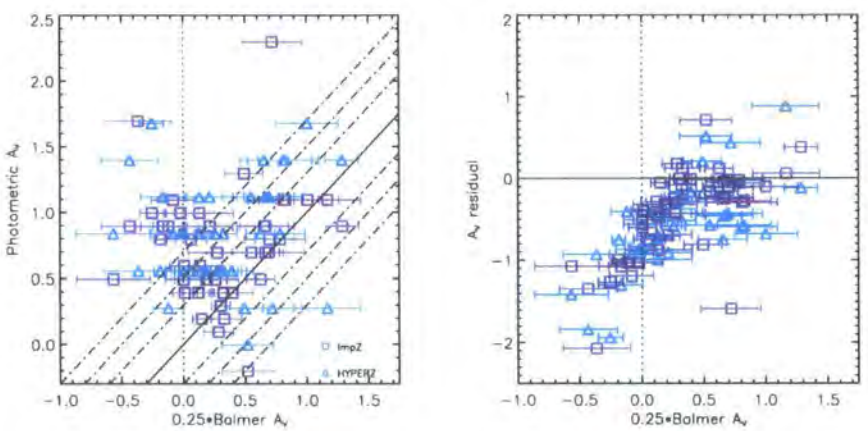

FIGURE 3.17: **Left:** A_V results for HYPERZ (cyan triangles) and IMPZ (purple squares). Plot is the Balmer[A_V] (multiplied by $\gamma = 0.25$) versus the photometrically–derived A_V. Dot–dashed lines denote residuals of 0.3, 0.5 and 0.7 in A_V. Errors are not defined for the Phot-A_V values. **Right:** A_V residuals for HYPERZ (cyan triangles) and IMPZ (purple squares). Plot is Balmer-A_V (multiplied by $\gamma = 0.25$) versus the residual (0.25*Balmer[A_V]-Phot[A_V]).

redshift derivation matures, it is useful to consider some of the other parameters that redshift solutions output.

In this paper we have asked the question 'Can a photometric redshift code reliably determine dust extinction?'. The short answer would be: 'Not to a great accuracy'.

Using a sample with extinctions derived from Balmer flux-ratios the A_V values produced by two photometric redshift codes, IMPZ and HYPERZ, have been compared to the Balmer-A_V values.

First, it was demonstrated that the inclusion of A_V was crucial in order to obtain

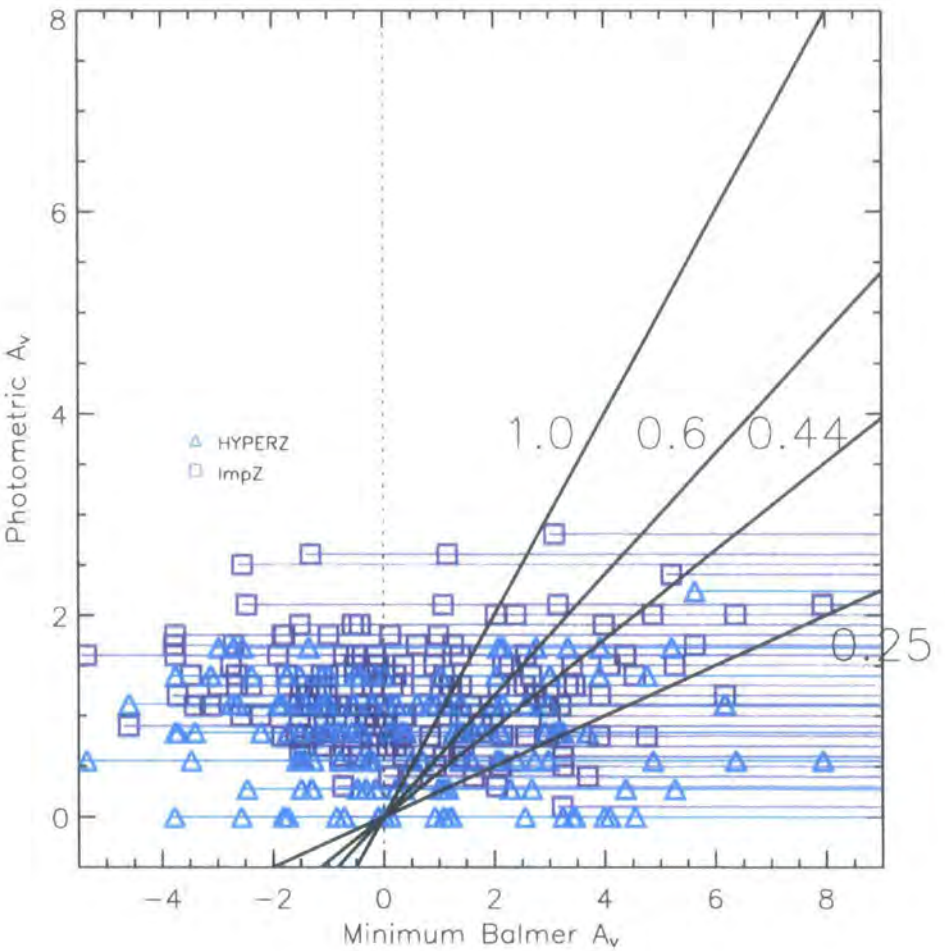

FIGURE 3.18: **'Limit' cases:** A_V results for HYPERZ (cyan triangles) and IMPZ (purple squares). Plot is the Balmer-derived A_V 'limits' versus the photometrically-derived A_V. Solid black lines denote γ values of 0.25, 0.44, 0.6 and 1.0 for the conversion factor relating Balmer-A_V and Phot-A_V. Sources need to lie on, or to the left of a line to imply consistency with that chosen ratio.

photometric redshifts of high accuracy and reliability, such that 95% of the IMPZ results agreed with the spectroscopic redshifts to better than 0.1 in log[1+z]). Without the inclusion of A_V freedom, there was a systematic and incorrect offset to higher photometric redshifts with many more incorrect redshift solutions. The existence of some negative A_V solutions may be indicative of the need for a bluer template in the template set, or for the inclusion of some additional free parameter in the fits. As the most important feature for template-fitted photometric redshifts is the location and identification of 'breaks' in the SED, the inclusion of A_V freedom can be seen, at first-order, as a modifier of the template SED's slope without having a strong effect on the breaks themselves. Hence a similar improvement may be achievable via a 'tilting' parameter or similar which would act to

alter the slope of the template SEDs. Since addition of dust extinction has a physical basis, however, this is a preferable parameter, as long as we can demonstrate that there is some correlation between the best-fitting phot-A_V and the actual (or in this case, that measured via the Balmer ratio) dust extinction of the source. Thus, once the ability to derive good redshifts for the sample had been demonstrated a comparison between the phot-A_V and Balmer-A_V was carried out:

The correlation between the Phot-A_V and the Balmer-A_V was similar for both codes, but was both noisy and not particularly strong. Based on direct comparison between the two codes, and investigations into the χ^2 solution space, a good part of this noise is derived from the inherent lack of precision the Phot-A_V solution has (perhaps 0.3 in A_V say), no doubt since it is based on only five photometric measurements. Additional noise arises from the precision of the Balmer-A_V, typically accurate to perhaps 30%, which is due to the resolution of the spectrographic data. Given these errors, the correlation seen was in fact quite good.

The correlation was improved somewhat when the empirical value of $\gamma = 0.44$, the ratio between gas- and star- derived extinction, as determined by Calzetti (2001b), was allowed to vary. From least-squares-fitting the minimum in the reduced χ^2 distribution was found for $\gamma \sim 0.25 \pm 0.2$.

The Calzetti ratio of 0.44 means that there is around a factor two difference in reddening such that the ionised gas (as measured by the Balmer decrement) is twice as reddened as the stellar continua (as measured by the photometry) (e.g Fanelli et al. 1988; Calzetti et al. 1994). This implies that the covering factor of the dust is larger for the gas than for the stars, which can be explained by the fact that the ionising stars are short-lived and so for their lifetime remain relatively close to their (dusty) birthplace, whilst the majority of stars, contributing to the galaxy's overall optical luminosity are longer-lived and can migrate away from their dusty origins.

For the sample of galaxies in this paper, this factor two difference in covering factor implied by the Calzetti ratio is found to be plausible, given the errors of the method. The sample has a some preference for an increased covering factor which would imply they are undergoing more rapid, 'bursty' star formation than the galaxies Calzetti used in her derivation. Perhaps more importantly, the results demonstrate the pitfalls of assuming

that star- and gas-based extinction measures will give the same dust extinction given some conversion factor. Thus, correlation to Balmer-derived values are modulo the uncertainty in comparing star- and gas-based extinction measures.

However the results presented here show that, given certain considerations, there is potential in the application of photometric codes to reliably derive an extinction measure, though the precision is currently low. It is expected that the ability of photometric redshift codes to determine extinction will improve with the availability of more photometric bands (here, there are five wide band filters between 3,000-9,000Å). A sample with a combination of wide and narrow-band filters, with good wavelength coverage and range (in particular, extension to near-IR) will break many of the degeneracies and allow the codes to accurately differentiate between different possible fits.

The results also show that it is important to note that this will be a measure of the star-based extinction, and will not necessarily be well correlated with the extinction to the ionised regions of a galaxy.

4

The Evolution Of Star Formation Rate Density

4.1 Introduction and Context

Study of the change in cosmic Star Formation Rate Density (SFRD) as a function of redshift is of great importance to our understanding of how galaxies evolve. Knowing the SFRD of an average volume of space as a function of the age of the Universe allows us to test the latest predictions from galaxy evolution models, and see if the underlying theories are correct. We are able to do this because star formation is a process that produces many emission features in galaxy spectra, making it traceable over the history of the Universe. Many observable properties of galaxies are correlated with SFR; in the work presented here we use the [O II] emission line as a SFR diagnostic. Its properties were reviewed in Chapter 1.

The ultimate goal in studying the evolution of the cosmic SFRD is to understand the driving forces that change the average star forming properties of the Universe as it ages. The field is a large one and is constantly being added to; papers on the subject are released

weekly. With the large volume of literature in mind, I present here a review of the state of knowledge, with specific focus on the big picture.

4.1.1 Redshift Zero

In recent years the two largest surveys of the local Universe have been the 2 Degree Field Galaxy Redshift Survey (2dFGRS, Colless et al., 2001) and the Sloan Digital Sky Survey (SDSS, York et al., 2000).

Figure 4.1, taken from Kauffmann et al. (2003), shows a result from the SDSS. The Figure shows the strength of the 4000Å break plotted against stellar mass, for galaxies in the local Universe. The contours denote iso-density regions, with white being the highest density. There is a bi-modality evident in the plot, whereby high mass galaxies have strong 4000Å breaks and the smallest galaxies have weaker breaks. The interpretation is that the smallest galaxies are the youngest.

4.1.2 High Redshift

Figure 4.2 shows the results of a study by Cowie et al. (1996). Plotted in the Figure is restframe K-band magnitude vs [O II] equivalent width for galaxies in various redshift bins. It can be seen that at higher redshifts ($z \gtrsim 0.6$) the most rapidly star forming galaxies are also the most luminous. There also appears the trend that as one moves to lower redshift the size of the most actively star forming galaxies becomes less luminous – the so-called phenomenon of "downsizing".

Contrast this picture with that of Kauffmann et al.. At low redshift we see that dwarf galaxies house the most active star formation in the Universe. There must be some cross over point at which the emphasis shifts from large to smaller galaxies. The problem of course is that dwarf galaxies become more and more difficult to observe as one moves to higher redshift.

To account for the fact that flux-limited surveys miss out on the contribution from dwarf galaxies, many authors use Schechter-style fits as a means to extrapolate to faint magnitudes. If done properly, these fits would account for the unobserved galaxies. The problem however, is that at high redshifts – when one has the most need to correct for the absence of dwarf galaxies – there is very little data with which to constrain the fit. This leads to the Schechter fit being made from only the brightest galaxies. Clearly this can

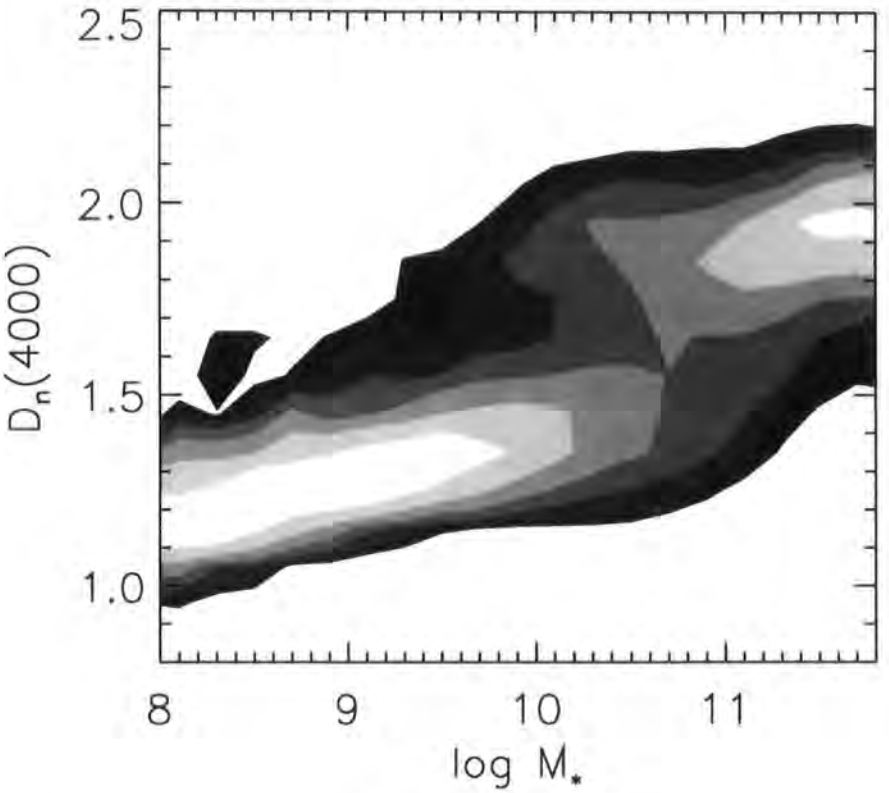

FIGURE 4.1: The strength of the 4000Å break plotted against stellar mass, for galaxies in the local Universe, taken from Kauffmann et al. (2003). The contours denote iso-density regions, with white being the highest density. A bi-modality is visible in which high mass galaxies have the largest 4000Å breaks and the smallest galaxies have the weakest 4000Å breaks. The interpretation is that the dwarf galaxies are the youngest.

only constrain one end of the fit and so the uncertainty remains.

4.1.3 Why Use CNOC2?

The CNOC2 Survey affords us an opportunity to more closely examine the redshift range $0.2 \lesssim z \lesssim 0.65$. As we have noted above, this marks a very important period in cosmic time, over which the SFRD is thought to be changing drastically. Furthermore, by using [O II] emission we will only use one indicator over the whole redshift range, avoiding problems from the intercomparison of indicators.

The CNOC2 dataset also gives us the ability to study some dwarf galaxies. Dwarf data extends out to $z \sim 0.25$.

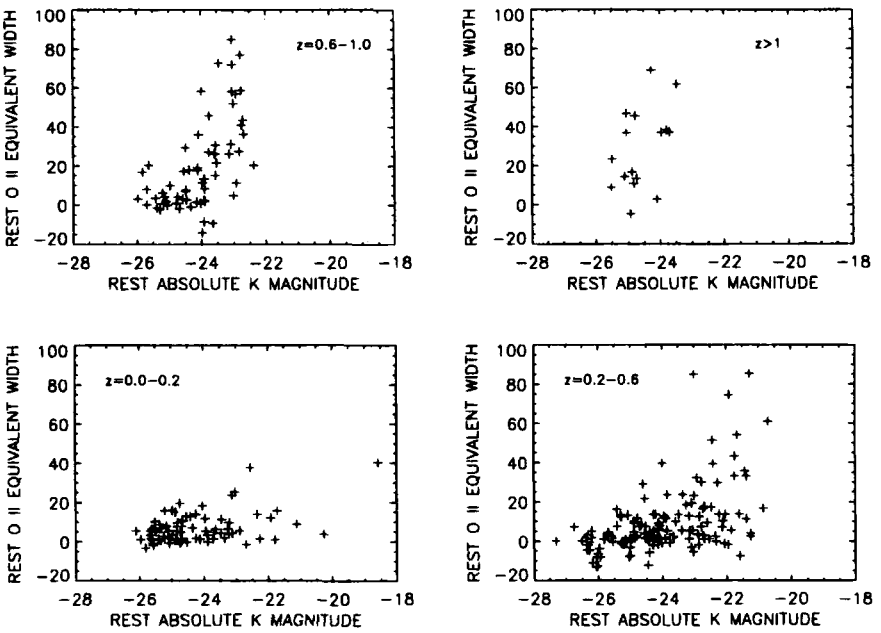

FIGURE 4.2: The distribution of restframe K-band absolute magnitude against [O II] equivalent width, taken from Cowie et al. (1996). The mean size of a rapidly star forming galaxy can be seen to shrink as one moves to lower redshift.

4.2 Preparation

In this section I present my work in preparing the CNOC2 sample for the analysis of the Universal SFH. This involves computing the SFRs of individual galaxies, combining the repeat observations into one measurement per galaxy and also establishing a selection criteria so we are able to remove from the sample any erroneous measurements that would otherwise adversely affect the results of the study. An example of such measurements might be ones whose SFR estimate possesses very large error bars or ones where the SFR estimate is a mismeasurement by the code, arising from a spurious feature in the spectra.

4.2.1 The Measurement of Individual Star Formation Rates

Using the flux measurements obtained in Section 2.2.1, we are able to compute the SFRs of individual galaxies. This can be done via use of one of the many [O II]–SFR calibrations from the literature, reviewed in Chapter 1. For the reasons discussed in that chapter we opt to use the calibration derived by Kewley et al. (2004) to compute the SFRs used for our "best estimate" of the Universal SFH.

Star formation rates of each galaxy for which there exists an [O II] flux measurement are computed using the [O II] line luminosity, $L_{[O\,II]}$, according to the equation

$$SFR(M_{\odot}/yr) = L_{[O\,II]} \times R, \tag{4.1}$$

where $R = 6.58 \times 10^{-42}$ is the coefficient derived by Kewley et al. (this is the same as Equation 1.2, it is given again here for completeness).

The [O II] line luminosity itself is calculated from the observed [O II] flux, $f_{[O\,II]\ obs}$, and an individual dust estimate for each galaxy. Once the dust correction has been taken into account, the extinction-corrected [O II] flux, $f_{[O\,II]\ corr}$, is used to compute the line luminosity, $L_{[O\,II]}$. A simple spherical geometry is assumed, according to the equation

$$L_{[O\,II]} = f_{[O\,II]\ corr} \times 4\pi \times D_{lum}^2 \times 10^{0.4 \times A_{[O\,II]}}, \tag{4.2}$$

where D_{lum} is the luminosity distance to the redshift of the galaxy being considered and $A_{[O\,II]}$ is defined in Section 4.2.2, below. The luminosity distance is calculated by a code written by the author. The reader is referred to Appendix A for an overview of cosmological distance measures.

4.2.2 Dust Corrections and Absolute Magnitudes

As noted above, before using Equations 4.1 and 4.2, we must first correct the observed [O II] flux of each galaxy for dust obscuration. A distinct advantage of this work over other SFH studies is that we employ individual dust corrections, specific to each galaxy. This is a far more accurate method than either of the two alternatives commonly used, namely not applying a dust correction at all, or simply adopting a blanket correction for every galaxy in the sample.

The dust estimates used here are derived by the photometric redshift code ImpZ (Babbedge et al., 2004), discussed in detail in the previous chapter. Ideally we would prefer to derive dust estimates from observations of the Balmer decrement, but this is not possible because the CNOC2 spectra do not cover the full Hα – Hβ wavelength range. Note that we have used an extension of the original CNOC2 dataset, which contains spectra with both Hα and Hβ lines, to test the reddening results of ImpZ (Chapter 3; Babbedge et al., 2005).

ImpZ

The ImpZ code was run on the five band CNOC2 photometry by Dr T. Babbedge of Imperial College London. He has provided the output of the code only; all the analysis of any data in this chapter has been undertaken by myself.

To recap, ImpZ (Babbedge et al., 2004) is a template fitting photometric redshift code: Given photometry of a galaxy, it finds the most likely redshift through a χ^2 minimisation procedure. As detailed in the last chapter, it can also be used to obtain a measure of the reddening, from photometry alone. Another very useful output of the code, is the restframe absolute magnitude in a user specified filter. These two outputs are of special importance to us here. Knowing the reddening allows us to correct the [O II] flux for dust absorption, while reporting the absolute magnitude in a fixed restframe band allows us to bypass a formal evaluation of k-corrections.

The pertinent details of the ImpZ run on the CNOC2 photometry are shown below.

- ImpZ was forced to find a photometric redshift that lay within 0.05 (in $log(1+z)$) of the true spectroscopic redshift. Constraining the photometric redshift in this way allows the code to focus on determining the reddening; it makes maximum use of the available information because we effectively tell ImpZ the answer to the redshift determination problem.

- The 6 templates described in Section 3.4.2 are used.

- The reddening corrected, restframe absolute B_{AB} magnitude is returned.

- Certain galaxies ($\sim 3\%$) fail the ImpZ runs through errors in the photometry. These are excluded from the subsequent analysis.

There remains the issue of the "intrinsic" reddenings in the ImpZ templates. Recall that it is possible to create a variety of very similar shaped SED templates using a range of A_v values (see Babbedge et al., 2004 and Section 3.4.1). The issue is whether or not these intrinsic A_v values should be included in the total A_v for a galaxy? If they are included they could considerably increase the A_v of individual objects. The values of the intrinsic A_v depend on the galaxy type assigned by ImpZ, but it could be as large as 0.74 magnitudes for the starburst template.

As discussed in Section 3.4.1, there is considerable freedom in the values the intrinsic A_v of a template can take, while still retaining its same broad shape. In light of this, we chose not to include the intrinsic A_v term in the analysis.

Applying the Reddening Correction

When folding a dust correction into the measurement of SFRs it is important to ensure that the correction is undertaken at the proper wavelength. For the Kewley et al. calibration, the dust correction should be made at the wavelength of the [O II] line itself. This is *not* the case with every calibration (see Section 1.7).

The reddenings reported by ImpZ are A_v, i.e. they are the reddenings at the central wavelength of the V band, 5464Å. They must be transformed to reddenings at [O II] in order that we can use them with the Kewley et al. calibration. We signify these reddenings by the symbol $A_{[O\,II]}$.

The transformation between A_v and $A_{[O\,II]}$ is done using the reddening curve of Cardelli et al. (1989, hereafter CCM). The extinction at [O II] is related to the extinction at V by the expression

$$A_{[O\,II]} = k_{3727} \times A_v / r_v, \tag{4.3}$$

where k_{3727} is the value of the CCM curve at 3727Å and $r_v = 3.1$ is its value at V.

The CCM curve was chosen in preference to the often used curve of Calzetti et al. (1993), for reasons of consistency: Kewley et al. make use of the CCM curve to derive a reddening free SFR-[O II] calibration.

Once the reddenings at [O II] have been obtained from Equation 4.3, the observed [O II] flux can then be transformed into the extinction-corrected flux, according to the equation

$$f_{[O\,II],\,corr} = F_{[O\,II],\,obs} \times 10^{0.4 \times A_{[O\,II]}}. \tag{4.4}$$

Equations 4.1 and 4.2 can then be employed to compute the SFRs as normal.

4.2.3 Removal Of Erroneous Measurements

When analysing any dataset it is important to remove from the sample erroneous data points that would otherwise adversely affect the results of the study being undertaken. In our application, that means spectra whose [O II] error bars are very large. Care must be taken however not to bias the results by only selecting high signal-to-noise data points, or conversely by discarding points with numerically large errors, despite those measurements being of reasonable signal-to-noise. The danger with the former issue is removing all low SFR galaxies that have relatively larger error bars. A simple signal-to-noise cut would cause this problem. The latter issue might exclude those galaxies that have very strong [O II] emission, possibly contributing a significant fraction of the total [O II] luminosity density at that epoch. Galaxies such as these could easily be excluded by a cut that only takes into account the numerical size of the error bar.

Aiming to encompass both low and high SFR objects while also excluding erroneous points is difficult. Beginning with a total (including repeat observations) of 8415 spectra[1], cuts are performed on the data set according to the following criteria:

- Any spectrum whose [O II] line measurement failed is removed from the sample. This amounts to $\sim$ 16% of the full number of spectra being rejected.
- All remaining galaxies with an [O II] equivalent width error of less than 10Å are kept in the sample. This ensures we do not exclude the low SFR objects whose errors may be relatively large.
- In addition, those galaxies whose [O II] equivalent width error is greater than 10Å *but* whose equivalent width measurement is at a certainty of above 2.5σ, are also kept. This ensures we do not discard the strong [O II] emitters with numerically large errors. Combining this cut with the step above removes a further 29% of spectra from the sample (visible in Figure 4.3, see text below).
- Finally, any galaxy for which the ImpZ determination of the reddening failed is also rejected. This step removes a further 3% of spectra.

The effects of these cuts may be seen in Figure 4.3. Shown in the Figure is the distribution of [O II] equivalent width vs its error, as derived in Section 2.2.1. The black

[1] *not* galaxies; at this stage we deal with removing erroneous individual spectra from the sample, the remaining good spectra are combined into one measurement per galaxy at a later stage.

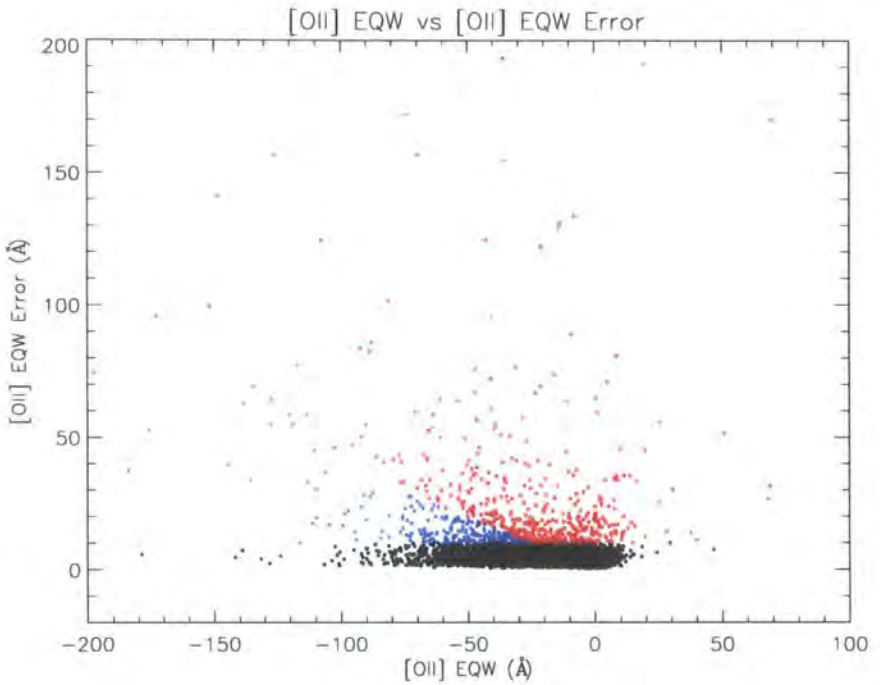

FIGURE 4.3: The distribution of [O II] equivalent width vs error. The black points are those whose equivalent width error is less than 10Å, while the red are those that do not satisfy this criterion. The blue points highlight the population of objects with errors $\sigma > 10$Å, but whose signal-to-noise ratio on those measurements is above 2.5σ. The set of both blue and black points are kept in the final dataset.

points are those whose equivalent width error is less than 10Å, while the red are those that do not satisfy this criterion. The blue points highlight the population of objects with errors $\sigma > 10$Å, but whose signal-to-noise ratio on those measurements is above 2.5σ. Clearly there is a significant number of objects in the blue population that could have easily been excluded by a simple equivalent width error cut. Note that there is a population of red points which appear very close to the 2.5σ limit we have imposed. Although some of these may be real measurements, we nevertheless still remove them; a limit must be set somewhere and they are of relatively low signal-to-noise.

The set of both blue and black points are kept in the final dataset. Weights associated with the removal of the other points are computed later in this chapter.

4.2.4 Combination of Duplicate Observations

After the cuts described above have been performed, we are left with a data set that is not necessarily free of SFR measurements from repeat observations. Any remaining repeat observations must now be combined into a single measurement per galaxy.

Repeat observations are identified and the data associated with the observation that has the highest signal-to-noise ratio, as measured by the [O II] equivalent width and its error, is selected for inclusion in the final analysis. The data associated with the lower signal-to-noise observations are removed from the sample.

The final number of individual galaxies carried through for the final analysis is 4814.

4.3 Results

4.3.1 Evolution Of Universal SFRD With Magnitude and Redshift

In light of the scientific community's interest in the phenomenon of downsizing, a very useful way to analyse the SFH is to examine how the contribution to the SFRD from galaxies of a given magnitude changes with redshift.

Plotted in Figure 4.4 is the distribution of reddening corrected, restframe absolute B_{AB} magnitude vs spectroscopic redshift, for all galaxies retained in the sample after the cuts described in Section 4.2.3. The sample is divided into bins in magnitude-redshift space, delineated by the black dot-dashed lines. The divisions are chosen to ensure that the corner of each of the faintest bins roughly coincides with the flux limit of the Survey. The bold numbers show the total SFRD contained within each bin, in the standard units of $10^{-4}\,M_{\odot}\,yr^{-1}\,Mpc^{-3}$. Statistical errors on these measurements are computed in two ways: Both by a simple bootstrap resampling of the data within each bin, and also by using the standard formula for the error on a summation. Both sets of errors are labelled in the Figure and further details of their computation are discussed below. The numbering scheme for the bins (in red) is arbitrary, and is used only for the purpose of relating the Figure to Table 4.1, in which are shown numerically the bin divisions and the SFRDs, with their associated errors. Also of note are the square points towards the left edge of the Figure. These show the brightnesses of the Milky Way and The Large Magellanic Clouds, labelled MW and LMC respectively.

Before we discuss any conclusions from the Figure, the details of its production are explained.

Magnitudes and Redshifts

The absolute B_{AB} magnitudes are derived by ImpZ, as explained in Section 4.2.2. They are reddening corrected, restframe magnitudes.

The spectroscopic redshifts are those measured by the Survey, as described in Section 2.1.4.

SFRDs and Weighting Scheme

The total SFRD in each magnitude-redshift bin, $\dot{\rho}_*$, is computed according to the equation

$$\dot{\rho}_* = \frac{1}{V_b} \sum_i \psi_i \times SFR_i, \tag{4.5}$$

where SFR_i is the SFR of each galaxy in the bin; ψ_i is the statistical weight associated with each galaxy and V_b is the cosmological volume between the upper and lower redshift bounds of the bin in question, normalised to the 1.5 square degree area of the Survey (see Appendix A).

The SFRs are computed as described in Section 4.2.1, using the Kewley et al. (2004) [O II]-SFR calibration with a dust correction derived from the ImpZ photometric redshift code. We include in the summation galaxies that have apparent negative SFRs. This is an important step and something not done by many authors in the field. The reasoning behind including such galaxies is that the statistical over-measurement of the high SFRs should be cancelled out by the negative SFRs, thus yielding a more accurate measurement. Studies in which the galaxies with apparent negative SFRs are simply discarded suffer a self-imposed biasing to high values of the SFRD; our methodology avoids such an error.

The statistical weights, ψ, are *not* simply the CNOC2 weights described in Section 2.1.5. Instead, ψ are composed of the multiple of three individual weighting schemes, one of which is the CNOC2 scheme. We compute ψ for each galaxy such that

$$\psi = W_{CNOC2} \times W_V \times W_{cut}, \tag{4.6}$$

where W_V and W_{cut} are the two additional weighting schemes. These concern corrections for the volume probed by the Survey (W_V), and the need to account for galaxies that were removed by the cuts in Section 4.2.3 (W_{cut}).

Taking each scheme in turn:

- **CNOC2 Weights:** These are the CNOC2 weights described in Section 2.1.5. We use the total weight, $W_{CNOC2} = 1/S$, where S is a function of magnitude, x-y position on the CCD, colour and redshift. We use the values of S_m and S_c derived from the R band, since the Survey was R band selected.

  As we stated when we discussed their calculation, the redshift weights, S_z, are computed only for the redshift range $0.12 < z < 0.55$. Note that the other weights (based on magnitude, colour and x-y position) *are* computed for the full redshift range. This presents us with a problem with regards to bin 4, since there are effectively no redshift weights defined for galaxies with $z > 0.55$.

  To compensate for this, we assign a value of $S_z = 1$ to every galaxy in bin 4. In doing so we are clearly mis-weighting the galaxies in that bin, but there is no simple alternative. To check the scale of the error introduced, we conduct a test whereby we artificially set the redshift weights in bin 3 equal to unity, and then recompute the SFRD. The result is a $\sim 36\%$ increase in the estimated SFRD in bin 3. An increase is seen because of the way the redshift weights function as modifiers to the underlying magnitude weighting scheme, W_m. There are two conclusions to be drawn. Firstly we note from the test on bin 3 that by assigning unity redshift weights to bin 4, we are overestimating the SFRD in bin 4. Secondly, the scale of the overestimation in bin 4 may be evaluated from the test on bin 3. However, the value of 36% should only be thought of as guide. The true amount is likely to be somewhat different, because the redshift weights in bin 4 will not be the same as those in bin 3.

- **Volume Weights:** The volume weight, W_V, associated with each galaxy is computed using the maximum redshift out to which it should be possible to observe that galaxy spectroscopically, given the brightness limits of the Survey. This maximum redshift is referred to as z_{max}.

  The thick red line in Figure 4.4 shows how z_{max} varies with absolute B_{AB} magnitude. The curve is computed from the lower envelope of the $B_{AB}-z$ distribution, using the data in bins 4, 6, 7 and 8. Six data points from the above bins were used to fit the z_{max} curve, these are marked on the Figure as purple triangles. The end points in bins 8 and 4 are constrained to be the minimum and maximum values in redshift and the faintest magnitude in bin 8 and the 80th percentile magnitude from bin 4.

The remaining points are then set to be the 60th and 95th percentile in redshift and magnitude respectively, from the bins they lie in. A least squares quadratic fit is then used to determine the value of z_{max} for every galaxy. By eye, the curve appears to be a good match to the $B_{AB}-z$ envelope. Since the brightness limit of the Survey is not sharply defined anyway, there is little benefit in attempting a more complex evaluation of z_{max}.

The volume weight is computed on a per-galaxy, per-bin basis according to the following prescription. If the z_{max} value of a galaxy is greater than the upper redshift limit of the bin it lies in, then the galaxy does not require any additional volume weighting and W_V is set equal to unity. If however the z_{max} value is less than the upper redshift limit of the bin, then the volume weight is computed as the ratio of the total volume in the bin to the volume between the start of the bin and z_{max}. Mathematically we can write

$$W_V = \begin{cases} 1.0 & z_{max} \geq z_u \\ V(z_l, z_{max})/V(z_l, z_u) & z_l < z_{max} < z_u, \end{cases} \tag{4.7}$$

where z_l and z_u are the lower and upper redshift limits of the bin and $V(z_1, z_2)$ is the cosmological volume evaluated between redshifts z_1 and z_2.

We impose the additional condition that the volume weight can have a maximum value of 10. Values that would otherwise be above this limit are set equal to the maximum. This ensures that no one galaxy dominates the SFRD sum in a bin.

- **Cut Weights:** An additional weight to account for the effect of the cuts described in Section 4.2.3 must also be computed. These weights are computed on a per-bin basis by taking the ratio of the number of galaxies with redshifts in the CNOC2 catalogue, N_{cat}, to the number contained in the bin in question, N_{bin}.

  This can be written as

$$W_{cut} = N_{cat}/N_{bin}. \tag{4.8}$$

Error Analysis and Considerations

As indicated above, the statistical errors on the SFRD measurement within each bin are computed in two ways, both through bootstrap resampling and also using the formula for the error on a summation.

For the bootstrap method, 100 resamplings of the galaxies and their associated weights are performed on the data in each bin. The galaxies are chosen at random, with repeat selections being allowed. The bootstrap error in the SFRD is then defined to be the variance of the distribution from the 100 separate realisations. We use the full weighting scheme for each galaxy when doing the resampling (Equation 4.6).

As a second statistical error estimate, the error on the summation used to find the SFRD (Equation 4.5) is evaluated. This is done according to the equation

$$\sigma_{\dot{\rho}_*} = \frac{1}{V_b} \sqrt{\sum_i (\psi_i \, \sigma_i)^2}, \tag{4.9}$$

where $\sigma_{\dot{\rho}_*}$ is the error in the sum of the SFRD and σ_i is the error in an individual measurement of SFR (set to have the same fractional error as the flux measurement). V_b and ψ retain their meanings from Equations 4.5 and 4.6.

The main cause of statistical error is the mis-measurement of [O II] flux by the line measurement code. These errors are well quantified through the analysis of repeat observations (Section 2.2.2).

It can be seen that the statistical errors in Figure 4.4 and Table 4.1 are relatively small; we have not considered however the more serious issue of systematic errors. These can be broken down into two groups. Firstly there are those which affect *any* analysis of the evolution of SFRD, and secondly there are those relevant only to this work.

Systematics present in all studies include: errors in the SFR indicator calibration itself, the uncertainty in redshift measurement (which in turn affects the absolute SFRs measured), the uncertainty in cosmological parameters, and, potentially – if one wishes to split the sample by absolute restframe magnitude – the k-correction, which depends in turn on the accuracy of the photometry and the redshift.

The largest of these errors – by far – is the uncertainty in the SFR calibration. We saw in Section 1.7 that there exist factors of ~ 13 difference between certain [O II]-SFR calibrations from the literature.

Bin number	B mag range		z range		SFRD	SFRD Error
1	−22.9	−21.0	0.18	0.30	35.88	3.79
2	−22.9	−21.0	0.30	0.40	85.88	6.97
3	−22.9	−21.0	0.40	0.55	131.70	13.95
4	−22.9	−21.0	0.55	0.67	208.28	41.70
5	−21.0	−19.0	0.18	0.30	68.80	3.83
6	−21.0	−19.0	0.30	0.40	147.61	9.68
7	−21.0	−19.0	0.40	0.55	154.59	22.56
8	−19.0	−17.5	0.18	0.30	145.33	23.94

TABLE 4.1: Bin definitions, Star Formation Rate Densities and their associated bootstrap errors from Figure 4.4. The SFRDs and errors are in units of $10^{-4}\,M_{\odot}\,yr^{-1}\,Mpc^{-3}$.

A large potential cause of what we will call a systematic error in this work is the evaluation of individual reddenings from ImpZ, A_v (see Chapter 3). However, despite the uncertainty in individual measurements of the A_v, comparisons between bins in Figure 4.4 should still be valid. This is especially true when one is examining a population of fixed magnitude, such as bins $1-4$. In this instance all the galaxies are generally fit with the same template type (as judged by ImpZ).

There is also a systematic error in the evaluation of absolute B_{AB} magnitudes. In the runs used here, ImpZ fixes the photometric redshifts to be within 0.05 in $log(1+z_{CNOC2})$, where z_{CNOC2} is the spectroscopic redshift. Not every galaxy will have an exactly matching photometric and spectroscopic redshift and the uncertainty in absolute magnitude needs to reflect this fact.

Discussion

There are many interesting conclusions to be drawn from Figure 4.4. Firstly, it is evident that, if we consider galaxies of a fixed magnitude, the SFRD in each bin is declining as we move towards low redshift. This holds not just for the very largest galaxies, but also for those in the central magnitude bins on the Figure ($-21 < B_{AB} < -19$). In particular, we note that for giant galaxies ($-23 < B_{AB} < -21$), the SFRD at $z \sim 0.6$ is 5.8 times higher than that at $z \sim 0.25$.

The change in SFRD between bins 1 and 2 is $50 \times 10^{-4}\,M_{\odot}\,yr^{-1}\,Mpc^{-3}$, this can be verified from Table 4.1. Compare this number to the change between bins 5 and 6, which are at the same redshifts but house lower luminosity galaxies. We see a difference of $\sim 78 \times 10^{-4}\,M_{\odot}\,yr^{-1}\,Mpc^{-3}$ (bin 6 − bin 5). Over the range $0.2 < z < 0.4$, the SFRD from

lower luminosity galaxies has dropped faster than that of the giants. This is an interesting result, but it should be compared to the findings of Section 4.3.3, in which it is shown that in spite of the absolute evolution, the *fraction* of giant galaxies that are rapidly star forming has declined faster than the corresponding fraction in lower luminosity galaxies.

We now take two slices at fixed redshift, and compare bin 1 to bin 5 and bin 2 to bin 6. At $z \sim 0.25$ the change in SFRD between bin 1 and bin 5 is $\sim 33 \times 10^{-4}\,\mathrm{M_{\odot}\,yr^{-1}\,Mpc^{-3}}$. At higher redshift, $z \sim 0.35$, the change between bin 2 and bin 6 is $\sim 62 \times 10^{-4}\,\mathrm{M_{\odot}\,yr^{-1}\,Mpc^{-3}}$. These numbers show a larger difference a higher redshift, which again implies that the evolution of absolute SFRD is stronger for lower luminosity galaxies. Again, we caution that in Section 4.3.3 the fractional contributions to the SFRD from rapidly star forming galaxies in each brightness band is assessed. It is shown that for the fractional contribution to their SFRD, giants suffer the stronger evolution.

At $z \sim 0.2$ the CNOC2 Survey reaches down to galaxies of similar luminosity to the Large Magellanic Cloud (LMC). At this redshift we see that the largest fraction of the Universal SFRD (from the sum of bins 1, 5 and 8), is coming from low luminosity galaxies, of similar magnitude to the LMC. This is in-keeping with the findings of Kauffmann et al. (2003) who find the local Universe to be abundant in star forming dwarf galaxies, but somewhat devoid of star forming larger galaxies.

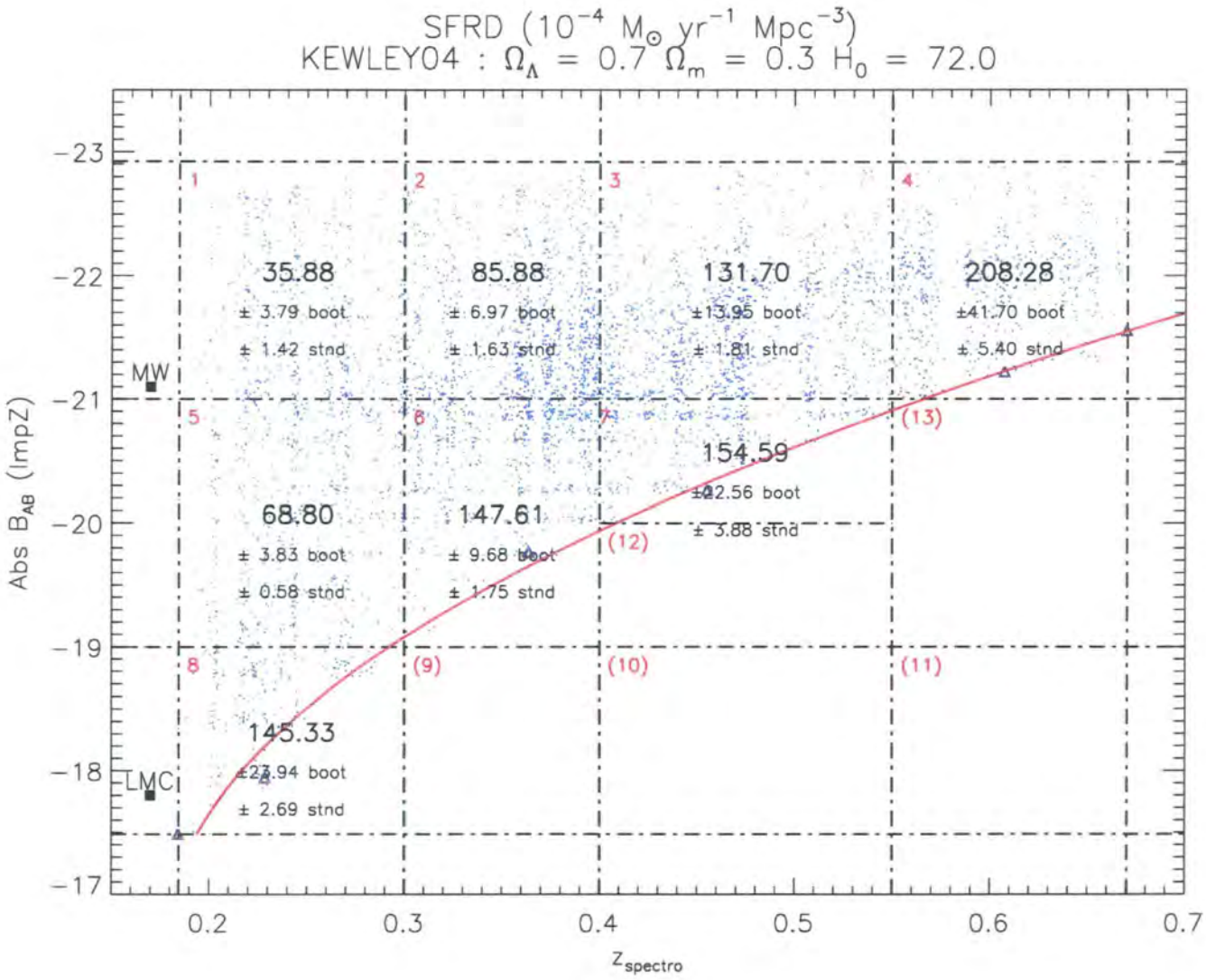

FIGURE 4.4: The SFRD of the Universe as measured from the CNOC2 Survey, binned in magnitude-redshift space. The blue points show the distribution of B_{AB} magnitude vs spectroscopic redshift. The black line delineate the bins; the bold numbers are the SFRD in a bin, computed using the weighting scheme described in the text. Errors in each bin are computed through bootstrap resampling and standard error formulae. There is a clear drop-off in the SFRD of giant galaxies from $z \sim 0.6$ to low redshift. See text for continued discussion.

4.3.2 Alternative Representations of the Data

Two alternative views of the data are shown in Figures 4.5 and 4.6. These show the SFR-B_{AB}-z data as a 3D surface (Figure 4.5) and a 3D scatter plot (Figure 4.6).

The surface was created using Delaunay triangulation and is smoothed to a resolution of 50 elements along each axis. Of note is the relatively flat area at low redshift, which contains very few low luminosity but highly star forming galaxies (c.f. Figure 4.11).

The scatter plot shows the raw data without any smoothing, each filled circle represents one galaxy. The colour coding of SFR values on the z-axis allows one to see more clearly the distribution of values. Some insight can be gained by manipulating this distribution of points in real-time on a computer, but it must be admitted that the 2D representations on the page add relatively little to what may be gleaned from Figure 4.4.

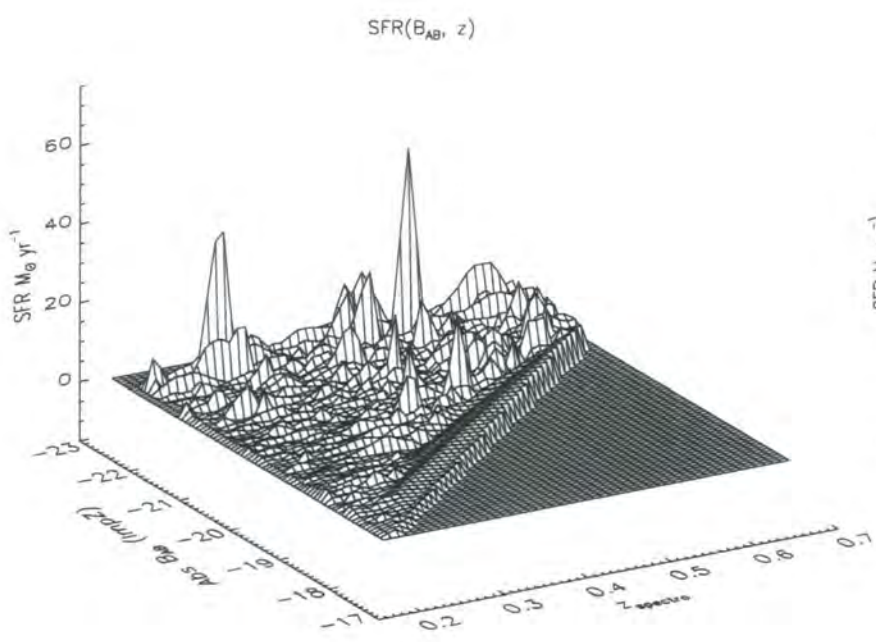

FIGURE 4.5: A 3D Surface of SFR-B_{AB}-z. The surface was created using Delaunay triangulation. Of note is the relatively flat area of the plot at low redshift, which contains very few low luminosity but highly star forming galaxies.

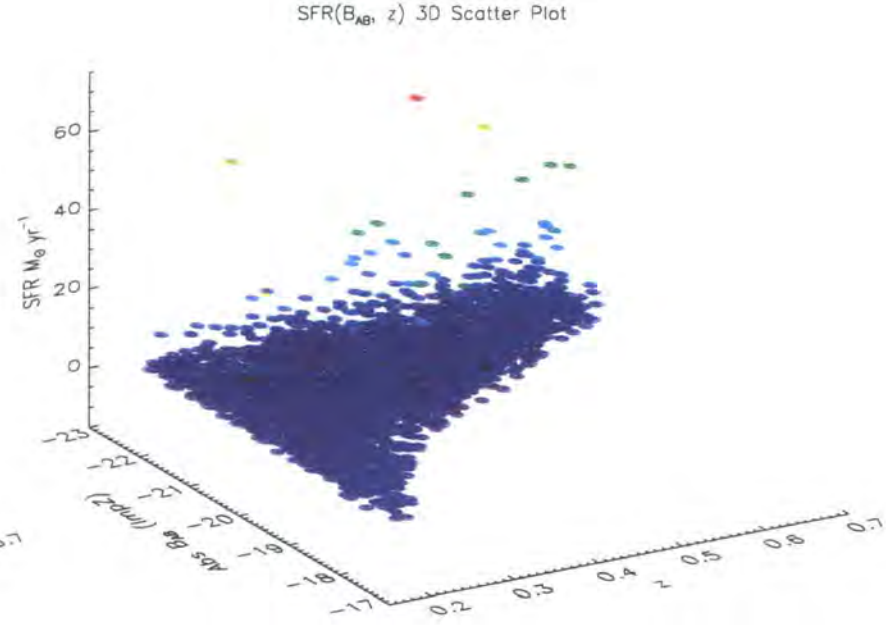

FIGURE 4.6: A 3D scatter plot of SFR-B_{AB}-z. The colour coding on the z-axis allows one to see more clearly the SFR values. The Survey's flux limit is clearly visible. Also of note is the scarcity of low redshift, low luminosity highly star forming galaxies.

4.3.3 The Variation of Equivalent Width at the 50% SFRD Contribution

An interesting quantity is the [O II] equivalent width at which half the SFRD in a bin comes from galaxies with emission stronger than that limit. Figure 4.7 shows the fractional contribution of galaxies, whose [O II] emission is stronger than a certain equivalent width, to the total SFRD in each bin (the bins and SFRDs are defined in Figure 4.4 and Table 4.1). The weighting scheme composed of three separate weights (CNOC2, volume and cut weights) is again used in the production of this Figure.

The dotted lines in each plot in the Figure show the 50% fractional contribution. It is clear that there is a substantial difference in the equivalent width at which this fraction occurs as one steps through the magnitude-redshift bins.

Bin 3 lies roughly in the middle of the cosmic time spanned by the survey.

Computing the look-back time, $t_{lookback}$, at redshifts $z = 0.2, 0.4$ and 0.6 gives look-back times of 2.85, 4.65 and 6.44 Gyr respectively (see discussion of the redshift-time relation in Chapter 1). Bin 3 (beginning at $z = 0.4$) therefore lies roughly in the middle of the cosmic look-back time spanned by the survey. It was therefore selected as the arbitrary bin from which to set the fiducial equivalent width at the 50% contribution; this is very close to 30Å. It is noted that this value is similar to that used by Cowie et al. (1996) to classify galaxies that are "undergoing rapidly star formation" (25Å: this value actually comes from Kennicutt, 1992b who showed that a value of 25Å roughly separates galaxies that double their mass in 10^{10} years and those that do not).

Using the 50% cut-off determined from Bin 3 we can examine how the fractional contribution (from galaxies with emission stronger than 30Å) to the total SFRD in each bin varies as we step through the sample, at either constant magnitude or constant redshift.

To this end, the fractional contribution in each bin from galaxies with emission stronger than 30Å is tabulated in Table 4.2. The values cannot be easily verified by inspection of Figure 4.7 because of the way in which the curves in the figure are produced: Each curve is made by dividing the bin into 25 slices in equivalent width and there is therefore no guarantee that any single division falls exactly at 30Å. Instead, the fractional contribution from above 30Å is calculated explicitly using a separate routine.

Discussion

We begin by examining the evolution in giant galaxies (bins 1, 2, 3 and 4). As one moves to lower redshift there is a clear decrease in the contribution to the SFRD from galaxies with large (> 30Å) equivalent widths. In bin 1 in particular, only $\sim 15\%$ of the total SFRD comes from such galaxies. Contrast this to the situation in bin 4 in which $\sim 58\%$ of the total SFRD is from emission stronger than 30Å. We already know that there is a decline in the SFRD from the brightest galaxies (Figure 4.4), but the results here show that the fraction of rapidly star forming, luminous galaxies drops *on top* of the general decline. Bins 2 and 3 also support this conclusion, showing a decreasing fractional contribution from large equivalent width galaxies with decreasing redshift.

Of course, there is a selection effect to consider here, since it is easier to obtain a redshift for a galaxy with a large equivalent width. The weighting scheme should however account for this effect.

At lower luminosity, bins 5, 6, and 7 show a similar trend, although the evolution appears to be somewhat less intense than for bins 1, 2, 3 and 4. Certainly the fractional contribution to the SFRD in a bin from galaxies with large equivalent widths drops between bins 5 and 6. Comparing bins 1 and 2 with bins 5 and 6 however, we see that over the same redshift interval it is the brighter galaxies that evolve more strongly (contrast this with the evolution of absolute SFRD, discussed in Section 4.3.1). They show a change in fractional contribution of ~ 0.21 (bin 2 $-$ bin 1) compared to ~ 0.17 (bin 6 $-$ bin 5). This can be verified from the numbers in Table 4.2. The suggestion is, that while giant galaxies change quite markedly over the cosmic time between $0.2 \lesssim z \lesssim 0.4$, the lower luminosity galaxies change in a more leisurely evolution.

Hammer et al. (1997) find a similar result for bright galaxies in their analysis of ~ 400 galaxies from the CFRS (Lilly et al., 1995). In that study it is found that 62% of bright galaxies ($M_B < -20$) have strong (> 15Å) [O II] emission at high redshift ($0.45 < z < 0.7$), compared to only 34% of galaxies with the same luminosity, but lower redshifts ($0.15 < z < 0.45$).

We cannot say for certain what occurs over the magnitude range covered by bins 5 and 6 at the redshift of bin 7, because the survey's flux limit begins to affect the number of galaxies that are detectable. However, although bin 7 does not probe the lower luminosity

Bin number	B mag range		z range		Fractional Contribution from $EQW > 30$Å to SFRD in bin
1	−22.9	−21.0	0.18	0.30	0.15
2	−22.9	−21.0	0.30	0.40	0.36
3	−22.9	−21.0	0.40	0.55	0.51
4	−22.9	−21.0	0.55	0.67	0.58
5	−21.0	−19.0	0.18	0.30	0.49
6	−21.0	−19.0	0.30	0.40	0.66
7	−21.0	−19.0	0.40	0.55	0.58
8	−19.0	−17.5	0.18	0.30	0.79

TABLE 4.2: The fractional contribution to the total SFRD in each bin from galaxies with [O II] emission stronger than 30Å. The bin definitions are the same as those in Figure 4.4 and Table 4.1.

galaxies covered by bins 5 and 6 (Figure 4.4; Table 4.1) but nevertheless has almost the same fractional contribution from large equivalent width galaxies as does bin 6, it is therefore possible that the same strength of evolution occurs between bins 6 and 7 ($0.3 < z < 0.55$) as between bins 5 and 6 ($0.2 < z < 0.4$).

At constant redshift ($z \sim 0.25$; bins 1, 5 and 8), we see that as one steps to lower luminosities the fractional contribution from large equivalent width galaxies increases drastically, from only $\sim 15\%$ in giant galaxies (bin 1) to 70% in dwarfs (bin 8). It is already clear from Figure 4.4 that the largest contributors to the universal SFRD at $z \sim 0.25$ are low luminosity dwarf galaxies, here however we are adding to that statement: the galaxy types with the highest fraction of rapid star formers at low redshift are dwarfs.

The same trend is also confirmed from bins 2 and 6: lower luminosity galaxies have the highest fraction of rapid star formers.

We can compare the change in the fractional contribution from large equivalent width galaxies between bins 1 and 5 to the change between bins 2 and 6. This corresponds to a magnitude difference of ~ 2 between the centres of the bins. The redshifts at the bin centres are $z \sim 0.25$ and $z \sim 0.35$ for bins 1 and 5 and bins 2 and 6 respectively. Computing (bin 5 − bin 1) gives a change of 0.34 while (bin 6 − bin 2) gives 0.30. We see that there is a larger difference in the fraction of rapidly star forming galaxies between the two luminosity bands at lower redshifts.

Finally we note from this Figure that the majority of bins have a 50% contribution to their SFRD coming from galaxies with emission weaker than 30Å equivalent width. This means that narrow band imaging surveys sensitive to only large equivalent width galaxies are generally missing most of the star formation at those epochs.

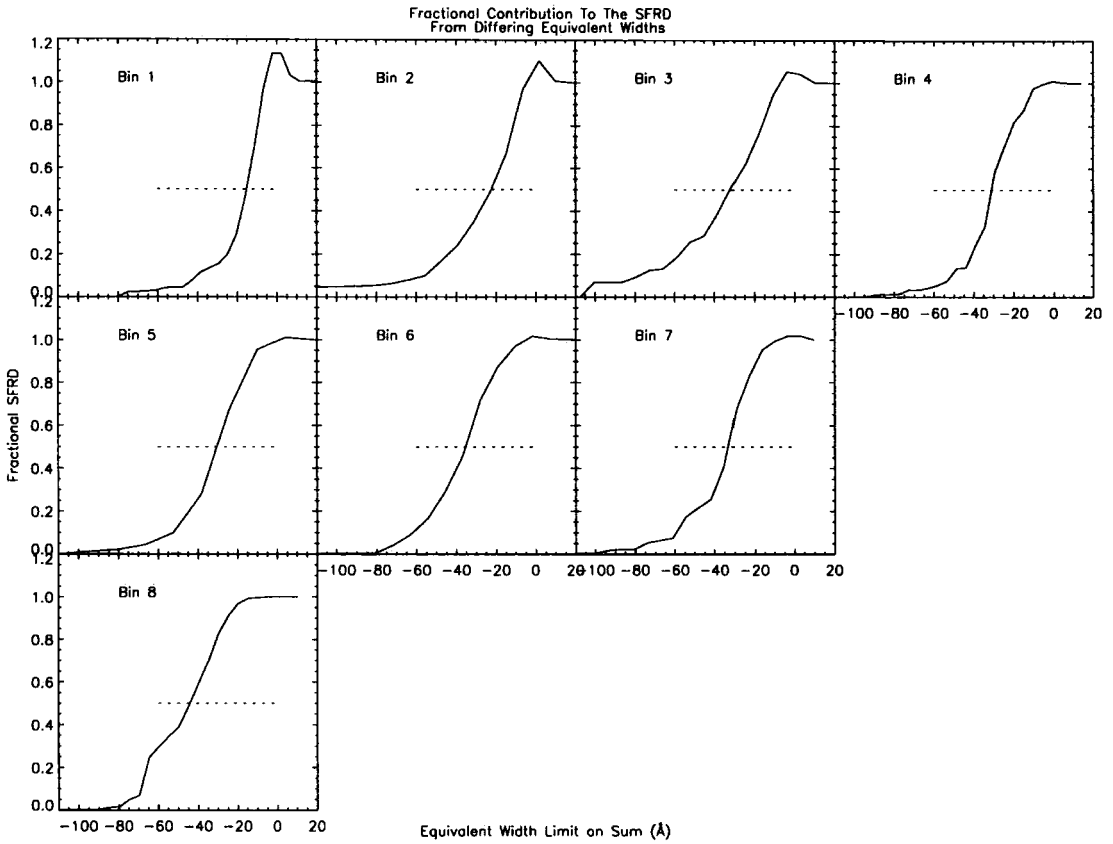

FIGURE 4.7: The fractional contribution to the total SFRD in each bin from galaxies whose equivalent width is stronger than the x-axis value. The bin numbering refers to the scheme in Figure 4.4. The dashed line marks the 50% contribution level. It is clear that at least 50% of the SFRD in most bins comes from galaxies with emission below 30Å equivalent width. This means that emission line or narrow band surveys that are only sensitive to large equivalent widths may miss a substantial fraction of the SFRD. Note the bumps in each of the curves that pass above the 100% complete level and then return to it. These exist because we include galaxies with apparent negative SFRs in the sum. See text for additional comments.

4.3.4 Comparison to Cowie et al. (1996)

Figure 4.8 shows plots similar to those presented by Cowie et al. (1996) (the original Cowie et al. plots are shown in Figure 4.2). Shown in Figure 4.8 is the distribution of [O II] equivalent width as a function of restframe absolute B_{AB} magnitude, for each redshift band that was defined in Figure 4.4 and Table 4.1.

The blue points show galaxies with equivalent width stronger than -30Å; the black points show the other galaxies whose emission is weaker than this limit. The mean B_{AB} magnitude of galaxies with strong [O II] emission (blue points) is shown by the dot-dashed line in each plot. The point of this plot is to test if the mean magnitude of such galaxies evolves as one steps to decreasing redshift.

In the downsizing framework, the characteristic magnitude of a rapidly star forming

galaxy should show a smooth drop off with redshift, with star formation activity moving from bright galaxies at high redshift to faint galaxies at low redshift. This suggests that the bright galaxies form their stars first with the fainter galaxies following as time goes on. The evolution of mean magnitude is seen clearly in the figure, as the dot-dashed line shifts from ~ -22 in the $0.55 < z < 0.67$ bin to ~ -19.5 in the $0.18 < z < 0.3$ bin.

A statistical test confirms this visual result: there are significant differences between the four mean magnitudes. An ANOVA test was conducted on the data and the resulting probability of the null hypothesis (i.e. that there is no difference between the mean magnitudes) being incorrect was found to be 99.99%.

Although there are some differences between the plots of Cowie et al. and those presented here, the general downsizing trend is still observed. One difference is that Cowie et al. have only one bin devoted to the entire redshift range covered by the CNOC2 Survey. Also, the Cowie et al. plots are made using the K-band restframe magnitude, not the B-band. The K-band is believed to be a better tracer of underlying stellar mass in galaxies, whereas the B-band will be more sensitive to recent star formation activity (note that K-band magnitudes are not available for all CNOC2 galaxies, despite several observing campaigns).

4.3.5 The Characteristic SFR of a Fixed Brightness Galaxy

We have seen how the mean magnitude of rapidly star forming galaxies varies with redshift. An alternative way of examining the data is to see how the SFRs of galaxies of a fixed brightness evolve with redshift. To this end, Figure 4.9 shows how the characteristic (mean and median) SFR of galaxies of a fixed brightness change with redshift.

The figure was produced as follows:

- The distribution shown in Figure 4.4 was cut into four separate divisions in magnitude (note that these *are not* the same as those shown in Figure 4.4).
- Each of the magnitude divisions was then sub-divided into 7 bins in redshift (again, these *are not* the redshift bins shown in Figure 4.4).
- After the division in magnitude and redshift, the mean and median SFR of galaxies in each magnitude-redshift bin was computed.

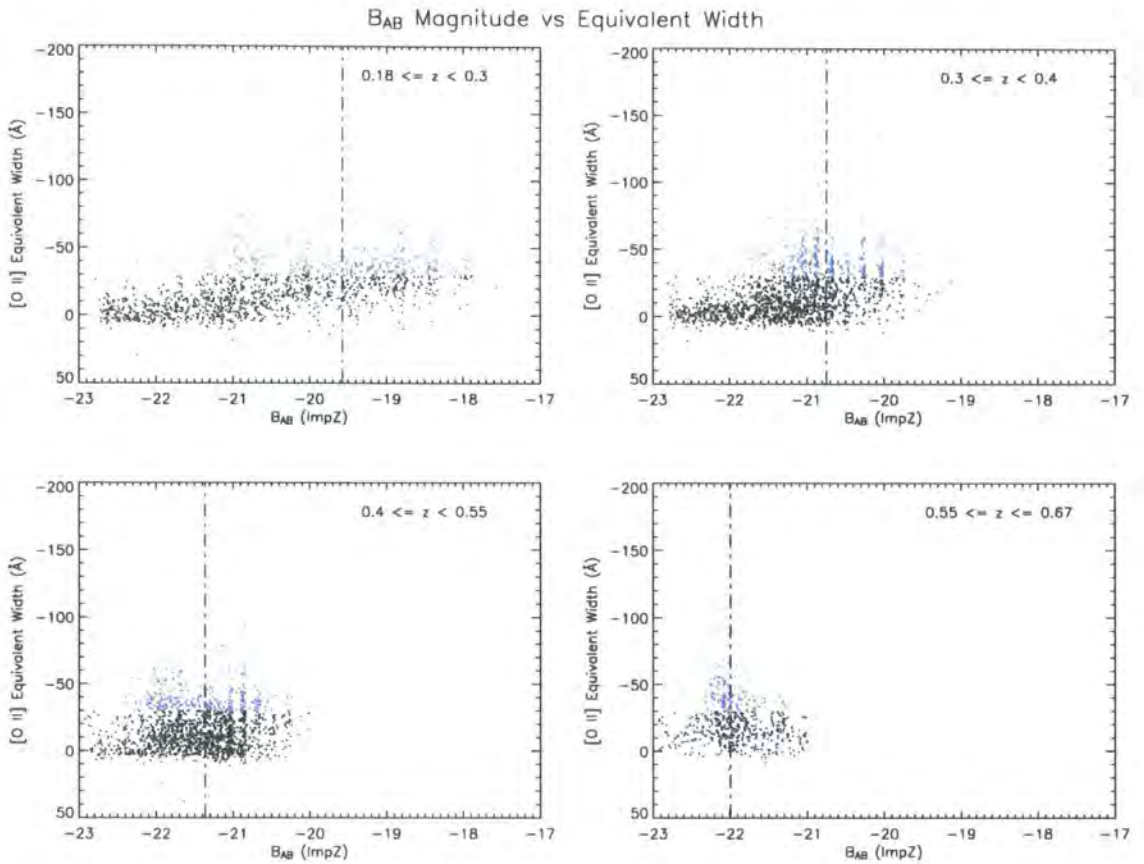

FIGURE 4.8: Plots of B_{AB} magnitude vs [O II] equivalent width in the style of Cowie et al. (1996). The four plots refer to the four redshift divisions defined in Figure 4.4 and Table 4.1. The data in each plot is split into rapidly star forming galaxies and non-rapidly star forming galaxies at the 30Å cut-off defined in Section 4.3.3. The mean magnitude of the rapidly star forming galaxies is plotted as the dot-dashed line. There is a clear evolution of this quantity with redshift, demonstrating the downsizing effect in which mean magnitude of a star forming galaxy shifts to fainter magnitudes at lower redshifts.

These mean and median values are shown on the Figure, as it the linear best-fit to the data; note that no weighting scheme has been used here.

There is no additional evidence for downsizing in this Figure. Indeed, at first inspection it appears that the figure does not support the downsizing scenario since there is no perceivable difference in the shape of the SFR-z relation between any of the magnitude bands. This result appears to be in conflict with Figure 4.8, however it is important to note a key difference between the two. Figure 4.8 shows the evolution of the mean magnitude of rapidly star forming galaxies *only*, while this figure shows the mean SFR of all galaxies in a fixed brightness band; i.e. both high and low star formation galaxies are included in the production of Figure 4.9, while only high equivalent width galaxies enter the analysis in Figure 4.8.

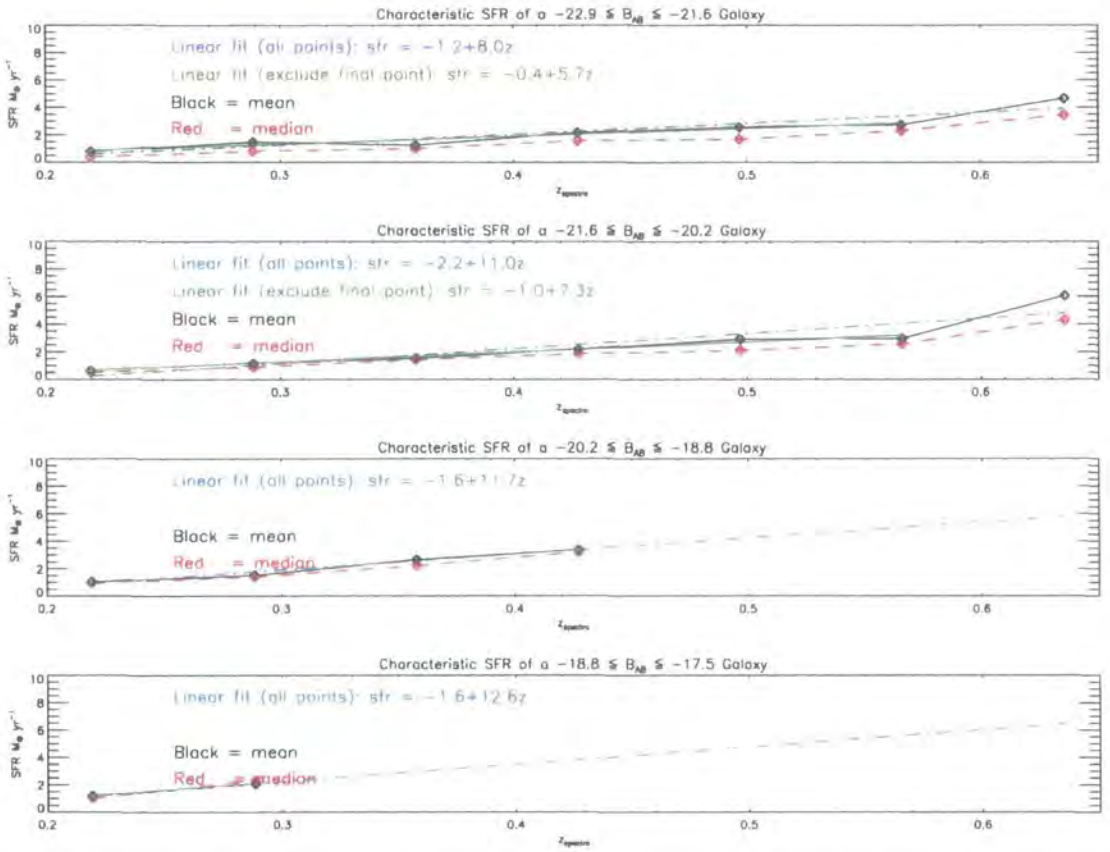

FIGURE 4.9: The characteristic (mean and median) SFR of galaxies of a fixed brightness as a function of redshift. The production of the Figure is described in the text (Section 4.3.5). A general decline in all magnitude bands is visible however there appears to be little difference in the shape of the decline between bands.

In relation to the work of Juneau et al. (2005), this figure is not in direct agreement with that study. They show that the evolution of cosmic SFRD has a dependence on galaxy mass such that massive galaxies ($M > 10^{10.8} M_{\odot}$), intermediate mass galaxies ($10^{10.2} M_{\odot} < M < 10^{10.8} M_{\odot}$) and low mass galaxies ($M < 10^{10.2} M_{\odot}$) evolve differently between $1 < z < 2$; this clearly supports the downsizing principle. We do not have any mass information for the CNOC2 galaxies, nor do we cover the $1 < z < 2$ redshift range, however, if we assume that the B_{AB} luminosity is linked directly to galaxy mass then we find that the SFRs of CNOC2 galaxies do not show different evolutions as a function of mass (again it must be noted that this can only be stated if one makes that assumption that there is a direct link between B_{AB} magnitude and galaxy mass).

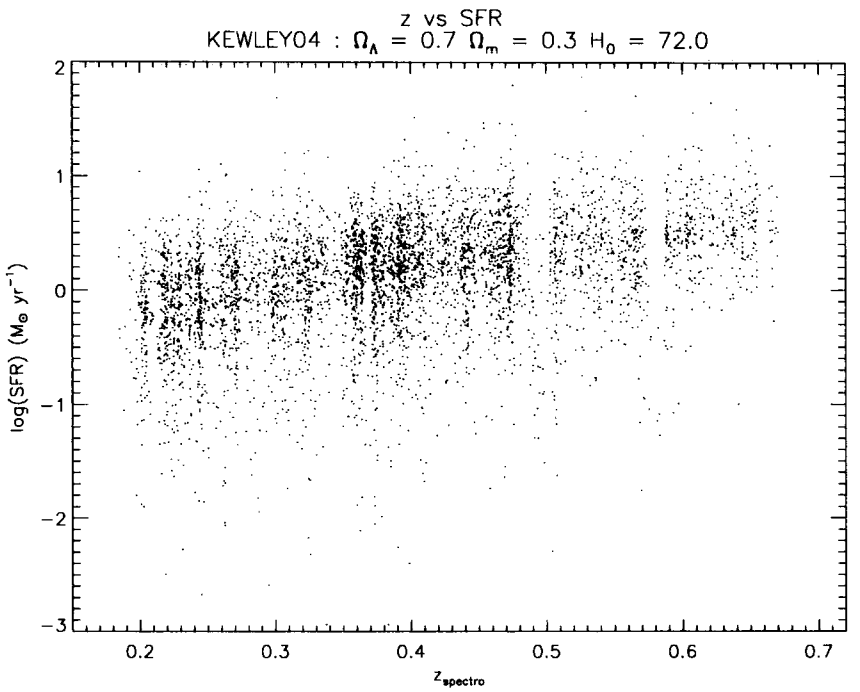

FIGURE 4.10: The distribution of the log of SFR vs spectroscopic redshift for all galaxies in the sample with a positive measured SFR.

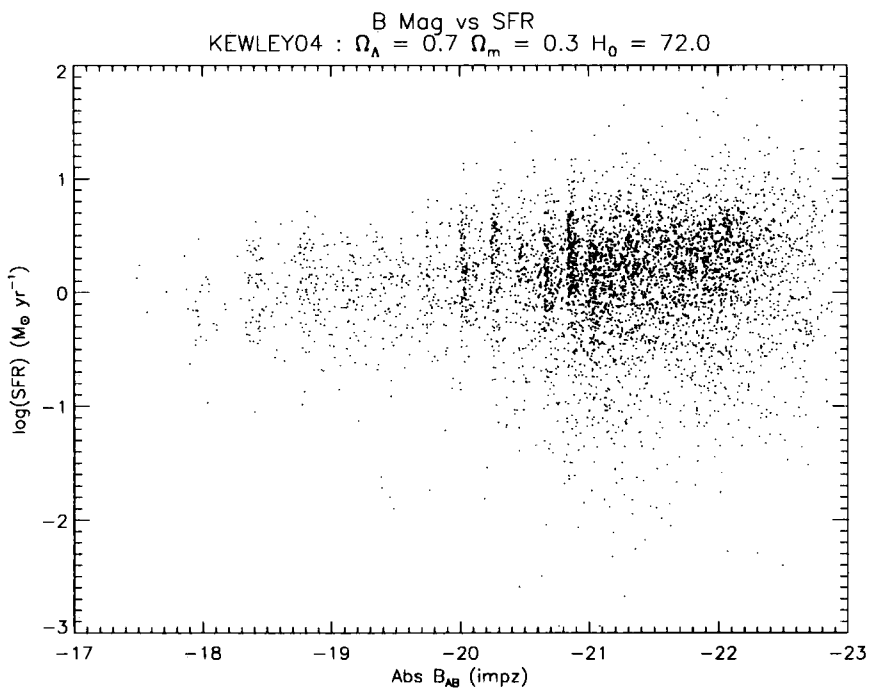

FIGURE 4.11: The distribution of the log of SFR vs B_{AB} magnitude for all galaxies in the sample with a positive measured SFR. There is a clear lack of galaxies with low luminosities but high SFRs. There do exist however, bright galaxies with large SFRs; these cannot be elliptical galaxies.

4.3.6 General Dataset Overview Plots

Star Formation Rate vs Redshift

Figure 4.10 shows the distribution of the log of the SFR vs spectroscopic redshift for every galaxy in the sample with a positive measured SFR. Galaxies that are measured to have apparent negative SFRs are not plotted. The study of high-SFR galaxies from this sample is being continued. Three IMACS IFU observations of such galaxies have been conducted and the data are being reduced. The aim is to observe the superwind outflows, thought be be a likely result of the star formation process.

The overall trend to lower SFRs with redshift is readily apparent and real, although proper use of the statistical weights has been needed to prove this.

Star Formation Rate vs Absolute Magnitude

Figure 4.11 shows the distribution of the log of SFR vs B_{AB} magnitude for every galaxy in the sample with a positive measured SFR. Galaxies that are measured to have apparent negative SFRs are not plotted. There is a distinct lack of high SFR galaxies at low luminosities. The upper envelope of the distribution appears to show that the SFR of individual galaxies is in some way related to their intrinsic brightness. Note the population of bright, high SFR galaxies. These might be luminous spiral galaxies.

Equivalent Width vs Redshift

Figure 4.12 shows the distribution of equivalent width vs redshift for all galaxies included in the final sample. There are no stark trends or areas of avoidance visible in the plot, although there appears to be a paucity of very high equivalent width ([O II] $>$ 100Å) galaxies at high redshift. It is difficult to determine if this is a genuine effect due to the small numbers of such objects in the sample.

Figure 4.13 shows the distribution of mean [O II] equivalent width vs redshift for various galaxy populations within the $-19 < B_{AB} < -23$ range (this range corresponds to the bins 1–7, as defined in Figure 4.4 and Table 4.1).

The plot is constructed as follows:

- The population of galaxies in each bin is divided into high and low equivalent width according to the 30Å cutoff discussed in Section 4.3.3.

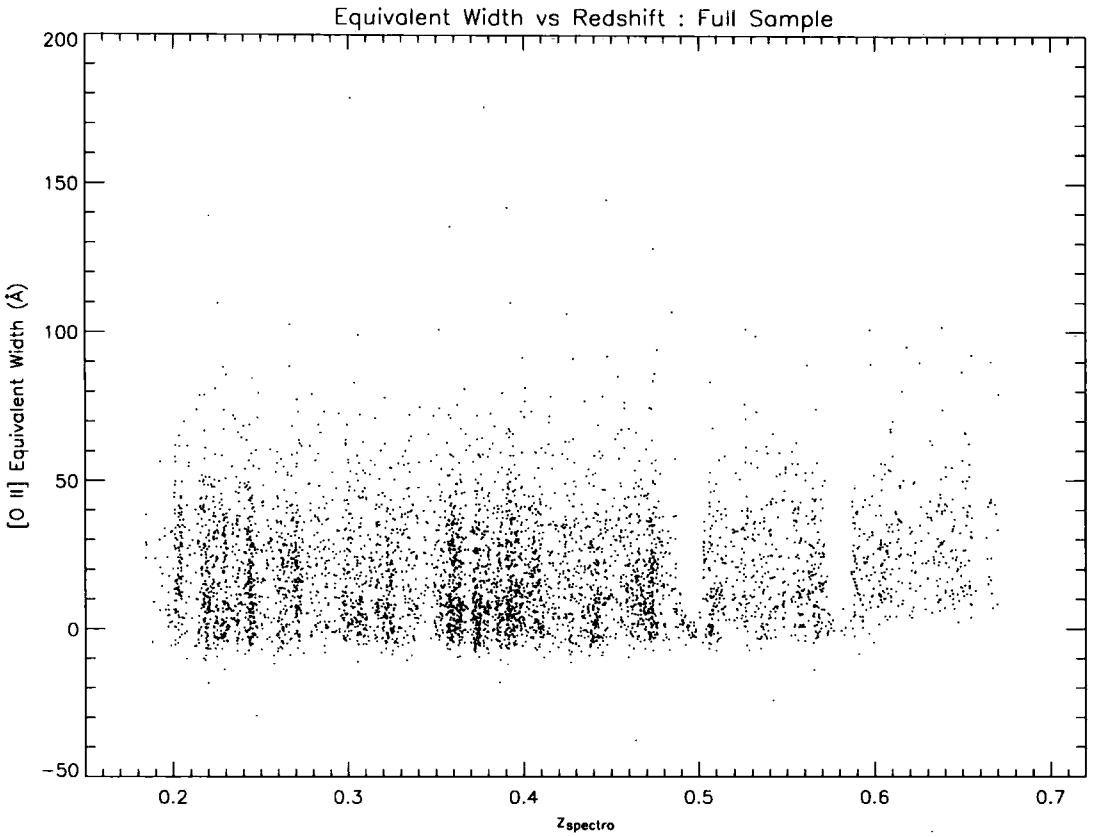

FIGURE 4.12: The distribution of equivalent width vs redshift for all galaxies in the survey.

- The mean of each sub-population is then computed and plotted at the redshift of the bin centre.
- Blue lines correspond to the magnitude range $-21 < B_{AB} < -23$ and red to the range -19 $< B_{AB} < -23$.
- The solid and dot-dashed lines denote the galaxies with strong or weak [O II] emission respectively.
- Also plotted in the figure are the means of all galaxies within a bin, irrespective of their [O II] properties (denoted by the black lines labelled 1 and 2).

Several trends are visible. Firstly it is evident that the mean equivalent width of galaxies with strong [O II] emission does not change considerably with redshift. This appears to be true for both the bright and faint sub-samples (see the blue and red solid lines in the figure). A statistical test confirms that this is the case: an ANOVA test returns the probability of no difference between the means for bright galaxies to be 38% (and 67%

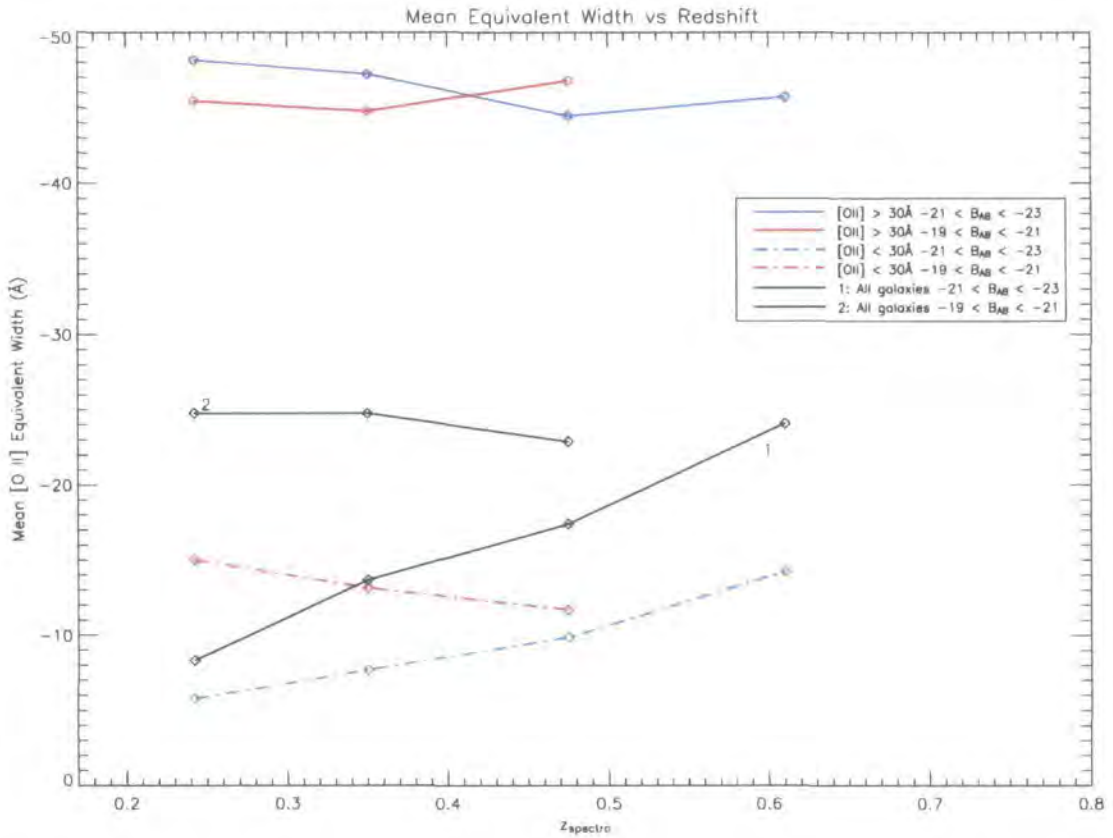

FIGURE 4.13: Mean equivalent width vs redshift for magnitude-redshift bins $1-7$. The very little evolution seen in the high equivalent width galaxies over this redshift range matches with the findings of Hammer et al. (1997) from the CFRS.

for faint galaxies).

A comparison can be made to the CFRS data examined by Hammer et al. (1997). In that work, very little evolution of the mean equivalent width from galaxies with emission stronger than 15Å is seen across redshifts $0.4 < z < 0.875$. We can confirm that a similar result holds with this data across the range $0.2 < z < 0.6$ and a cutoff of 30Å. Unfortunately, the redshift range covered by CNOC2 does not allow us to compare to the CFRS data at higher redshift.

The lack of evolution in high equivalent width galaxies in both bright and faint galaxy populations is interesting. It suggests that the evolution in the global SFRD is brought about by changes in the low equivalent width population. Indeed, if we consider the evolution of low equivalent width galaxies (the dot-dashed lines in the figure) then we see considerable evolution across the redshift range. A second ANOVA test reveals the changes are genuinely significant (the probability of significant difference was found to be

$> 99.99\%$ for both the bright and faint sub-samples).

The bright sub-sample shows a steady decline over the whole redshift range while the faint sub-sample actually shows an increase. It is noted however that the highest redshift point for the faint sub-sample comes from bin 7, which (as can be seen in Figure 4.4), does not extend down to $B_{AB} = -19$. If the data did extend that far, it is likely the mean from the bin would be higher and hence the data would be consistent with a gradual decline from high redshift. We are unable to say for certain.

Our two conclusions from this figure are that for bright galaxies ($-21 < B_{AB} < -23$) the decline in global SFRD is driven by the evolution of the low equivalent width population and that a different mechanism must act on the low equivalent width galaxies than acts on the high equivalent width galaxies because the shape of the decline in each population is different.

The first of these conclusions matches with the findings in Section 4.3.3 (Figure 4.7) where we showed that the fractional contribution from the highly star forming population to the total SFRD from bright galaxies has declined with redshift.

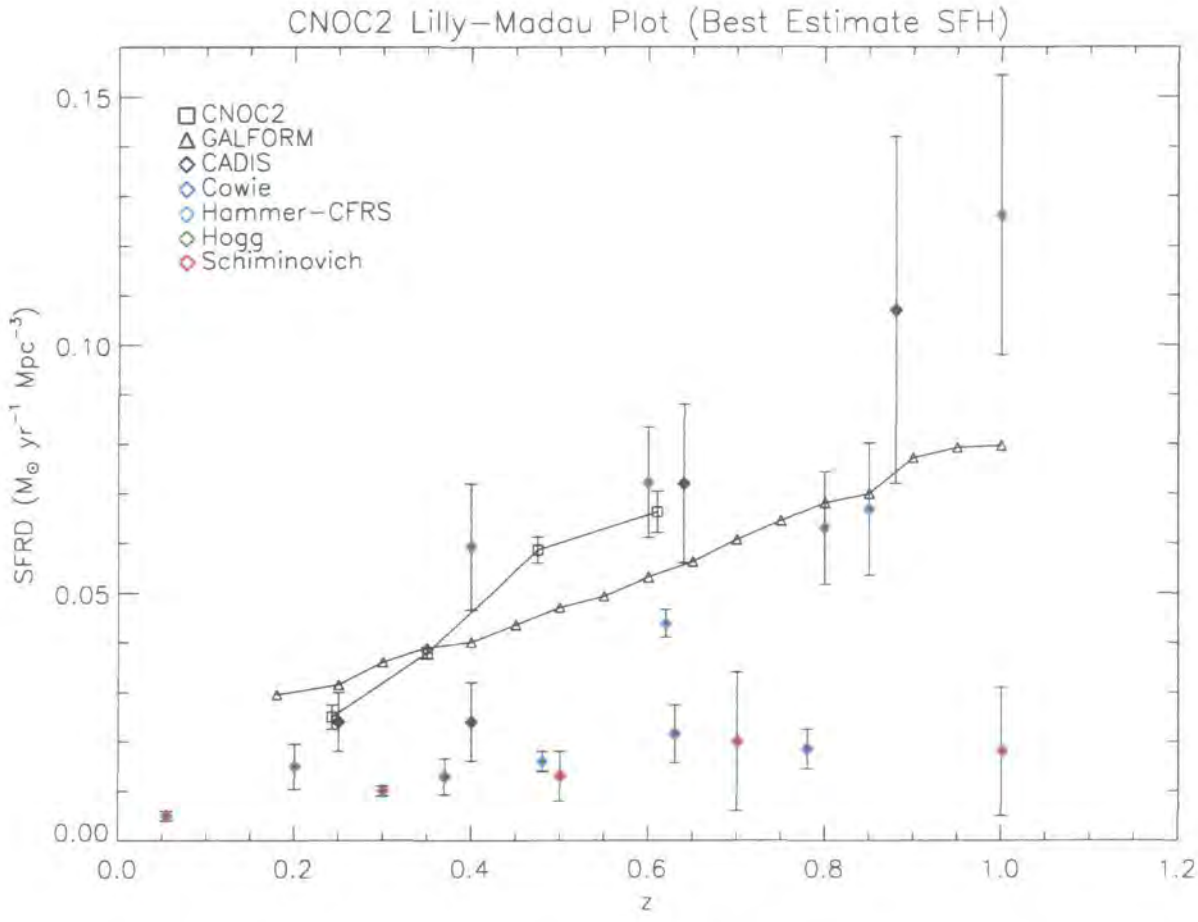

FIGURE 4.14: The CNOC2 Lilly-Madau plot. Shown in the Figure is the evolution of the total SFRD of the Universe as a function of redshift. Various studies are shown, including the results from this thesis (CNOC2, black squares) and the results from the Baugh et al. (2005) Galform models (black triangles). Also shown are the results from CADIS (black diamonds, Hippelein et al., 2003), those of Cowie et al. (1999, blue diamonds), those of Hammer et al. (1997, light blue diamonds), those of Hogg et al. (1998, green diamonds) and those of Schiminovich et al. (2005, red diamonds). The error bars on the CNOC2 measurements are formed from the quadrature sum of the bootstrap errors on the individual bins from Figure 4.4, which were summed together to form the total SFRD at each redshift. See text for additional discussion about the construction of this Figure.

4.3.7 Lilly-Madau Plot and Best Estimate SFH

No analysis of the evolution of the Universal SFRD would be complete without the presentation of a Lilly-Madau plot.

The Lilly-Madau plot for the CNOC2 data analysed in this thesis is therefore presented in Figure 4.14.

An important problem is encountered when constructing this type of plot: How is it possible to correct for the unobserved faint galaxies at high redshift? This question plagues all studies in this field and none are free from it.

A method employed by many authors is to use the luminosity function to correct for unobserved galaxies. The idea is to construct [O II] luminosity functions are various different redshift intervals and then integrate under them to give the total [O II] luminosity density at those particular epochs. The luminosity densities are then converted into a SFR using a standard conversion factor and these values are used in the Lilly-Madau plot.

The method is reasonable, at least in principle, at low redshifts where it is possible to observe faint galaxies. At higher redshifts, it is not possible to observe the faint galaxies and so the fit to the luminosity function relies exclusively on bright galaxies. Bright galaxies can only constrain one end of the fit and it is therefore simply impossible to determine the shape of the faint end of the luminosity function based on information from bright galaxies alone. SFRDs computed in this way are susceptible to errors arising from this problem. In light of this, we do not adopt this method in correcting for unobserved galaxies.

Instead, the Lilly-Madau plot in Figure 4.14 is formed using our best estimate for the evolution of the total SFRD, which is based on the results derived thus far in this thesis; the method is explained below.

From Sections 4.3.3 and 4.3.1 we know the following:

- The absolute SFRD from giant galaxies ($-21 < B_{AB} < -23$) has declined between redshifts $0.2 \lesssim z \lesssim 0.6$.

- The fractional contribution to the total SFRD from giant galaxies that comes from strongly star forming galaxies ([O II] emission > 30Å) has dropped over the same redshift range.

- At lower luminosities a similar trend is seen, with the same drop in the fractional contribution of strongly star forming galaxies to the SFRD. The decline is less severe for these lower luminosity galaxies than for giants however (Section 4.3.3).

These results points towards the idea that giant galaxies have evolved more strongly with redshift than dwarfs.

If this trend continues to very low luminosity galaxies then it could be true to say that dwarf galaxies have evolved very little indeed since $z \sim 0.6$. Of course, with the data presented here we are unable to observe what is actually occurring in dwarf galaxies beyond a redshift of $z \sim 0.25$. However, based on the above findings – that lower luminosity galaxies appear to evolve more leisurely than giants – our best estimate for the evolution of the SFRD in dwarf galaxies is to assume that they do not evolve at all, but remain as we see them at $z = 0.25$, out to $z = 0.6$ at least.

This means the empty bins along the base of Figure 4.4 (numbered 9, 10 and 11) each can be assumed to take on the value of bin 8 for their SFRD.

Two empty bins on Figure 4.4 remain, these are the bin directly below bin 7 in magnitude (bin 12), and the bin directly adjacent to bin 7 at higher redshift (bin 13). For these two bins we use multiples of the value in bin 7. The smaller bin (bin 12) is assigned the same SFRD as bin 7 (because it covers the same magnitude range), while the larger, higher redshift bin (13) is assigned twice the SFRD in bin 7 (because it covers twice the magnitude range).

Once we have assigned SFRDs to the empty bins, the Lilly-Madau Plot in Figure 4.14 is then formed by summing all the SFRDs of Figure 4.4 in the magnitude direction. By definition, the SFRD refers only to galaxies with B_{AB} brighter than -17.5 mag.

While the above method does not guarantee that we have correctly taken account of the unobserved, faint galaxies, it is based on an extrapolation of trends observed in the data and not on a potentially ill-constrained fit.

Discussion

The SFRD measurements from this thesis are shown as the open squares on Figure 4.14. The data show a uniform rise in SFRD from redshifts $z \sim 0.25$ to $z \sim 0.475$, followed by what seems to be a turn-over in the evolution at $z \sim 0.6$. It is interesting that we do

not observe a continual, steep rise over the range $0.2 \lesssim z \lesssim 0.6$, as has been reported by several authors.

Our data agree well with the overall shape of the first three points of Hogg et al. (1998), with the note that the redshifts of the points are not the same. That dataset extends to higher redshift so we are not able to compare beyond those three points.

Recall that the highest redshift CNOC2 data point ($z \sim 0.6$) is subject to a large uncertainty, resulting from the redshift weights, S_z. It is likely that this point is overestimated by $\sim 36\%$ (Section 4.3.1) and should therefore lie at a lower SFRD. This would imply the evolution of SFRD was slower at higher redshift, only increasing in ferocity as we move nearer to the present day.

The CADIS results of Hippelein et al. (2003) suggest an exponential evolution in SFRD, with the strongest evolution occurring at higher redshift (these results are also shown on Figure 4.14). Note that they use several indicators (including [O II]) to trace the SFRD. The CNOC2 points do not agree with their conclusion over the redshift range of overlap ($0.2 < z < 0.6$).

The Schiminovich et al. (2005) results from the Galex Satellite show a very different evolution of the SFRD with redshift than that measured by this thesis. Since the Schiminovich et al. data is from the UV, and is uncorrected for reddening, the difference most likely reflects the effects of dust. This highlights the need to understand the reddening correction if using UV data.

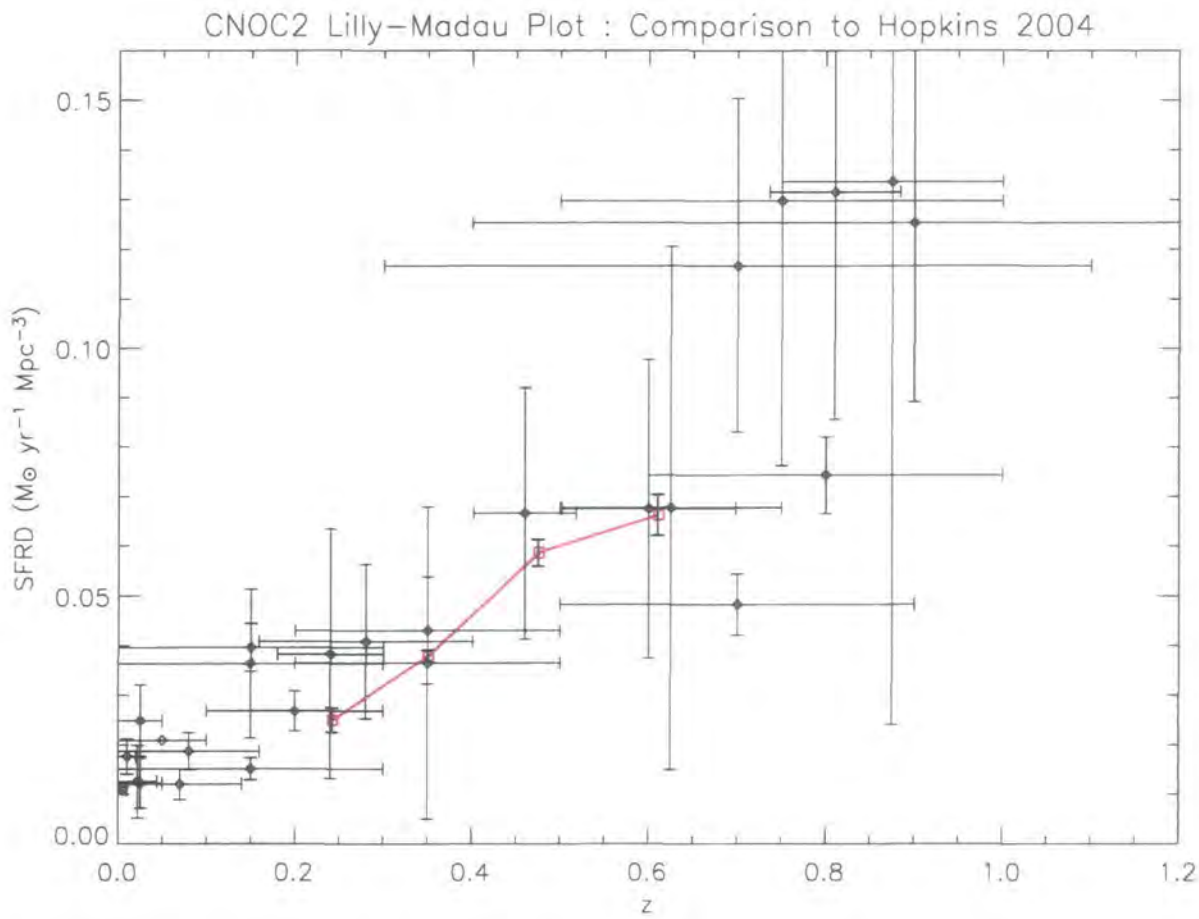

FIGURE 4.15: The CNOC2 Lilly-Madau plot in comparison with the data from Hopkins (2004), which includes measurements from the optical, infra-red, radio and X-ray, all corrected for dust extinction. The CNOC2 data points are shown in red.

Comparison to Hopkins (2004) Data

In recent times the largest compilation of SFRD data from the literature has been made by Hopkins (2004). The data from that paper comprise measurements from the optical, infra-red, radio and X-ray, all corrected for dust extinction.

Figure 4.15 shows the CNOC2 Lilly-Madau plot in comparison to the data from Hopkins (2004). The CNOC2 points are in general agreement with all the data shown, however the most notable feature of the CNOC2 results is the apparent turn-over at $z \sim 0.6$. This lies well inside the region spanned by other results at that redshift, but suggests a much flatter SFRD thereafter, whereas the other data is consistent with a uniform increase.

The question remains as to what drives the decline in SRFD. Given our results from Figures 4.8 and 4.9 we know that there is a contribution from the change in the average SFR per galaxy. This does not rule out any contributions from mergers however. Indeed Figures 4.7 and 4.13 may actually support the idea of mergers: they show that the fractional contribution from highly star forming giant galaxies, to the SFRD from giants, has declined with redshift but also that the mean properties of those highly star forming galaxies have not changed significantly. This can be explained if we assume that there are different numbers of such galaxies at different redshifts, thus lending support to the idea that mergers affect the SFRD (see e.g. Conselice et al. 2003).

Comparison With Galform

Galform (Cole et al., 2000) is semi-analytic galaxy formation code that can predict the properties of galaxies as a function of redshift. Using the updated Galform models of Baugh et al. (2005) we are able to predict the SFRD as a function of cosmic epoch. The Galform prediction for the evolution of the SFRD is shown on the Lilly-Madau plot in Figure 4.14. We now describe how the Galform SFRDs were computed. The models were run by Dr. C. Baugh of the University of Durham, however all the analysis presented here has been undertaken by myself.

Galform is capable of outputting many parameters relating to a simulated halo, at any desired redshift. Quantities of interest for this analysis are the following, the halo weight (W_g), the mass of the halo (M_h), the disk star formation rate ($\dot{M}_*$), the mass of stars formed in the last burst (M_b), the time since the last burst (t_b), and the e-folding

z	0.18	0.25	0.30	0.35	0.40	0.45	0.50	0.55	
SFRD	0.0295	0.0316	0.0361	0.0389	0.0401	0.0436	0.0471	0.0494	
z	0.60	0.65	0.70	0.75	0.80	0.85	0.90	0.95	1.00
SFRD	0.0532	0.0562	0.0607	0.0645	0.0682	0.0700	0.0772	0.0793	0.0797

TABLE 4.3: Galform outputs: redshifts and SFRD in units of $M_\odot\,yr^{-1}\,Mpc^{-3}$. The SFRDs are computed as described in the text.

time for the burst (t_e). The output redshifts were set to be the minimum redshift of the CNOC2 dataset ($z = 0.18$), followed by steps of 0.05 in redshift, beginning at $z = 0.25$. The output redshifts and total SFRDs can be seen in Table 4.3.

We chose to use all halo masses output by Galform when computing the SFRD, and do not limit ourselves to a subset, as might want to be done to isolate galaxy groups or the like. This is because we are interested in the global evolution of the SFRD. Having selected which halos to use, we then proceed as follows.

- For each halo at each redshift we determine if the halo is undergoing a burst of star formation. This is set by the requirement that the time since the last burst is less than 3 e-folding times of the burst timescale. Bursting halos therefore satisfy the condition

$$t_b < 3 \times t_e. \tag{4.10}$$

- The Baugh et al. (2005) model uses two separate IMFs to model star formation, depending on whether the star formation is quiescent or from bursts. For those halos which are undergoing a burst, we compute the burst SFR, SFR_b, according to the equation

$$SFR_b = 10^{-9} \times M_b \times \frac{1}{t_e} \times exp(-t_b/t_e). \tag{4.11}$$

  The burst SFR for those halos that do not satisfy Equation 4.10 is set equal to zero.

- The quiescent SFR, SFR_q, is computed for all halos according to the equation

$$SFR_q = 10^{-9} \times \dot{M}_*. \tag{4.12}$$

- The total SFR of a halo at every redshift is finally computed by summing together the quiescent and burst contributions, as follows

$$SFR_{total} = SFR_q + SFR_b. \tag{4.13}$$

- Finally, we compute the SFRD at each redshift by multiplying each halo's total SFR by its Galform weight, W_g,

$$SFRD = \sum_i SFR_{total,\ i} \times W_{g,\ i}, \tag{4.14}$$

where the sum, i, runs over all halos at a given redshift. Note that the Galform weights are related to the space density of each halo, and hence their use in the above equation yields the SFRD.

From Figure 4.14 we can see a reasonable agreement between the Galform results and those of this thesis. There are no data points in disagreement at a greater than 3σ level. However, it must be noted that the shape of the evolution reported by Galform differs substantially from that measured here. Galform shows an almost linear increase in SFRD with redshift up to $z = 1$, and does not show the sharp rise followed by an apparent slowing that we see in CNOC2. It must also be noted however, that the significance of this result is not quantified.

5

Conclusions

5.1 Conclusions

In this thesis we have measured the evolution of the SFRD of the Universe over the redshift range $0.2 \lesssim z \lesssim 0.6$ using data from the CNOC2 Survey.

We have reviewed the various SFR indicators available in the literature and shown quantitatively that [O II] can provide a very similar measure of the SFR to that given by the Hα line (Chapter 1).

We have explained the purpose written measurement code that was used to obtain line flux measurements and errors from the CNOC2 sample. We have also explained how the line measurement errors have been scaled to account for systematic underestimation. This leaves them very well quantified (Chapter 2).

We have conducted tests in the accuracy of the reddening estimates reported by photometric redshift codes, by comparing their predictions with measurements from the Balmer Decrement (Chapter 3).

The measurements of [O II] line flux have been combined with the reddening estimates from the photometric redshift code ImpZ to give individual galaxy SFRs. These have been used to measure the SFRD of the Universe in magnitude-redshift bins (Chapter 4).

The advantages of this study are numerous. They include: that it is a large sample over a redshift range across which the SFRD of the Universe is believed to change drastically; that we have used a dust correction specific to each individual galaxy; that the [O II] line flux measurement errors are very well quantified through repeat observations; that we adopt a statistically sound approach to dealing with apparently negative SFRs and that we do have some dwarf galaxy data and are not limited to examining only the brightest galaxies at all redshifts.

We have shown the following. The SFRD from giant ($-23 < B_{AB} < -21$) galaxies has declined by a factor of ~ 5.8 between $0.2 \lesssim z \lesssim 0.6$. We are able to observe slightly less luminous galaxies ($-21 < B_{AB} < -19$) between redshifts $0.2 \lesssim z \lesssim 0.4$ and these have also suffered a decline in SFRD. Between these redshifts ($0.2 < z < 0.4$) the SFRD from the less luminous galaxies has changed more than that of the giants (Section 4.3.1, Figure 4.4).

At redshift $z \sim 0.25$, dwarf galaxies ($-19 < B_{AB} < -17$) contribute the largest fraction of the total SFRD of the Universe. This is in-keeping with results from the local Universe (Section 4.3.1).

We have also analysed the variation of percentage contribution to the total SFRD from strongly star forming galaxies, in bins of luminosity and redshift. We have shown that, although the absolute SFRD in giants changes slower than the corresponding value for slightly less luminous galaxies, the fraction of giants that have strong (> 30Å equivalent width) [O II] emission, evolves faster than the corresponding fraction in $-21 < B_{AB} < -19$ galaxies (Section 4.3.3).

We have shown that at all redshifts covered by the Survey, a substantial fraction of the total SFRD is from galaxies with emission weaker than 30Å equivalent width. This implies that narrow band imaging surveys that are sensitive to only large equivalent width galaxies generally miss out on much of the star formation activity.

Comparing to the work of Cowie et al. (1999), the CNOC2 data do show evidence for downsizing in galaxies between redshift $0.2 \lesssim z \lesssim 0.6$.

We have compiled a Lilly-Madau plot using our best estimate for the evolution of the

cosmic SFRD. The global evolution seen in the CNOC2 data is consistent with a global increase in the SFRD with increasing redshift. The shape of the evolution observed in this thesis is however marginally different to many other studies, including the semi-analytic galaxy formation code, Galform. The significance of the different shape has not been quantified however (Section 4.3.7).

It is apparent that one must obtain data for dwarf galaxies if we are to ever constrain fully the evolution of SFRD with cosmic epoch. Future work in this field should focus on such a goal. In particular the Gemini Deep Deep Survey (e.g. Abraham et al., 2004) and the Vimos Deep Survey (e.g. Le Fèvre et al.) are working towards this. Concerning our own endeavours in this field, we have used a photometric redshift code in conjunction with CNOC2 photometry to select low luminosity, high redshift candidates for spectroscopy on the Very Large Telescope in Chile. These observations would push further down the luminosity function and hence enable a better quantification of the SFRD contribution from dwarf galaxies at high redshift.

A

Cosmology

In this appendix I present some of the basic principles of the current cosmological world model and the necessary formulae for computing cosmological distances and volumes from redshifts.

The cosmological world model is of importance when determining absolute Star Formation Rates (SFRs) of galaxies, since a given redshift corresponds to different luminosity distances in different models; this leads to a different inferred line luminosity and hence a different SFR. Cosmological volumes computed from redshifts also vary according to the world model, and so the absolute Star Formation Rate Density (SFRD) is affected by the cosmological parameters in the same way.

A.1 Expansion and Cosmic Background Radiation

A.1.1 The Hubble Law

In the 1920s Hubble famously discovered that the Universe was expanding (Hubble, 1929). By measuring the redshifts of galaxies of known distances, he noted that the ones farthest away from us were apparently moving away at a greater speed than those nearby. We now refer to this as the Hubble Law, in which cosmological distance (d), is linearly related to recession velocity (v) through the Hubble Constant (H_0).

$$v = H_0 d \tag{A.1}$$

The units of the Hubble Constant are $\mathrm{km\,s^{-1}\,Mpc^{-1}}$. The two distance units may be cancelled giving units of $\mathrm{s^{-1}}$; the inverse of the Hubble Constant therefore roughly gives the age of the Universe.

From the Hubble Law comes the idea of the Hubble Flow, whereby the distance between galaxies is increasing solely as a result of the expansion of the Universe, and not because of their individual (so-called peculiar) motions. Galaxies locked into the Hubble Flow are said to be co-moving.

Considering two co-moving observers, it is obvious that we can write the distance between them (d) as some fixed length (R_0) multiplied by some cosmic scale factor (a), which applies to the Universe as a whole. We know the Universe is expanding and so clearly a will be a function of time, increasing with the age of the Universe, so $d = R_0\, a(t)$.

The distance between co-moving observers grows by a factor $1 + H_0\, \Delta t$ per time interval Δt. This means that the scale factors at times t and $t + \Delta t$ are in the ratio $1 + H_0\, \Delta t$.

$$1 + H_0\, \Delta t = a(t + \Delta t)/a(t)$$

Therefore the Hubble Constant can be written as a function of the scale factor a.

$$H = \frac{1}{a}\frac{da}{dt}$$

Note that the Hubble Law is not altered through either rotation or translation of coordinates. To prove the second point we consider two observers, ourselves and an another astronomer on galaxy X. Galaxy X is at some distance r_x away from ourselves, moving

with the Hubble Flow such that $v_x = H_0 r_x$.

Astronomers on galaxy X measure the position and velocity of some other object relative to themselves such that $r' = r - r_x$ and $v' = v - v_x$. The velocity of that object, v', is given by

$$v' = H_0 r - H_0 r_x = H_0 (r - r_x) = H_0 r'$$

Hence proving that the Hubble Law is the same as observed at any point; note that there is no centre of expansion defined in the Hubble Law.

A.1.2 The Cosmic Microwave Background

In 1965 Penzias and Wilson discovered the Cosmic Microwave Background Radiation (CMB) by measuring excess radio noise in an antenna (Penzias and Wilson, 1965). The noise corresponded to a black body with temperature $T \sim 3.5$K and it was realised that this was actually the echo of the Big Bang which had been predicted years before.

Today we have modern measurements of the CMB from both the Cosmic Background Explorer (COBE, Smoot et al. 1991) and the Wilkinson Anisotropy Probe (WMAP, Bennett et al. 2003). These satellites place the temperature of the CMB to be $T = 2.735$K. The CMB is amazingly uniform across the sky with very tiny variations in temperature on the order of 11 parts per million, implying that the Universe was almost perfectly isotropic at that point in time.

Combining the CMB result that the Universe is isotropic (on large scales) with the idea that our location in the Universe is not in any way special, we arrive at the Cosmological Principle. This is often expressed in the statement "The Universe is homogeneous and isotropic".

A.2 Redshift, Geometry and Cosmological Parameters

A.2.1 Redshift

A direct consequence of the Universe expanding is that the light we observe from distant galaxies is redshifted to longer wavelengths. A spectral line emitted at some rest wavelength λ_{em} is observed at a longer wavelength λ_{obs}. Observationally we define the redshift

of a galaxy (z), to be as follows

$$1 + z = \frac{\lambda_{obs}}{\lambda_{em}}. \tag{A.2}$$

Defined in this way, the redshift includes the effects of peculiar velocities – i.e. those motions which result from gravitational interactions in addition to the motion from the Hubble Flow. We will show how redshift is related to the expansion factor of the Universe (a) below.

A.2.2 The Metric

The metric of an expanding space-time that has homogeneous and isotropic spatial sections is given by the Friedmann, Robertson and Walker metric.

$$ds^2 = c^2dt^2 - a(t)^2R_0^2\left(\frac{dr^2}{1-kr^2} + r^2[d\theta^2 + sin^2\theta\, d\phi^2]\right) \tag{A.3}$$

In this metric ds is the line element; c is the speed of light; $a(t)$ and R_0 retain their meanings from above; k is the curvature sign and r, θ and ϕ are the coordinates. Co-moving observers (those moving with the Hubble Flow) have constant r, θ, ϕ.

The physical meaning of redshift which we have defined above in equation A.2 can be derived from the above metric. We begin with a photon, following a geodesic in space-time and therefore $ds = 0$. Placing an observer at the origin furthermore means $d\theta = d\phi = 0$.

$$c\,dt = a(t)\,R_0\,dr/\sqrt{(1-kr^2)}$$

Integrating we find the following,

$$\int_{t_e}^{t_o} \frac{c\,dt}{a} = R_0 \int_0^{r_s} \frac{dr}{\sqrt{(1-kr^2)}},$$

where t_e and t_o are the time of emission and observation of the photon. r_s is the (?) which is fixed for co-moving coordinates. Since r_s is fixed, the right hand integral does not depend on time. Considering a second photon emitted at some later time, $t_e + dt_e$ and observed at $t_o + dt_o$ we then have the following.

$$\int_{t_e}^{t_o} \frac{c\,dt}{a} = \int_{t_e+dt_e}^{t_o+dt_o} \frac{c\,dt}{a}$$

This gives $dt_o/a(t_o) = dt_e/a(t_e)$. Since the emitted wavelength (λ_{em}) is proportional to dt_e and the observed wavelength (λ_{obs}) proportional to dt_o we have the following relation

$$\frac{a(t_o)}{a(t_e)} = \frac{dt_o}{dt_e} = \frac{\lambda_{obs}}{\lambda_{em}} = 1 + z. \tag{A.4}$$

A.2.3 Density Parameters

The geometry of the Universe is defined by four key parameters, the Hubble Constant (H_0), the density of matter in the Universe ($\Omega_{\rm M}$), the density of the so-called dark energy (Ω_Λ) and the curvature of space-time (Ω_k). The Hubble Constant has been defined above, the remainder of the parameters are now defined.

$$\Omega_{\rm M} \equiv \frac{8\pi\, G\, \rho_0}{3\, H_0^2} \tag{A.5}$$

$$\Omega_\Lambda \equiv \frac{\Lambda\, c^2}{3\, H_0^2} \tag{A.6}$$

We define Ω_k through the relation $\Omega_m + \Omega_l + \Omega_k = 1$.

In the above equations, ρ_0 is the mean density of the Universe at the present day, c is the speed of light and G is Newton's gravitational constant.

A.3 Cosmological Distances and Volumes

In this section I introduce the various cosmological distance and volume measures used in this thesis. In particular we require an understanding of the luminosity distance (for the calculation of SFRs), but we also need to know how a given redshift corresponds to a certain volume (for SFRDs), hence a knowledge of the volume element (dV/dz), is also important.

A.3.1 Co-moving Distance

The co-moving distance is the distance between two objects which remains constant with epoch if the objects are locked into the Hubble Flow. In other words, it is the proper distance (that measured with a hypothetical ruler) multiplied by the ratio of scale factors between the time of observation and now, i.e. $(1 + z)$.

To compute the Co-moving Distance we introduce the function $E(z)$ defined as

$$E(z) \equiv \sqrt{\Omega_{\rm M}\,(1+z)^3 + \Omega_k\,(1+z)^2 + \Omega_\Lambda} \tag{A.7}$$

where the symbols retain their meanings from the above section.

The co-moving distance is then given by

$$d_{\rm C} = \frac{c}{H_0}\int_0^z \frac{dz'}{E(z')} \tag{A.8}$$

A.3.2 Luminosity distance

The luminosity distance is the distance we use to compute SFRs of galaxies and is defined by the equation

$$F = \frac{L}{4\pi d_L^2}. \tag{A.9}$$

It is related to the co-moving distance (defined above) through the relation

$$d_L = d_C(1+z). \tag{A.10}$$

Because of the way in which it is defined, we use the luminosity distance to compute SFRs, not the co-moving distance.

A.3.3 Angular Diameter Distance

The Angular Diameter Distance is defined to be the ratio of an objects physical transverse size to its angular size in radians, i.e.

$$D_A = D/\theta. \tag{A.11}$$

It is related to the co-moving distance as follows

$$D_A = D_C/(1+z). \tag{A.12}$$

A.3.4 Co-moving Volume

The co-moving volume is defined in a similar fashion to the co-moving distance. It is the volume in which the number densities of objects which are locked into the Hubble flow does not change with epoch.

The co-moving volume to a certain redshift is computed by integration of the volume element, dV/dz, which is (see e.g. Hogg, 1999; Carroll et al., 1992)

$$dV = \frac{c}{H_0} \frac{(1+z)^2 D_A^2}{E(z)} d\Omega \, dz \tag{A.13}$$

Calculations of the comoving volume and the luminosity distance in this thesis are done using a code written by the author.

B

Physics of [O II] Emission

B.1 Atomic Processes in Nebular Gas

This thesis is concerned with charting the evolution of star formation rates in galaxies using the [O II] emission line as a diagnostic tool. An explanation of how the [O II] line itself is formed is therefore worthwhile. This appendix fulfils that need and explains the origin of [O II] emission from star forming galaxies and the physics underlying its formation.

The nebula gas surrounding young stars is seen in emission by astronomers. Many lines are observed in the optical, typically those of Hydrogen (Hα, Hβ), Nitrogen ([NII]) and Oxygen ([O II] and [O III]). The mechanisms for exciting these lines differ substantially and so to explain how the [O II] line is formed I begin by examining the different physical processes which occur in the nebular gas.

B.1.1 Excitation

Atomic interactions with photons, collisional excitations or electron-ion recombination are some of the methods through which an electron may find itself in an excited state within an atom.

For atomic interactions with photons, the energy of an incident photon may be used to promote an electron in a lower state to a higher level, although this requires that the photon energy be equal to that of an energy gap in the atom's structure. If the energy of the incident photon is sufficiently greater than the energy gap then the electron *may*[1] be removed from the atom and the species becomes an ion. Subsequent recombination of the electron with an ion will place the electron into a high energy state, from which it may decay, resulting in emission (see below).

Alternatively, in the process of collisional excitation, the physical interaction of an atom with free floating electrons in the nebular gas may transfer some of the kinetic energy from the collision into exciting a captive electron to a high energy level. This process clearly depends on the density and temperature of free electrons in the gas. A low density will mean that very few captive electrons become excited, since there are few collisions. A low temperature means the collisions are relatively unenergetic, and therefore less likely to result in the promotion of a captive electron.

B.1.2 Decay With and Without Emission

Once elevated to an excited state through the methods outlined above, an electron may decay back down to a lower energy level. For a permitted transition, typically the decay time is of order 10^{-8} s (e.g. Zeilik and Gregory, 1998). The event results in the release of a photon, of wavelength defined by the energy gap. An electron which cascades through many energy levels on it's return to the ground state will produce emission of several different spectral lines.

An alternative method of returning an electron from a high energy state to a lower energy one – in which no photon is emitted – is collisional de-excitation. In this process a super-elastic collision occurs between an atom containing excited electrons and another particle, the particle gains kinetic energy from the downward transition of the electron in the atom.

[1] If the photon energy $h\nu$ is greater than the ionisation potential.

B.1.3 Allowed and Forbidden Transitions

As we have stated above, the typical decay time for many energy level transitions by electrons is of order 10^{-8} s. The Hα line at 6536 Å is a good example of a transition with a short lifetime. It is a so-called *recombination line*, i.e. a line formed when electrons recombine with ions and subsequently decay from a high energy state (to the $n = 2$ level of the atom in this case). Because Hα is formed in this way it is easy to see why it is strongly related to SFR: the UV flux from the young stars ionises the Hydrogen gas which subsequently recombines to emit Hα.

In addition to short lifetime transitions, there are those which have a *much* longer decay time, of order 1 s or even greater ([O II] has decay times of $\sim 10^4$ s). These transitions occur from so-called *metastable* states to the ground state of the atom and are called forbidden transitions. They are "forbidden" in the sense that there is no electric dipole connection between the initial and final states, instead they occur as either magnetic dipole or electric quadrupole transitions, which are much more unlikely – hence the extended lifetime of the initial state.

Since the lifetime of excited metastable states is so long, the electron is often de-excited by collisional effects before it has had time to decay and emit a photon. In the early part of the last century astronomers had great difficulty understanding observations of forbidden transitions in planetary nebula for this very reason: forbidden transition are not reproducible in a laboratory due to the densities being too high (the counteractive effect of collisional de-excitation wins out over emission). In particular, the astronomers Huggins and Miller (1864) observed a spectrum of a planetary nebula which contained emission features which were not at the time attributable to any known element. They suggested that a new element had been found, "Nebulium", something not existing on Earth. It was much later that Bowen (1928) showed these lines to be from forbidden transitions in ionised Oxygen.

Forbidden lines are excited predominantly by collisions, with recombination playing an almost negligible role. In order to produce forbidden lines, it is therefore important to be in the correct density environment, too high a density will mean that the metastable state is de-excited before emission can occur and too low a density will result in very few electrons becoming excited at all. Note that there exists a critical density at which the

emission and de-excitation rates are equal. This density depends on the temperature of the gas (because so, in turn, do the cross sectional areas for collisional excitation).

Finally, we note that since the transition probability of forbidden lines is low, so is the chance of absorption. This means that (in the absence of dust at least) the line photons always escape freely from the nebula.

B.2 Transitions In Singly Ionised Oxygen

The singly ionised Oxygen species (O^+) is confusingly referred to as [O II] in modern astronomy. The brackets which occur in the "[O II]" symbol indicate that the line in question arises from a forbidden transition.

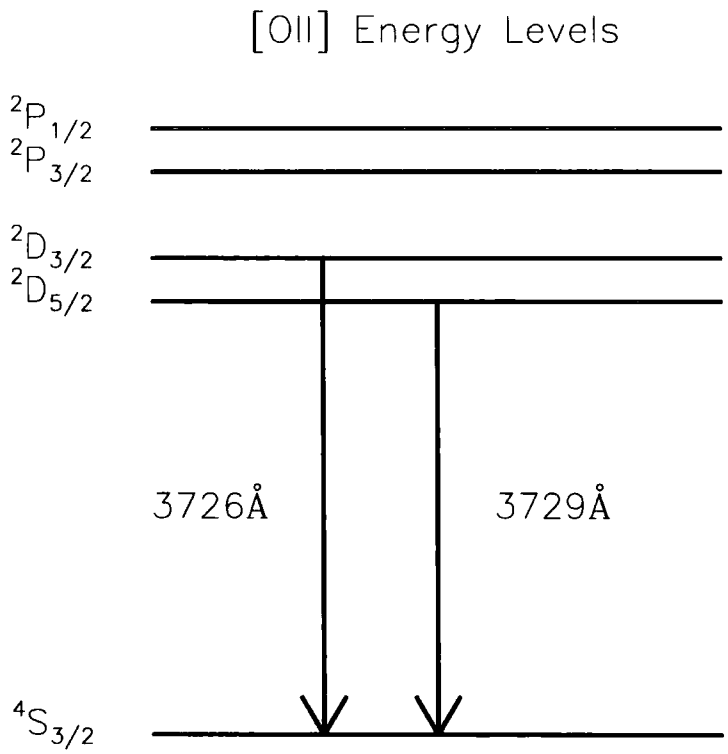

FIGURE B.1: The atomic structure of the singly ionised Oxygen, showing the transitions responsible for the formation of the [O II] lines at 3726 and 3729Å.

The [O II] line is often stated to lie at 3727 Å although it is actually composed of two individual transitions at 3726 and 3729 Å. These are from the $^2D_{3/2}$ to $^4S_{3/2}$ and $^2D_{5/2}$ to $^4S_{3/2}$ levels respectively[2]. The atomic structure of O^+ is shown schematically

[2]In this notation the letters S and D refer to the orbital angular momentum (l), the superscript refers

in Figure B.1, along with the transitions which form the [O II] lines. The higher energy states of Oxygen (upwards of ^2P) are rarely excited because typical nebula gas is too cool to promote electrons to such energies. The transitions which form [O II] are forbidden and so the spontaneous emission probabilities are very small. The 3726Å transition has a spontaneous emission probability of $1.8 \times 10^{-5}\,\mathrm{s}^{-1}$; the 3729Å transition has probability $4.2 \times 10^{-4}\,\mathrm{s}^{-1}$.

Note that the first ionisation potential of Oxygen is *very* similar to that of Hydrogen (H: 13.598 eV, O: 13.618 eV) and so wherever we find ionised Hydrogen in a nebula we expect to find ionised Oxygen also, providing of course that Oxygen is present in the nebula itself. In addition, there is a charge exchange reaction which also affects the ionisation state of Oxygen. A reaction can occur such that an electron is transferred from O to H^+ meaning the Oxygen becomes ionised and the Hydrogen returns to its neutral state (the reverse reaction also occurs). Such a reaction is possible due to the attractive force between O and H^+. Since the typical temperatures of H II regions are high compared with the difference in ionisation potentials between Oxygen and Hydrogen, an equilibrium is established whereby the ratio of neutral/ionised species is related only to their statistical weights. This means that the degree of ionisation of Oxygen is locked to that of Hydrogen, so long as charge exchange is the dominant process for ionising Oxygen.

The energy gap over which the [O II] 3727Å transitions occur is $\sim 3.3\,\mathrm{eV}$, which in normal nebula temperatures of $T \sim 10 - 20,000\,\mathrm{K}$ is of order the thermal electron energy, kT. Because of this similarity between gap energy and thermal energy, we expect [O II] emission to be significant, despite the relatively low abundance of Oxygen compared to Hydrogen, since many transitions should be excited (Osterbrock, 1989).

B.3 The Relation Of [O II] Emission To The SFR

We begin with a gas cloud from which stars are born. The distribution of masses is described by the IMF (Section 1.3). The abundance of elements within each star at birth clearly depends on the abundance of the parent cloud, and whether it has been enriched with metals by supernovae or winds. There are two factors that affect the bolometric luminosity of the ensemble of stars: the IMF and the abundances of individual stars.

to the spin $(2s+1)$ while the subscript refers to the total angular momentum (j, where $j = s + l$).

When the stars reach the Zero Age Main Sequence and begin to fuse Hydrogen into Helium, the hard UV spectrum emitted by the hot, large stars ionises the surrounding cloud of Hydrogen, forming a so-called H II region. It is important to understand if the temperature varies throughout the nebula, since as we stated earlier, free floating electrons are responsible for exciting the forbidden transition of [O II]. This can only occur at certain temperatures.

In order to explain how the temperature and ionisation state of the nebula gas are linked to the UV flux, consider the following. If the nebula were composed solely of Hydrogen, the only cooling mechanism would be emission as a result of electron-ion recombination; in this case the kinetic energy of the recombined electron is emitted as radiation. The gas should therefore cool. This mechanism is not able to cool the gas to the observed temperatures. The conclusion is that the nebula is not composed solely of Hydrogen.

Oxygen is the single most important element for cooling processes in nebula gas. The forbidden transitions require kinetic energy to be excited and hence the gas cools when [O II] is emitted. Note that if the temperature of the central stars increase then the recombination rate for Hydrogen decreases, since the electrons become too energetic. This results in an increased density of free floating electrons. These then elicit more forbidden transitions in Oxygen, cooling the gas. If the opposite occurs, and the temperature of the central stars decrease then the recombination rate increases, producing more neutral Hydrogen. This in turn means the heating rate increases, since recombination is an ineffective cooling mechanism. The temperature and ionisation state of the gas therefore remain tightly controlled.

The relation of [O II] emission to SFR is now clear, since the presence of hot, large, shortlived stars is necessary in order to both create free floating electrons (through ionisation), and also to heat them to the correct temperatures for exciting the forbidden transitions.

Bibliography

K. Abazajian, J. K. Adelman-McCarthy, M. A. Agüeros, S. S. Allam, S. F. Anderson, J. Annis, N. A. Bahcall, I. K. Baldry, S. Bastian, A. Berlind, M. Bernardi, M. R. Blanton, N. Blythe, J. J. Bochanski, W. N. Boroski, H. Brewington, J. W. Briggs, J. Brinkmann, R. J. Brunner, T. Budavári, L. N. Carey, M. A. Carr, F. J. Castander, K. Chiu, M. J. Collinge, A. J. Connolly, K. R. Covey, I. Csabai, J. J. Dalcanton, S. Dodelson, M. Doi, F. Dong, D. J. Eisenstein, M. L. Evans, X. Fan, P. D. Feldman, D. P. Finkbeiner, S. D. Friedman, J. A. Frieman, M. Fukugita, R. R. Gal, B. Gillespie, K. Glazebrook, C. F. Gonzalez, J. Gray, E. K. Grebel, L. Grodnicki, J. E. Gunn, V. K. Gurbani, P. B. Hall, L. Hao, D. Harbeck, F. H. Harris, H. C. Harris, M. Harvanek, S. L. Hawley, T. M. Heckman, J. F. Helmboldt, J. S. Hendry, G. S. Hennessy, R. B. Hindsley, D. W. Hogg, D. J. Holmgren, J. A. Holtzman, L. Homer, L. Hui, S.-i. Ichikawa, T. Ichikawa, J. P. Inkmann, Ž. Ivezić, S. Jester, D. E. Johnston, B. Jordan, W. P. Jordan, A. M. Jorgensen, M. Jurić, G. Kauffmann, S. M. Kent, S. J. Kleinman, G. R. Knapp, A. Y. Kniazev, R. G. Kron, J. Krzesiński, P. Z. Kunszt, N. Kuropatkin, D. Q. Lamb, H. Lampeitl, B. E. Laubscher, B. C. Lee, R. F. Leger, N. Li, A. Lidz, H. Lin, Y.-S. Loh, D. C. Long, J. Loveday, R. H. Lupton, T. Malik, B. Margon, P. M. McGehee, T. A. McKay, A. Meiksin, G. A. Miknaitis, B. K. Moorthy, J. A. Munn, T. Murphy, R. Nakajima, V. K. Narayanan, T. Nash, E. H. Neilsen, H. J. Newberg, P. R. Newman, R. C. Nichol, T. Nicinski, M. Nieto-Santisteban, A. Nitta, M. Odenkirchen, S. Okamura, J. P. Ostriker, R. Owen, N. Padmanabhan, J. Peoples, J. R. Pier, B. Pindor, A. C. Pope, T. R. Quinn, R. R. Rafikov, S. N. Raymond, G. T. Richards, M. W. Richmond, H.-W. Rix, C. M. Rockosi, J. Schaye, D. J. Schlegel, D. P. Schneider, J. Schroeder, R. Scranton, M. Sekiguchi, U. Seljak, G. Sergey, B. Sesar, E. Sheldon, K. Shimasaku, W. A. Siegmund, N. M. Silvestri, A. J. Sinisgalli, E. Sirko, J. A. Smith, V. Smolčić, S. A.

Snedden, A. Stebbins, C. Steinhardt, G. Stinson, C. Stoughton, I. V. Strateva, M. A. Strauss, M. SubbaRao, A. S. Szalay, I. Szapudi, P. Szkody, L. Tasca, M. Tegmark, A. R. Thakar, C. Tremonti, D. L. Tucker, A. Uomoto, D. E. Vanden Berk, J. Vandenberg, M. S. Vogeley, W. Voges, N. P. Vogt, L. M. Walkowicz, D. H. Weinberg, A. A. West, S. D. M. White, B. C. Wilhite, B. Willman, Y. Xu, B. Yanny, J. Yarger, N. Yasuda, C.-W. Yip, D. R. Yocum, D. G. York, N. L. Zakamska, I. Zehavi, W. Zheng, S. Zibetti, and D. B. Zucker. The First Data Release of the Sloan Digital Sky Survey. AJ, 126: 2081–2086, October 2003.

R. G. Abraham, K. Glazebrook, P. J. McCarthy, D. Crampton, R. Murowinski, I. Jørgensen, K. Roth, I. M. Hook, S. Savaglio, H. Chen, R. O. Marzke, and R. G. Carlberg. The Gemini Deep Deep Survey. I. Introduction to the Survey, Catalogs, and Composite Spectra. AJ, 127:2455–2483, May 2004.

K. L. Adelberger and C. C. Steidel. Multiwavelength Observations of Dusty Star Formation at Low and High Redshift. ApJ, 544:218–241, 2000.

J. Afonso, A. Hopkins, B. Mobasher, and C. Almeida. Dependence of Dust Obscuration on Star Formation Rates in Galaxies. ApJ, 597:269–273, November 2003.

A. Aragón-Salamanca, A. Alonso-Herrero, J. Gallego, C. E. García-Dabó, P. G. Pérez-González, J. Zamorano, and A. Gil de Paz. Star Formation Rate Estimators: [OII]3727 vs Hα for Local Star-forming Galaxies. In *ASP Conf. Ser. 297: Star Formation Through Time*, pages 191–+, 2003.

S. Arnouts, D. Schiminovich, O. Ilbert, L. Tresse, B. Milliard, M. Treyer, S. Bardelli, T. Budavari, T. K. Wyder, E. Zucca, O. Le Fèvre, D. C. Martin, G. Vettolani, C. Adami, M. Arnaboldi, T. Barlow, L. Bianchi, M. Bolzonella, D. Bottini, Y.-I. Byun, A. Cappi, S. Charlot, T. Contini, J. Donas, K. Forster, S. Foucaud, P. Franzetti, P. G. Friedman, B. Garilli, I. Gavignaud, L. Guzzo, T. M. Heckman, C. Hoopes, A. Iovino, P. Jelinsky, V. Le Brun, Y.-W. Lee, D. Maccagni, B. F. Madore, R. Malina, B. Marano, C. Marinoni, H. J. McCracken, A. Mazure, B. Meneux, R. Merighi, P. Morrissey, S. Neff, S. Paltani, R. Pellò, J. P. Picat, A. Pollo, L. Pozzetti, M. Radovich, R. M. Rich, R. Scaramella, M. Scodeggio, M. Seibert, O. Siegmund, T. Small, A. S. Szalay, B. Welsh, C. K. Xu,

G. Zamorani, and A. Zanichelli. The GALEX VIMOS-VLT Deep Survey Measurement of the Evolution of the 1500 Å Luminosity Function. ApJ, 619:L43–L46, January 2005.

T. S. R. Babbedge, M. Rowan-Robinson, E. A. Gonzales-Solares, M. Polletta, S. Berta, I. Pérez-Fournon, S. Oliver, M. Salaman, and M. Irwin. ImpZ: a new photometric redshift code for galaxies and quasars. MNRAS, 353:654–672, 2004.

T. S. R. Babbedge, R. Whitaker, and S. Morris. Can a photometric redshift code reliably determine dust extinction? MNRAS, 361:437–450, August 2005.

M. Balogh, R. G. Bower, I. Smail, B. L. Ziegler, R. L. Davies, A. Gaztelu, and A. Fritz. Galaxy properties in low X-ray luminosity clusters at z=0.25. MNRAS, 337:256–274, 2002.

M. L. Balogh. The recent star formation history of galaxies in X-ray clusters. *Ph.D. Thesis*, 1999.

A. J. Barger, A. Aragon-Salamanca, R. S. Ellis, W. J. Couch, I. Smail, and R. M. Sharples. The life-cycle of star formation in distant clusters. MNRAS, 279:1–24, March 1996.

C. M. Baugh, C. G. Lacey, C. S. Frenk, G. L. Granato, L. Silva, A. Bressan, A. J. Benson, and S. Cole. Can the faint submillimetre galaxies be explained in the Λ cold dark matter model? MNRAS, 356:1191–1200, January 2005.

E. F. Bell. Dust-induced Systematic Errors in Ultraviolet-derived Star Formation Rates. ApJ, 577:150–154, September 2002.

E. F. Bell. Estimating Star Formation Rates from Infrared and Radio Luminosities: The Origin of the Radio-Infrared Correlation. ApJ, 586:794–813, April 2003.

C. L. Bennett, M. Halpern, G. Hinshaw, N. Jarosik, A. Kogut, M. Limon, S. S. Meyer, L. Page, D. N. Spergel, G. S. Tucker, E. Wollack, E. L. Wright, C. Barnes, M. R. Greason, R. S. Hill, E. Komatsu, M. R. Nolta, N. Odegard, H. V. Peiris, L. Verde, and J. L. Weiland. First-Year Wilkinson Microwave Anisotropy Probe (WMAP) Observations: Preliminary Maps and Basic Results. ApJS, 148:1–27, September 2003.

S. Berta, J. Fritz, A. Franceschini, A. Bressan, and C. Lonsdale. Photometric estimates of stellar masses in high-redshift galaxies. A&A, 418:913–926, 2004.

P. Biermann. On the radio continuum flux from the disks of spiral galaxies. A&A, 53: 295–303, December 1976.

A. W. Blain, I. Smail, R. J. Ivison, and J.-P. Kneib. The history of star formation in dusty galaxies. MNRAS, 302:632–648, February 1999.

M. R. Blanton, J. Brinkmann, I. Csabai, M. Doi, D. Eisenstein, M. Fukugita, J. E. Gunn, D. W. Hogg, and D. J. Schlegel. Estimating Fixed-Frame Galaxy Magnitudes in the Sloan Digital Sky Survey. AJ, 125:2348–2360, May 2003.

R. C. Bohlin, E. B. Jenkins, L. Spitzer, D. G. York, J. K. Hill, B. D. Savage, and T. P. Snow. A survey of ultraviolet interstellar absorption lines. ApJS, 51:277–308, March 1983.

M. Bolzonella, J.-M. Miralles, and R. Pelló. Photometric redshifts based on standard SED fitting procedures. A&A, 363:476–492, November 2000.

G. D. Bothun, C. J. Lonsdale, and W. Rice. IRAS observations of optically selected galaxies. I - The properties of the UGC redshift sample. ApJ, 341:129–150, June 1989.

I. S. Bowen. The origin of the nebular lines and the structure of the planetary nebulae. ApJ, 67:1–15, January 1928.

A. Bressan, G. L. Granato, and L. Silva. Modelling intermediate age and old stellar populations in the Infrared. A&A, 332:135–148, 1998.

G. Bruzual and S. Charlot. Spectral evolution of stellar populations using isochrone synthesis. ApJ, 405:538–553, March 1993.

G. Bruzual and S. Charlot. Stellar population synthesis at the resolution of 2003. MNRAS, 344:1000–1028, October 2003.

V. Buat, J. M. Deharveng, and J. Donas. Star formation rate and gas surface density in late-type galaxies. A&A, 223:42–46, October 1989.

V. Buat and C. Xu. Star formation and dust extinction in disk galaxies. Comparison between the UV non-ionizing and the FIR emissions. A&A, 306:61–+, February 1996.

D. Burstein, S. M. Faber, and J. J. Gonzalez. Old stellar populations. III - The metallicities of M5, M71, and M67. AJ, 91:1130–1139, May 1986.

D. Calzetti. UV opacity in Nearby Galaxies and application to Distant galaxies. *astro-ph/9706121*, 1997.

D. Calzetti. The Dust Opacity of Star-forming Galaxies. PASP, 113:1449–1485, 2001a.

D. Calzetti. The effects of dust on the spectral energy distribution of star-forming galaxies. *New Astronomy Review*, 45:601–607, 2001b.

D. Calzetti, L. Armus, R. C. Bohlin, A. L. Kinney, J. Koornneef, and T. Storchi-Bergmann. The Dust Content and Opacity of Actively Star-forming Galaxies. ApJ, 533:682–695, 2000.

D. Calzetti and T. M. Heckman. The Evolution of Dust Opacity in Galaxies. ApJ, 519: 27–47, 1999.

D. Calzetti, A. L. Kinney, and T. Storchi-Bergmann. Dust extinction of the stellar continua in starburst galaxies: The ultraviolet and optical extinction law. ApJ, 429:582–601, July 1994.

D. Calzetti, A. L. Kinney, and T. Storchi-Bergmann. Dust Obscuration in Starburst Galaxies from Near-Infrared Spectroscopy. ApJ, 458:132–+, 1996.

D. Calzetti, A. L. Kinney, T. Storchi-Bergmann, and N. Panagia. Properties of Dust Extinction in Starburst Galaxies. *Bulletin of the American Astronomical Society*, 25: 841–+, 1993.

J. A. Cardelli, G. C. Clayton, and J. S. Mathis. The relationship between infrared, optical, and ultraviolet extinction. ApJ, 345:245–256, 1989.

N. Cardiel, D. Elbaz, R. P. Schiavon, C. N. A. Willmer, D. C. Koo, A. C. Phillips, and J. Gallego. A Multiwavelength Approach to the Star Formation Rate Estimation in Galaxies at Intermediate Redshifts. ApJ, 584:76–99, February 2003.

R. G. Carlberg, H. K. C. Yee, S. L. Morris, H. Lin, P. B. Hall, D. Patton, M. Sawicki, and C. W. Shepherd. Galaxy Clustering Evolution in the CNOC2 High-Luminosity Sample. ApJ, 542:57–67, October 2000.

B. W. Carroll and D. A. Ostlie. *An Introduction to Modern Astrophysics.* An Introduction to Modern Astrophysics, by B.W. Carroll and D.A. Ostlie. Benjamin Cummings, 1996. ISBN 0-201-54730-9., 1996.

S. M. Carroll, W. H. Press, and E. L. Turner. The cosmological constant. ARA&A, 30: 499–542, 1992.

S. C. Chapman, A. W. Blain, R. J. Ivison, and I. R. Smail. A median redshift of 2.4 for galaxies bright at submillimetre wavelengths. Nature, 422:695–698, April 2003.

S. C. Chapman, E. A. Richards, G. F. Lewis, G. Wilson, and A. J. Barger. The Nature of the Bright Submillimeter Galaxy Population: A Radio-preselected Sample with I>˜25. ApJ, 548:L147–L151, February 2001.

X. Chi and A. W. Wolfendale. Implications of the correlation between radio and far-infrared emission for spiral galaxies. MNRAS, 245:101–107, July 1990.

P. I. Choi, L. Yan, M. Im, G. Helou, B. T. Soifer, L. J. Storrie-Lombardi, R. Chary, H. I. Teplitz, D. Fadda, F. R. Marleau, M. Lacy, G. Wilson, P. N. Appleton, D. T. Frayer, and J. A. Surace. Star Formation Rates and Extinction Properties of IR-luminous Galaxies in the Spitzer First Look Survey. ApJ, 637:227–241, January 2006.

S. Cole, C. G. Lacey, C. M. Baugh, and C. S. Frenk. Hierarchical galaxy formation. MNRAS, 319:168–204, November 2000.

M. Colless, G. Dalton, S. Maddox, W. Sutherland, P. Norberg, S. Cole, J. Bland-Hawthorn, T. Bridges, R. Cannon, C. Collins, W. Couch, N. Cross, K. Deeley, R. De Propris, S. P. Driver, G. Efstathiou, R. S. Ellis, C. S. Frenk, K. Glazebrook, C. Jackson, O. Lahav, I. Lewis, S. Lumsden, D. Madgwick, J. A. Peacock, B. A. Peterson, I. Price, M. Seaborne, and K. Taylor. The 2dF Galaxy Redshift Survey: spectra and redshifts. MNRAS, 328: 1039–1063, December 2001.

J. J. Condon. Radio emission from normal galaxies. ARA&A, 30:575–611, 1992.

J. J. Condon, M. L. Anderson, and G. Helou. Correlations between the far-infrared, radio, and blue luminosities of spiral galaxies. ApJ, 376:95–103, July 1991.

J. J. Condon and Q. F. Yin. A new starburst model applied to the clumpy irregular galaxy Markarian 325. ApJ, 357:97–104, July 1990.

C. J. Conselice, M. A. Bershady, M. Dickinson, and C. Papovich. A Direct Measurement of Major Galaxy Mergers at z<~3. AJ, 126:1183–1207, September 2003.

L. L. Cowie, E. M. Hu, A. Songaila, and E. Egami. The Evolution of the Distribution of Star Formation Rates in Galaxies. ApJ, 481:L9+, May 1997.

L. L. Cowie, A. Songaila, and A. J. Barger. Evidence for a Gradual Decline in the Universal Rest-Frame Ultraviolet Luminosity Density for Z < 1. AJ, 118:603–612, August 1999.

L. L. Cowie, A. Songaila, E. M. Hu, and J. G. Cohen. New Insight on Galaxy Formation and Evolution From Keck Spectroscopy of the Hawaii Deep Fields. AJ, 112:839–+, September 1996.

P. Cox, E. Kruegel, and P. G. Mezger. Principal heating sources of dust in the galactic disk. A&A, 155:380–396, February 1986.

L. Cram, A. Hopkins, B. Mobasher, and M. Rowan-Robinson. Star Formation Rates in Faint Radio Galaxies. ApJ, 507:155–160, November 1998.

D. Crampton, , , , , and et al. MOS/SIS Project. In M.H Ulrich, editor, *Proc. ESO Conf. on Progress in Telescop and Instrumentation Technologies*, 1992.

D. Crampton, W. A. Grundmann, B. Leckie, C. L. Morbey, J. P. Lemonnier, P. Felenbok, M. Marteaud, P. Vola, Y. Georgelin, O. Le Fèvre, B. Grundseth, G. Monnet, and D. Salmon. Multi-Aperture and Subarcsecond Imaging Spectrograph for CFHT. In *Progress in Telescope and Instrumentation Technologies*, pages 609–+, 1992.

D. A. Dale, G. Helou, G. Neugebauer, B. T. Soifer, D. T. Frayer, and J. J. Condon. Multiwavelength Observations of the Low-Metallicity Blue Compact Dwarf Galaxy SBS 0335-052. AJ, 122:1736–1746, October 2001.

L. P. David, C. Jones, and W. Forman. X-ray properties of bright far-infrared galaxies. ApJ, 388:82–92, March 1992.

T. de Jong, U. Klein, R. Wielebinski, and E. Wunderlich. Radio continuum and far-infrared emission from spiral galaxies - A close correlation. A&A, 147:L6–L9, June 1985.

J.-M. Deharveng, T. P. Sasseen, V. Buat, S. Bowyer, M. Lampton, and X. Wu. Ultraviolet observations of galaxies with the FAUST experiment. A&A, 289:715–728, September 1994.

N. A. Devereux and J. S. Young. The rate and efficiency of high-mass star formation along the Hubble sequence. ApJ, 371:515–524, April 1991.

M. A. Dopita, M. Pereira, L. J. Kewley, and M. Capaccioli. Star Formation Rates in Interacting Starburst Galaxies. ApJS, 143:47–72, November 2002.

A. Dressler and S. A. Shectman. Systematics of the 4000 angstrom break in the spectra of galaxies. AJ, 94:899–905, October 1987.

G. Fabbiano. X rays from normal galaxies. ARA&A, 27:87–138, 1989.

S. M. Faber. Quadratic programming applied to the problem of galaxy population synthesis. A&A, 20:361–+, September 1972.

S. M. Faber, E. D. Friel, D. Burstein, and C. M. Gaskell. Old stellar populations. II - an analysis of K-giant spectra. ApJS, 57:711–741, April 1985.

M. N. Fanelli, R. W. O'Connell, and T. X. Thuan. Spectral synthesis in the ultraviolet. II - Stellar populations and star formation in blue compact galaxies. ApJ, 334:665–687, 1988.

G. J. Ferland, K. T. Korista, D. A. Verner, J. W. Ferguson, J. B. Kingdon, and E. M. Verner. CLOUDY 90: Numerical Simulation of Plasmas and Their Spectra. PASP, 110: 761, 1998.

J. S. Gallagher, D. A. Hunter, and H. Bushouse. Star-formation rates and forbidden O II emission in blue galaxies. AJ, 97:700–707, March 1989.

J. Gallego, J. Zamorano, A. Aragon-Salamanca, and M. Rego. The Current Star Formation Rate of the Local Universe. ApJ, 455:L1+, December 1995.

J. Gallego, J. Zamorano, M. Rego, O. Alonso, and A. G. Vitores. Observations of a complete sample of Hα emission-line galaxies. Long-slit spectroscopy of galaxies in UCM lists 1 and 2. A&AS, 120:323–356, December 1996.

R. D. Gehrz, R. A. Sramek, and D. W. Weedman. Star bursts and the extraordinary galaxy NGC 3690. ApJ, 267:551–562, April 1983.

A. Georgakakis, B. Mobasher, L. Cram, A. Hopkins, C. Lidman, and M. Rowan-Robinson. The Phoenix Survey: optical and near-infrared observations of faint radio sources. MNRAS, 306:708–726, July 1999.

G. Gilmore and D. Howell, editors. *The Stellar Initial Mass Function (38th Herstmonceux Conference)*, 1998.

K. Glazebrook, C. Blake, F. Economou, S. Lilly, and M. Colless. Measurement of the star formation rate from Hα in field galaxies at z=1. MNRAS, 306:843–856, July 1999.

G. L. Granato, L. Danese, and A. Franceschini. Thick Tori around Active Galactic Nuclei: The Case for Extended Tori and Consequences for Their X-Ray and Infrared Emission. ApJ, 486:147–+, September 1997.

R. E. Griffiths and P. Padovani. Star-forming galaxies and the X-ray background. ApJ, 360:483–489, September 1990.

D. B. Haarsma, R. B. Partridge, R. A. Windhorst, and E. A. Richards. Faint Radio Sources and Star Formation History. ApJ, 544:641–658, December 2000.

F. Hammer, H. Flores, S. J. Lilly, D. Crampton, O. Le Fevre, C. Rola, G. Mallen-Ornelas, D. Schade, and L. Tresse. Canada-France Redshift Survey. XIV. Spectral Properties of Field Galaxies up to z=1. ApJ, 481:49–+, May 1997.

M. G. Hauser, R. G. Arendt, T. Kelsall, E. Dwek, N. Odegard, J. L. Weiland, H. T. Freudenreich, W. T. Reach, R. F. Silverberg, S. H. Moseley, Y. C. Pei, P. Lubin, J. C. Mather, R. A. Shafer, G. F. Smoot, R. Weiss, D. T. Wilkinson, and E. L. Wright. The COBE Diffuse Infrared Background Experiment Search for the Cosmic Infrared Background. I. Limits and Detections. ApJ, 508:25–43, 1998.

A. Heavens, B. Panter, R. Jimenez, and J. Dunlop. The star-formation history of the Universe from the stellar populations of nearby galaxies. Nature, 428:625–627, April 2004.

A. F. Heavens, R. Jimenez, and O. Lahav. Massive lossless data compression and multiple parameter estimation from galaxy spectra. MNRAS, 317:965–972, October 2000.

T. M. Heckman, K. R. Sembach, G. R. Meurer, C. Leitherer, D. Calzetti, and C. L. Martin. On the Escape of Ionizing Radiation from Starbursts. ApJ, 558:56–62, September 2001.

G. Helou. The IRAS colors of normal galaxies. ApJ, 311:L33–L36, December 1986.

H. Hippelein, C. Maier, K. Meisenheimer, C. Wolf, J. W. Fried, B. von Kuhlmann, M. Kümmel, S. Phleps, and H.-J. Röser. Star forming rates between z = 0.25 and z = 1.2 from the CADIS emission line survey. A&A, 402:65–78, April 2003.

H. Hirashita, V. Buat, and A. K. Inoue. Star formation rate in galaxies from UV, IR, and Hα estimators. A&A, 410:83–100, October 2003.

D. W. Hogg, J. G. Cohen, R. Blandford, and M. A. Pahre. The O II Luminosity Density of the Universe. ApJ, 504:622–+, September 1998.

David W. Hogg. Distance measures in cosmology. 1999.

J. A. Holtzman, J. R. Mould, J. S. Gallagher, A. M. Watson, C. J. Grillmair, G. E. Ballester, C. J. Burrows, J. T. Clarke, D. Crisp, R. W. Evans, R. E. Griffiths, J. J. Hester, J. G. Hoessel, P. A. Scowen, K. R. Stapelfeldt, J. T. Trauger, and J. A. Westphal. Stellar Populations in the Large Magellanic Cloud:Evidence for a Significant Number of Older Stars or a Steeper IMF? AJ, 113:656–668, February 1997.

J. A. Holtzman, A. M. Watson, W. A. Baum, C. J. Grillmair, E. J. Groth, R. M. Light, R. Lynds, and E. J. O'Neil. The Luminosity Function and Initial Mass Function in the Galactic Bulge. AJ, 115:1946–1957, May 1998.

A. M. Hopkins. On the Evolution of Star-forming Galaxies. ApJ, 615:209–221, November 2004.

A. M. Hopkins, C. J. Miller, R. C. Nichol, A. J. Connolly, M. Bernardi, P. L. Gómez, T. Goto, C. A. Tremonti, J. Brinkmann, Ž. Ivezić, and D. Q. Lamb. Star Formation Rate Indicators in the Sloan Digital Sky Survey. ApJ, 599:971–991, December 2003.

E. Hubble. A Relation between Distance and Radial Velocity among Extra-Galactic Nebulae. *Proceedings of the National Academy of Science*, 15:168–173, March 1929.

W. Huggins and W. A. Miller. On the Spectra of Some of the Nebulae. By William Huggins, F.R.A.S. A Supplement to the Paper "On the Spectra of Some of the Fixed

Stars William Huggins F.R.A.S., and W. A. Miller, M.D., LL.D., Treas. and V.P.P.S.". *Philosophical Transactions Series I*, 154:437–444, 1864.

D. A. Hunter and J. S. Gallagher. Stellar populations and star formation in irregular galaxies. PASP, 98:5–28, January 1986.

M. Hurwitz, P. Jelinsky, and W. V. D. Dixon. Reexamining the Lyman Continuum in Starburst Galaxies Observed with the Hopkins Ultraviolet Telescope. ApJ, 481:L31+, May 1997.

I. J. Iben. Stellar Evolution Within and off the Main Sequence. ARA&A, 5:571–+, 1967.

R. A. Jansen, M. Franx, and D. Fabricant. [O II] As a Tracer of Current Star Formation. ApJ, 551:825–832, April 2001.

R. A. Jansen, M. Franx, D. Fabricant, and N. Caldwell. Surface Photometry of Nearby Field Galaxies: The Data. ApJS, 126:271–329, February 2000.

S. Juneau, K. Glazebrook, D. Crampton, P. J. McCarthy, S. Savaglio, R. Abraham, R. G. Carlberg, H.-W. Chen, D. Le Borgne, R. O. Marzke, K. Roth, I. Jørgensen, I. Hook, and R. Murowinski. Cosmic Star Formation History and Its Dependence on Galaxy Stellar Mass. ApJ, 619:L135–L138, February 2005.

G. Kauffmann, T. M. Heckman, S. D. M. White, S. Charlot, C. Tremonti, E. W. Peng, M. Seibert, J. Brinkmann, R. C. Nichol, M. SubbaRao, and D. York. The dependence of star formation history and internal structure on stellar mass for 10^5 low-redshift galaxies. MNRAS, 341:54–69, May 2003.

K. Kawara, Y. Sato, H. Matsuhara, Y. Taniguchi, H. Okuda, Y. Sofue, T. Matsumoto, K. Wakamatsu, H. Karoji, S. Okamura, K. C. Chambers, L. L. Cowie, R. D. Joseph, and D. B. Sanders. ISO deep far-infrared survey in the "Lockman Hole". A search for obscured objects at high redshift. I. Observations. A&A, 336:L9–L12, August 1998.

R. C. Kennicutt. The rate of star formation in normal disk galaxies. ApJ, 272:54–67, September 1983.

R. C. Kennicutt. A spectrophotometric atlas of galaxies. ApJS, 79:255–284, April 1992a.

R. C. Kennicutt. The integrated spectra of nearby galaxies - General properties and emission-line spectra. ApJ, 388:310–327, April 1992b.

R. C. Kennicutt. Star Formation in Galaxies Along the Hubble Sequence. ARA&A, 36: 189–232, 1998.

L. J. Kewley, M. J. Geller, and R. A. Jansen. [O II] as a Star Formation Rate Indicator. AJ, 127:2002–2030, April 2004.

L. J. Kewley, M. J. Geller, R. A. Jansen, and M. A. Dopita. The Hα and Infrared Star Formation Rates for the Nearby Field Galaxy Survey. AJ, 124:3135–3143, December 2002.

L. J. Kewley, C. A. Heisler, M. A. Dopita, and S. Lumsden. Optical Classification of Southern Warm Infrared Galaxies. ApJS, 132:37–71, January 2001.

J. G. Kirk. Particle Acceleration (With 26 figures). In *Saas-Fee Advanced Course 24: Plasma Astrophysics*, pages 225–+, 1994.

U. Klein. Radio emission and star formation in dwarf galaxies. *Proceedings of the Astronomical Society of Australia*, 9:253–+, 1991.

U. Klein, H. Weiland, and E. Brinks. A radio-optical study of blue compact dwarf galaxies. I - Radio continuum observations. A&A, 246:323–340, June 1991.

U. Klein, R. Wielebinski, and T. X. Thuan. Radio continuum observations of blue compact dwarf galaxies. A&A, 141:241–247, December 1984.

R. G. Kron. Photometry of a complete sample of faint galaxies. ApJS, 43:305–325, June 1980.

R. Kurucz. ATLAS9 Stellar Atmosphere Programs and 2 km/s grid. *ATLAS9 Stellar Atmosphere Programs and 2 km/s grid. Kurucz CD-ROM No.13.Cambridge, Mass. Smithsonian Astrophysical Observatory, 1993.*, 13, 1993.

E. S. Laird, K. Nandra, K. L. Adelberger, C. C. Steidel, and N. A. Reddy. X-ray properties of UV-selected star-forming galaxies at z$\sim$ 1 in the Hubble Deep Field North. MNRAS, 359:47–56, May 2005.

A. U. Landolt. UBVRI photometric standard stars in the magnitude range 11.5-16.0 around the celestial equator. AJ, 104:340–371, July 1992.

R. B. Larson. Dynamical models for the formation and evolution of spherical galaxies. MNRAS, 166:585–616, March 1974.

O. Le Fèvre, G. Vettolani, S. Paltani, L. Tresse, G. Zamorani, V. Le Brun, C. Moreau, D. Bottini, D. Maccagni, J. P. Picat, R. Scaramella, M. Scodeggio, A. Zanichelli, C. Adami, S. Arnouts, S. Bardelli, M. Bolzonella, A. Cappi, S. Charlot, T. Contini, S. Foucaud, P. Franzetti, B. Garilli, I. Gavignaud, L. Guzzo, O. Ilbert, A. Iovino, H. J. McCracken, D. Mancini, B. Marano, C. Marinoni, G. Mathez, A. Mazure, B. Meneux, R. Merighi, R. Pellò, A. Pollo, L. Pozzetti, M. Radovich, E. Zucca, M. Arnaboldi, M. Bondi, A. Bongiorno, G. Busarello, P. Ciliegi, L. Gregorini, Y. Mellier, P. Merluzzi, V. Ripepi, and D. Rizzo.

O. Le Fevre, D. Crampton, P. Felenbok, and G. Monnet. CFHT MOS/SIS spectrograph performance. A&A, 282:325–340, February 1994.

C. Leitherer, H. C. Ferguson, T. M. Heckman, and J. D. Lowenthal. The Lyman Continuum in Starburst Galaxies Observed with the Hopkins Ultraviolet Telescope. ApJ, 454: L19+, November 1995.

A. Li and B. T. Draine. Infrared Emission from Interstellar Dust. II. The Diffuse Interstellar Medium. ApJ, 554:778–802, June 2001.

S. J. Lilly, O. Le Fevre, D. Crampton, F. Hammer, and L. Tresse. The Canada-France Redshift Survey. I. Introduction to the Survey, Photometric Catalogs, and Surface Brightness Selection Effects. ApJ, 455:50–+, December 1995.

S. J. Lilly, O. Le Fevre, F. Hammer, and D. Crampton. The Canada-France Redshift Survey: The Luminosity Density and Star Formation History of the Universe to Z approximately 1. ApJ, 460:L1+, March 1996.

H. Lin, H. K. C. Yee, R. G. Carlberg, S. L. Morris, M. Sawicki, D. R. Patton, G. Wirth, and C. W. Shepherd. The CNOC2 Field Galaxy Luminosity Function. I. A Description of Luminosity Function Evolution. ApJ, 518:533–561, June 1999.

C. J. Lonsdale Persson and G. Helou. On the origin of the 40-120 micron emission of galaxy disks A comparison with H-alpha fluxes. ApJ, 314:513–524, March 1987.

P. Madau, H. C. Ferguson, M. E. Dickinson, M. Giavalisco, C. C. Steidel, and A. Fruchter. High-redshift galaxies in the Hubble Deep Field: colour selection and star formation history to z$\sim$4. *MNRAS*, 283:1388–1404, 1996.

P. Madau, L. Pozzetti, and M. Dickinson. The Star Formation History of Field Galaxies. ApJ, 498:106–+, May 1998.

J. M. Mas-Hesse and D. Kunth. Evolutionary population synthesis in starburst regions. A&AS, 88:399–450, June 1991.

M. Massarotti, A. Iovino, and A. Buzzoni. A critical appraisal of the SED fitting method to estimate photometric redshifts. A&A, 368:74–85, 2001.

P. Massey. The Initial Mass Function of Massive Stars in the Local Group. In *ASP Conf. Ser. 142: The Stellar Initial Mass Function (38th Herstmonceux Conference)*, pages 17–+, 1998.

G. R. Meurer, T. M. Heckman, and D. Calzetti. Dust Absorption and the Ultraviolet Luminosity Density at z$\sim$3 as Calibrated by Local Starburst Galaxies. ApJ, 521:64–80, 1999.

G. E. Miller and J. M. Scalo. The initial mass function and stellar birthrate in the solar neighborhood. ApJS, 41:513–547, November 1979.

N. A. Miller and F. N. Owen. Evolution of Star-forming and Active Galaxies in Nearby Clusters. AJ, 124:2453–2470, 2002.

C. L. Morbey. Optical design of two spectrographs for the Canada-France-Hawaii telescope. Appl. Opt., 31:2291–2300, May 1992.

C. R. O'dell and Z. Wen. Postrefurbishment mission Hubble Space Telescope images of the core of the Orion Nebula: Proplyds, Herbig-Haro objects, and measurements of a circumstellar disk. ApJ, 436:194–202, November 1994.

S. J. Oliver, P. Goldschmidt, A. Franceschini, S. B. G. Serjeant, A. Efstathiou, A. Verma, C. Gruppioni, N. Eaton, R. G. Mann, B. Mobasher, C. P. Pearson, M. Rowan-Robinson,

T. J. Sumner, L. Danese, D. Elbaz, E. Egami, M. Kontizas, A. Lawrence, R. McMahon, H. U. Norgaard-Nielsen, I. Perez-Fournon, and J. I. Gonzalez-Serrano. Observations of the Hubble Deep Field with the Infrared Space Observatory - III. Source counts and P(D) analysis. MNRAS, 289:471–481, August 1997.

D Osterbrock. *Astrophysics of Gaseous Nebulae and Active Galactic Nuclei.* Mill Valley CA: University Science Books, 1989.

B. E. J. Pagel, M. G. Edmunds, and G. Smith. On the composition of H II regions in southern galaxies. II - NGC 6822 and 1313. MNRAS, 193:219–230, October 1980.

B. Panter, A. F. Heavens, and R. Jimenez. Star formation and metallicity history of the SDSS galaxy survey: unlocking the fossil record. MNRAS, 343:1145–1154, August 2003.

F. Paresce and G. De Marchi. On the Globular Cluster Initial Mass Function below 1 $M_{\odot}$. ApJ, 534:870–879, May 2000.

Y. C. Pei. Interstellar dust from the Milky Way to the Magellanic Clouds. ApJ, 395: 130–139, August 1992.

W. Pence. CFITSIO, v2.0: A New Full-Featured Data Interface. In *ASP Conf. Ser. 172: Astronomical Data Analysis Software and Systems VIII*, pages 487–+, 1999.

A. A. Penzias and R. W. Wilson. A Measurement of Excess Antenna Temperature at 4080 Mc/s. ApJ, 142:419–421, July 1965.

M. Pettini, M. Kellogg, C. C. Steidel, M. Dickinson, K. L. Adelberger, and M. Giavalisco. Infrared Observations of Nebular Emission Lines from Galaxies at Z $\tilde{?}$= 3. ApJ, 508: 539–550, 1998.

A. J. Pickles. A Stellar Spectral Flux Library: 1150-25000 Å. PASP, 110:863–878, 1998.

C. C. Popescu, A. Misiriotis, N. D. Kylafis, R. J. Tuffs, and J. Fischera. Modelling the spectral energy distribution of galaxies. I. Radiation fields and grain heating in the edge-on spiral NGC 891. A&A, 362:138–150, October 2000.

R. Price and N. Duric. New results on the radio-far-infrared relation for galaxies. ApJ, 401:81–86, December 1992.

J. L. Puget, A. Abergel, J. P. Bernard, F. Boulanger, W. B. Burton, F. X. Desert, and D. Hartmann. Tentative detection of a cosmic far-infrared background with COBE. A&A, 308:L5, 1996.

J. L. Puget, G. Lagache, D. L. Clements, W. T. Reach, H. Aussel, F. R. Bouchet, C. Cesarsky, F. X. Désert, H. Dole, D. Elbaz, A. Franceschini, B. Guiderdoni, and A. F. M. Moorwood. FIRBACK. I. A deep survey at 175 microns with ISO, preliminary results. A&A, 345:29–35, May 1999.

P. Ranalli, A. Comastri, and G. Setti. The 2-10 keV luminosity as a Star Formation Rate indicator. A&A, 399:39–50, February 2003.

M. Robberto, S. V. W. Beckwith, N. Panagia, S. G. Patel, T. M. Herbst, S. Ligori, A. Custo, P. Boccacci, and M. Bertero. The Orion Nebula in the Mid-Infrared. AJ, 129:1534–1563, March 2005.

D. Rosa-González, E. Terlevich, and R. Terlevich. An empirical calibration of star formation rate estimators. MNRAS, 332:283–295, May 2002.

M. Rowan-Robinson. Quantifying dust and the ultraviolet radiation density in the local Universe. MNRAS, 344:13–21, 2003.

M. Rowan-Robinson and J. Crawford. Models for infrared emission from IRAS galaxies. MNRAS, 238:523–558, May 1989.

M. Rowan-Robinson, R. G. Mann, S. J. Oliver, A. Efstathiou, N. Eaton, P. Goldschmidt, B. Mobasher, S. B. G. Serjeant, and et al. Observations of the Hubble Deep Field with the Infrared Space Observatory - V. Spectral energy distributions, starburst models and star formation history. MNRAS, 289:490–496, 1997.

E. E. Salpeter. The Luminosity Function and Stellar Evolution. ApJ, 121:161–+, January 1955.

D. B. Sanders and I. F. Mirabel. Luminous Infrared Galaxies. ARA&A, 34:749–+, 1996.

M. Sauvage and T. X. Thuan. On the use of far-infrared luminosity as a star formation indicator in galaxies. ApJ, 396:L69–L73, September 1992.

B. D. Savage and J. S. Mathis. Observed properties of interstellar dust. ARA&A, 17: 73–111, 1979.

J. M. Scalo. The stellar initial mass function. *Fundamentals of Cosmic Physics*, 11:1–278, May 1986.

P. Schechter. An analytic expression for the luminosity function for galaxies. ApJ, 203: 297–306, January 1976.

D. Schiminovich, O. Ilbert, S. Arnouts, B. Milliard, L. Tresse, O. Le Fèvre, M. Treyer, T. K. Wyder, T. Budavári, E. Zucca, G. Zamorani, D. C. Martin, C. Adami, M. Arnaboldi, S. Bardelli, T. Barlow, L. Bianchi, M. Bolzonella, D. Bottini, Y.-I. Byun, A. Cappi, T. Contini, S. Charlot, J. Donas, K. Forster, S. Foucaud, P. Franzetti, P. G. Friedman, B. Garilli, I. Gavignaud, L. Guzzo, T. M. Heckman, C. Hoopes, A. Iovino, P. Jelinsky, V. Le Brun, Y.-W. Lee, D. Maccagni, B. F. Madore, R. Malina, B. Marano, C. Marinoni, H. J. McCracken, A. Mazure, B. Meneux, P. Morrissey, S. Neff, S. Paltani, R. Pellò, J. P. Picat, A. Pollo, L. Pozzetti, M. Radovich, R. M. Rich, R. Scaramella, M. Scodeggio, M. Seibert, O. Siegmund, T. Small, A. S. Szalay, G. Vettolani, B. Welsh, C. K. Xu, and A. Zanichelli. The GALEX-VVDS Measurement of the Evolution of the Far-Ultraviolet Luminosity Density and the Cosmic Star Formation Rate. ApJ, 619: L47–L50, January 2005.

D. J. Schlegel, D. P. Finkbeiner, and M. Davis. Maps of Dust Infrared Emission for Use in Estimation of Reddening and Cosmic Microwave Background Radiation Foregrounds. ApJ, 500:525–+, June 1998.

L. Searle, W. L. W. Sargent, and W. G. Bagnuolo. The History of Star Formation and the Colors of Late-Type Galaxies. ApJ, 179:427–438, January 1973.

C. W. Shepherd, R. G. Carlberg, H. K. C. Yee, S. L. Morris, H. Lin, M. Sawicki, P. B. Hall, and D. R. Patton. The Galaxy Correlation Function in the CNOC2 Redshift Survey: Dependence on Color, Luminosity, and Redshift. ApJ, 560:72–85, 2001.

I. Smail, R. J. Ivison, and A. W. Blain. A Deep Sub-millimeter Survey of Lensing Clusters: A New Window on Galaxy Formation and Evolution. ApJ, 490:L5+, November 1997.

G. F. Smoot, C. L. Bennett, A. Kogut, J. Aymon, C. Backus, G. de Amici, K. Galuk, P. D. Jackson, P. Keegstra, L. Rokke, L. Tenorio, S. Torres, S. Gulkis, M. G. Hauser, M. A. Janssen, J. C. Mather, R. Weiss, D. T. Wilkinson, E. L. Wright, N. W. Boggess, E. S. Cheng, T. Kelsall, P. Lubin, S. Meyer, S. H. Moseley, T. L. Murdock, R. A. Shafer, and R. F. Silverberg. Preliminary results from the COBE differential microwave radiometers - Large angular scale isotropy of the cosmic microwave background. ApJ, 371:L1–L5, April 1991.

B. T. Soifer and G. Neugebauer. The properties of infrared galaxies in the local universe. AJ, 101:354–361, February 1991.

H. Spinrad and B. J. Taylor. The Stellar Content of the Nuclei of Nearby Galaxies. I. M31, M32, and M81. ApJS, 22:445–+, April 1971.

C. C. Steidel, M. Giavalisco, M. Dickinson, and K. L. Adelberger. Spectroscopy of Lyman Break Galaxies in the Hubble Deep Field. AJ, 112:352–+, August 1996.

C. C. Steidel, M. Pettini, and K. L. Adelberger. Lyman-Continuum Emission from Galaxies at Z ˜= 3.4. ApJ, 546:665–671, January 2001.

M. Sullivan, B. Mobasher, B. Chan, L. Cram, R. Ellis, M. Treyer, and A. Hopkins. A Comparison of Independent Star Formation Diagnostics for an Ultraviolet-selected Sample of Nearby Galaxies. ApJ, 558:72–80, September 2001.

M. Sullivan, M. A. Treyer, R. S. Ellis, T. J. Bridges, B. Milliard, and J. Donas. An ultraviolet-selected galaxy redshift survey - II. The physical nature of star formation in an enlarged sample. MNRAS, 312:442–464, February 2000.

T. T. Takeuchi, T. T. Ishii, H. Hirashita, K. Yoshikawa, H. Matsuhara, K. Kawara, and H. Okuda. Exploring Galaxy Evolution from Infrared Number Counts and Cosmic Infrared Background. PASJ, 53:37–52, February 2001.

G. Tenorio-Tagle, S. A. Silich, D. Kunth, E. Terlevich, and R. Terlevich. The evolution of superbubbles and the detection of Lyα in star-forming galaxies. MNRAS, 309:332–342, October 1999.

H. I. Teplitz, N. R. Collins, J. P. Gardner, R. S. Hill, and J. Rhodes. Emission-Line

Galaxies in the STIS Parallel Survey. II. Star Formation Density. ApJ, 589:704–708, June 2003.

T. X. Thuan and J. E. Gunn. A new four-color intermediate-band photometric system. PASP, 88:543–547, August 1976.

B. M. Tinsley. Evolution of the Stars and Gas in Galaxies. ApJ, 151:547–+, February 1968.

D. Tody. IRAF in the Nineties. In *ASP Conf. Ser. 52: Astronomical Data Analysis Software and Systems II*, page 173, 1993.

L. Tresse and S. J. Maddox. The H alpha Luminosity Function and Star Formation Rate at Z approximately 0.2. ApJ, 495:691–+, March 1998.

L. Tresse, C. Rola, F. Hammer, G. Stasinska, O. Le Fevre, S. J. Lilly, and D. Crampton. The Canada-France Redshift Survey - XII. Nature of emission-line field galaxy population up to z=0.3. MNRAS, 281:847–870, August 1996.

R. A. M. Walterbos and P. B. W. Schwering. Infrared emission from interstellar dust in the Andromeda Galaxy. A&A, 180:27–49, June 1987.

P. Westera, F. Cuisinier, E. Telles, and C. Kehrig. Stellar populations in HII galaxies. A&A, 423:133–146, 2004.

S. D. M. White and C. S. Frenk. Galaxy formation through hierarchical clustering. ApJ, 379:52–79, September 1991.

R. E. Williams, B. Blacker, M. Dickinson, W. V. D. Dixon, H. C. Ferguson, A. S. Fruchter, M. Giavalisco, R. L. Gilliland, I. Heyer, R. Katsanis, Z. Levay, R. A. Lucas, D. B. McElroy, L. Petro, M. Postman, H. Adorf, and R. Hook. The Hubble Deep Field: Observations, Data Reduction, and Galaxy Photometry. AJ, 112:1335–+, October 1996.

D. J. Wilman, M. L. Balogh, R. G. Bower, J. S. Mulchaey, A. Oemler, R. G. Carlberg, S. L. Morris, and R. J. Whitaker. Galaxy groups at $0.3 \leq z \leq 0.55$ - I. Group properties. MNRAS, 358:71–87, March 2005.

G. Wilson, L. L. Cowie, A. J. Barger, and D. J. Burke. Star Formation History since z=1.5 as Inferred from Rest-Frame Ultraviolet Luminosity Density Evolution. AJ, 124: 1258–1265, September 2002.

G. Worthey, S. M. Faber, J. J. Gonzalez, and D. Burstein. Old stellar populations. 5: Absorption feature indices for the complete LICK/IDS sample of stars. ApJS, 94:687–722, October 1994.

R. F. G. Wyse, G. Gilmore, M. L. Houdashelt, S. Feltzing, L. Hebb, J. S. Gallagher, and T. A. Smecker-Hane. Faint stars in the Ursa Minor dwarf spheroidal galaxy: implications for the low-mass stellar initial mass function at high redshift. *New Astronomy*, 7:395–433, October 2002.

C. Xu, U. Lisenfeld, H. J. Volk, and E. Wunderlich. Star-formation histories and the mass-normalized FIR/ratio correlation in late-type galaxies. A&A, 282:19–33, February 1994.

H. K. C. Yee. A faint-galaxy photometry and image-analysis system. PASP, 103:396–411, April 1991.

H. K. C. Yee, E. Ellingson, and R. G. Carlberg. The CNOC Cluster Redshift Survey Catalogs. I. Observational Strategy and Data Reduction Techniques. ApJS, 102:269–+, February 1996.

H. K. C. Yee, S. L. Morris, H. Lin, R. G. Carlberg, P. B. Hall, M. Sawicki, D. R. Patton, G. D. Wirth, E. Ellingson, and C. W. Shepherd. The CNOC2 Field Galaxy Redshift Survey. I. The Survey and the Catalog for the Patch CNOC 0223+00. ApJS, 129: 475–492, August 2000.

D. G. York, J. Adelman, J. E. Anderson, S. F. Anderson, J. Annis, N. A. Bahcall, J. A. Bakken, R. Barkhouser, S. Bastian, E. Berman, W. N. Boroski, S. Bracker, C. Briegel, J. W. Briggs, J. Brinkmann, R. Brunner, S. Burles, L. Carey, M. A. Carr, F. J. Castander, B. Chen, P. L. Colestock, A. J. Connolly, J. H. Crocker, I. Csabai, P. C. Czarapata, J. E. Davis, M. Doi, T. Dombeck, D. Eisenstein, N. Ellman, B. R. Elms, M. L. Evans, X. Fan, G. R. Federwitz, L. Fiscelli, S. Friedman, J. A. Frieman, M. Fukugita, B. Gillespie, J. E. Gunn, V. K. Gurbani, E. de Haas, M. Haldeman, F. H. Harris,

J. Hayes, T. M. Heckman, G. S. Hennessy, R. B. Hindsley, S. Holm, D. J. Holmgren, C.-h. Huang, C. Hull, D. Husby, S.-I. Ichikawa, T. Ichikawa, Ž. Ivezić, S. Kent, R. S. J. Kim, E. Kinney, M. Klaene, A. N. Kleinman, S. Kleinman, G. R. Knapp, J. Korienek, R. G. Kron, P. Z. Kunszt, D. Q. Lamb, B. Lee, R. F. Leger, S. Limmongkol, C. Lindenmeyer, D. C. Long, C. Loomis, J. Loveday, R. Lucinio, R. H. Lupton, B. MacKinnon, E. J. Mannery, P. M. Mantsch, B. Margon, P. McGehee, T. A. McKay, A. Meiksin, A. Merelli, D. G. Monet, J. A. Munn, V. K. Narayanan, T. Nash, E. Neilsen, R. Neswold, H. J. Newberg, R. C. Nichol, T. Nicinski, M. Nonino, N. Okada, S. Okamura, J. P. Ostriker, R. Owen, A. G. Pauls, J. Peoples, R. L. Peterson, D. Petravick, J. R. Pier, A. Pope, R. Pordes, A. Prosapio, R. Rechenmacher, T. R. Quinn, G. T. Richards, M. W. Richmond, C. H. Rivetta, C. M. Rockosi, K. Ruthmansdorfer, D. Sandford, D. J. Schlegel, D. P. Schneider, M. Sekiguchi, G. Sergey, K. Shimasaku, W. A. Siegmund, S. Smee, J. A. Smith, S. Snedden, R. Stone, C. Stoughton, M. A. Strauss, C. Stubbs, M. SubbaRao, A. S. Szalay, I. Szapudi, G. P. Szokoly, A. R. Thakar, C. Tremonti, D. L. Tucker, A. Uomoto, D. Vanden Berk, M. S. Vogeley, P. Waddell, S.-i. Wang, M. Watanabe, D. H. Weinberg, B. Yanny, and N. Yasuda. The Sloan Digital Sky Survey: Technical Summary. AJ, 120:1579–1587, September 2000.

M. Zeilik and S. Gregory. *Introductory Astronomy and Astrophysics.* Introductory Astronomy and Astrophysics, 4/e, published by Harcourt College Publishers, 1998; ISBN number: 0-03-006228-4, 1998.